Process-structure-property relationship of edible oil-based foams investigated with Process Analytical Technologies (PAT) tools and X-ray tomography

Lorenzo Metilli

Submitted in accordance with the requirements for the degree of

Doctor of Philosophy

The University of Leeds

School of Food Science and Nutrition

October 2021

The candidate confirms that the work submitted is his own, except where work that has formed part of jointly-authored publication has been included. The contribution of the candidate and the other authors to this work has been explicitly indicated below. The candidate confirms that appropriate credit has been given within the thesis where reference has been made to the work of others. Details of the jointly-authored publications and the contribution of the candidate and the other authors to the work are outlined on the page iv.

List of publications and corresponding thesis chapters

Chapter 3

Metilli L, Lazidis A, Francis M, Marty-Terrade S, Ray J, Simone E. The Effect of Crystallization Conditions on the Structural Properties of Oleofoams Made of Cocoa Butter Crystals and High Oleic Sunflower Oil. *Cryst. Growth Des.* 2021, 21, 3, 1562–1575.

Chapter 4

Metilli L, Morris L, Lazidis A, Marty-Terrade S, Povey M., Simone E. Real-time monitoring of fat crystallization using pulsed acoustic spectroscopy.

Manuscript to be submitted to Soft Matter

Chapter 5

Metilli L, Storm M, Bodey AJ, Wanelik K, Tyler AII, Lazidis A, Simone E. Investigating the microstructure of soft, microporous matter with synchrotron X-ray tomography. *Mater. Charact.* 2021;180:111408

Chapter 6

Metilli L, Storm M, Marathe S., Lazidis A, Marty-Terrade S., Simone E. Effect of aeration, storage and heating on the microstructure of cocoa butter oleofoams probed by X-Ray Tomography and Radiography

Manuscript to be submitted to ACS Applied Materials and Interfaces.

Details of authorship contributions:

The Effect of Crystallization Conditions on the Structural Properties of Oleofoams Made of Cocoa Butter Crystals and High Oleic Sunflower Oil

The experimental work in this paper was carried out by myself; Dr. Elena Simone helped by discussing the design of the experiments. Data analysis, and writing was done by myself as well. The authors contributed with comments on the manuscript during its preparation.

Real-time monitoring of fat crystallization using pulsed acoustic spectroscopy

The experimental work was carried out mostly by myself. Liam Morris developed the MATLAB code, and data interpretation of the ultrasound-differential scanning calorimetry (US-DSC) section presented in the chapter. The other authors provided useful insight for the discussion of the data, and contributed to the manuscript by reviewing it during its preparation

Investigating the microstructure of soft, microporous matter with synchrotron X-ray Tomography

The experiments were carried out by myself. Andrew Bodey, Malte Storm and Kaz Wanelik assisted with the operation of the synchrotron beamline, and provided useful insights for developing the method presented in the chapter. Data analysis and writing was done by myself as well. The authors contributed with comments on the manuscript during its preparation.

Effect of aeration, storage and heating on the microstructure of cocoa butter oleofoams probed by X-Ray Tomography and Radiography

The experiments were carried out by myself. Dr. Elena Simone, Panayiotis Klitou and Monty Reed are acknowledged for their help during the synchrotron beamtime. Data analysis and writing was done by myself as well. The authors contributed with comments on the manuscript during its preparation. All of the papers were read and corrected mainly by my main academic supervisor, Dr. Elena Simone, and by my industrial supervisors (Dr. Aris Lazidis and Dr. Stephanie Marty-Terrade).

Rationale for submitting the thesis in an alternative format

The thesis will be submitted in an alternative format (thesis by publication), due to the fact that my experimental work is divided into four chapters, each one formatted as an original, experimental journal publication in which I am the first author. Two of the four manuscripts are already published in peer-reviewed journal (Crystal Growth and Design, and Materials Characterization journals), and the remaining two are ready for submission. As such, I meet the requirements set by the Faculty of university for submitting the thesis in an alternative format. I performed the majority of the experiments described in the chapters. The papers or manuscripts were written by me, and are all co-authored with my main academic supervisor and with my industrial supervisors. The thesis will be organized as required by the Faculty of Earth and Environment protocol for alternative format, and will include an introduction to describe the context of research, the state of the art and the current gap of knowledge in the field, and the approach adopted throughout the research. The introduction will be followed by a literature review chapter, containing the fundamental aspects of the topics investigated in this dissertation, including the main characterization techniques. Afterwards, there will be four experimental chapters, represented by the four publications mentioned earlier, each one including its own introduction with literature review, materials and method, results and discussion and references at the end of each chapter. The supporting information of each chapter will be added in an appendix at the end of the dissertation. The results and discussion of each chapter will therefore constitute a coherent body of work, where all the findings are linked and summarized in the Conclusions, and provide directions for future work. The thesis will also include all the sections required by the alternative format thesis, such as title page, intellectual property and publications page, acknowledgements page, abstracts, list of contents and abbreviation, references and appendices.

List of accepted conference abstracts and awards

Poster presentations

L. Metilli, E. Simone, (2018) State of the art and new developments in fat crystallization. *6th International School of Crystallization: Drugs, Foods, Agrochemicals, Minerals, New Materials. Granada, Spain.*

L. Metilli, M. Francis, M. Povey, A. Lazidis, S. Marty-Terrade, E. Simone, (2018) Characterization of edible oil foams and fast inline measurements using acoustic and ultrasound spectroscopy. *High Resolution Ultrasonic Spectroscopy for Analysis of Biomolecular Processes, Brno, Czech Republic*.

L. Metilli, M. Francis, M. Povey, A. Lazidis, S. Marty-Terrade, E. Simone, (2019) Characterization of edible oil foams and fast inline measurements using acoustic and ultrasound spectroscopy. *Physics in Food Manufacturing, Campden, United Kingdom.*

L. Metilli, M. Francis, M. Povey, A. Lazidis, S. Marty-Terrade, E. Simone, (2019) Characterization of edible oil foams and fast inline measurements using acoustic and ultrasound spectroscopy. *Food innovation for delivering health, nutrition and wellness, Leeds, UK.*

L. Metilli, M. Francis, M. Povey, A. Lazidis, S. Marty-Terrade, E. Simone, (2019) Characterization of edible oil foams and fast inline measurements using acoustic and ultrasound spectroscopy. *Soft Matter and Functional Interfaces Showcase, Leeds, UK.*

L. Metilli, M. Francis, M. Povey, A. Lazidis, S. Marty-Terrade, E. Simone, (2019) Characterization of edible oil foams and fast inline measurements using acoustic and ultrasound spectroscopy. *8th Delivery of Functionality in Food Formulation, Porto, Portugal.*

L. Metilli, M. Povey, A. Lazidis, S. Marty-Terrade, E. Simone, (2021) Effects of crystallization conditions on the physical properties of cocoa butter–based oleofoams: a multi-technique approach. *International Symposium on Industrial Crystallization, Online.*

L. Metilli, M. Povey, A. Lazidis, S. Marty-Terrade, E. Simone, (2021) Effects of crystallization conditions on the physical properties of cocoa butter–based oleofoams: a multi-technique approach. *11th Crystalline Forms*, *Online.*

Oral presentations

L. Metilli, M. Francis, M. Povey, A. Lazidis, S. Marty-Terrade, E. Simone, (2019) Preparation and physical characterization of edible oil foams. *12th European Conference of Chemical Engineering, Firenze, Italy*

Metilli L, Storm M, Bodey AJ, Wanelik K, Tyler AII, Lazidis A, Simone E. (2020) Investigating the microstructure of soft, microporous matter with synchrotron X-ray tomography. *Food Science PhD Conference, Online*

L. Metilli, M. Povey, A. Lazidis, S. Marty-Terrade, E. Simone, (2021) Monitoring fat crystallization with ultrasonic velocimetry. *British Association of Crystal Growth, Online*

Awards

Travel Grant for: *6th International School of Crystallization: Drugs, Foods, Agrochemicals, Minerals, New Materials. Granada, Spain.*

2nd Poster prize for: L. Metilli, M. Francis, M. Povey, A. Lazidis, S. Marty-Terrade, E. Simone, (2019) Characterization of edible oil foams and fast inline measurements using acoustic and ultrasound spectroscopy. *Food innovation for delivering health, nutrition and wellness, Leeds, UK.*

Best oral presentation for: Metilli L, Storm M, Bodey AJ, Wanelik K, Tyler AII, Lazidis A, Simone E. (2020) Investigating the microstructure of soft, microporous matter with synchrotron X-ray tomography. *Food Science PhD Conference, Online*

Acknowledgements

The realisation of this PhD thesis deserves several acknowledgements, as it was no easy task and I could not had done it without the precious help of other amazing human beings.

First and foremost, I want to thank my main supervisor, Dr. Elena Simone, who provided unending guidance and support to me in all these years. I was struck immediately with her passion to do research in a competent, enthusiastic fashion, and always aimed at being as bright and excellent as she is. Thank you for all your time and patience you had with me, I hope this work makes you proud!

I want to thank also my other supervisors, Prof. Megan Povey, whose wisdom and passion for science was a guiding beacon through my experience at Leeds. Dr. Melvin Holmes is also acknowledged, for sharing his vast knowledge on acoustics and maths, which I sincerely appreciated! I want also to thank my industrial supervisors from Nestlé, Dr. Aris Lazidis and Dr. Stephanie Marty-Terrade, for all the useful discussion and support in this project. It was quite an experience for me to collaborate with such experts from an established company like Nestlé. My gratitude goes also to Dr. Arwen Tyler and Professor Michael Rappolt, for all their support and knowledge while we were working at the synchrotron.

I want to express my gratitude to other fellow PhDs and post-doctoral researchers, who helped me not only in the laboratory, but also outside of it: Panayiotis Klitou, Liam Morris, Sam Stubley, Dr. Alessandro Gulotta and Dr. Teresa Roncal-Herrero. Such an amazing team!

Then, a special “grazie!” goes to all the Italians from Maths, who took me in and made me feel at home, even when I was far away from it. El Pub(e) is acknowledged for all the beers at the Fenton, home-made pizzas at Casaitalia, the music and cineforums, and occasional bottle-breaking in the middle of the street at 2 am. So thank you Leonardo, Giovanni, Rosario, Gabriele, Francesco, Andrea, Matteo, Luca, Celeste and Dario (in particular for the maths lessons!).

Then, the most heartfelt thanks is given to my family, where I was taught the values of hard, dedicated work. Thank you Ornella, Riccardo and especially thank you, Diego. I hope that you can get a copy of this, wherever you are right now.

Abstract

Oil-based foams, also called oleofoams, are a novel type of soft matter material with great potential in the field of foods, cosmetic and pharmaceuticals. Oleofoams comprise a liquid oil phase, and dispersed gas bubbles which are stabilized by surfactant crystals through a Pickering mechanism. Oleofoams are routinely prepared through the aeration of a dispersion of fat crystals in oil, also called oleogels. Compared to their aqueous counterparts, however, limited literature is available on oleofoams, due to the narrow range of suitable surfactants able to stabilize the air-oil interface. In order to promote the use of oleofoams in the manufacturing industry, further research is required, both fundamental and applied. The physical properties of oleofoams are affected by the properties of the stabilizing crystals (size, shape, polymorphism and concentration), the processing conditions (i.e., crystallization and aeration), as well as by the microstructure, that is, the three-dimensional arrangement of the gas bubbles, fat crystals and oil.

In this doctoral project, the complex process-structure-property relationship of cocoa butter–based oleofoams was investigated using online Process Analytical Technologies (PAT) tools, synchrotron radiation X-ray tomography and a wide range of traditional offline characterization techniques such as differential scanning calorimetry, polarized optical microscopy and small angle X-ray scattering. The effect of the crystallization conditions on the properties of the oleofoams were studied by preparing cocoa butter (CB) and high oleic sunflower oil (HOSO) oleogels by varying the CB concentration and cooling rate. The crystallization was carried out in a small-scale vessel and monitored *in-situ* with light turbidimetry and pulsed acoustic spectroscopy. The oleogels were then aerated with a planetary mixer, and the air incorporation was measured gravimetrically with a cup of fixed volume. Both the oleogels and oleofoams were characterized *ex-situ* using optical and electron microscopy, X-ray diffraction, differential scanning calorimetry, oscillatory rheology and nuclear magnetic resonance. Results showed that CB crystallized as spherical aggregates of crystalline nanoplatelets (CNPs) in the β(V) form. The nucleation was detected by light turbidimetry, whereas crystal growth could be monitored also by a novel acoustic probe, which was also used to measure the solid fat content (SFC%) through a novel predictive machine learning model. The aeration process broke the spherical aggregates to individual CNPs of similar size, which stabilized the entrained air bubbles by adsorbing

at the air/oil interface. Therefore, the main parameter affecting the oleofoam aeration was the total amount of solid cocoa butter crystals (e.g., SFC%). The rearrangement of the crystals around the air bubbles caused an increase in the G' and G" moduli by an order of magnitude for 15% CB samples, while for 22% and 30% CB samples the viscoelasticity was not significantly affected. Nevertheless, all oleofoams samples had a density reduced by a factor of 3 to 1.6, and displayed stability against oil drainage for a least 3 months.

Due to the soft and opaque appearance of oleofoams, a novel methodology to characterize their internal microstructure was developed. The method was based on the use of synchrotron radiation X-ray tomography and radiography, combined with cryogenic conditions to prevent sample deformation and melting. Temperature control on the sample also enabled the study of the effects of heating on the microstructure in real time, through radiography images. The methodology was applied to the study of two reference samples, one with low and one with high CB %, in relation to the aeration time, storage conditions and heating. The aeration resulted in similar bubble size distributions for both samples, whereas the thickness of the continuous phase decreased in favour of air incorporation, which was higher for samples with lower CB%. Samples with higher CB% displayed higher stability against air loss and bubble size disproportionation after 3 months and 15 months of storage. For both samples, an increase in the bubble sphericity was observed, resulting from the dissolution of smaller CNPs in favour of larger crystal aggregates. Finally, the heating caused bubble coalescence in the oleofoam microstructure; samples with low % of CB were affected more significantly, due to the lower amount of stabilizing crystals. The bubble size distribution increased, as well as the bubble sphericity, due to the dissolution of the smaller CNPs adsorbed at the interface, and due to the less dense packing of air bubbles.

The results gathered during this doctoral project aim at expanding the fundamental knowledge about oleofoams, both regarding the effect of the processing conditions, also via the development of characterization techniques that can probe the internal microstructure of oleofoams and how it evolved during manufacturing, storage and external stimuli.

Contents

List of Figures

List of Tables

List of Abbreviations

CB	Cocoa Butter
HOSO	High Oleic Sunflower Oil
CNP	Crystalline Nanoplatelet
API	Active Pharmaceutical Ingredient
PLM	Polarized Light Microscopy
CSLM	Confocal Scanning Laser Microscopy
SEM	Scanning Electron Microscopy
pNMR	Pulsed Nuclear Magnetic Resonance
PAT	Process Analytical Technologies
DSC	Differential Scanning Calorimetry
SAXS	Small Angle X-ray Scattering
WAXS	Wide Angle X-ray Scattering
XRD	X-ray Diffraction
XCT	X-ray Tomography
XRR	X-ray Radiography
TAG	Triacylglyceride
FA	Fatty Acid
VOI	Volume of Interest

Nomenclature

k_B	Boltzmann Constant
λ	Wavelength
f	Frequency
T_{Cr}	Crystallization Temperature
T_{Cr}	Melting Temperature
$OR(\%)$	Overrun
G'	Storage Modulus
$G"$	Loss Modulus
c	Velocity of Sound
ρ	Density
κ	Adiabatic Compressibility
$SFC(\%)$	Solid Fat Content (%)
ϕ	Air Volume Fraction
D_{eq}	Bubble Equivalent Diameter
Φ	Sphericity
$D[4,3]$	Volume-weighted mean diameter

Chapter 1: Introduction

1.1 Background

The term “soft matter” is used to describe a wide range of materials which span the range between nanometre and micrometre, and are found in a state of constant fluctuation called Brownian motion. The length scale of the soft matter regime is delimited, on the lower end, by the atomic scale which is dominated by quantum effects and, on the upper end, by the granular scale (millimetres) which is affected by gravity effects. Soft matter encompasses materials such as gels, emulsions, foams, liquid crystals, synthetic and biological polymers, as well as bacteria and organelles, to name a few. The weak nature of its interactions, such as hydrogen bonding, van der Waals and London forces, endows soft matter with another relevant property, which is self-assembly. A typical example are surfactant molecules in soaps and detergents: these exhibit a rich variety of possible self-assembled structures that includes micelles, hexagonal and lamellar liquid phases, which form upon changes in the surfactant concentration and/or temperature (Raut et al., 2008). As such, apparently simple soft matter materials exhibit interesting macroscopic properties, such as a complex rheological behaviour. Finally, as the interactions in soft matter are broken and reformed with energies comparable to thermal fluctuations, soft materials are often found in non-equilibrium states with relatively long relaxation times, exhibiting a complex energetic landscape with many local minima (van der Gucht, 2018).

Soft matter may be divided in three broad categories: colloids, polymers, and surfactants, although this division is not clear-cut for some examples (Yakhmi, 2011). Colloids feature a dispersion of solid particles, liquid droplets or gas bubbles (the dispersed phase) in a medium (the continuous phase) that can also be liquid, solid, or gaseous. The length scales of the dispersed phase are between the nanometre and the micrometre. The occurrence of different phases leads to the creation of interfaces, a phenomenon that has an inherent energy cost, called surface tension. Furthermore, the phases have likely different densities. These two features of soft colloidal matter cause thermodynamic instability, which leads eventually to phase separation. To slow down such process, amphiphilic molecules that place themselves at interfaces can be

added to lower the surface tension (Jones, 2002). Common types of colloids include single and double emulsions, liquid and solid foams, suspensions and aerosols.

Soft colloids are ubiquitous in many consumers products, such as food (Vilgis, 2015), cosmetics (Zoabi et al., 2021) and pharmaceuticals (Bonacucina et al., 2009; Pavoni et al., 2020). In the case of foods, common examples include milk, which contains fat droplets stabilized by lipoproteins dispersed in water, or bread dough, which is a viscous suspension of starch granules in water. As soft colloids, food materials are susceptible to a wide variety of transformations and phase transitions induced by external stimuli, such as shear, heating, changes in humidity and pH, which has been extensively exploited in food technology. At the same time, however, foods are subject to decay, which causes loss in functionality, nutritional profile and overall quality (Ubbink, 2012).

The engineering of soft materials such as foods started early back in human history, driven by the need of preserving foods against spoilage, or to increase their nutritional value. Nowadays, food scientists are faced with several important challenges: including feeding a growing population while reducing the calorific intake per person in developed countries, or providing adequate and healthy access to food in underdeveloped countries. At the same time, food production (from harvesting or farming to food processing, packaging, delivery and consumption) must become more sustainable for the environment and ethically handled for local communities, (McClements, 2020). Reformulation of existing food products is also paramount, due to continuously updated dietary guidelines (EFSA, 2010; FAO, 2008) as well as changing consumers preferences, for example in relation to ingredients deemed “synthetic” or generally perceived as detrimental to human health (Asioli et al., 2017; Hartmann et al., 2018). On the other hand, personalized nutrition is on the rise, with consumers seeking enhanced nutritional properties from the so called “functional foods”, which contain additional bioactive ingredients (Ubbink, 2012; Wells et al., 2017).

In order to address these challenges, a strong understanding of the underlying soft matter physics and chemistry of foods is required, as well as how foods interact with the human body, both at the sensorial and nutritional level. Control over food material properties must be maintained also at the industrial scale, in

order to enhance the final product quality and improve the efficiency of the process. This specific point may be addressed through the application of process analytical technologies (PAT) in the food industry (Rathore et al., 2010). This term is used to describe collectively analytical techniques, mathematical approaches and design strategies to provide real-time measurements of critical quality and performance attributes of materials and processes, with the aim of ensuring final product quality (Food and Drug Administration, 2004). As a result, the quality is "built into" the process, rather than tested on final products. While for the biopharmaceutical and chemical sector the use of PAT is established and encouraged, the food industry has lagged behind in its implementation (Rathore & Kapoor, 2016).

One of the major efforts in food science and nutrition is to regulate the intake of three health-sensitive ingredients in foods: salt, sugar and fat, without altering the macroscopic properties of the food material and compromising consumer acceptance (Belc et al., 2018). Salt may be decreased in food products through the ingenuous design of single or double emulsions, which enhance saltiness perception during mastication (Wang et al., 2021) or by reducing the size of salt crystals to improve dissolution rates in the mouth (Hurst et al., 2021). Sugars, or more specifically, sucrose, may be replaced with mixtures of natural or artificial sweeteners and bulking agents, such as complex carbohydrates (Palzer, 2017). Reduction or removal of saturated fat (*i.e.*, "solid" fat) represents another challenge, as it affects significantly the rheology of food materials, as well as dissolving lipophilic vitamins in its matrix. Chocolate, for example, owes its plasticity and gloss appearance to the solid fat phase of cocoa butter (Ewens et al., 2021). One particularly successful strategy to reduce the amount of saturated fats in food is oleogelation, which imparts structure to liquid oils through the addition of suitable gelator molecules or particles, such as substituted acyl glycerides, waxes, nanocellulose, sterols and fatty alcohols, in concentrations as low as 1% by weight ratio to the liquid oil (Co & Marangoni, 2012; Rogers et al., 2009). The structuring of the oils occurs as the result of a self-assembly process of the gelator that forms a three-dimensional, supramolecular network that entraps the liquid oils and provides solid-like behaviour to the material (Patel & Dewettinck, 2016). The stability and resulting viscoelasticity of oleogels are strongly dependent on the type of gelator, and the processing conditions applied to produce this type of material. Moreover, oleogels have shown promising efficacy in the delivery

of lipid-soluble bioactive molecules (Singh et al., 2017), extending their possible uses to the field of pharmaceuticals and cosmetic products.

The approach of oil structuring may be extended further by incorporating stable gas bubbles, which lower the calorific density of the material, while providing novel rheological properties and texture to the oil. Oil-continuous foams, also termed oleofoams, are an emerging type of soft matter, which comprise a liquid oil phase, and a dispersed gas phase where the air bubbles are stabilized by fat crystals (Pickering effect combined with bulk stabilization) or surfactant molecules. Therefore, oleogels may be used as a precursor for the production of oleofoams (Fameau & Saint-Jalmes, 2017; Heymans et al., 2017). Compared to aqueous foams, the available literature on oleofoams is limited, due to the narrower choice of suitable stabilizers for the air/oil interface. Over the last five years, however, several scientific articles were published on the use of food-grade fat crystals to produce oleofoams with high air volume fraction and stability (Binks & Vishal, 2021); Nevertheless, further research, both fundamental and applied, is required to promote the use of oleofoams in consumer products, such as low-fat confectionery, cosmetic products and as drug delivery systems for topical applications (Fameau & Binks, 2021). The main focus is on the "process-structure-function" relationship, which needs to be thoroughly investigated to enable the efficient production of materials with tailored properties (Aguilera, 2005; Herremans et al., 2013). More specifically, it is necessary to understand how the microstructure of the oleofoam is affected, on one side, from the processing conditions of crystallization of the oleogel precursor and its aeration and, on the other side, how the microstructure affects its functionality (*e.g.*, stability, rheology, efficiency of encapsulation of active ingredients and their release).

The properties of the fat crystals – size, shape, and polymorphism, and their concentration – all affect the foamability, foam stability and rheology of the oleofoams (Heymans et al., 2017). Hence, controlling the crystallization of fat crystals is essential to ensure adequate oleofoam microstructure. The crystallization of lipids, however, is a complex phenomenon, due to the multi-component nature of natural fats and oils, and the occurrence of several crystal polymorphs. The presence of impurities, and the effect of shear during crystallization also affect the crystallization of fats (Himawan et al., 2006; Sato et al., 2013). The techniques

used to study fat crystallization feature mostly *ex-situ* methods, such as nuclear magnetic resonance, rheology, optical microscopy (Rigolle et al., 2018). Ultrasonic spectroscopy is a fast, non-invasive, non-destructive technique that has shown promising application for monitoring fat crystallization and to measure the total amount of solids (solid fat content, SFC%) (Martini et al.2005); however, its use in large scale manufacturing as a PAT tool is not yet commonplace (Morris et al., 2021).

Another challenge in the characterization of oleofoams is given by their soft nature and opaque appearance. Probing the internal microstructure of oleofoams in its native state is not trivial, making it difficult to relate its features – gas bubbles, fat crystals and liquid oil – to both the processing conditions, and to the macroscopic properties of the material. Advanced techniques able to image soft, multiphasic matter in a non-invasive fashion are required for this task (Metilli et al., 2020).

Therefore, the main focus of this doctoral project is on the investigation of the process-structure-function of a model oleofoam system, comprising cocoa butter and sunflower oil. To achieve this objective, two approaches were applied: the use of PAT tools to monitor crystallization of the oleogel precursor, and the development of a novel methodology to image opaque, soft microporous matter.

1.2 Aims of the thesis

This thesis will try to address the following research questions:

1. What are the crystal properties that more significantly affect the processability and functionality of cocoa butter–based oleofoams in terms of foamability and foam stability against phase separation, melting point, viscoelastic profile, morphology and stability of air bubbles?
2. Can ultrasound spectroscopy, which is a non-invasive, non-destructive technique, be implemented as an *in situ*, real-time tool to monitor fat crystallization, and to extract quantitative information about the amount of crystals in the oleogel?

3. What is a suitable technique for investigating the internal microstructure of oleofoams, which are soft, low-melting and opaque materials? What parameters may be obtained and used to describe the microstructure of oleofoams?
4. How does the three-dimensional microstructure of oleofoams evolve during manufacturing, storage and upon application of external stimuli such as heating?

1.3 Delivery Plan

The following delivery plan aims at answering the previous research questions, by applying a multi-technique experimental approach to the study of oleofoams:

1. Crystallization of cocoa butter and sunflower oil under different processing conditions (*i.e.*, weight ratios and cooling rates) to obtain oleogels with diverse crystalline properties, which will be then aerated using a mechanical mixer.
2. Analysis of the properties of the oleogels and oleofoams with optical and electron microscopy, X-Ray diffraction, differential scanning calorimetry and oscillatory rheology.
3. Crystallization of cocoa butter and sunflower oil oleogels in a laboratory scale vessel (500-1000 mL), under shear, and monitoring the process with light turbidimetry and pulsed acoustic spectroscopy. Evaluation of the turbidimetry and acoustic parameters to provide a model to measure the solid fat content (SFC%) during crystallization, and validate it with ex-situ pulsed nuclear magnetic resonance (*p*NMR) on crystallized oleogels.
4. Development of a methodology to probe the internal microstructure of opaque, soft microporous matter with synchrotron X-Ray tomography and radiography. Optimization of the setup parameters, such as exposure time, number of projections, and creation of a reconstruction workflow to obtain high quality three-dimensional images of oleofoam samples. Development of a post-processing workflow to segment the air phase from the continuous phase from tomography data, and to obtain relevant descriptors of both phases from a set of reference oleofoam samples.

5. Application of the developed methodology for imaging soft, microporous matter for the study of the microstructure of two oleofoam samples, in relation to the aeration time, storage conditions, and thermal treatment.

1.4 Thesis Outline

Chapter 2 – *Background*

Chapter 2 is a literature review focused on the fundamental aspects of fat crystallization, particle-stabilized foams, and the physics of the characterization techniques used in this doctoral project.

Chapter 3 - *The Effect of Crystallization Conditions on the Structural Properties of Oleofoams Made of Cocoa Butter Crystals and High Oleic Sunflower Oil*

This chapter contains an initial study into the effects of different crystallization conditions of cocoa butter and sunflower oil on the crystal properties of the resulting oleogels (size, shape, polymorphism) and how those affected, in turn, the foamability and foam stability of the respective oleofoams. The crystallization process was carried out in a 300 mL vessel under shear and characterized with light turbidimetry. The properties of the oleogel and oleofoams were investigated with a multi-technique approach, including optical and electron microscopy, X-Ray diffraction and differential scanning calorimetry, and oscillatory rheology. This chapter was published in *Cryst. Growth Des.* 2021, 21, 3, 1562–1575.

Chapter 4 - *Real-time monitoring of fat crystallization using pulsed acoustic spectroscopy*

This chapter introduces the use of pulse acoustic spectroscopy as a process analytical technology (PAT) tool to monitor fat crystallization *in situ* in a non-invasive, non-destructive fashion. In particular, the acoustic data were used to calculate the solid fat content (SFC%) during the crystallization process. SFC(%) is one relevant parameter that affects the foamability and foam stability of cocoa butter–based oleofoams. The technique was applied to a small-scale crystallization vessel (1L volume) and validated with light turbidimetry and pulsed nuclear magnetic resonance (*p*NMR). The SFC% was calculated by applying a machine learning based prediction model. This chapter will be submitted to Chemical Engineering Science or a similar journal.

Chapter 5 - *Investigating the microstructure of soft, microporous matter with synchrotron X-ray tomography.*

In this chapter, a novel methodology to probe the internal microstructure of soft, microporous matter with X-Ray tomography is presented. Soft microporous materials are challenging to characterize using commonplace imaging techniques in their native state, as the samples are optically opaque, have melting point close to room or body temperature, and deform under small levels of shear. In this chapter the optimal experimental conditions for tomography and radiography (i.e., sample preparation, exposure times, number of projections, reconstruction method) to provide high quality, three-dimensional images of the internal microstructure of oleofoams were determined. The tomography data was analysed with a post-processing workflow to extract meaningful parameters about the dispersed gas phase – bubble size and shape distribution, air volume fraction – as well as the thickness of the continuous oleogel phase, which may be used to link the processing conditions to the resulting microstructure of oleofoams. This chapter was published in *Mater. Charact.* 2021;180:111408.

Chapter 6 - *Effect of aeration, storage and heating on the microstructure of cocoa butter oleofoams probed by X-Ray Tomography and Radiography*

The methodology developed in the previous chapter was applied to the systematic study of the microstructure of two reference oleofoam samples – one with low (15% w/w) and one with high (30% w/w) SFC% - in relation to the aeration time, storage, and response to thermal stimuli (e.g., heating). In particular, the evolution of the air phase and continuous phase was monitored throughout the aeration process, elucidating the effect of different SFC% in the material. The ageing of the samples was investigated by comparing the microstructure of the two reference samples after 3 and 15 months of storage, discussing in particular the changes occurring in the bubble size and shape distribution and in the oleogel thickness phase. Lastly, the effect of heating on the samples was studied in real-time using X-Ray radiography, which enable visualization of bubble coalescence. The heated microstructure was compared to the fresh microstructure by X-Ray tomography. This chapter will be submitted to a Material Science journal.

Chapter 7 – *Conclusions and future studies*

This section contains a summary and discussion of the findings obtained throughout the current doctoral project, as well as an outlook for new directions of research in the field.

Appendices – Appendices A, B and C provide the supporting information for Chapter 3, 5 and 6, respectively.

References

Aguilera, J. M. (2005). Why food micro structure? *Journal of Food Engineering*, *67*(1–2), 3–11. https://doi.org/10.1016/j.jfoodeng.2004.05.050

Asioli, D., Aschemann-Witzel, J., Caputo, V., Vecchio, R., Annunziata, A., Næs, T., & Varela, P. (2017). Making sense of the "clean label" trends: A review of consumer food choice behavior and discussion of industry implications. *Food Research International*, *99*(April), 58–71. https://doi.org/10.1016/j.foodres.2017.07.022

Belc, N., Smeu, I., Macri, A., Vallauri, D., & Flynn, K. (2018). Reformulating foods to meet current scientific knowledge about salt, sugar and fats. *Trends in Food Science and Technology*, *84*(October 2018), 25–28. https://doi.org/10.1016/j.tifs.2018.11.002

Binks, B. P., & Vishal, B. (2021). Particle-stabilized oil foams. *Advances in Colloid and Interface Science*, *291*, 102404. https://doi.org/10.1016/j.cis.2021.102404

Bonacucina, G., Cespi, M., Misici-Falzi, M., & Palmieri, G. F. (2009). Colloidal soft matter as drug delivery system. *Journal of Pharmaceutical Sciences*, *98*(1), 1–42. https://doi.org/10.1002/jps.21423

Co, E. D., & Marangoni, A. G. (2012). Organogels: An alternative edible oil-structuring method. *JAOCS, Journal of the American Oil Chemists' Society*, *89*(5), 749–780. https://doi.org/10.1007/s11746-012-2049-3

EFSA. (2010). Scientific Opinion on Dietary Reference Values for fats, including saturated fatty acids, polyunsaturated fatty acids, monounsaturated fatty acids, trans fatty acids, and cholesterol. *EFSA Journal*, *8*(3), 1–107. https://doi.org/10.2903/j.efsa.2010.1461

Ewens, H., Metilli, L., & Simone, E. (2021). Analysis of the effect of recent reformulation strategies on the

crystallization behaviour of cocoa butter and the structural properties of chocolate. *Current Research in Food Science*, *4*(November 2020), 105–114. https://doi.org/10.1016/j.crfs.2021.02.009

Fameau, A. L., & Binks, B. P. (2021). Aqueous and Oil Foams Stabilized by Surfactant Crystals: New Concepts and Perspectives. *Langmuir*, *37*(15), 4411–4418. https://doi.org/10.1021/acs.langmuir.1c00410

Fameau, A. L., & Saint-Jalmes, A. (2017). Non-aqueous foams: Current understanding on the formation and stability mechanisms. *Advances in Colloid and Interface Science*, *247*, 454–464. https://doi.org/10.1016/j.cis.2017.02.007

FAO. (2008). *Food and Agriculture Organization of the United Nations, Fats and fatty acids in human nutrition - Report of an expert consultation"*. *Fats and fatty acids in human nutrition* (Vol. 91). https://doi.org/I1953E/1/11.10

Food and Drug Administration. (2004). Guidance for Industry, PAT-A Framework for Innovative Pharmaceutical Development, Manufacturing and Quality Assurance, (September). Retrieved from http://www.fda.gov/downloads/Drugs/GuidanceComplianceRegulatoryInformation/Guidances/ucm070305.pdf

Hartmann, C., Hieke, S., Taper, C., & Siegrist, M. (2018). European consumer healthiness evaluation of 'Free-from' labelled food products. *Food Quality and Preference*, *68*(December 2017), 377–388. https://doi.org/10.1016/j.foodqual.2017.12.009

Herremans, E., Bongaers, E., Estrade, P., Gondek, E., Hertog, M., Jakubczyk, E., … Nicolaï, B. (2013). Microstructure-texture relationships of aerated sugar gels: Novel measurement techniques for analysis and control. *Innovative Food Science and Emerging Technologies*, *18*, 202–211. https://doi.org/10.1016/j.ifset.2013.02.003

Heymans, R., Tavernier, I., Dewettinck, K., & Van der Meeren, P. (2017). Crystal stabilization of edible oil foams. *Trends in Food Science and Technology*, *69*, 13–24. https://doi.org/10.1016/j.tifs.2017.08.015

Himawan, C., Starov, V. M., & Stapley, A. G. F. (2006). Thermodynamic and kinetic aspects of fat

crystallization, *Advances in Colloidal and Interface Science, 122*, 3–33. https://doi.org/10.1016/j.cis.2006.06.016

Hurst, K. E., Ayed, C., Derbenev, I. N., Hewson, L., & Fisk, I. D. (2021). Physicochemical design rules for the formulation of novel salt particles with optimised saltiness. *Food Chemistry*, *360*(January), 129990. https://doi.org/10.1016/j.foodchem.2021.129990

Jones, R. A. L. (2002). *Soft Condensed Matter*. First Edition, Oxford, Oxford University Press.

Martini, S., Herrera, M. L., & Marangoni, A. (2005). New technologies to determine solid fat content on-line. *JAOCS, Journal of the American Oil Chemists' Society*, *82*(5), 313–317. https://doi.org/10.1007/s11746-005-1072-7

McClements, D. J. (2020). Future foods: A manifesto for research priorities in structural design of foods. *Food and Function*, *11*(3), 1933–1945. https://doi.org/10.1039/c9fo02076d

Metilli, L., Francis, M., Povey, M., Lazidis, A., Marty-Terrade, S., Ray, J., & Simone, E. (2020). Latest advances in imaging techniques for characterizing soft, multiphasic food materials. *Advances in Colloid and Interface Science*, *279*, 102154. https://doi.org/10.1016/j.cis.2020.102154

Morris, L., Simone, E., Glover, Z. J., Powell, H., Marty-Terrade, S., Francis, M., & Povey, M. J. (2021). Dynamic monitoring of glycine crystallisation with low power ultrasound reflection spectroscopy. *Chemical Engineering Research and Design*, *170*, 213–223. https://doi.org/10.1016/j.cherd.2021.04.003

Palzer, S. (2017). Technological solutions for reducing impact and content of health sensitive nutrients in food. *Trends in Food Science and Technology*, *62*, 170–176. https://doi.org/10.1016/j.tifs.2016.11.022

Patel, A. R., & Dewettinck, K. (2016). Edible oil structuring: An overview and recent updates. *Food and Function*, *7*(1), 20–29. https://doi.org/10.1039/c5fo01006c

Pavoni, L., Perinelli, D. R., Bonacucina, G., Cespi, M., & Palmieri, G. F. (2020). An overview of micro-and nanoemulsions as vehicles for essential oils: Formulation, preparation and stability. *Nanomaterials*,

10(1). https://doi.org/10.3390/nano10010135

Rathore, A. S., Bhambure, R., & Ghare, V. (2010). Process analytical technology (PAT) for biopharmaceutical products. *Analytical and Bioanalytical Chemistry*, *398*(1), 137–154. https://doi.org/10.1007/s00216-010-3781-x

Rathore, Anurag S., & Kapoor, G. (2016). Implementation of Quality by Design for processing of food products and biotherapeutics. *Food and Bioproducts Processing*, *99*, 231–243. https://doi.org/10.1016/j.fbp.2016.05.009

Raut, J. S., Naik, V. M., Singhal, S., & Juvekar, V. A. (2008). Soap: The polymorphic genie of hierarchically structured soft condensed-matter products. *Industrial and Engineering Chemistry Research*, *47*(17), 6347–6353. https://doi.org/10.1021/ie0714753

Rigolle, A., Van Den Abeele, K., & Foubert, I. (2018). Conventional and New Techniques to Monitor Lipid Crystallization. In K. Sato. *Crystallization of Lipids* (pp. 465–492). Hoboken, NJ, USA: Wiley [2018].

Rogers, M. A., Wright, A. J., & Marangoni, A. G. (2009). Oil organogels: The fat of the future? *Soft Matter*, *5*(8), 1594–1596. https://doi.org/10.1039/b822008p

Sato, K., Bayés-García, L., Calvet, T., Cuevas-Diarte, M. À., & Ueno, S. (2013). External factors affecting polymorphic crystallization of lipids. *European Journal of Lipid Science and Technology*, *115*(11), 1224–1238. https://doi.org/10.1002/ejlt.201300049

Singh, A., Auzanneau, F. I., & Rogers, M. A. (2017). Advances in edible oleogel technologies – A decade in review. *Food Research International*, *97*(April), 307–317. https://doi.org/10.1016/j.foodres.2017.04.022

Ubbink, J. (2012). Soft matter approaches to structured foods: From “cook-and-look” to rational food design? *Faraday Discussions*, *158*, 9–35. https://doi.org/10.1039/c2fd20125a

van der Gucht, J. (2018). Grand challenges in soft matter physics. *Frontiers in Physics*, *6*(AUG), 6–8. https://doi.org/10.3389/fphy.2018.00087

Vilgis, T. A. (2015). Soft matter food physics - The physics of food and cooking. *Reports on Progress in Physics*, *78*(12). https://doi.org/10.1088/0034-4885/78/12/124602

Wang, X., Ullah, N., Shen, Y., Sun, Z., Wang, X., Feng, T., … Xia, S. (2021). Emulsion delivery of sodium chloride: A promising approach for modulating saltiness perception and sodium reduction. *Trends in Food Science and Technology*, *110*(October 2020), 525–538. https://doi.org/10.1016/j.tifs.2021.02.020

Wells, M. L., Potin, P., Craigie, J. S., Raven, J. A., Merchant, S. S., Helliwell, K. E., … Brawley, S. H. (2017). Algae as nutritional and functional food sources: revisiting our understanding. *Journal of Applied Phycology*, *29*(2), 949–982. https://doi.org/10.1007/s10811-016-0974-5

Yakhmi, J. V. (2011). Soft Matter: A Perspective. *Journal of Materials Education*, *33*(3–4), 149–160.

Zoabi, A., Touitou, E., & Margulis, K. (2021). Recent advances in nanomaterials for dermal and transdermal applications. *Colloids and Interfaces*, *5*(1). https://doi.org/10.3390/colloids5010018

Chapter 2: Background

2.1 Physicochemical features of triacylglycerides (TAGs)

Triacylglycerides (TAGs) are one of the major molecular species found in natural lipids, along with free fatty acids, phospholipids and waxes. From a chemical point of view, TAGs are three-fold esters of glycerol and fatty acids (FAs) which are hydrocarbon chains with a carboxylic end group (Figure 2.1).

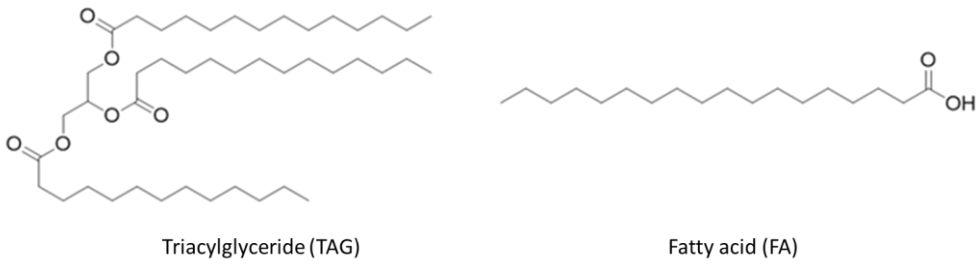

Figure 2.1. Chemical structure of a triacylglyceride (TAG) and a free fatty acid (FA) molecule.

The chemical and physical properties of TAGs depend heavily on the nature of the esterified FAs, and how those moieties interact with each other both in the same TAGs molecule and with other TAGs. For convenience, TAGs are usually identified as a series of three letters, each one representing a certain fatty acid, with the middle character always representing the second esterified position on the glycerol backbone. Fatty acids feature a varying carbon atom number in the hydrocarbon chain, with values between 12 and 24 being the most common. If only single carbon-carbon bonds are present, the FA is called saturated; presence of one or more double carbon-carbon bonds will define a FA as unsaturated. A list of the most common fatty acids is given in Table 2.1.

Table 2.1. Commonly occurring fatty acid molecules in TAGs, with chain length, presence of unsaturation and code letter for identification. Reproduced from Himawan et al. (2006).

Nomenclature of commonly occurring fatty acids

Code	Fatty acid	Chain length	Double bonds	Code	Fatty acid	Chain length	Double bonds
2	acetic acid (ethanoic acid)	2	none	P	palmitic acid (hexadecanoic acid)	16	none
4	butyric acid (butanoic acid)	4	none	S	stearic acid (octadecanoic acid)	18	none
6	caproic acid (hexanoic acid)	6	none	O	oleic acid (cis-9-octadecanoic acid)	18	1
8	caprilic acid (octanoic acid)	8	none	E	elaidic acid (trans-9-octadecanoic acid)	18	1
C	capric acid (decanoic acid)	10	none	*l*	linoleic acid (cis-cis-9,12-octadecadienoic acid)	18	2
L	lauric acid (dodecanoic acid)	12	none	R	ricinoleic acid (12-hydroxy-9-octadecenoic acid)	18	1
M	myristic acid (tetradecanoic acid)	14	none	A	arachidic acid (eicosanoic acid)	20	none
				B	behenic acid (docosanoic acid)	22	none

Since double carbon-carbon bonds create a kink in the aliphatic chain, unsaturated FA are bent molecules, whose crystallization requires more energy as the packing is less effective compared to saturated FAs, which are instead linear. This structural difference alters the melting point significantly, with saturated TAGs being solid at room temperature (fats) and unsaturated TAGs being liquid (oils) (Himawan et al., 2006). In addition, there is a further classification of TAGs depending on the identity of their fatty acid chains. Triacylglycerides containing one type of fatty acid chain are termed monoacid; if different moieties are present, then TAGs are called mixed-acid.

TAGs can crystallize in more than one crystalline packing (polymorphism). TAGs commonly exhibit three types of polymorphic arrangements, namely α, β' and β, which present distinct X-ray diffraction (XRD) patterns (Himawan et al., 2006). Different polymorphs display different physical properties, such as melting point, solubility, crystal morphologies and wettability properties. Furthermore, TAGs display two levels of crystal structure. The lateral packing mode of aliphatic chains is defined by the subcell structure, which defines readily the type of polymorphic form: α has a hexagonal subcell, β' an orthorhombic perpendicular subcell and β a triclinic parallel subcell (Figure 2.2, left). TAGs can also form structures vertically along the long chain axis, which are defined by the chain-length structure. One unit layer made up of one aliphatic chain is called a leaflet. TAGs can form double chain length (DCL) structures, triple chain length (TCL) structure, quatro (QCL) and hexa chain length structures (HCL) (Figure 2.2, right) (Sato & Ueno, 2005).

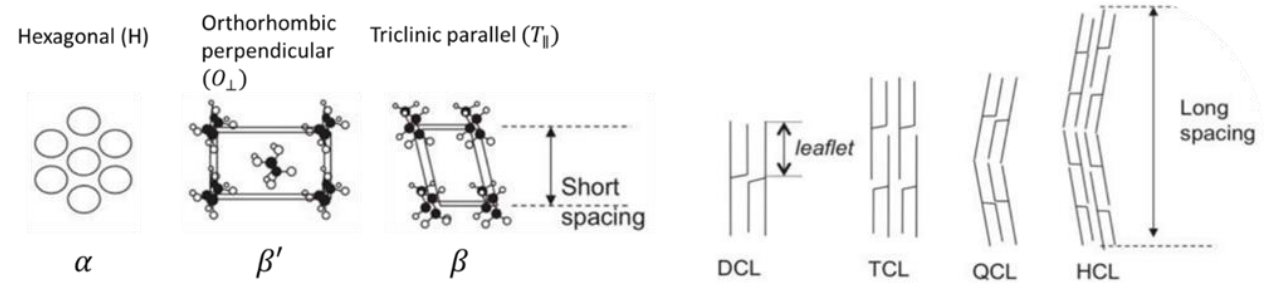

Figure 2.2. Subcell structure (left) and chain-length structure (right) in TAGs molecules. The three main polymorphs are designed as α, β′ and β. Hydrogen atoms are represented as white circles, carbon atoms as black circles. Possible chain-length structures are termed double (DCL), triple (TCL), quatro (QCL) and hexa (HCL) chain-length. Reproduced from Sato & Ueno (2005).

The α-form displays a single, strong short spacing peak at 0.42 nm (Figure 2.3a); the aliphatic chains are arranged in a hexagonal fashion, rotating freely without inter-chain interactions and with no angle of tilt. The α form has been found in double chain-length only. The β'-form is characterized by two strong short spacing peaks at 0.37-0.40 nm and 0.42-0.43 nm (Figure 2.3b). The chain packing is orthorhombic perpendicular, with adjacent chains "out of step" with each other, thus not being able to pack closely. The chains have a tilt angle between 50 and 70°; this polymorph can exist in both double and triple chain length structure. The β-form shows a strong lattice spacing peak near 0.46 nm, and a series of other strong peaks between 0.36-0.39 nm (Figure 2.3c). This is the most dense polymorph, with a triclinic parallel packing in which adjacent chains are "in step" and form a very tight structure. As for the β' polymorph, the chain tilt angle varies between 50 and 70° and can exists both in double and triple chain length structure.

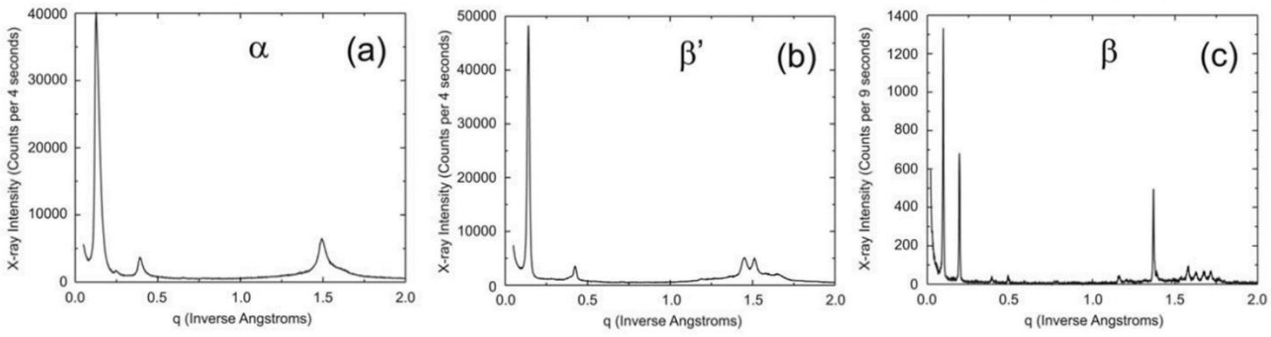

Figure 2.3. X-ray diffraction pattern of the three main polymorphic forms of TAGs, alpha (a), beta' (b) and beta (c). Adapted from Idziak (2012).

While saturated monoacid TAGs polymorphism is well represented by this three forms, as the fatty acid content starts to vary in length and unsaturation level, additional forms start to appear, which are usually related to the original structure and named by adding a subscript (*e.g.* β_1' *and* β_2'*).*

In mixed TAGs molecules, the type of chain-length structure adopted by a certain compound depends on the relative chemical affinity between the FAs chains. A DCL structure will form if the residues have similar properties, whereas if one or two chains are significantly different from the others, they will self-sort in a TCL structure. QCL and HCL arrangements are present when the TAGs molecules are asymmetrical with respect to their FAs residues (Sato & Ueno, 2005). The chain-length structure affects the mixing phase behaviour of TAGs, which has important consequences during the manufacturing of fat products and their fractionation (Sato, 2001). Three types of phase behaviour may occur, as shown in Figure 2.4.

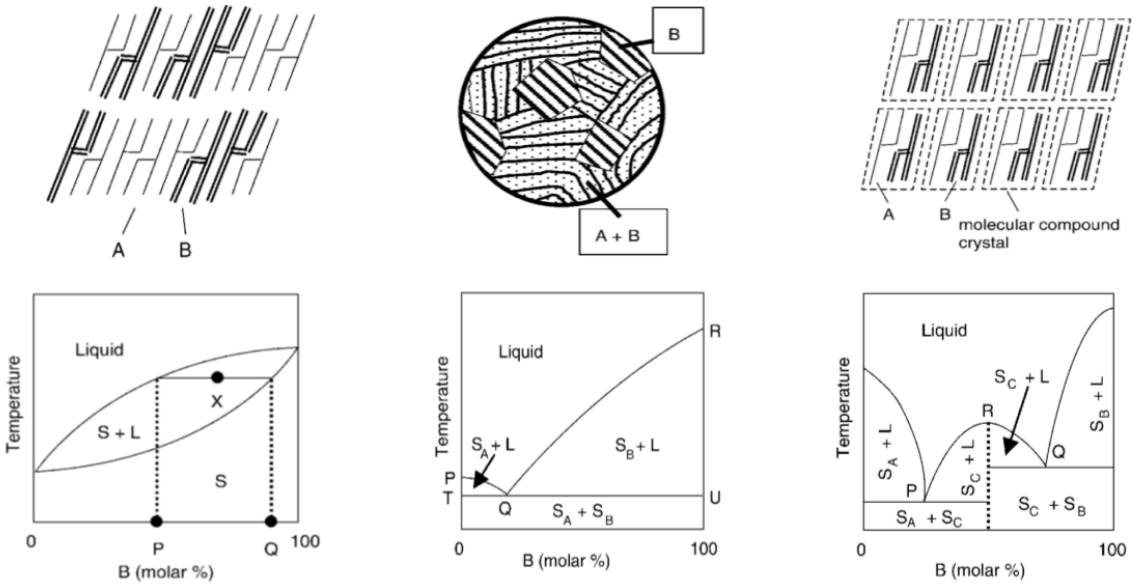

Figure 2.4. Phase behaviour of binary TAGs mixtures: solid solution (left), eutectic (centre) and molecular compound forming mixture (right). Adapted from Sato & Ueno (2005).

TAGs with similar physical and chemical properties (melting points, chain-length, molecular volume and polymorph) develop solid solutions. In this system only two homogeneous phases can exist: a liquid solution and a solid solution, as one component cannot solidify without containing some of the other. When TAGs have different properties but similar melting points, a eutectic mixture occurs. This is the most common system found in binary TAGs mixtures. As shown in the central diagram in Figure 2.4, above the PQR line the

system is a homogeneous liquid. Depending on the relative molar concentration of the components, a single TAG is going to crystallize out of the melt – represented by the small and large areas in the graph TQP and RQU. Below the line TQU a solid mixture of component A and B is formed. It's important to note that the eutectic system is a physical mixture, not a molecular compound. When specific molecular interaction occur in the crystalline state between TAGs, a molecular compound is formed. A molecular compound can coexist in equilibrium with a liquid of the same composition, and has a congruent melting point R, as seen in the graph on the right in Figure 2.4. The phase diagram can be split in two sub-diagrams: A-molecule/molecular compound and molecular compound/B-component, as if each was an eutectic mixture.

2.2 Thermodynamic and kinetic aspects of fat crystallization

Although a solid becomes the thermodynamically stable phase when a melt is cooled down below its melting temperature, the formation of a solid phase does not happen spontaneously. Two events are required to initiate the liquid-solid transition: the formation of crystal nuclei in the melt phase, followed by the growth of such nuclei. Furthermore, fat systems are subject to post-crystallization phenomena such as sintering (*i.e.* formation of solid bridges between crystals), solid-state polymorphic transformation, and Ostwald ripening of crystals, which results from disproportionation of crystals below the micron level in favour of larger crystals (Himawan et al., 2006).

In TAGs melts, it has been proposed that molecules start to align into lamellae, acting as a precursor for the formation of a crystalline phase (Sato, 2001). This process follows a path through transitory states with several energy barriers to overcome for the formation of the different polymorphs as shown in Figure 2.5.

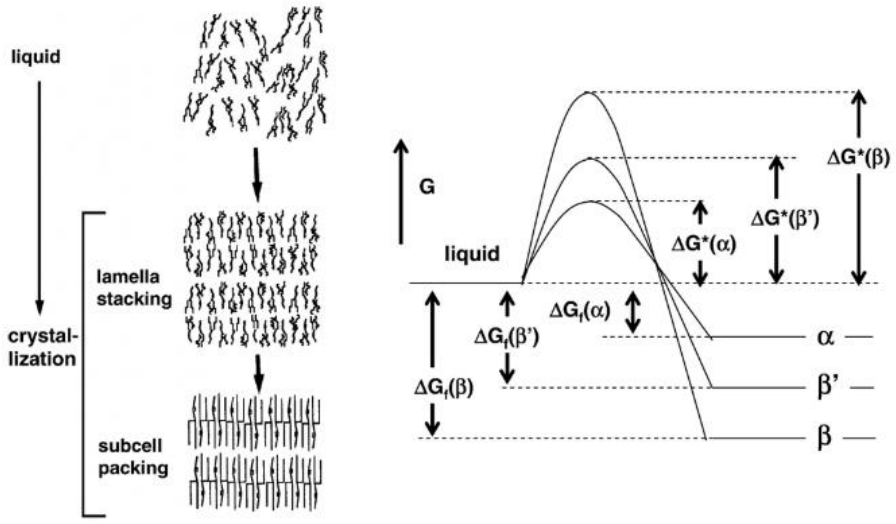

Figure 2.5. Proposed crystallization mechanism for TAGs (left) and activation energies for different polymorphic transitions (right). Reproduced from Himawan et al. (2006).

For a system of pure TAGs, nucleation is considered as a bimolecular event explained by classical nucleation theory (Himawan et al., 2006). The Gibbs free energy for homogeneous spherical nucleation of TAGs clusters (ΔG_{hom}) contains two opposing energetic terms: a decrease of free energy per unit volume, arising from the enthalpy of fusion (ΔG_V) and an increase in free energy due to the surface tension between solid and liquid (ΔG_S) (Eq. 2.1)

$$\Delta G_{hom} = -\Delta G_V V + \Delta G_S S = -\frac{4}{3}\pi r^3 \Delta G_V + 4\pi r^2 \sigma \qquad \text{Eq. 2.1}$$

Where V and S are the volume and the surface of the spherical nucleus, r is the radius of the nucleus, and σ is the surface tension of the interface. The value of ΔG_{hom} increases with *r* until a critical (maximum) value $\Delta G^*_{\mathrm{hom}}$ is reached at a *r** critical size: any nuclei larger than $r^* = -2\sigma/\Delta G_V$ will decrease the total free energy of the system when growing, hence becoming more stable (Figure 2.6).

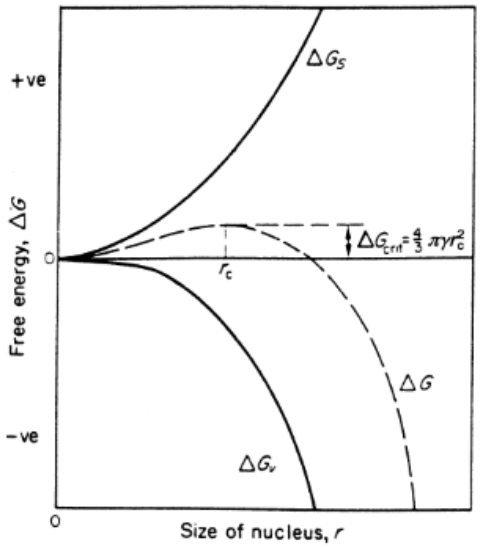

Figure 2.6. Variations of free energy of nucleation depending on the radius of a spherical cluster of crystallizing molecules. Reproduced from Mullin (2001).

For TAGs crystallizing from the melt the free volume energy can be approximated to the enthalpy of fusion and a temperature factor, as shown in Equation 2.2

$$\Delta G_V \approx -\Delta H_m \left(\frac{\Delta T}{T_m V_m}\right). \qquad \text{Eq. 2.2}$$

Where ΔH_m is the molar fusion enthalpy at the reference temperature T_m, and V_m is the molar volume of the cluster; $\Delta T = T_m - T$, the difference between the melting temperature of the cluster and the actual temperature of the system, is defined as the supercooling of the melt. To relate the free activation energy of homogeneous nucleation to the temperature of the system and the fusion enthalpy of the crystals, Equation 2.1 and 2.2 can be combined into Equation 2.3

$$\Delta G^*_{hom} = \frac{16}{3}\frac{\pi\sigma^3 V_m^2 T_m^2}{(\Delta H_m \Delta T)^2} \qquad \text{Eq. 2.3}$$

While Equation 2.3 provides the thermodynamic framework for the nucleation barrier to overcome for nucleation, it does not provide any information on the nucleation rate, *i.e.* the number of nuclei created per

unit volume, per unit time. The frequency of nuclei formation was formulated by Fisher and Turnbull in 1949, whose equation takes their names (Eq. 2.4) (Turnbull & Fisher, 1949):

$$J_{hom} = \frac{N_A kT}{h} \exp\left(-\frac{\Delta G^*_{hom}}{kT}\right) \exp\left(-\frac{\Delta G^*_{diff}}{kT}\right) \quad \text{Eq. 2.4}$$

The Fisher-Turnbull equation takes also into account also the diffusivity of molecules and their arrangement into a suitable conformation for forming a nucleus $\left(\Delta G^*_{diff}\right)$, due to the large entropy factor for long-chained molecules such as TAGs. In real systems, however, nucleation deviates from ideality due to the inherent presence of impurities in natural fats and oils, which can act as catalytic sites. Therefore, nucleation can be considered heterogeneous, which displays always a lower activation energy than homogeneous nucleation (Eq. 2.5)

$$\Delta G^*_{het} = \Delta G^*_{hom} f(\theta) \quad \text{Eq. 2.5}$$

Where $f(\theta)$ represents the wetting properties of foreign particles and impurities by the supercooled melt.

Furthermore, once clusters grow and form crystals, secondary nucleation is likely to occur. In this case, additional nuclei are generated through fragments of growing crystals that are chipped away mechanically, by collisions between two or more crystals, or when the liquid lamellae phase is aligned under shearing, leading to increased nucleation rate. All those conditions are commonly found in large crystallizing vessels typical of industrial fat manufacturing.

TAGs exhibit monotropic polymorphism, which means that one form is always the most thermodynamically stable. Polymorphic occurrence of TAGs crystals depends on several factors. As displayed in Figure 2.5, the activation energy for nucleation is smaller for the metastable forms (α and β') and higher for β. This is a consequence of the increasing surface energy from α to β; therefore, in absence of external stimuli such as shearing or applied pressure, TAGs will nucleate in the metastable forms due to their higher nucleation rate. With time, they will convert to the most stable polymorph through step-by-step transitions described by

Ostwald rule of stages (Himawan et al., 2006). However, this rule can be overridden if supercooling (ΔT) is low and external influences are present during crystallization. Local pressure and temperature fluctuations, shearing and seeding are in fact used to accelerate and/or direct the crystallization towards a certain polymorph (Sato et al., 2013).

In general, the overall morphology of a crystal is determined by the relative growth rates on the different crystal surfaces. A slow advancement rate of a certain face will likely produce a large surface area in the final crystal habit. The high anisotropy in TAGs molecules results in large density differences in crystal planes, which in turn affects the growth on each facet. As a result, TAGs crystals usually growth as anisotropic needle-like crystals. Depending on the polymorphic form, slightly different morphologies can be found: usually the α form crystallizes in a compact mass of thin crystals, the β' form appears as a bulky shape (platelets) or as a radially-grown bundle of needles (spherulites), whereas β crystal are needle-like. The crystal morphology, however, cannot be used to determine the polymorphic occurrence of a solid fat, due to the potential ambiguity arising from different crystallizing conditions (Himawan et al., 2006).

2.3 Particle-stabilized foams

Foams are materials comprising gas bubbles dispersed in a continuous phase which may be liquid or solid. Foams are ubiquitous in nature and in manufactured products, as their structure endows them with interesting thermal, acoustic, optical and rheological properties (Drenckhan & Saint-Jalmes, 2015). Similarly to other multiphasic materials, liquid foams are thermodynamically metastable materials and will eventually phase-separate through three main mechanisms: drainage, coalescence and coarsening (Figure 2.7) (Lazidis et al., 2017).

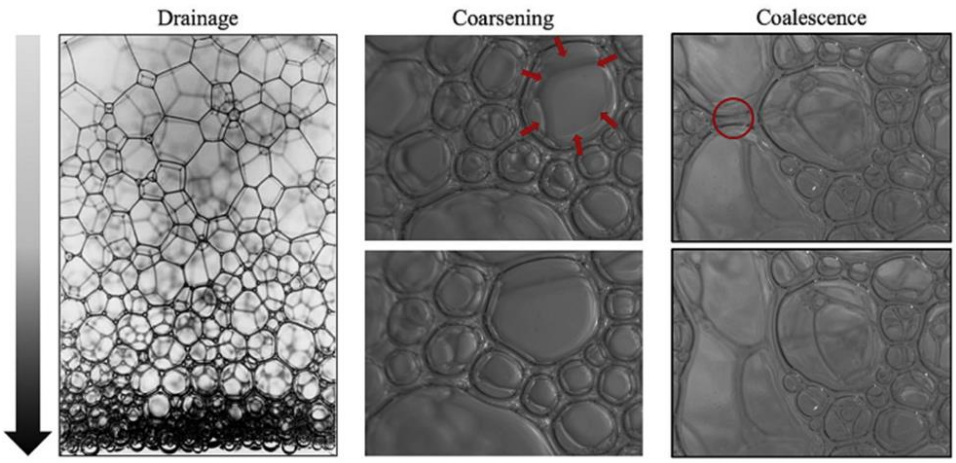

Figure 2.7. Main destabilization mechanisms occurring in liquid foams: drainage (or creaming, left), coarsening (centre) and coalescence (right). Adapted from Lazidis et al. (2017).

Drainage is caused by the large density difference between the dispersed phase and the continuous phase. Gravity will cause any air bubbles larger than few microns to rise to the top of the foam, while the liquid flows towards the bottom, resulting in the thinning of the liquid films separating the air bubbles (Rio et al., 2014). Dry foams, which are characterized by low liquid volume fractions (ϕ_{liquid} = 0.05) and polyhedral-shaped bubbles, are more susceptible to bursting and phase-separation (Cantat et al., 2013).

Foams are characterized by the presence of a gas/liquid interface (for liquid foams), which has an inherent energy cost due to the unfavourable interactions between the liquid and gas molecules. The energy associated with the formation of a new interface (dE_{surf}) with area dS is defined as (Equation 2.6)

$$dE_{surf} = \gamma dS \qquad \text{Eq. 2.6}$$

Where γ is the surface tension. The surface tension can be considered either as an energy per unit area (J m^{-2}) or as a force per unit length (mN m^{-1}); a segment dl on the surface produces a force γdl which is normal to the segment dl (Figure 2.8a).

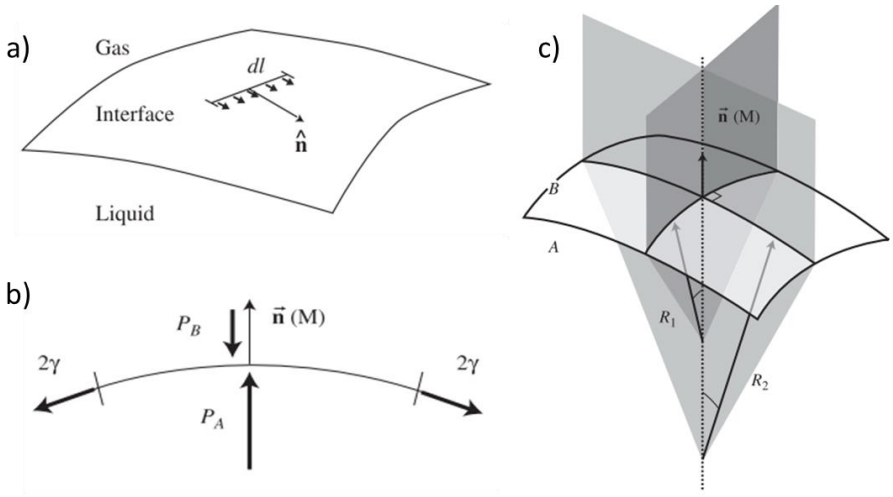

Figure 2.8. Surface tension exerting a force along a gas-liquid interface (a) and the counteracting pressures preventing deformation on the surface of a bubble (b). Curved interface separating the phase A from phase B and the two radii of curvature R_1 and R_2 (c). Adapted from Cantat et al. (2013).

Surface tension therefore tends to minimize the interface area to reduce the energy associated with it. At equilibrium, the surface tension is counteracted by pressures on both sides of the interface (Figure 2.8b). Consider a surface S which separates two phases, A and B, characterized by a surface tension γ. The interface is characterized locally by the two main radii of curvature, R_1 and R_2 (Figure 2.8c). A deformation of the interface S towards M (which is normal to S) of a distance dx would result in a change of volume of $dV = Sdx$, and a change in surface area of $dS = HSdx$, where $H = \frac{1}{R_1} + \frac{1}{R_2}$ is the mean curvature of the surface. At equilibrium the change in energy due to this deformation is zero, hence (Eq. 2.7)

$$-\Delta P dV + \gamma dS = 0 \qquad \text{Eq. 2.7}$$

Where $\Delta P = P_A - P_B$, the difference of the pressures on each side of the interface. Equation 2.7 is simplified to Equation 2.8

$$\Delta \mathrm{P} = \mathrm{P_A} - P_B = \gamma H = \gamma \left(\frac{1}{R_1} + \frac{1}{R_2}\right) \qquad \text{Eq. 2.8}$$

Equation 2.8 is also known as the Young-Laplace law. It demonstrates that surface tension tends to reduce the curvature of an interface, whereas pressure differences respond by bending the same interface (Cantat et al., 2013). In spherical air bubbles, $R_1 = R_2$ and therefore

$$\Delta P = \frac{2\gamma}{R} \qquad \text{Eq. 2.9}$$

The Young-Laplace law is useful for understanding foam coarsening. Equation 2.9 states that the pressure difference between bubbles and the liquid increases for smaller R values. As a consequence, gas diffuses from smaller air bubbles towards larger and more stable air bubbles, resulting eventually in an increase of the average bubble size.

Coalescence occurs when the film separating two neighbouring bubbles is ruptured and the two adjacent bubbles form a larger bubble. Similarly to coarsening, coalescence results in an increase in the mean bubble size. The mechanism of film rupturing is still under investigation, however it is generally accepted that coalescence is more likely to occur below a threshold liquid fraction value (Hill & Eastoe, 2017).

Aqueous foams are widely used in several consumer products (food, cosmetics, pharmaceuticals), firefighting and oil recovery materials, to name a few. Hence, production of highly stable foams is sought to improve their performance and shelf-life (Rio et al., 2014). Low-molecular-weight surfactants are typically used in the stabilization of foams, owing to their amphiphilic nature which allows them to adsorb at the gas/liquid interface, lowering the surface tension (Murray & Ettelaie, 2004). The use of colloidal particles for stabilizing emulsions and foams was first discovered by Ramsden and Pickering in the early 1900s, but has experienced renewed interest due to the ability to produce foams with high stability against coarsening and coalescence (Binks, 2002; Martinez et al., 2008). While surfactants provide stabilization by lowering the surface tension, Pickering stabilization (*i.e.*, using colloidal particles) is based on the irreversible adsorption of particles at the interface.

Consider an air-liquid interface and a spherical colloidal particle. Depending on the wettability of the particle, three scenarios might occur (Figure 2.9).

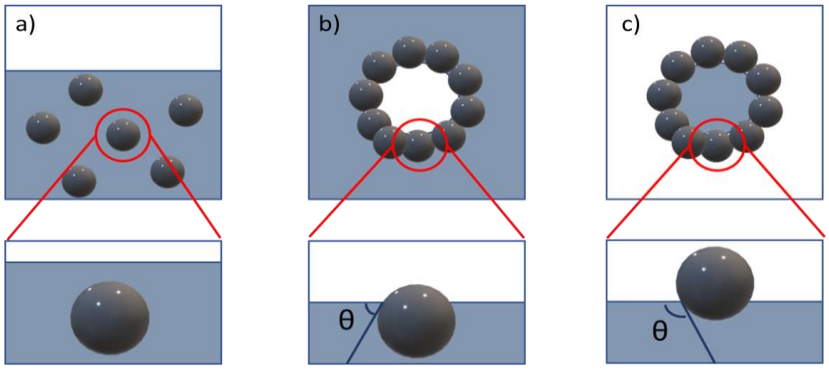

Figure 2.9. Adsorption of spherical colloidal particles at the liquid/air interface, with increasing contact angle values: $\vartheta = 0°$ (a), $0 < \vartheta < 90°$ (b) and $90° < \vartheta < 180°$ (c).

When the particle is completely wetted by the liquid, it displays no surface activity (Figure 2.9a). When the contact angle θ, measured between the air phase, particle surface and the liquid phase, is between 0 and 90°, the particle will be preferentially wetted by the liquid, but will exhibit surface activity and will stabilize the air phase to yield a foam (Figure 2.9b). If θ is comprised between 90° and 180°, the particle will be mainly wetted by the air phase, and will stabilise the liquid phase leading to a powder (Figure 2.9c). The contact angle is dependent on the relative surface energy of the liquid/air interface (γ_{AL}), liquid/particle interface (γ_{LP}), and air/particle (γ_{AP}) interface, as described by the Young Equation (Eq. 2.10):

$$\cos\theta = \frac{\gamma_{AP} - \gamma_{LP}}{\gamma_{AL}} \qquad \text{Eq. 2.10}$$

The adsorption of the particle at the interface is thermodynamically favoured when the formation of two new interfaces, *i.e.*, the particle-liquid and the particle-air, is lower than the energy of the air-liquid interface with the same area. The attachment energy for a spherical particle can be calculated with Equation 2.11:

$$\mathrm{E} = \pi \mathrm{r}^2 \gamma_{AL} (1 \pm \cos\theta)^2 \qquad \text{Eq. 2.11}$$

For example, nanometre-sized particles of fumed silica at the air/water interface (γ = 72 mN m^{-1}) have an attachment energy of ~ 1000 k_BT. Molecular surfactants, which span few angstroms (10^{-10} m) in size, display attachment energies around few k_BT. This difference of several orders of magnitude results in slow, but almost irreversible adsorption of colloidal particles at the interfaces, while surfactants display weaker, but faster adsorption and desorption kinetics at the interface (Binks, 2002).

Despite the abundant literature reporting highly stable Pickering foams, the underlying mechanisms which endow particle-coated bubbles outstanding stability are still elusive and under investigation (Rio et al., 2014). Early studies demonstrated that, for armoured bubbles (*i.e.*, particle-coated bubbles) stabilized by particles one-tenth of the bubble radius $\left(\frac{R_{particle}}{R_{bubble}} \approx 0.1\right)$, gas dissolution is halted by adoption of a non-spherical, faceted bubble shape. Results from computer simulations showed that the faceted configuration constitutes an energetic minimum for the bubble, for which the Laplace over-pressure is counteracted by the deformation of the air-liquid interface around the adsorbed particles (Figure 2.10) (Abkarian et al., 2007).

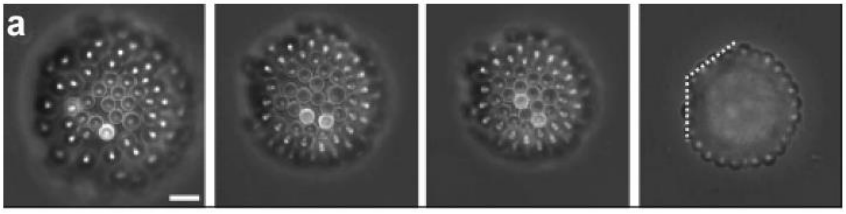

Figure 2.10. Air bubble coated with polystyrene latex particles observed during dissolution. Scale bar is 8 µm. Reproduced from Abkarian et al. (2007).

More recent experimental work studied the stability of individual armoured bubbles against the application of increasing external pressures. These conditions simulate the coarsening of gas bubbles occurring in a foam. The bubbles were prepared and coated using a microfluidic device, and their shape and size were monitored with microscopy techniques (Beltramo et al., 2017; Taccoen et al., 2016). In line with previous findings, armoured bubbles were stable against dissolution, and were able to withstand several millibars of over-pressure (up to 20 mbar) before buckling and dissolving. The mechanism of failure is attributed to dislocation of the adsorbed particles from interface plane with increasing pressure, which leads to irreversible bubble collapse and eventually complete dissolution. The Laplace over-pressure was found to be inversely proportional to the bubble radius $\Delta P_{collapse} \propto R^{-1}$, while the size of the adsorbed particles (0.5 – 4.5 µm) had no significant effect on the stability of the armoured bubble (Taccoen et al., 2016). Further investigation revealed that bubble dissolution could be arrested by developing a sufficiently high interfacial yield stress. Interestingly, this could be achieved at sub-monolayer surface coverages, which were dependent on the particle shape. In particular, ellipsoidal particles were able to stabilize air bubbles with surface coverage as

low as ϕ = 0.4, owing to their ability to form a percolated network on the interface, whereas spherical particles required a higher (ϕ = 0.7 – 0.8) surface coverage to prevent dissolution (Beltramo et al., 2017).

2.4 Optical and Polarized Microscopy

Optical microscopy is one of the most common characterization techniques for complex soft materials. Compared to more modern and advanced microscopies, such as electron-based ones, optical images preserve full colour information, which leads to the possibility of using dyes to differentiate phases in samples. More importantly, light microscopy can be operated at room temperature and pressure, allowing study of samples in their native, hydrated state (Gunning, 2013). The main drawbacks of the technique are its diffraction-limited resolution power (around 0.5 µm) and poor depth of focus, confining light microscopy to the study of flattened, thin objects in the micron to millimetre range. However, some of these disadvantages can, in principle, be overcome or mitigated by enhancing image quality (e.g. contrast and brightness, removing background noise) with computer processing software (Russ, 2015). A popular approach in soft matter characterization consists of using Polarized Light Microscopy (PLM), which enables visualization of anisotropic (liquid) crystals in the sample. A schematic illustrating the principle of the technique is given in Figure 2.11.

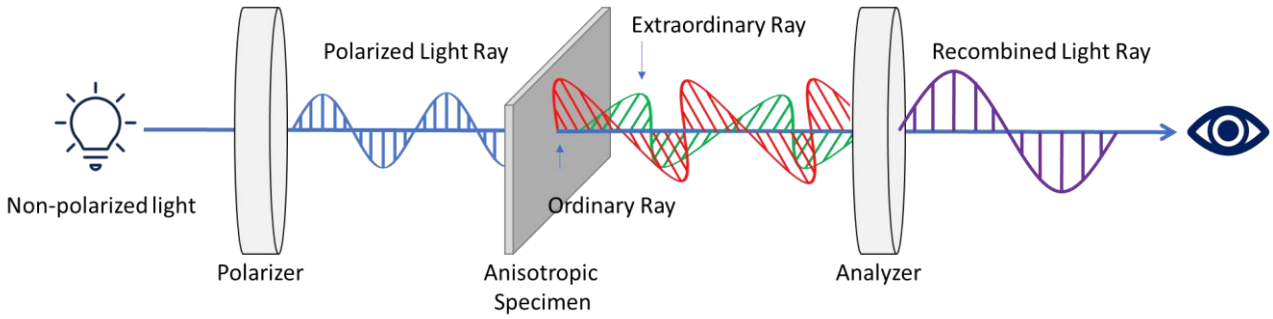

Figure 2.11. Illustration of the principle of polarized light microscopy (PLM).

Polarized light is generated using a polarizing sheet mounted below the sub-stage condenser lens; a second sheet is placed above the objective lenses, filtering the incoming light from the specimen. All the light radiating from the object that is not subject to a change in polarization angle is extinguished. When the polarized light ray enters the anisotropic material, it is resolved into two perpendicular rays which vibrate in

planes orthogonal to each other. This phenomenon arises from preferential orientation of atoms and molecules in the sample that cause light to travel at different velocities. The first component, called the ordinary ray (*o-ra*y, refractive index n_0), exhibits a constant velocity through the material independent of the direction (hence constant refractive index). The other component, termed extraordinary ray (*e*-ray, refractive index n_e), has a velocity that depends on the orientation and varies between n_0 and n_e. The two rays are then recombined with either constructive or destructive interference by the analyser. The magnitude of the refractive indexes' difference is called birefringence and can be expressed as (Equation 2.12) (Sanderson, 2019).

$$\Delta \mathrm{M} = \mathrm{n}_0 - n_e \qquad \text{Eq. 2.12}$$

Birefringence occurs commonly in soft food materials and polymers (Crist & Schultz, 2016; Den Engelsen, 1976; Liu et al., 1991; Oriel & Schellman, 1966), when they are present either as solid crystals or as ordered liquid crystalline phases. Rapid detection and phase behaviour of these compounds can therefore be investigated with this imaging method.

2.5 Scanning Electron Microscopy

Electron microscopy is a key technique in the characterization of structure at the molecular, nano- and micro-scale in different areas of science, including soft materials. It can provide information on the surface and the internal structure of samples, and reveal the role of single biomolecules such as proteins, fat crystals and polysaccharides in multiphasic systems such as emulsions, gels, foams (Groves & Parker, 2013). While conventional light microscopes have limited resolution due to the use of visible light radiation, electron-based microscopy can achieve sub-nanometre resolution, depending on the applied acceleration voltage. The term "electron microscopy" encompasses several techniques, of which the two main methods are transmission (TEM) and scanning electron microscopy (SEM). The common working principle behind these techniques involves accelerating electrons and focusing the resulting beam on the sample by using a voltage between 1 and 100 keV. Conventional electron microscopes require vacuum conditions so that the electron beam is not scattered by gaseous molecular species, which would deteriorate the image quality (McClements & McClements, 2016). High resolution and image quality are achieved by maintaining high vacuum in the

enclosed instrument. In turn, samples require severe treatment in order to withstand the operating conditions of an electron microscope. In fact, this single criterion poses limitations to the suitability of studying biological and food samples with this technique, which can be partly overcome by using reduced levels of vacuum.

In SEM, the electron beam scans the specimen line by line, across a rectangular cross-section (also termed *raster mode*), collecting scattered electrons from the surface of the sample. With a typical accelerating voltage of 30 keV, modern instruments can achieve a resolution of 1 nm (Dudkiewicz et al., 2011). During the measurement the primary beam electrons (PEs) interact with the specimen surface, and are either scattered inelastically as secondary electrons (SEs) or elastically as back-scattered electrons (BSEs). The former are collected by a specific detector and used to build a topographic image, while the latter can be used to increase contrast based upon atomic number (Z) differences of the analysed surface features (Dudkiewicz et al., 2011). Additionally, X-Rays are generated in the chamber and can be collected to combine topological and chemical composition of the sample with a technique called Energy Dispersive X-Ray Spectroscopy (EDS) (Figure 2.12).

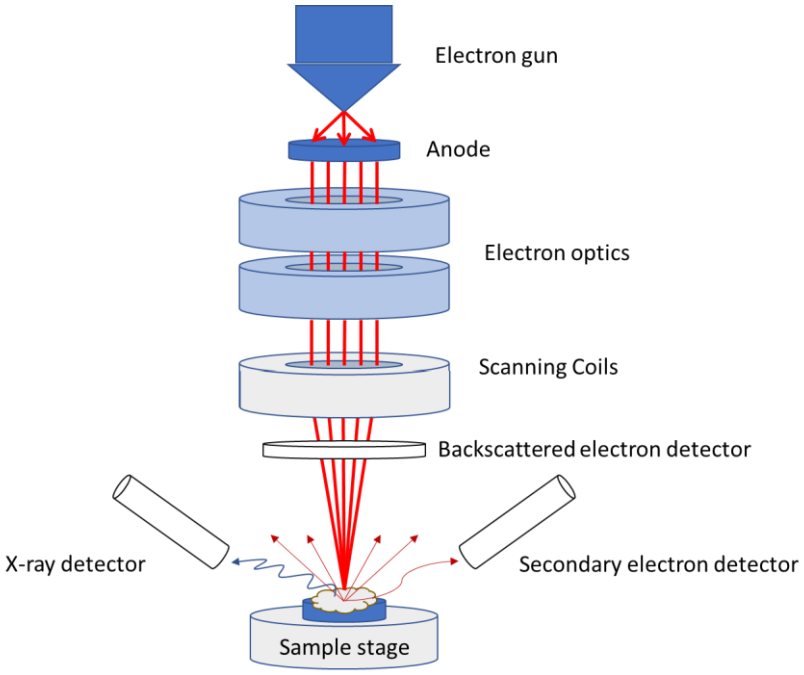

Figure 2.12. Scheme illustrating the working principle of Scanning Electron Microscopy (SEM).

The field of view can vary from millimetres to nanometres, thus being able to probe samples at different length scales. The resulting image is very similar to a conventional optical microscopy micrograph (albeit without colour) but with much higher magnification; this enables rapid and easy interpretation (Groves & Parker, 2013). As the majority of soft materials are electrically insulating, a conductive coating is applied to the surface of the sample in order to avoid damage as well as loss in image quality due to charge build-up. Samples prone to degradation require chemical fixation and, for hydrated or liquid samples, drying is usually carried out prior to the measurement in the vacuum chamber. This process, however, can result in significant microstructure alteration compared to the native-state structure of the sample. Therefore, a popular alternative to chemical fixation or drying involves quick-freezing, which is considered less invasive than other methods. Frozen samples and SEM are combined in a technique called Cryogenic Scanning Electron Microscopy (CryoSEM). However, the formation and successive sublimation of ice crystals during pre-treatment occurs with this technique, potentially leading to the presence of artefacts in the images (James, 2009).

2.6 Oscillatory Rheology

Rheology is the study of flow and deformation of matter in response to forces applied to it. Rheology is based on the theoretical description of ideal solids and liquids, formulated several centuries ago by Robert Hooke and Isaac Newton. The deformation of an ideal elastic solid is proportional to the load imposed on it, and the deformation is recovered once the load is removed. An ideal liquid, on the other hand, will exhibit an irreversible flow that persists as long as the stress is applied, with a flow rate proportional to the stress. Real materials, in particular soft matter, exhibit features that are in between the solid and liquid, hence being termed “viscoelastic” and hence display complex flow behaviour (Chen et al., 2010). The aim of rheological experiments is to quantify the viscoelasticity of samples in relation to time and deformation extent, and to relate these viscoelastic properties to the (micro)structure.

Rheometers generally measure two physical quantities: stress, which is the amount of force per area applied to the sample, and strain, which is the dimensionless degree of material deformation. The properties of the

material, quantified as elastic moduli for solids and viscosity for liquids , are calculated from Equations 2.13 and 2.14

$$\sigma = G\gamma \qquad \text{Eq. 2.13}$$

$$\sigma = \eta\dot{\gamma} \qquad \text{Eq. 2.14}$$

Where σ is the stress (Pa), G is the elastic moduli (Pa), η is the viscosity (Pa s) and γ is the strain. To obtain a significant description of the material viscoelasticity, the measurements are carried out over a range of strain, strain rates and timescales. In rheology experiments, the sample is placed into the measuring system of the instrument, which can adopt different geometries (Figure 2.13).

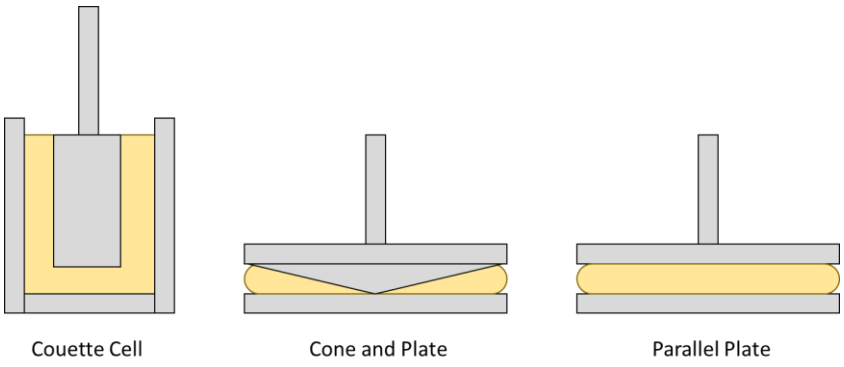

Figure 2.13. Common measuring system geometries used in rheology experiments.

Amplitude sweeps are a routine type of measurement in which the sample is subject to oscillating strain with increasing magnitude at a fixed frequency. The stress-strain curve of the sample can be represented as the scheme in Figure 2.14 (Goodwin & Hughes, 2008).

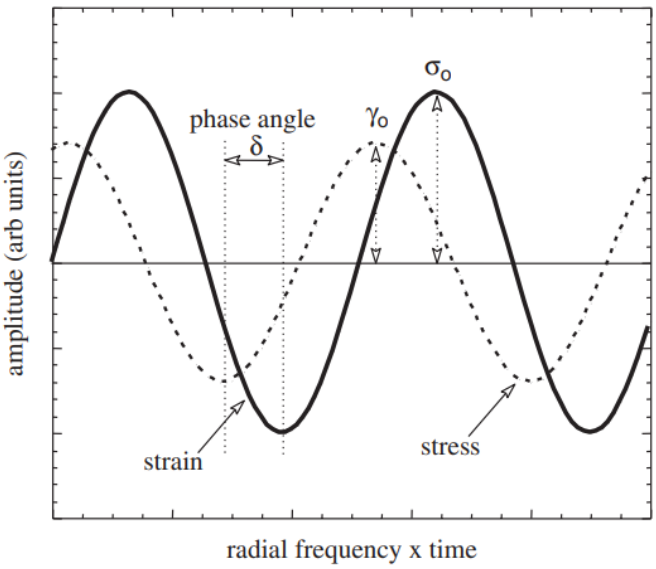

Figure 2.14. Relationship between the applied strain and the stress developed by the sample during an oscillatory experiment. Reproduced from Goodwin & Hughes (2008).

The instrument measures the maximum applied strain (γ_0) and the resulting maximum stress (σ_0), which are then used to calculate the complex modulus G* (Equation 2.15)

$$|G^*(\omega)| = \frac{\sigma_0}{\gamma_0} \qquad \text{Eq. 2.15}$$

The complex modulus contains two relevant terms, the storage modulus (G') and the loss modulus (G"), which depend on the phase angle δ (Equation 2.16)

$$G'(\omega) = G^* \cos(\delta) \qquad G"(\omega) = G^* \sin(\delta) \qquad \text{Eq. 2.15}$$

The storage modulus G' describes the stress component which is in phase with the applied strain, and it is a measure of the stored energy during the strain (hence the "elasticity" of a material). The loss modulus, on the other hand, describes the stress component which is out of phase with respect to the applied strain, and is a measure of the energy lost during the strain (hence the "liquid" behaviour of a material) (Goodwin & Hughes, 2008). A typical amplitude sweep experiment is shown in Figure 2.15.

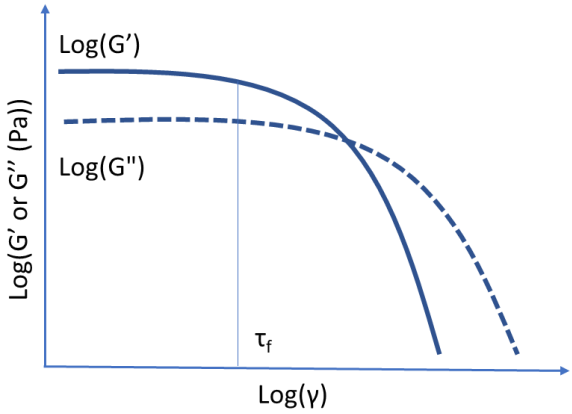

Figure 2.15. Amplitude sweep experiment of a viscoelastic material which displays solid-like behaviour.

Materials which display G' > G'' at relatively low strain values are considered solid-like. The interval in which both G' and G" are independent of the applied strain is termed Linear Viscoelastic Regime (LVER); The strain value at which G' begins to decrease is called the flow point (τ_f).

2.7 Ultrasonic Spectroscopy

The use of low-power ultrasonic waves (*i.e.*, acoustic waves exceeding 20 kHz) for characterizing food materials is long established (Povey, 1998). The technique is based on the propagation of an ultrasonic pulse in the material from one transducer, and received at the other end of the sample from another transducer (pitch-and-catch mode) or reflected at the end of the sample container, and received by the same transducer (pulse-echo mode) (Povey, 1997). The velocity of sound c is then calculated from the time-of-flight (Δt) and the travelled pathlength L (Equation 2.16):

$$c = \frac{L}{\Delta t} \qquad \text{Eq. 2.16}$$

In homogeneous fluids and gases, the velocity of sound depends on the elasticity and density of the material or, more precisely, the density (ρ) and adiabatic compressibility (κ), and it is independent of the frequency of the propagating pulse, as first described by Wood's law (Wood, 1946) (Equation. 2.17)

$$c = \frac{1}{\sqrt{\kappa\rho}} \qquad \text{Eq. 2.17}$$

In heterogeneous media, such as mixtures and suspensions, the velocity will depend on the mean density and mean compressibility, as proposed by Urick (1947) (Equation 2.18)

$$c = \frac{1}{\sqrt{\kappa\rho}} \qquad \kappa = \sum_j \phi_j \kappa_j \qquad \rho = \sum_j \phi_j \rho_j \qquad \text{Eq. 2.18}$$

where ϕ represents the volume fraction of the j-th constituent phase. Therefore, the composition of a multi-phasic material may be calculated from velocity of sound measurements, if the properties of the individual phases are known. As both density and compressibility are a function of temperature, the ultrasound measurements must be accompanied by temperature measurements as well. This method can be applied for determining the alcohol content in water, sugar concentration in aqueous solutions, or the triacylglyceride composition of edible oils (Povey, 1997). Furthermore, ultrasonic techniques can be applied to the study of phase transitions (e.g., crystallization); not only ultrasound can be detect the onset of the transition, but may also calculate the volume fraction involved in said transition. Phase changes are usually accompanied by significant variations in density and compressibility, which affect the measured velocity of sound. Moreover, the acoustic attenuation (α) is also sensitive to any phase transition occurring in the sample, and may be calculated from Equation 2.19

$$\alpha = -20 \log\left(\frac{A}{A_0}\right) \qquad \text{Eq. 2.19}$$

Where A_0 and A are the reference and sample amplitude of the ultrasonic pulse, respectively (Povey, 1997). Calculation of the volume fraction of solids in a material, for example, might be possible by measuring the velocity of the sound of the mixture *c*, and using Equation 2.20:

$$\phi = \frac{c^{-2} - c_L^{-2}}{c_S^{-2} - c_L^{-2}} \qquad \text{Eq. 2.20}$$

where the subscript L and S represent the velocity of sound in the fully liquid and fully solid sample, respectively.

2.8 X-ray diffraction and X-ray tomography

X-Ray diffraction (XRD) is an established technique for studying crystal structures and atomic spacings in material science. The technique is based on the interaction of X-Rays, which can be described as either electromagnetic waves with 0.10 nm wavelength, or as particles (photons) with energies around 10 keV. X-Ray diffractometers generate X-Rays from a cathode ray tube, and filtered to produce a monochromatic beam which is concentrated and directed towards the sample. The diffracted XR intensity is collected and measured by a detector (Bunaciu et al., 2015) X-Rays interact with the electrons of atoms in the sample, resulting in either destructive or constructive interference. Only in the latter case a diffraction peak may be detected from the instrument. The relationship between the X-Ray wavelength (λ), the distance between the scattering planes in the sample (d) and the diffraction angle (θ) is given by the Bragg Law (Equation 2.21):

$$n\lambda = 2d \sin\theta \qquad \text{Eq. 2.21}$$

where n is the order of the diffraction peak.

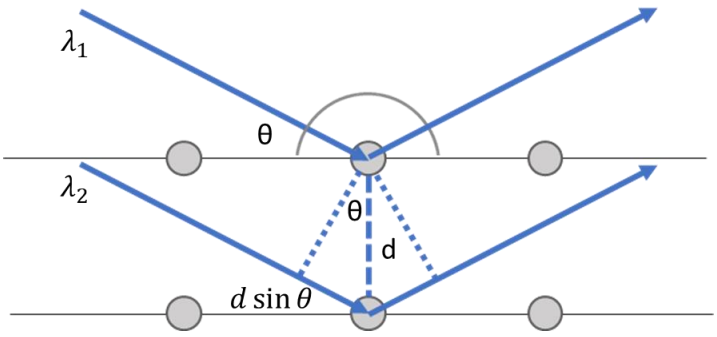

Figure 2.16. Demonstration of Bragg's Law on a sample containing scattering planes separated by a distance d.

An XRD instruments therefore measures the intensity of the incoming XR radiation at a given θ angle. Conversion of the diffraction peaks to d-values allows to determine the spacings in the subcell of a specific crystalline form, or to measure the distance between lamellar planes. These two groups of structural information are termed short spacings and long spacings, respectively, and are fundamental in the study of lipid crystallization, for example (Idziak, 2012). Modern instruments enable real-time observation of crystallization and polymorphic transitions, with precise temperature control and application of external stimuli such as shear or ultrasonication. A combination of XRD and heat flow measurements (XRD-DSC)

enables to characterize unambiguously the kinetics of polymorphic transformation in mixed lipid systems, for example (Sato & Ueno, 2005). X-Ray diffraction can be performed with benchtop instruments, or by using high-intensity sources such as synchrotron light, which allow higher resolution and throughput in terms of samples analysed.

X-Rays may also be used to provide a two or three-dimensional map of the density distribution of a sample; this technique is called X-Ray Radiography (XRR) and Tomography (XCT), respectively. Both techniques are non-destructive and non-invasive, reaching a sub-micron resolution and a field of view ranging from few centimetres to a few millimetres. XCT equipment consists of an X-Ray source, a rotating sample holder, and a detector. The sample is mounted into a movable stage that rotates during the tomography measurement. Detectors convert the X-Ray radiation to visible light, which is then focused by optical lenses into a CCD camera (Barigou & Douaire, 2013) (Figure 2.17). Furthermore, the sample can be accommodated in an enclosed chamber to control temperature and pressure and perform dynamic studies on the sample microstructure.

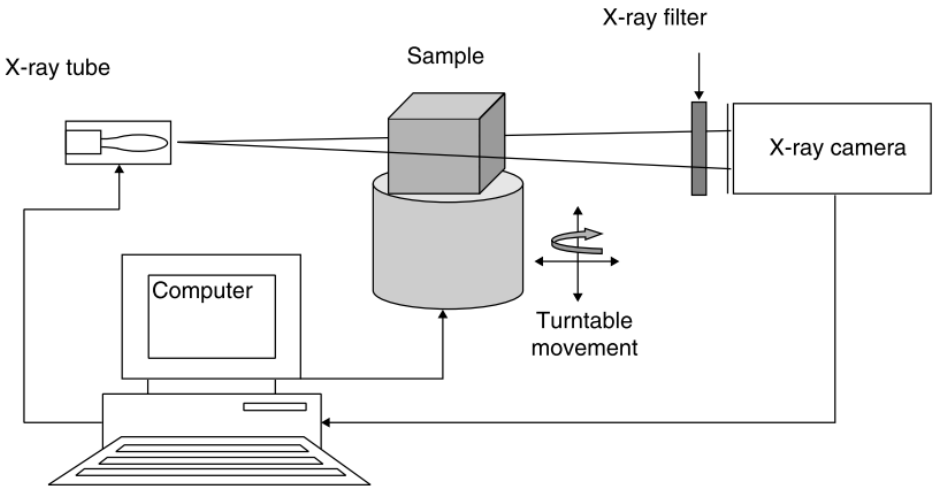

Figure 2.17. X-ray tomography experiment setup. Reproduced from Barigou & Douaire (2013).

For benchtop XCT equipment a conical X-Ray beam is generated, which is however polychromatic and may cause artefacts due to the selective attenuation of low-energy X-rays, with higher-energy X-rays reaching the detector unaltered (beam hardening). Synchrotron facilities instead produce a beam of parallel rays, allowing better resolution (hundreds of nm) due to the homogeneous signal obtained. Furthermore, the use of a

monochromator permits selection of specific X-Ray energies, improving qualitative and quantitative analysis. The synchrotron beam size is smaller (1×30mm), thus limiting its applicability to samples of comparable size only. In XCT, the sample attenuates X-Rays by absorption and scattering, depending on factors such as atomic mass, density and absorption coefficient of the material. As the sample is being rotated, several 2D radio-graphs are acquired, which represent the spatial distribution of the radio-opacity of the sample. The stack of generated images are then reconstructed into a 3D volume by software processing and yields the internal microstructure of the sample. This is particularly advantageous as light microscopes cannot penetrate opaque samples, and electron microscopes – despite their resolution being higher in certain configurations – require invasive sample preparation in order to penetrate inside samples (Barigou & Douaire, 2013). In soft matter applications soft X-Rays (up to 50 keV) are preferentially used, both to limit sample damage and to increase contrast between phases with similar density. In fact, as the attenuation of X-Rays is affected by density, emulsions constitute a challenging sample to investigate, due to the close density of water and oils, at small length scales. Aerated materials, on the other hand, are more straightforward to image due to the large density difference between air and liquids or solids. Phase-contrast imaging exploits the differences in refractivity displayed by X-Rays that cross different domains, which is used to generate additional contrast in the image. This emerging mode of operation complements attenuation-based measures and it is useful especially for biological samples that display low absorption of X-Rays (Willner et al., 2016). Parameters such as density, porosity, and surface to volume ratio of the object analysed, together with particle size and sample thickness are used to characterize the microstructure of the sample. However, data processing for XCT data is very demanding in terms of time and computational power, as well as requiring a large volume of data storage. Segmentation is usually performed on the images in order to extract features of interest via distinct greyscales or morphological characteristics, including particles, voids or layers. The presence of noise in the image can make segmentation very challenging and pre-processing of the images is often required (Wang et al., 2018).

References

Abkarian, M., Subramaniam, A. B., Kim, S. H., Larsen, R. J., Yang, S. M., & Stone, H. A. (2007). Dissolution

arrest and stability of particle-covered bubbles. *Physical Review Letters*, *99*(18), 1–4. https://doi.org/10.1103/PhysRevLett.99.188301

Barigou, M., & Douaire, M. (2013). *X-ray micro-computed tomography for resolving food microstructures*. *Food Microstructures: Microscopy, Measurement and Modelling*. Woodhead Publishing Limited. https://doi.org/10.1533/9780857098894.1.246

Beltramo, P. J., Gupta, M., Alicke, A., Liascukiene, I., Gunes, D. Z., Baroud, C. N., & Vermant, J. (2017). Arresting dissolution by interfacial rheology design. *Proceedings of the National Academy of Sciences of the United States of America*, *114*(39), 10373–10378. https://doi.org/10.1073/pnas.1705181114

Binks, B. P. (2002). Particles as surfactants: similarities and differences. *Current Opinion in Colloid & Interface Science*, *7*(1), 21–41. https://doi.org/10.2118/141256-PA

Bunaciu, A. A., Udriştioiu, E. gabriela, & Aboul-Enein, H. Y. (2015). X-Ray Diffraction: Instrumentation and Applications. *Critical Reviews in Analytical Chemistry*, *45*(4), 289–299. https://doi.org/10.1080/10408347.2014.949616

Cantat, I., Cohen-Addad, S., Elias, F., Graner, F., Hohler, R., Pitois, O., … Saint-Jalmes, A. (2013). *Foams, Structure and Dynamics*. (S. J. Cox, Ed.) (First Edition). Oxford: Oxford University Press.

Chen, D. T. N., Wen, Q., Janmey, P. A., Crocker, J. C., & Yodh, A. G. (2010). Rheology of soft materials. *Annual Review of Condensed Matter Physics*, *1*, 301–322. https://doi.org/10.1146/annurev-conmatphys-070909-104120

Crist, B., & Schultz, J. M. (2016). Polymer spherulites: A critical review. *Progress in Polymer Science*, *56*, 1–63. https://doi.org/10.1016/j.progpolymsci.2015.11.006

Den Engelsen, D. (1976). Optical anisotropy in ordered systems of lipids. *Surface Science*, *56*(C), 272–280. https://doi.org/10.1016/0039-6028(76)90452-0

Drenckhan, W., & Saint-Jalmes, A. (2015). The science of foaming. *Advances in Colloid and Interface Science*, *222*, 228–259. https://doi.org/10.1016/j.cis.2015.04.001

Dudkiewicz, A., Tiede, K., Loeschner, K., Jensen, L. H. S., Jensen, E., Wierzbicki, R., … Molhave, K. (2011). Characterization of nanomaterials in food by electron microscopy. *TrAC - Trends in Analytical Chemistry*, *30*(1), 28–43. https://doi.org/10.1016/j.trac.2010.10.007

Goodwin, J., & Hughes, R. (2008). Linear viscoelasticity I. Phenomenological approach. In *Rheology for Chemists* (Second Edi, pp. 98–145). Cambridge, UK: RSC Publishing. https://doi.org/10.1039/9781847551832-00098

Groves, K., & Parker, M. L. (2013). *Appendix: Electron microscopy: principles and applications to food microstructures*. *Food Microstructures*. Woodhead Publishing Limited. https://doi.org/10.1533/9780857098894.2.386

Gunning, P. A. (2013). *Light microscopy: Principles and applications to food microstructures*. *Food Microstructures: Microscopy, Measurement and Modelling* (Vol. 1665). Woodhead Publishing Limited. https://doi.org/10.1533/9780857098894.1.62

Hill, C., & Eastoe, J. (2017). Foams: From nature to industry. *Advances in Colloid and Interface Science*, *247*(May), 496–513. https://doi.org/10.1016/j.cis.2017.05.013

Himawan, C., Starov, V. M., & Stapley, A. G. F. (2006). Thermodynamic and kinetic aspects of fat crystallization. *Advances in Colloid and Interface Science*, *122*, 3–33. https://doi.org/10.1016/j.cis.2006.06.016

Idziak, S. H. J. (2012). Powder X-ray Diffraction of Triglycerides in the Study of Polymorphism. *Structure-Function Analysis of Edible Fats*, 79–106.

James, B. (2009). Advances in “wet” electron microscopy techniques and their application to the study of food structure. *Trends in Food Science and Technology*, *20*(3–4), 114–124. https://doi.org/10.1016/j.tifs.2009.01.057

Lazidis, A., de Almeida Parizotto, L., Spyropoulos, F., & Norton, I. T. (2017). Microstructural design of aerated food systems by soft-solid materials. *Food Hydrocolloids*, *73*, 110–119.

https://doi.org/10.1016/j.foodhyd.2017.06.032

Liu, H., Lelievre, J., & Ayoung-Chee, W. (1991). A study of starch gelatinization using differential scanning calorimetry, X-ray, and birefringence measurements. *Carbohydrate Research*, *210*(C), 79–87. https://doi.org/10.1016/0008-6215(91)80114-3

Martinez, A. C., Rio, E., Delon, G., Saint-Jalmes, A., Langevin, D., & Binks, B. P. (2008). On the origin of the remarkable stability of aqueous foams stabilised by nanoparticles: Link with microscopic surface properties. *Soft Matter*, *4*(7), 1531–1535. https://doi.org/10.1039/b804177f

McClements, J., & McClements, D. J. (2016). Standardization of Nanoparticle Characterization: Methods for Testing Properties, Stability, and Functionality of Edible Nanoparticles. *Critical Reviews in Food Science and Nutrition*, *56*(8), 1334–1362. https://doi.org/10.1080/10408398.2014.970267

Murray, B. S., & Ettelaie, R. (2004). Foam stability: Proteins and nanoparticles. *Current Opinion in Colloid and Interface Science*, *9*(5), 314–320. https://doi.org/10.1016/j.cocis.2004.09.004

Oriel, P. J., & Schellman, J. A. (1966). Studies of the birefringence and birefringence dispersion of polypeptides and proteins. *Biopolymers*, *4*(4), 469–494. https://doi.org/10.1002/bip.1966.360040408

Povey, M. J. (1997). *Ultrasonic techniques for fluid characterization*. San Diego: Academic Press.

Povey, M. J. W. (1998). Ultrasonics of food. *Contemporary Physics*, *39*(6), 467–478. https://doi.org/10.1080/001075198181784

Rio, E., Drenckhan, W., Salonen, A., & Langevin, D. (2014). Unusually stable liquid foams. *Advances in Colloid and Interface Science*, *205*, 74–86. https://doi.org/10.1016/j.cis.2013.10.023

Russ, J. C. (2015). Image Analysis of Foods. *Journal of Food Science*, *80*(9), 1974–1987. https://doi.org/10.1111/1750-3841.12987

Sanderson, J. (2019). *Understanding Light Microscopy* (First Edition). Hoboken, NJ: John Wiley & Sons Ltd.

Sato, K. (2001). Crystallization behaviour of fats and lipids—a review. *Chemical Engineering Science*, *56*(7),

2255–2265. Retrieved from http://www.sciencedirect.com/science/article/pii/S0009250900004589

Sato, K., Bayés-García, L., Calvet, T., Cuevas-Diarte, M. À., & Ueno, S. (2013). External factors affecting polymorphic crystallization of lipids. *European Journal of Lipid Science and Technology*, *115*(11), 1224–1238. https://doi.org/10.1002/ejlt.201300049

Sato, K., & Ueno, S. (2005). Polymorphism in Fats and Oils. *Bailey's Industrial Oil and Fat Products*, 77–120. https://doi.org/10.1002/047167849X.bio020

Taccoen, N., Lequeux, F., Gunes, D. Z., & Baroud, C. N. (2016). Probing the mechanical strength of an armored bubble and its implication to particle-stabilized foams. *Physical Review X*, *6*(1), 1–11. https://doi.org/10.1103/PhysRevX.6.011010

Turnbull, D., & Fisher, J. C. (1949). Rate of nucleation in condensed systems. *The Journal of Chemical Physics*, *17*(1), 71–73. https://doi.org/10.1063/1.1747055

Urick, R. J. (1947). A sound velocity method for determining the compressibility of finely divided substances. *Journal of Applied Physics*, *18*(11), 983–987. https://doi.org/10.1063/1.1697584

Wang, Z., Herremans, E., Janssen, S., Cantre, D., Verboven, P., & Nicolaï, B. (2018). Visualizing 3D Food Microstructure Using Tomographic Methods: Advantages and Disadvantages. *Annual Review of Food Science and Technology*, *9*(1), 323–343. https://doi.org/10.1146/annurev-food-030117-012639

Willner, M., Viermetz, M., Marschner, M., Scherer, K., Braun, C., Fingerle, A., … Herzen, J. (2016). Quantitative three-dimensional imaging of lipid, protein, and water contents via x-ray phase-contrast tomography. *PLoS ONE*, *11*(3), 1–13. https://doi.org/10.1371/journal.pone.0151889

Wood, A. B. (1946). *A textbook of Sound* (Second Edition). London: G. Bell and Sons Ltd.

Chapter 3: Effect of crystallization conditions on the structural properties of oleofoams made of cocoa butter crystals and high oleic sunflower oil

Abstract

Edible air-in-oil systems, also referred to as oleofoams, constitute a novel promising material for healthier, low-calorie fat replacers in confectionary products. Oleofoams can be formed by whipping oleogels, which are dispersions of fat crystals in an oil phase. Understanding how the properties of the fat crystals (*i.e.,* size, shape, polymorphism) contained in oleogels affect the microstructure and stability of oleofoams is essential for both the efficient design and manufacture of novel food products. In this work, cocoa butter – one of the main fat phases present in confectionary productions, which is responsible for pleasant texture and mouthfeel properties – was mixed with high oleic sunflower oil and crystallized to obtain an oleogel. This was subsequently whipped to yield a stable, highly aerated oleofoam. The effect of the crystallization conditions (oleogel composition and cooling rate) on the properties of the oleogels and related oleofoams was investigated with a multi-technique characterization approach, featuring polarized light microscopy, cryogenic scanning electron microscopy, X-Ray diffraction, differential scanning calorimetry and oscillatory rheology. Oleogel crystallization was performed in a lab-scale vessel, and was monitored using light turbidimetry as an *in*-situ technique. Results showed that the concentration of cocoa butter in sunflower oil was the parameter that affected most strongly the foamability and rheology of oleofoam samples. The size and shape of cocoa butter crystals within the oleogel was found to have a less significant effect, since crystals were broken or partially melted during the aeration process. Oleofoams whipped from oleogels containing 15% w/w and 22% w/w cocoa butter displayed an overrun of 200% – corresponding to a calorific density reduction to one-third – and an increase in both the elastic and viscous moduli compared to their oleogel precursor. This was explained by a structuring effect caused by the aeration process, where cocoa butter β(V) crystal nanoplatelets (CNPs) in the oleogel rearranged

to stabilize the air bubbles *via* a Pickering mechanism. Oleofoams prepared from 30% w/w cocoa butter oleogels, on the other hand, incorporated less air (overrun between 150% and 180%) and displayed a similar viscoelastic profile to their un-whipped precursors, potentially due to air incorporation being limited by the relatively high elastic modulus of the parent oleogels. Nevertheless, the calorific density of these samples was reduced by a factor of 1.6 to 2.5 compared to their full-fat analogues.

3.1 Introduction

The prevalence of overweight and obese population in several countries has been described as a global pandemic, causing in 2015 an estimated 4.0 million deaths, along with 120 million people living with disabilities (Afshin et al., 2017). Several factors promote obesity and related health conditions in individuals, but excessive dietary caloric intake is the predominant cause (Ng et al., 2014). Edible lipids (such as fats and oils) constitute the most energy-dense macronutrient, and their effects on health have been studied since the 1950s, with a particular focus on saturated fats. The role of saturated fats in directly promoting obesity has still not fully been proven (Ruiz-Núñez et al., 2016), but dietary guidelines issued by the Food and Agriculture Organization (FAO) and the European Food Safety Authority (EFSA) advised the reduction of saturated fats to 10% of the total daily caloric intake, and their replacement with polyunsaturated fatty acids (PUFAs), commonly found in oils (EFSA, 2010; FAO, 2008). Therefore, food research has recently focused on reformulating food products with a reduced level of saturated fats, while maintaining desirable sensory attributes (McClements, 2020). Nevertheless, saturated fats have a critical role in determining desirable physicochemical and sensorial attributes in foods, hence making their replacement or reduction challenging. Confectionary products are an example of food rich in saturated fats (Ghotra et al., 2002; Rios et al., 2014). The main ingredient of chocolate and chocolate fillings, cocoa butter, contains around 60% w/w saturated fats, mainly from stearic acid. Cocoa butter beneficially affects the rheology of such products, their melting behaviour and flavour release (Rios et al., 2014). Reducing

this type of fats in food products is not only driven by health concerns, but is further underscored by environmental and economic issues related to sustainable cocoa butter production (Beg et al., 2017; Jahurul et al., 2013).

Oleogelation of edible oils has been proposed as a viable replacement of saturated fats in food formulation, as it results in similar rheological and sensorial properties, but lower saturated fat content. Oleogelation is the process of adding an edible oil (up to 90% w/w) to gelator molecules that are able to convert the liquid oil into a gel, with solid-like properties. This is achieved through the formation of a three-dimensional, supramolecular network of either molecules or crystals that entraps the oil phase. Commonly used gelators are high-melting triacylglycerides (TAGs), di-glycerides (DAGs) or monoglycerides (MAGs), fatty acids and fatty alcohols, as well as edible waxes, ethyl cellulose or native phytosterols (Patel & Dewettinck, 2016). Oleogels have been used to replace saturated fat in foods, such as baking shortenings, spreads and margarines (Demirkesen & Mert, 2019; Pehlivanoğlu et al., 2018). Additionally, oleogels have been used to reformulate confectionery fillings and chocolate pastes with reduced saturated fat and resistance to oil migration (Doan et al., 2016; Patel et al., 2014; Si et al., 2016).

While oleogelation improves significantly the nutritional profile of full-fat products through the reduction in saturated fats, it still involves the use of large amounts of edible oils in their formulation, retaining a similar calorific content to solid fat. Incorporating gas bubbles in oleogels is a possible solution to decrease their calorific content while maintaining appealing rheological and sensory (*e.g.* creaminess) properties (Campbell & Mougeot, 1999). Moreover, aerated foods induce satiety independently of their calorific content (Blom et al., 2016), and deliver a comparable mouth coating to their non-aerated analogues, stimulating the oral mechanoreceptors in a similar fashion (Palzer, 2017). Stable air bubbles can also be incorporated in oleogels and stabilized *via* a Pickering mechanism, whereby solid fat crystals are adsorbed at the air/oleogel interface preventing phase separation and coalescence. Aerated oleogels, also called oleofoams, have recently gained attention due to their potential to reformulate food products with lower

calorific density (Heymans et al., 2017). In fact, the use of oleofoams for reducing fat content and calorific density in confectionery has been reported in at least two patents (Chisholm et al., 2016; Gunes et al., 2016).

Typically, oleofoams are produced by adding a high-melting fat (*e.g.,* a food-grade monoglyceride) to a vegetable oil in the molten state, followed by cooling to yield a dispersion of fat crystals. Subsequently, the material is whipped to entrain air bubbles under shear, which are coated by the fat crystals to produce a stable foam. Hence, controlling the crystal size dispersity by fine-tuning the crystallization process parameters is a fundamental aspect of oleofoam production. Other methods of aeration involved the injection of inert gases in the continuous phase, or application of vacuum followed by expansion of small gas bubbles in the continuous phase (Haedelt et al., 2005).

Given the central role of crystals in the formation of oil-base foams, their concentration in the oil, their size, shape and polymorphism are pivotal to determining the microstructure, foamability (*i.e.* the amount of incorporated air), the viscoelasticity and stability of oleofoams (Fameau & Saint-Jalmes, 2017a). TAGs, one of the main chemical species in fats and oils, also exhibit complex polymorphism. The main crystal polymorphs are, in increasing order of thermodynamic stability, α (hexagonal subcell), β' (orthorhombic subcell) and β (triclinic subcell) (Himawan et al., 2006).

Oleofoam aeration can only be achieved in a specific range of crystalline concentrations. Below the lower limit there is an insufficient quantity of fat crystals to stabilize the foam, whereas an excessive amount of solids results in a very firm oleogel, which is difficult to aerate (Binks et al., 2016; Brun et al., 2015; Fameau et al., 2015). Those limits are, however, system-dependent and also affected by the aeration equipment used to produce oleofoams (Fameau & Saint-Jalmes, 2017a).

Micron-sized needle or platelet-shaped crystals were found to be most effective at stabilizing air bubbles, as opposed to larger or aggregated crystals. Mishima et al. (2016) prepared oleogels from TAGs crystals

(fully hydrogenated rapeseed oil rich in behenic acid, FHR-B) in salad oil (a mixture of soybean and rapeseed oil) using different tempering protocols. The study found that oleogels containing small (2-6 μm in length) crystals were able to incorporate more air in less whipping time, compared to oleogels containing larger crystals (10-30 μm in length) (Mishima et al., 2016). In some cases, oleogels containing large crystals of monostearin and native phytosterol (NPS) obtained with slow cooling rates could not be aerated at all, as reported by Truong et al. (2019) (Truong et al., 2019).

Lack of control over the polymorphic form nucleated during crystallization resulted in poor foamability, as reported by Mishima et al. (2016) for the above-mentioned salad oil and FHR–B system. The authors showed that oleogels containing tempered β crystals were able to produce highly aerated foams, whereas untempered β' oleogels barely incorporated any air (Mishima et al., 2016). Heymans et al. (2018) investigated further the effect of polymorphism on the foamability of oleogels (Heymans et al., 2018). In this work, five tempering protocols were used to prepare oleogels with sub-α crystals (SAC), partially and fully crystallized α crystals (PAC and AC, respectively), melt-mediated β crystals (MMACS) and solid-state transformed β crystals (ACS) from a commercial monoglyceride and sunflower oil. AC and MMACS oleogels produced oleofoams with similar overruns, PAC oleogels incorporated slightly more air but were unstable and subject to oil drainage in storage, while SAC oleogels could not be aerated at all. However, it is not clear from the study whether the latter polymorph melted during aeration or if it was not surface-active. Control over crystallization is critical to ensure oleogel precursors with suitable crystalline properties for aeration. In industrial settings, crystallization is a complex process, affected by several factors, such as shearing, thermal fluctuations and presence of impurities (Agrawal & Paterson, 2015; Toro-vazquez et al., 2005).

Vegetable oils could be aerated in absence of added high-melting fat species, as recently demonstrated by Liu & Binks (2021) (Liu & Binks, 2021). The authors prepared oleogels by cooling peanut oil and olive oil down to –20°C in order to crystallize the unsaturated TAGs present in the oil. Oleofoams were

produced with modest overrun values (40% for peanut oil, 110% for olive oil oleogels) while maintaining the aeration temperature below 0°C. In a previous publication, Binks & Marinopoulos (2017) demonstrated also the ability of natural fats to produce oleofoams, including cocoa butter (Binks & Marinopoulos, 2017).

However, the properties of cocoa butter crystals and how they relate to the final oleofoam microstructure were not considered in such work. Cocoa butter has a complex crystallization behaviour and it is a key ingredient in many confectionary products, including chocolate fillings. Therefore, obtaining a better understanding of how the properties of cocoa butter crystals affect the stability and microstructure of oleofoams is essential for the design of novel confectionary products and manufacturing processes. In particular, this work aims to investigate the effect of crystallization conditions on the properties of oleogels as well as on the microstructure and stability of the derived oleofoams. The crystallization of cocoa butter-based oleogels was carried out in a laboratory-scale vessel and monitored *in situ* with light turbidimetry. Cocoa butter was mixed with high oleic sunflower oil, which displays high resistance to oxidation (Raß et al., 2008), in order to reduce the total amount of saturated fats of the system compared to pure cocoa butter.

Three cooling rates and three suitable concentrations of cocoa butter in sunflower oil were chosen for preparing the oleogel precursor. These concentrations were selected to ensure the presence of a sufficient amount of stabilizing crystals without yielding oleogels that were too firm to aerate. The effects of the size, morphology and polymorphism of cocoa butter crystals on the microstructure, rheology and foamability of oleogels and related oleofoams was then investigated with a multi-technique approach. This included polarized light microscopy (PLM), cryogenic scanning electron microscopy (CryoSEM) for the crystal morphology, X-Ray diffraction (XRD) for crystal polymorphism, differential scanning calorimetry (DSC) for the melting properties and oscillatory rheology for the viscoelasticity.

3.2 Materials and Methods

3.2.1 Materials

Refined, bleached and deodorized cocoa butter (CB) and high-oleic sunflower oil (HOSO) were kindly provided by Nestlé PTC (York, UK) and used without any further purification. Typical fatty acid composition by weight of HOSO is 86 % oleic acid, 5% stearic acid, 3% linoleic acid, 3 % palmitic acid, 1.5% behenic acid and 0.7% arachidic acid (Fernández-Moya et al., 2000). CB normally contains by weight about 26 % palmitic acid, 36% stearic acid, 34% oleic acid, 2.7% linoleic and 0.9% of arachidic acid (Lipp et al., 2001).

CB was melted at 65°C for at least 30 minutes, using a stirring hot plate. It was then mixed with HOSO in three different concentrations (15, 22 and 30% of CB by weight). Samples with % CB w/w below 15% were also tested but they melted rapidly and produced oleofoams with significant oil drainage; hence, they were not investigated further. Throughout this paper, oleogel and oleofoam samples were named based on their CB concentration and the cooling rate used during crystallization: F for fast cooling (0.75°C/min), M for medium cooling (0.25°C/min) and S for slow cooling (0.10°C/min). Cocoa butter seeds in the β(V) polymorph were purchased from Callebaut (Zurich, Switzerland) and used as reference for the crystalline form in oleogel and oleofoam samples in this paper.

3.2.2 Synchrotron Radiation X-Ray Diffraction (SR-XRD)

The crystallization behaviour of cocoa butter in sunflower oil in quiescent conditions was investigated with synchrotron radiation X-Ray diffraction (SR-XRD, λ = 0.69 Å) using beamline I22 at Diamond Light Source (DLS, Didcot, UK). The sample-to-detector distance (SDD) was set to 8.732 m and the 2D diffraction patterns were recorded on a Pilatus 2M detector (Dectris Ltd, Switzerland). Disposable polycarbonate capillaries (diameter 2 mm) were filled with mixtures of melted CB and HOSO in different weight ratios (15%, 22%, 32% w/w) and loaded into a temperature-controlled multi-capillary rack, controlled with an external water circulator (Lauda, Germany). The temperature was initially set to 65°C for 5 minutes,

followed by stepwise cooling to 20, 15 10 and 7 °C at approximately -1 °C/min. Each temperature was maintained for 5 minutes prior to the measurement, after that the diffraction pattern of each sample was collected. The exposure time was set to 1.0 seconds. An empty polycarbonate capillary was used for background scattering subtraction. Diffraction images were analysed using the DAWN software and following the procedure outlined by Filik et al. (2017)(Filik et al., 2017)(Filik et al., 2017)(Filik et al., 2017). The signal of the melted samples was subtracted using MATLAB 2020a (MathWorks, USA). A detailed explanation of the subtraction procedure used is provided in Appendix A.

3.2.3 Oleogel Crystallization and Aeration

A total mass of 450g of molten cocoa butter and sunflower oil mixtures at the three concentrations of 15, 22 and 30% CB w/w were poured into a custom-made steel jacketed vessel (capacity *ca.* 2 L, diameter 25 cm) connected to a Huber Ministat 250 thermostat (Huber, Germany) filled with mineral oil as heating/cooling medium. Samples were stirred continuously at 200 rpm with a DLH Overhead Stirrer (VELP Scientifica, Italy), equipped with a 4 pitched-blade impeller (4 cm diameter). A Pt-100 temperature probe was placed inside the vessel to measure the temperature of the mixture during crystallization. A schematic of the crystallization setup used for the experiments is shown in Figure 3.1.

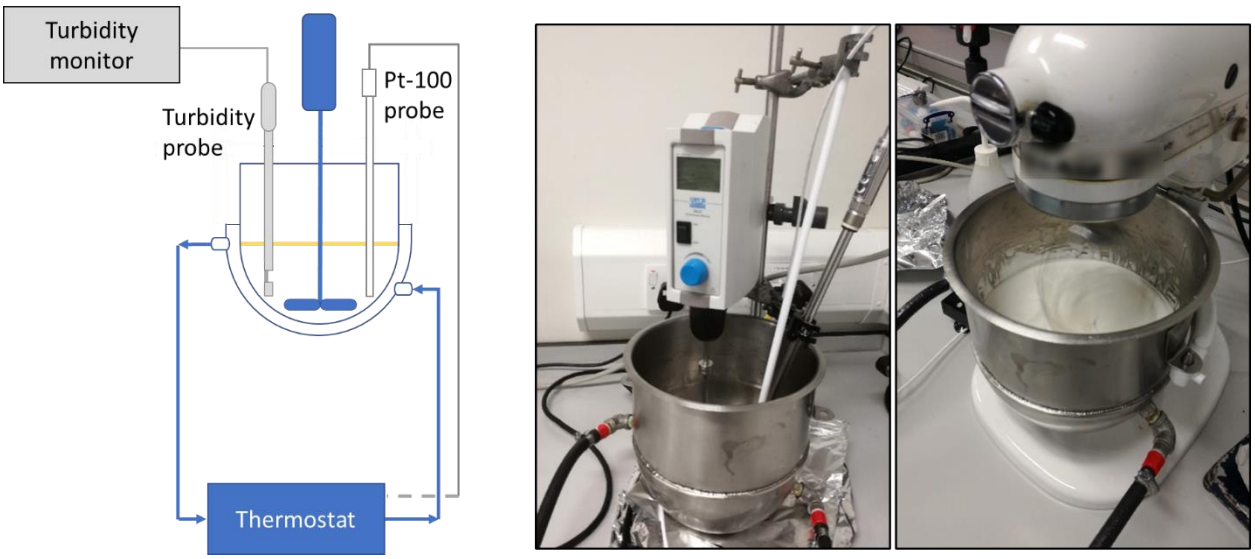

Figure 3.1. Schematics and photographs of the rig used for the crystallization and aeration experiments.

The initial thermal profile for the cocoa butter crystallization and the formation of the oleogels was the same for all experiments performed and it was set as following: after being molten at 65 °C for 30 minutes, the mixture was transferred in the crystallization vessel and left to equilibrate at 65 °C for further 5 minutes, and then cooled from 65 °C to 37 °C at –1 °C/min cooling rate. After that, each oleogel mixture (15, 22 and 30% CB w/w) was cooled from 37 °C to 0 °C with a nominal rate of –0.75, –0.25 or –0.10 °C/min (C_r). Each experiment was repeated in triplicates. The crystallization process was monitored with a Control 4000 turbidity meter (Optek, Germany) fitted with an ASD12-N Absorption Probe. This instrument measures the light transmittance and absorbance, which can be calculated from the Lamber-Beer's law (Equation 3.1):

$$\frac{I}{I_0} = \exp -\tau l c \qquad \text{Eq. 3.1}$$

where I and I_0 are the intensity of the light beam through the sample and of the incident light beam, respectively; τ is the turbidity parameter (m^2 kg^{-1}), similar to the extinction coefficient, *l* is the sample thickness (m) and *c* is the concentration of scattering material (kg m^{-3}). Transmittance (T) and absorbance (A) are defined as (Equation 3.2 and 3.3)

$$T = 100 \times \frac{I_0}{I} \qquad \text{Eq. 3.2}$$

$$A = -\log\left(\frac{I}{I_0}\right) \qquad \text{Eq. 3.3}$$

Upon the onset of crystallization, the transmittance signal started to drop due to increased turbidity in the sample. Once crystallized, the sample was left to equilibrate at the final temperature until a stable absorbance reading was seen. Light absorbance is approximately correlated to the amount of solid particles scattering the incoming light (Wright et al., 2000); hence, a stable absorbance reading was

interpreted as the reach of crystallization equilibrium at the final temperature. The oleogels thus obtained were manually mixed to obtain a homogeneous sample and their density measured volumetrically by weighting a measuring cup of a fixed volume of 30 mL. Density measurements were conducted in triplicates for each oleofoam produced. The effective cooling rates were calculated by linearly fitting the measured temperature of the samples between 37 °C and their crystallization temperatures (T_{Cr}).

The crystallized oleogel samples were then aerated using a Heavy Duty model 5KPM50 planetary mixer (Kitchenaid, USA) machine equipped with a wire beater. The temperature of the jacketed vessel was maintained at 0 °C during the aeration process. The temperature of the oleofoam was monitored during whipping using a portable kitchen thermometer, measuring the sample in five different points inside the aeration vessel. The whipping speed was set to 180 rpm for all experiments. Oleogels were whipped in cycles of 5 minutes with 10 minutes rest, for a total aeration time of 30 minutes. Solid un-whipped oleogel on the vessel walls was reintroduced with a spatula as necessary. During the resting stage the overrun of the oleofoams was calculated by measuring the weight of the measuring cup of known volume filled with the aerated sample. Measurements were done in triplicates. The overrun was calculated according to Equation 3.4 (Heymans et al., 2018) and then plotted as a function of whipping time:

$$OR(\%) = 100 \times \frac{\left(w_{oleogel} - w_{foam}\right)}{w_{foam}} \qquad \text{Eq. 3.4}$$

Where $w_{oleogel}$ is the weight of a fixed volume of oleogel, while w_{foam} is the weight of the same volume of oleofoam. Oleofoam and oleogel samples were collected at each aeration step and stored in a temperature-controlled cabinet at 20 °C for three months.

3.2.4 Polarized Light Microscopy

Cocoa butter crystals formed in sunflower oil were observed with a Leitz Dialux 22 polarized microscope (Leica, Germany) in both oleogel and oleofoam samples. A small amount of sample (tip of a spatula) was

placed on a glass microscope slide and gently covered with a glass cover slip. Digital images of each sample were acquired with a Canon DLSR camera at 10x and 40x magnification, and processed with ImageJ 1.52a (National Institute of Health, USA). The pixel size for 10x and 40x images was 0.48x0.48 μm^2 and 0.12x0.12 μm^2, respectively. An estimate of the average crystals' diameter was calculated by measuring the size of around 100 crystals from 5 different images collected for each sample.

3.2.5 Cryogenic Scanning Electron Microscopy

The microstructure of oleogel and oleofoam samples was investigated by using a Helios G4 CX DualBeam scanning electron microscope (FEI, USA), coupled with a PP3010T Cryo-FIG/SEM preparation system (Quorum Technologies, UK). A small amount of the sample was placed in a pre-cooled rivet holder and quickly transferred into a container filled with liquid nitrogen. The rivet containing the sample was then inserted in the preparation chamber and kept at –145 °C under vacuum ($<10^{-7}$ mbar). The frozen sample was then fractured in the middle of the rivet using a cooled sharp knife and sublimed at –90 °C to avoid any frost depositing on the surface, then cooled again to –145 °C. In order to avoid charge build-up while imaging, the sample surface was sputtered with iridium (10 mA for 30 s). The sample was then transferred inside the microscope chamber and imaged using a 2 kV accelerating voltage and 0.10 nA beam current. The diameter of the air bubbles and the size of the crystals were evaluated using ImageJ 1.52a (National Institute of Health, USA).

3.2.6 Benchtop X-Ray Diffraction

Cocoa butter polymorphism in oleogels and oleofoams prepared in the laboratory-scale vessel was determined by X-Ray diffraction experiments, with a SAXSpace instrument (Anton Paar GmbH, Austria) equipped with a Cu-anode operating at 40 kV and 50 mA (λ=0.154 nm). The temperature inside the sample chamber was regulated with a TCStage 150 Peltier element (Anton Paar, Austria) and set to 20 °C for all

experiments, to resemble the oleogel and oleofoam storage temperature. Samples were loaded into a Paste Cell equipped with X-Ray transparent Kapton windows. The 1D diffraction patters were recorded with a Mythen X-ray detector (Dectris Ltd, Switzerland). Small-angle and wide-angle measurements were obtained by changing the sample to detector distance (SDD) to 317 or 130 mm, respectively. The acquisition time used was 200 s for all experiments. Three measurements for each sample were collected.

3.2.7 Differential Scanning Calorimetry

The melting temperature (T_m) of the produced oleogels and oleofoams was determined by differential scanning calorimetry (DSC) using a Perkin Elmer 8000 calorimeter (Perkin Elmer, USA) and a TA 8000 (TA Instruments, USA). The samples were melted from 10 °C to 65 °C at a heating rate of 5 °C/min. DSC measurements were carried out in triplicate, and the average endothermic peak maximum temperature (T_m) was calculated.

3.2.8 Oscillatory Rheology

Amplitude sweeps of oleogel and oleofoam samples were carried out on an MCR 302 stress-controlled rheometer in order to measure sample elastic and viscous moduli. A 25mm parallel plate was used for all experiments, with a sample gap of 1.0 mm. Amplitude sweeps at a fixed frequency of 1 Hz were performed from 0.001% to 10% strain. The temperature was maintained constant with a Peltier hood connected to a F25-HE water circulator (Julabo, Seelbach, Germany) at 20°C. Samples were measured 24 hours after they were crystallized or aerated. Each sample was measured in triplicates. Data analysis was carried out with the Rheocompass version 1.21 (Anton Paar GmbH, Austria). The elastic modulus in the linear viscoelastic regime (G'_{LVER}) was calculated by averaging the G' values between 0.001% and 0.01% strain, where both viscous and elastic moduli were observed to be independent of the applied strain (Binks et al., 2016). The flow point (τ_f) was calculated as the crossing point of the elastic and viscous curve.

3.2.9 Oil Drainage and Stability Test

In order to assess the destabilization of oleofoam samples due to oil drainage, 50 mL of oleofoam samples from the final whipping cycle were transferred into graduated cylinders (2 cm diameter) and left in temperature-controlled storage at 20°C. Samples were visually inspected every 2 weeks for 3 months. The volume of drained oil was measured volumetrically over time.

3.3 Results and Discussion

3.3.1 Crystallization behaviour of CB/HOSO mixtures in capillaries

The effect of CB concentration on the crystallization behaviour of CB/HOSO mixtures was investigated first in quiescent conditions (small volume and absence of shear) with SR-XRD. The aim of this set of experiments was to get a basic understanding of the crystallization behaviour of CB/HOSO mixtures and to relate these results with the behaviour of the same oleogels in the lab-scale crystallization rig, under the effect of shear and using a larger volume.

Figure 3.2 shows the diffraction patterns of CB/HOSO mixtures cooled down to different temperatures from the melt. In order to highlight the presence of peaks from the cocoa butter crystals, the WAXS patterns in Figure 3.2 were obtained by subtracting the signal of the molten mixture at 20 °C from the respective signals of the crystallizing mixtures at 15, 10 and 7 °C.

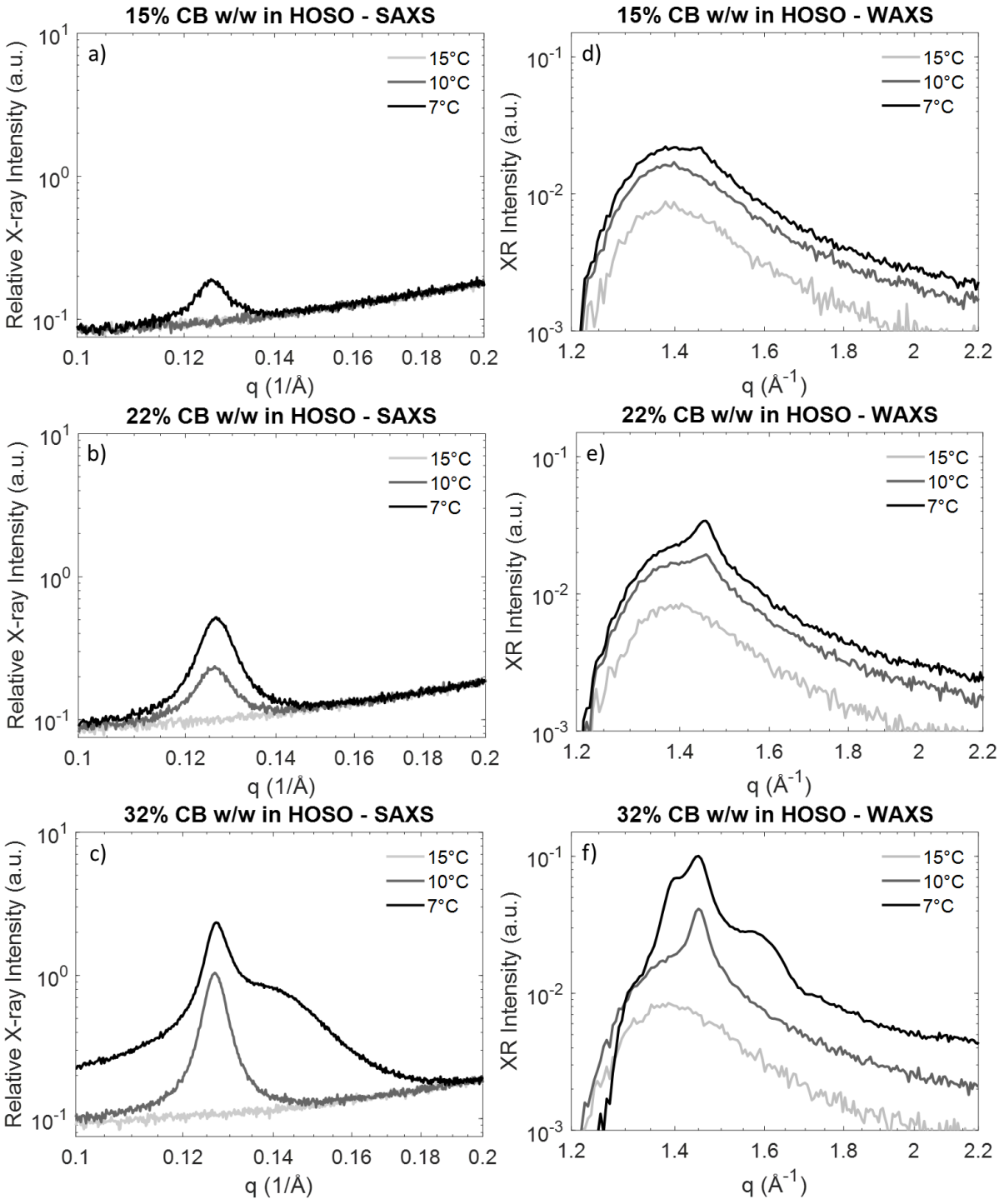

Figure 3.2. Synchrotron X-Ray diffraction patterns for the crystallization of CB/HOSO mixtures in capillaries during cooling. Small angle region from a) to c) (without melt subtraction), wide angle region from d) to f) (with melt subtraction).

The molten phase generates a broad scattering peak between q = 1.2 $Å^{-1}$ and q = 2.3 $Å^{-1}$ in the wide-angle region. Sections of this region were used to determine the baseline for each WAXS pattern. A detailed description of the baseline determination and subtraction procedure is provided in Appendix A. Unfortunately, the position of the broad signal of the molten CB shifted towards higher q values with decreasing temperatures. This is why it is still partly visible in some diffraction pattern even after baseline subtraction; this artefact is likely affecting the position of the WAXS peaks.

In the CB/HOSO mixture with 15% CB w/w crystals were detected only at 7 °C, with the appearance of a peak at q = 0.126 $Å^{-1}$ in the small angle scattering region (Figure 3.2a) and a weak intensity peak at around q = 1.46 $Å^{-1}$ (Figure 3.2d). These peaks corresponds to long and short spacing values of 49.9 and around 4.3 Å respectively; and they can be both associated to the formation of the 2L lamellar structure of the metastable α form of cocoa butter (Loisel et al., 1998). At higher concentrations of cocoa butter (22 and 32% w/w) crystalline material is detected also at 10°C. This is because increasing the concentration of CB generates an increase in the melting temperature of CB/HOSO mixtures, determining a higher level of undercooling at a given temperature, thus higher driving force for crystal nucleation and growth. As shown in Figure 3.2b and 2.2e, the observed peaks for the sample at 22% w/w CB are in the same position of the ones observed for the 15% w/w CB sample (q = 0.127 $Å^{-1}$ and 1.46 $Å^{-1}$), indicating the presence of the α polymorph of cocoa butter also for this oleogel. The same polymorphic structure can be observed in the 32% w/w CB oleogel at both 10 and 7°C (Figure 3.2c and 2.2f). As shown in Figure 3.2c and 3.2f, at 7°C this last oleogel sample presents an additional peak in the small angle region at q = 0.137 $Å^{-1}$ (long spacing equivalent to 45.9 Å), and extra two peaks in the wide-angle region at around q = 1.39 $Å^{-1}$ (d = 4.51 Å) and q = 1.59 $Å^{-1}$ (d = 3.96 Å). The presence of these peaks indicates the formation of the more compact 2L lamellar structure of the β'(IV) polymorph, which co-exist with the α polymorph at 7 °C (Loisel et al., 1998). The observed deviations in the position of the WAXS peak from the reported values for cocoa butter crystals in Loisel et al. (1998) might be due to the presence of mixed crystals, which may include

TAGs from the liquid HOSO in their lattice (Loisel et al., 1998). This observation was previously reported for blends of vegetable oils and cocoa butter content below 30% w/w in Perez-Martinez et al. (2005) (Pérez-Martínez et al., 2005).

The 32% w/w CB sample is the only one that formed the β'(IV) crystal structure during the experiment. This CB/HOSO mixture has the highest melting point and, at 7 °C, it is the most undercooled in respect to the β'(IV) form. This can explain why this polymorph is only observed for this oleogel. Finally, it is worth noticing that the intensity of the α form peaks at the same temperature increases with increasing concentration of CB in HOSO due to the higher amount of solid material formed.

3.3.2 Laboratory scale crystallization and offline characterization of CB/HOSO oleogels

Figure 3.3 shows the temperature (jacket and sample) and turbidity signals (transmittance and absorbance, see Equations 3.2 and 3.3) during the crystallization of a selected CB/HOSO oleogel in the lab-scale setup. As the mixture was stirred and cooled down to its nucleation temperature, its visual appearance changed from a transparent liquid to a turbid, viscous gel. Light turbidimetry was used to detect the onset of crystallization, which was associated to a steep decrease in transmittance, as well as to determine end-of-crystallization, at which a constant absorbance value was reached.

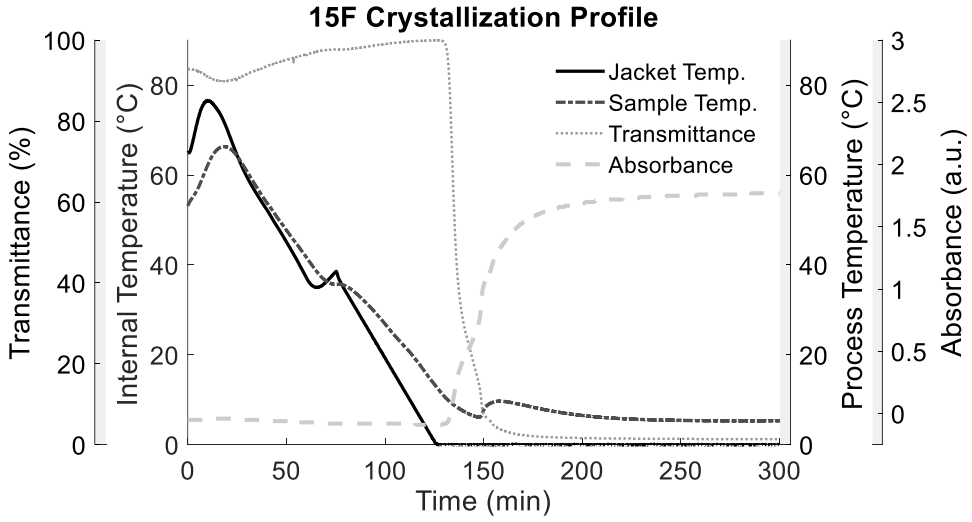

Figure 3.3. Crystallization of CB/HOSO oleogel with fast cooling rate at 15% CB by weight (15F). The Process Analytical Technologies (PAT) tools plot display the jacket temperature (-), sample temperature (-·-), light transmittance (···) and light absorbance (--) over time.

Soon after the crystallization onset, a temperature increase was observed for all oleogel samples, which was attributed to the latent heat of solidification for cocoa butter. Details of the crystallization process for each CB/HOSO mixture are summarized Table 3.1. Due to the limited maximum heat transfer rate of the setup used, the temperature profile of the crystallizing mixtures did not follow the nominal cooling rates set for the experiments. The recalculated cooling rates are shown in Table 3.1.

Table 3.1 Cooling rates, crystallization temperatures, light absorbance and the measured increase in temperature recorded at the crystallization onset for oleogel samples prepared in this article.

Sample (oleogel)	**Recalc. cooling rate (°C/min)**	**Crystallization temperature (°C)**	**Increase in temperature at nucleation (°C)**	**Absorbance at equilibrium (a.u.)**
15F	-0.52 ± 0.08	11.0 ± 0.7	3.9 ± 0.7	1.99 ± 0.15
15M	-0.20 ± 0.02	10.5 ± 1.5	3.3 ± 0.3	2.13 ± 0.17
15S	-0.08 ± 0.01	9.5 ± 0.6	2.7 ± 0.2	2.21 ± 0.30
22F	-0.51 ± 0.04	13.2 ± 0.8	3.3 ± 1.7	2.41 ± 0.11
22M	-0.19 ± 0.02	12.5 ± 0.1	4.5 ± 0.8	2.56 ± 0.06
22S	-0.08 ± 0.01	13.2 ± 0.8	3.6 ± 1.1	2.62 ± 0.09
30F	-0.46 ± 0.08	15.7 ± 0.4	6.2 ± 0.8	2.73 ± 0.14

30M	-0.18 ± 0.02	14.8 ± 0.8	4.3 ± 0.9	2.76 ± 0.05
30S	-0.08 ± 0.01	15.0 ± 0.6	4.2 ± 0.6	2.87 ± 0.05

The recalculated cooling rate was *ca.* –0.50 °C/min for a nominal value of –0.75 °C/min, *ca.* –0.20 °C/min for a set rate of –0.25 °C/min and –0.08°C/min instead of –0.10 °C/min. The composition of the mixture, which affects the specific heat capacity and viscosity of the crystallizing oleogel, also affected the actual cooling rate. For fast cooling experiments the recalculate cooling rates were –0.46 °C/min for sample 30F, –0.51 °C/min for sample 22F and –0.52 °C/min for sample 15F. As shown in Table 3.1 the nucleation temperature of oleogels was mainly affected by the concentration of cocoa butter, whereas the cooling rate did not significantly affect it. The effect of using a larger processing volume and applying shear on the kinetics of crystal nucleation is evident upon comparison with the experiments described in the previous section. Within small capillaries, the nucleation of oleogels was observed between 10 °C and 7 °C for all the CB concentration investigated, whereas in the lab-scale vessel the crystallization temperature was between approximately 10 and 15 °C. As shown in Figure 3.3, the emergence of CB crystals coincided with an increase in temperature, indicating that primary nucleation of CB is an exothermic process. The measured increase in temperature was between 3 and 6 °C and directly proportional to the amount of CB in the CB/HOSO mixture. With regards to the absorbance values at equilibrium, their values increased with the amount of cocoa butter in the crystallizing oleogel. However, it must be noted that the relationship presented in Equation 3.1 is valid only for diluted suspensions or solutions; hence, turbidimetry may not be highly sensitive to changes in the concentration of scatterers in the oleogel. As such, it is more suited to determine crystal nucleation rather than crystal growth (Wright et al., 2000). At the end of the crystallization process, all oleogels reached a final, constant temperature of *ca.* 7 °C.

Polarized light microscopy images of the oleogel sample obtained in this set of experiments are shown in Figure 3.4

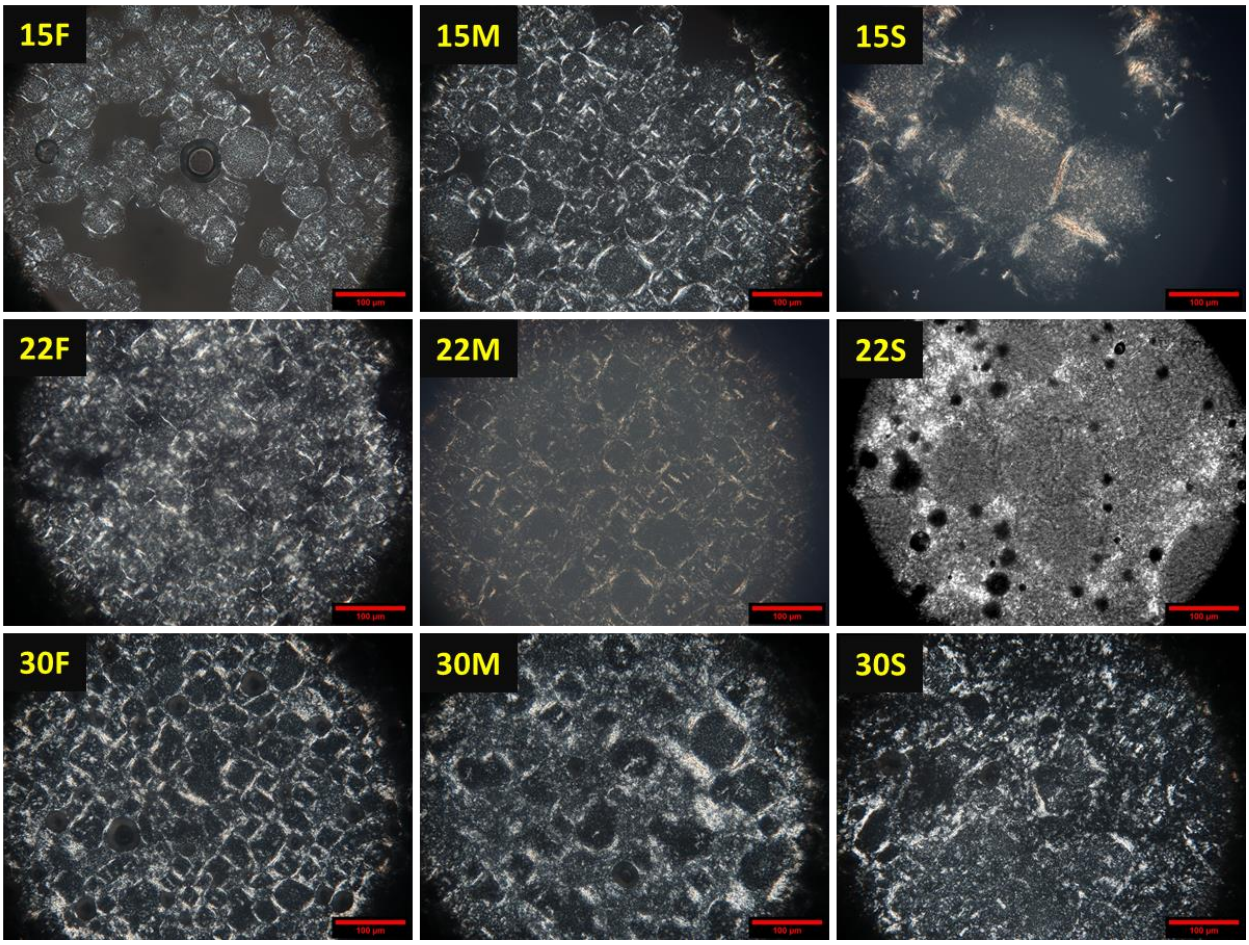

Figure 3.4. Polarized light images of oleogel samples investigated in this paper. Sample 22S is displayed as a grayscale image of a polarized micrograph with the lambda plate. Scale bar represents 100 µm.

Cocoa butter crystallized as spherical aggregates, which is the typical morphology for TAGs obtained using moderate to slow cooling rates, either in quiescent conditions (Pérez-Martínez et al., 2005; Perez-Martınez et al., 2007) or under shear (Acevedo et al., 2012; Tran et al., 2014). These crystalline aggregates are formed through the nucleation of nanometre-sized crystal nanoplatelets, followed by radial growth from the centre of the aggregate (Acevedo & Marangoni, 2010)-(Bayés-García et al., 2011). In particular, such crystal morphology was previously observed both in quiescent conditions in blends of cocoa butter

and vegetable oils (soybean and canola oil) (Pérez-Martínez et al., 2005), and in dynamic crystallization conditions for a fully hydrogenated soybean oil (FHSO) in soybean oil (SO) mixture (Acevedo et al., 2012) and in fully hydrogenated canola oil (FHCO) in canola oil (CO) system (Tran et al., 2014). In both systems it was observed that the size of the spherical aggregates decreased with increasing shear rate.

Figure 3.4 shows oleogel samples containing a network of spherical aggregates entrapping the sunflower oil, which appeared dark under polarized light. Table 3.2 shows the average diameter size for the individual spherical aggregate in the oleogel samples, as measured manually from the microscopic images.

Table 3.2. Mean diameter of the spherical aggregates measured by image analysis of polarized light images of oleogels.

Sample (oleogel)	CB w/w %	Recalc. cooling rate (°C/min)	Spherical aggregates average diameter (µm)
15F	15	-0.52 ± 0.08	40.34 ± 7.89
22F	22	-0.51 ± 0.04	46.41 ± 12.08
30F	30	-0.46 ± 0.08	39.43 ± 9.98
15M	15	-0.20 ± 0.02	56.24 ± 13.78
22M	22	-0.19 ± 0.02	52.27 ± 11.05
30M	30	-0.18 ± 0.02	63.29 ± 12.41
15S	15	-0.08 ± 0.01	118.44 ± 32.42
22S	22	-0.08 ± 0.01	151.77 ± 51.58
30S	30	-0.08 ± 0.01	n/a

As a reference, an image focused on a single spherical aggregate is available in Appendix A, showing how these crystal aggregates were measured with image analysis (Figure A1). Fast-cooled samples (15F, 22F and 30F) presented spherical aggregates of around 40 µm in diameter, while medium (15M, 22M and 30M) and slow (15S and 22S) cooled samples showed larger aggregates of 50-60 µm and 100-150 µm respectively. The measurement of the size of the spherical aggregates in sample 30S (Figure 3.4, bottom right) was not possible, as this sample displayed a continuous network of crystalline CB where the edges of each aggregate could not be distinguished unambiguously. Slow cooling rates caused nucleation to happened at lower levels of undercooling compared to fast cooling rates, which promoted crystal growth over nucleation (Sato et al., 2013). Therefore, the average diameter of crystalline spherical aggregates in the oleogels increased as the cooling rate decreases. The concentration of CB did not appear to affect significantly the average spherical aggregate diameter; however, it can be seen from Figure 3.4 that the number of spherical aggregates dispersed in sunflower oil increased with increasing CB concentration.

Cocoa butter polymorphism in oleogels was determined with X-Ray diffraction; samples were collected prior to aeration and their diffraction patterns are shown in Figure 3.5

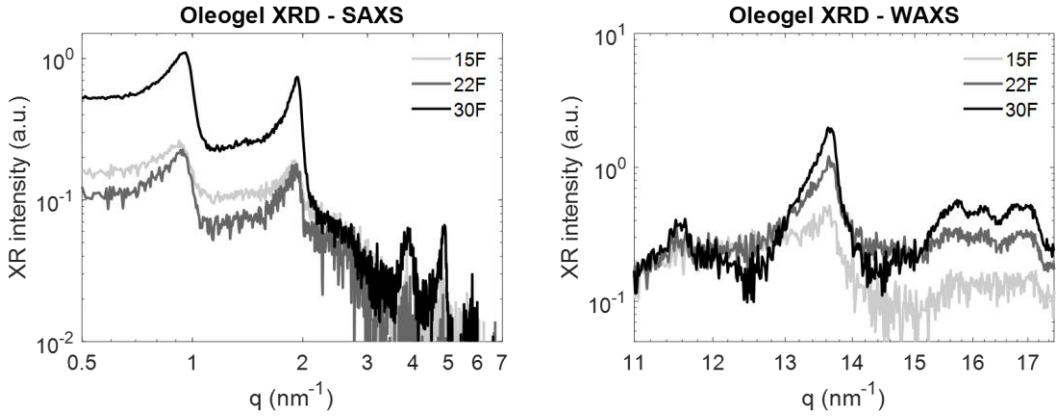

Figure 3.5. Solvent-subtracted X-Ray diffraction patterns of oleogel samples 15F, 22F and 30F prior to aeration.

All oleogels displayed two intense peaks in the small angle region at q values of around 0.96 nm^{-1} and 1.9 nm^{-1}, and in the wide-angle region a peak at around 13.7 nm^{-1} and a series of low-intensity peaks between 15.7 and 17.1 nm^{-1}. These peaks correspond to the β(V) cocoa butter polymorph (Loisel et al., 1998). The more metastable α and β'(IV) forms detected in the capillary experiments showed in the previous section were not detected. This can be explained by evaluating several factors that affected the lab scale crystallization of the oleogel samples. Application of shear during fat crystallization promotes faster polymorphic transformation, as shear-induced viscous heat generation can melt the less stable polymorphs, while leaving behind and provide the thermal energy to overcome the activation barrier for nucleation of the more stable structures (Tran & Rousseau, 2016). Specifically, shear was reported to accelerate the transition of cocoa butter crystals from β'(IV) to β(V) (Sonwai & Mackley, 2006). In the experiments shown here, X-Ray diffraction was performed immediately at the end of each crystallization process; therefore, it is possible that lower-stability CB polymorphs that might have nucleated first transformed into the observed β(V) structure under the effect of shear. Furthermore, shear favours the secondary nucleation of stable polymorphs by enhancing crystal-crystal, crystal-impeller and crystal-vessel wall collisions (Agrawal & Paterson, 2015). In quiescent conditions, such as the capillary experiments described in the previous section, the reduced volume and the absence of shear-induced flow favoured primary over secondary nucleation instead, with unstable polymorphs being more persistent compared to large-scale crystallizers (Simone et al., 2018). Lastly, the increase in temperature observed for oleogels soon after the crystallization onset (Figure 3.3) could have triggered a melt-mediated transformation of the nucleated metastable α or β'(IV) crystals to the detected β(V) polymorph.

The presence of a single crystal structure of CB in the oleogel samples was also supported by DSC measurements. A broad melting peak endotherm was observed for all oleogels between 20 and 30°C, whose position and intensity increased with CB concentration in the sample. The onset and maximum

temperatures of the melting peaks of all analysed oleogels are shown in Table 3.3. A broad melting endotherm is characteristic of multi-component mixtures of fats, where TAGs with different fatty acid moieties form eutectic phases upon solidification (Himawan et al., 2006). Pérez-Martínez et al. (2012) reported similar DSC thermograms for a 30% w/w cocoa butter in soybean oil oleogel, crystallized under shear in a surface-scraper heat exchanger (Pérez-Martínez et al., 2012).

Table 3.3. Temperature of melting onset and peak melting temperature of oleogel samples.

Sample (oleogel)	T_{onset} **oleogel (°C)**	T_m **oleogel (°C)**
15F	21.34 ± 0.18	25.55 ± 0.92
15M	21.44 ± 0.27	24.07 ± 0.3
15S	21.54 ± 0.35	25.06 ± 0.82
22F	21.79 ± 0.42	26.17 ± 0.07
22M	20.91 ± 0.25	25.41 ± 0.34
22S	21.64 ± 0.02	26.25 ± 0.53
30F	21.90 ± 0.11	28.83 ± 1.82
30M	22.32 ± 0.06	28.08 ± 0.86

30S	21.37 ± 0.08	28.03 ± 1.02

The viscoelastic properties of the oleogel samples were investigated with oscillatory rheology at 20°C (Figure 3.6). Rheology profiles of medium and slow-cooled samples are available in Appendix A, Figure A2.

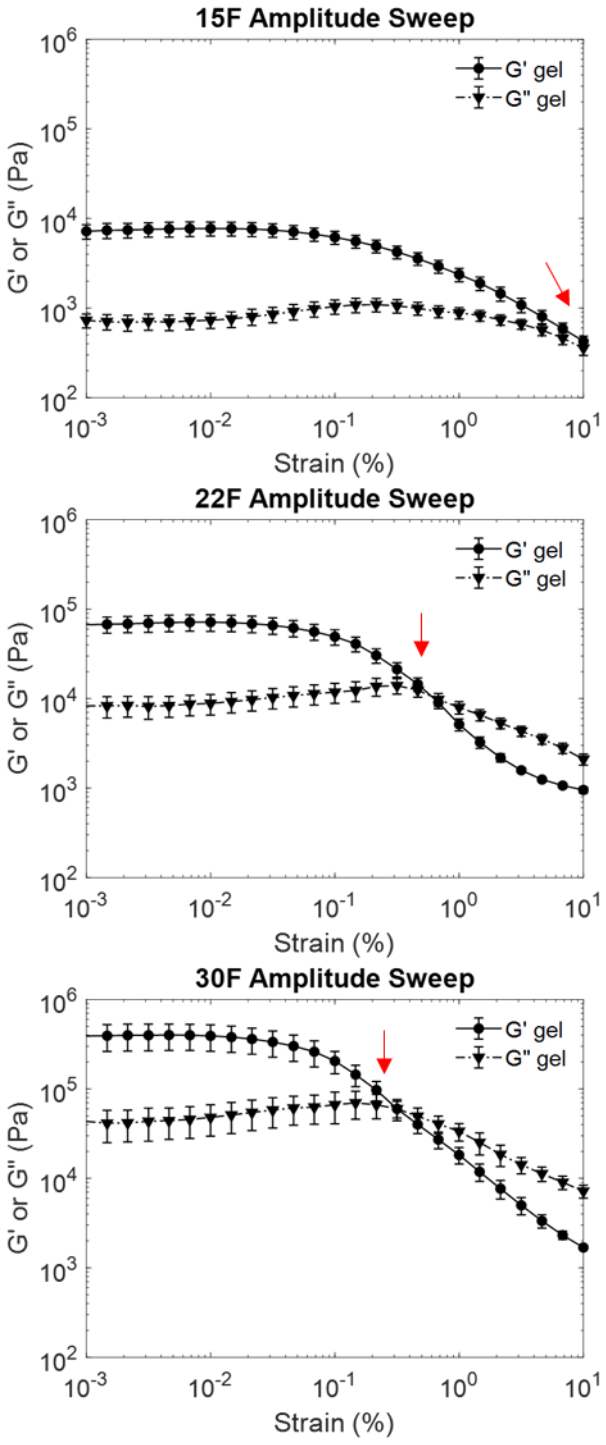

Figure 3.6. Oscillatory rheology of fast-cooled oleogels crystallized in the lab-scale vessel. Elastic modulus (G') and viscous modulus (G") are plotted as a function of strain (%). The flow point (τ_f) is highlighted with a red arrow.

The CB/HOSO oleogels prepared in this work exhibited predominantly elastic behaviour in the range 0.001 – 1% strain, after which they started to flow like liquid materials. Table 3.4 contains the oleogels' elastic modulus in the linear viscoelastic regime (G'_{LVER}) and the flow point (τ_f), which corresponds to the crossing point of the G' and G" curves.

Table 3.4 Elastic modulus in the linear viscoelastic regime (G'_{LVER}) and flow point (τ_f) of oleogel samples.

Sample	Oleogel G'_{LVER} (kPa)	Oleogel τ_f (kPa)
15F	7.52 ± 0.20	0.78 ± 0.39
15M	7.69 ± 0.07	0.46 ± 0.14
15S	9.16 ± 0.18	0.50 ± 0.12
22F	69.67 ± 1.82	16.55 ± 5.45
22M	71.21 ± 1.12	8.28 ± 0.85
22S	56.24 ± 0.59	11.89 ± 5.82
30F	396.14 ± 3.79	44.53 ± 15.50
30M	497.99 ± 6.66	49.72 ± 3.55
30S	472.31 ± 5.76	55.35 ± 3.42

The value of G'_{LVER} increased with increasing of CB concentration from 10^4 Pa to 10^6 Pa (Table 3.4), which is in agreement with the increasing amount of crystalline cocoa butter in the oleogels, as highlighted by DSC measurements. The flow point of the oleogels (τ_f) followed the same trend, increasing logarithmically

from *ca.* 0.5 kPa to 50 kPa between 15% and 30% CB w/w. The size of CB crystal aggregates, on the other hand, did not affect significantly the rheology of oleogels, which exhibited similar viscoelastic profiles at fixed concentration of CB (see Figure A2 in Appendix A). As a comparison, Gunes et al. (2017) were able to aerate myristic acid–sunflower oil oleogels between with an elastic modulus between 10^3 Pa to 10^8 Pa (Gunes et al., 2017).

3.3.3 Aeration of oleogels and characterization of oleofoams

The aeration profiles of oleogel samples and the temperature evolution during aeration are presented in Figure 3.7. Air incorporation was evident as all oleogels turned from a deep yellow to a white colour and mousse-like consistency. The oleogels prepared in this work exhibited high foamability, with an average overrun of 100% just after 5 minutes of aeration and up to 200% after 30 minutes or less. In comparison, the oleofoams prepared by Mishima et al. (2016), Gunes et al. (2017) and Heymans et al. (2018) required between 15 to 30 minutes aeration to surpass 100% overrun (Gunes et al., 2017; Heymans et al., 2018; Mishima et al., 2016).

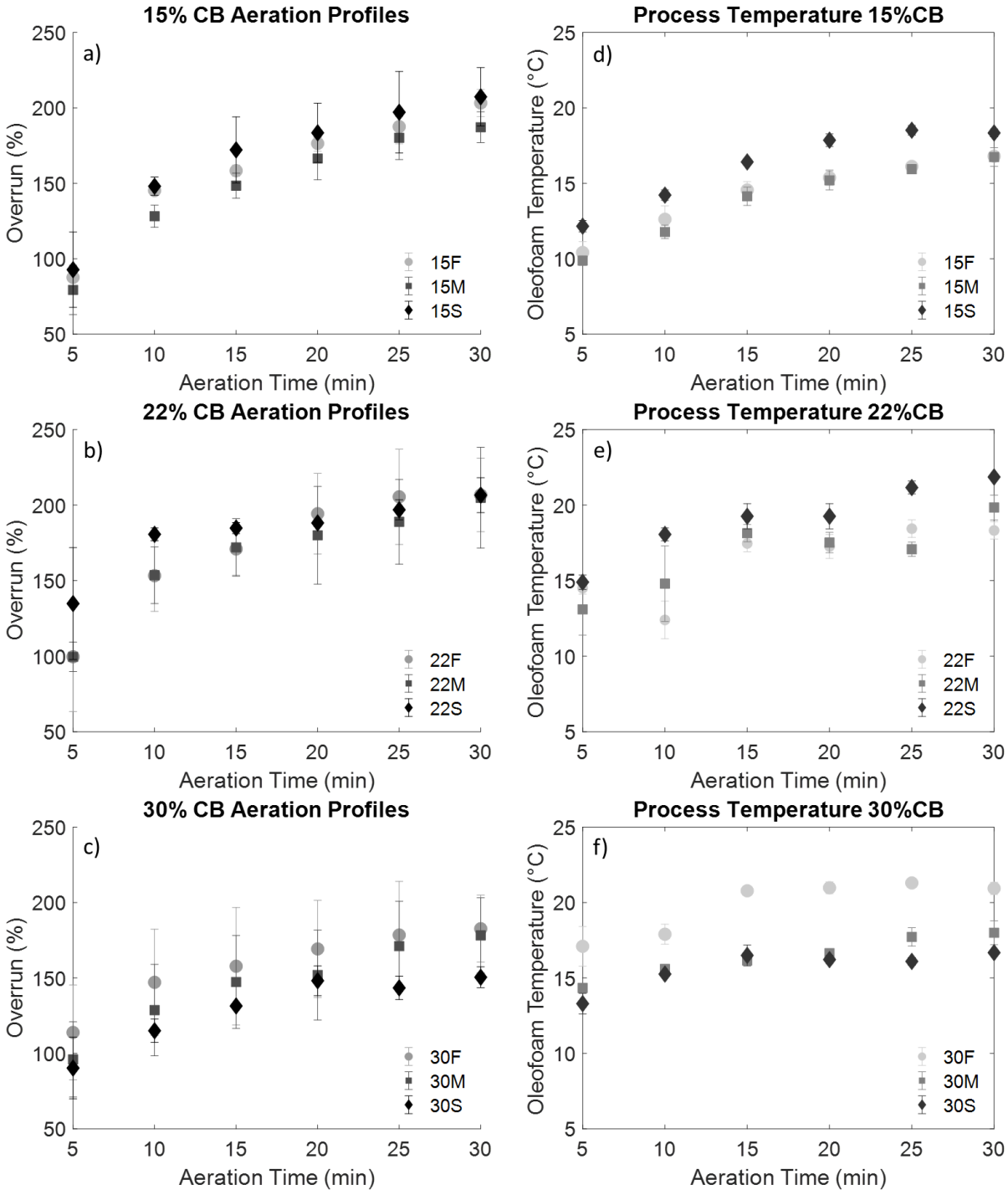

Figure 3.7. Foamability over time of oleofoams for 15% CB w/w, 22% CB w/w and 30% CB w/w samples (a, b and c) and their temperature evolution during aeration (d, e and f).

For 15% CB w/w oleogels, air incorporation proceeded in a steady, stepwise fashion, without large variation in the mean overrun between different cooling rates. Oleogels containing 22% CB w/w displayed slightly higher overrun values over the first 10-15 minutes, potentially due to the larger amount of crystals available for bubble stabilization. In particular, sample 22S reached about 175% overrun after just 10 minutes of aeration, and maintained, on average, a similar overrun afterwards. This suggests that this sample reached air incorporation equilibrium after 10 min of aeration. While the relatively large error bars point to a high degree of variability, the mean overrun value increased just slightly after this time. The aeration of 30% CB w/w oleogels was less efficient; in fact, sections of unaerated oleogel were still visible at the end of the aeration process. Sample 30S, in particular, could only achieve a lower overrun (around 150%) compared to all the other samples. This observation suggests that, for CB/HOSO oleogels, 30% CB might be close to the upper limit of processability for aeration with the setup used in this work, due to their higher elastic modulus compared to the other samples. Previous experiments on the aeration of oleofoams prepared from 10% CB w/w oleogels, on the other hand, displayed good foamability, but also significant oil drainage shortly after the whipping. This confirms that the lower limit of CB concentration in HOSO was 15% w/w.

The temperature of every sample during aeration was also monitored with an external thermometer, as shown Figure 3.7d – 7f. The shear-induced viscous heat generation was partly counterbalanced by the cooling liquid flowing in the vessel jacket, which was kept at a constant temperature of 0°C. Nevertheless, all oleogel samples displayed an increase in temperature from *ca.* 7°C (the final crystallization temperature shown in Figure 3.3) to 10 – 15°C after 5 minutes of aeration. Throughout the rest of the whipping process, the oleofoams were heated gradually by a further 5 – 10 °C after 30 minutes of whipping, reaching a maximum temperature of 20°C.

Such increase in temperature is sufficient to dissolve the smaller CB crystals, and affect the morphology and size distribution of spherical aggregates, as well as the strength of the crystalline network for samples

at 30% CB w/w. This can help explaining why sample foamability was mainly affected by the amount of cocoa butter crystals in the oleogels, rather than the cooling rate at which oleogel were formed. As shown in the previous sections, slower cooling rates promote the growth of fewer and larger crystals in the oleogels in comparison to faster cooling. Figure 3.8 contains polarized micrographs of oleofoams at the end of the aeration process, which shows that the concentration, size and shape of the cocoa butter crystals is very similar for samples containing the same amount of CB. The cocoa butter crystals appeared as bright objects in between air bubbles. It can be noticed that the size and shape distributions of both air bubbles and CB spherical aggregates in the oleofoams seem to be affected exclusively by the content of CB, with the only exception of sample 30S that, as mentioned earlier, was very difficult to aerate. It is likely that the increase in temperature during aeration, in combination with the mechanical breaking action of the mixer, can disrupt the crystalline network and reduce the size of large CB aggregates within the oleogels, resulting in very similar size and shape distributions of crystal aggregates in all whipped samples containing the same amount of CB. In other words, the aeration process seems to eliminate the effect of using different cooling rates in the formation of oleogels.

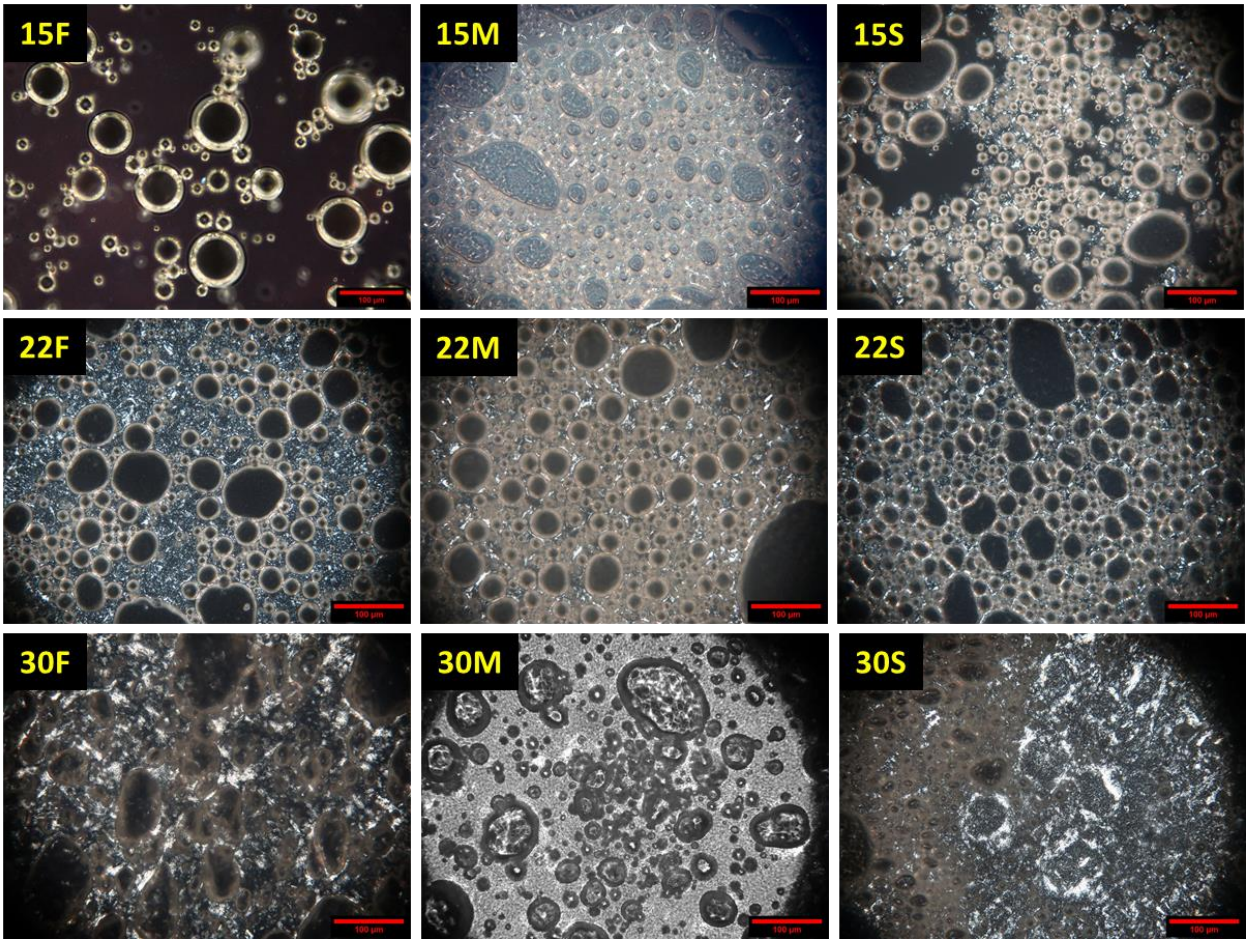

Figure 3.8. Polarized light images of oleofoam samples at the end of the aeration step. Sample 30M is displayed as a greyscale image of a polarized micrograph with the lambda plate. Scale bar represents 100 µm.

Air bubbles had an estimated diameter between 5 and 100 µm, with several bubbles being non-spherical, which is common for these type of materials (Binks et al., 2016; Binks & Marinopoulos, 2017; Gunes et al., 2017; Heymans et al., 2018; Mishima et al., 2016; Truong et al., 2019). Oleofoam samples with 15% CB w/w contained more loosely dispersed bubbles, with more rounded shape and large domains of the foam did not present any crystal or bubble but were dominated by HOSO. In contrast, oleofoams prepared with 22% CB w/w displayed a more compact packing of non-spherical air bubbles, with a network of crystals in between the air bubbles. Samples with 30% CB w/w displayed a coarser microstructure, with fewer, larger,

and more deformed air bubbles, as well as large domains of crystal aggregates. The latter observation was in agreement with the lower overrun and macroscopically visible traces of un-whipped material.

CryoSEM was used to resolve the structure of CB crystals in the oleofoam samples. Furthermore, the ability to freeze-fracture the sample enabled visualization of the foam microstructure closer to the native state compared to PLM, where oleofoams are subject to deformation during sample preparation. Figure 3.9 shows the microstructure of a 30F oleofoam, which presented several bubbles tightly packed and separated by thin layers of frozen oleogel (shown in Figure 3.9a).

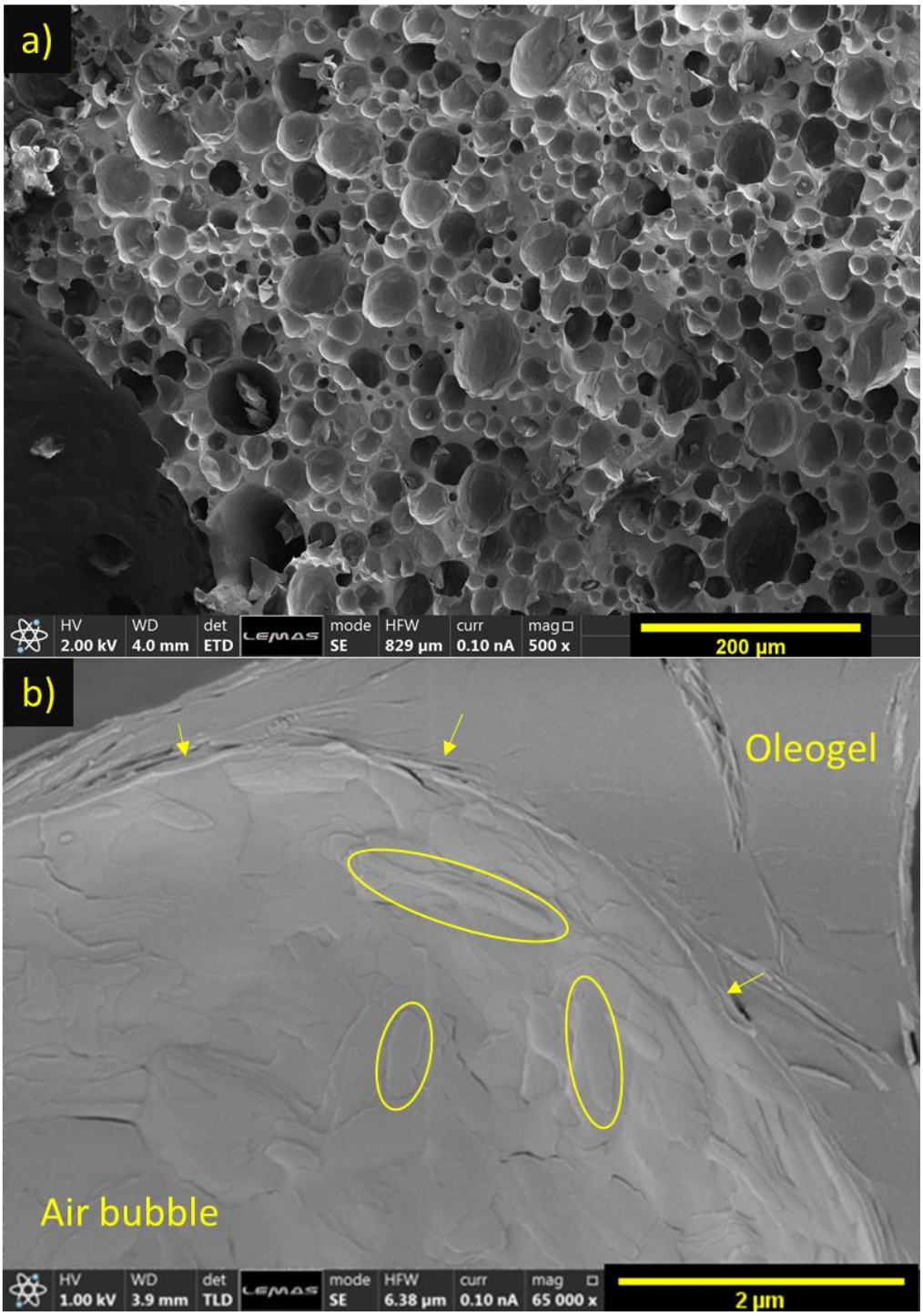

Figure 3.9. CryoSEM images of an oleofoam sample (30F). Low magnification (top, a), high magnification with detail of the inside of an air bubble (bottom, b). The scale bars represent 200 µm and 2 µm, respectively.

The bubble diameter was found to be between 5 and 150 µm, similar to the range measured by PLM. Figure 3.9b shows the inside of an air bubble at higher magnification. Cocoa butter nanoplatelets (CNP) that form the spherical aggregates observed with PLM were detected both at the interface and in the continuous phase of the oleofoams. The CNPs had a variable length between 400 nm and 1 µm, as highlighted in Figure 3.9b by the yellow circles, and an approximate thickness of *ca.* 50 nm. Further CryoSEM images are provided in Appendix A (Figures A4 – A7).

For all oleofoam samples, XRD and DSC measurements confirmed that these CB crystals were the same polymorph, β(V), as the one found in the parent oleogels (Figure A3 in Appendix A). It can be noticed that CNPs are all exposing their larger facet at the air/oil interface as shown with the yellow arrows in Figure 3.9b. The presence of bundles of CNPs within the oleogel surrounding bubbles is also evident in Figure A4-A5 of Appendix A.

This crystalline arrangement around air bubbles supports the hypothesis of a Pickering stabilization mechanism, where CB crystals are adsorbed at the air/oil interfaces providing stabilization from coalescence and coarsening (Fameau & Saint-Jalmes, 2017a; Heymans et al., 2017). The presence of a birefringent layer surrounding bubbles confirms the presence of absorbed crystals at the air/oil interface, as shown in the PLM images of Figure A8 in Appendix A. Therefore, the crystal-stabilized air bubbles form a network through the presence of additional CNPs in the continuous phase, which also entrap the liquid oil. This hypothesis is also in agreement with the findings of Mishima et al. (2016), Binks et al. (2016), Binks & Marinopoulos (2017) and Heymans et al. (2018) for similar oleofoams (Binks et al., 2016; Binks & Marinopoulos, 2017; Heymans et al., 2018; Mishima et al., 2016). The stabilization mechanism of the oleofoam investigated in this work is summarized in Figure 3.10.

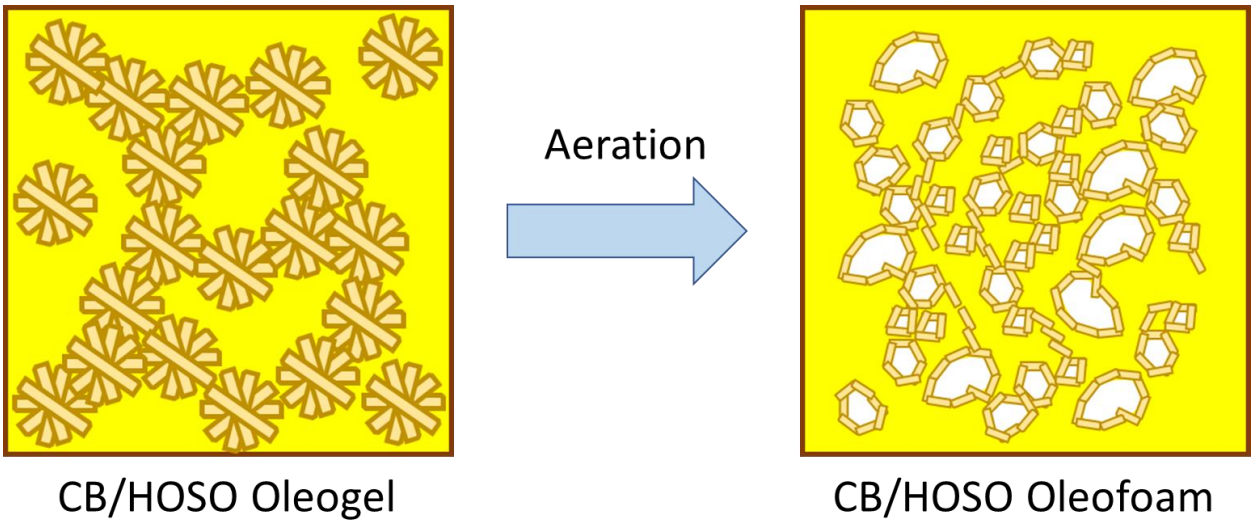

Figure 3.10. Diagram summarizing the effect of aeration on the cocoa butter oleogels prepared in this work. The spherical CB crystals aggregates in the oleogels are disrupted during the aeration producing a novel structure comprising of crystal-stabilized air bubbles interconnected in a fat-crystal network that entraps liquid oil as well.

The viscoelastic properties of oleofoams were investigated with oscillatory rheology. The elastic (G') and viscous (G") moduli of selected oleofoams are shown in Figure 3.11, compared with their relative oleogel precursors.

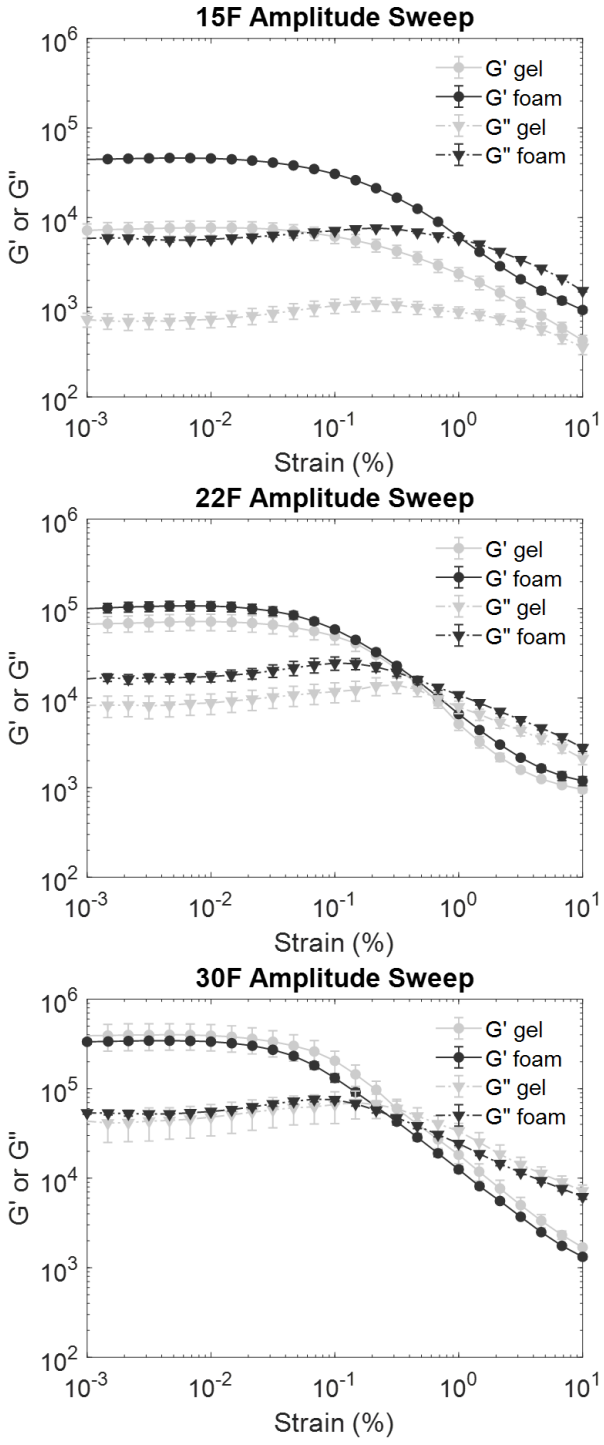

Figure 3.11. Oscillatory rheology experiments of fast-cooled oleofoam samples (grey) compared to the results for their analogue oleogel samples (black).

Similarly to oleogel samples, oleofoams behaved as solid-like materials in a strain range between 0.001% and 1%, after which they started flowing like a liquid. Their G'_{LVER} increased with the CB concentration, as seen in the oleogel analogues. The aeration process resulted in increased G' and G" for oleofoams containing 15% and 22% CB w/w, while for samples containing 30% CB w/w both elastic and viscous moduli decreased slightly compared to the originating oleogels. Therefore, at low CB concentrations, the structural changes in oleogels caused by aeration led to a stronger (*i.e.* with higher elastic modulus) material compared to the starting oleogels, as reported also by Gunes et al. (2017) for oleofoams prepared with 5% w/w monoglyceride crystals in oil (Gunes et al., 2017). This effect became less pronounced in samples with 30% CB w/w, whose oleofoams presented a viscoelastic profile very similar to their oleogel precursors. A possible explanation could be that, for oleofoams prepared from 30% w/w cocoa butter oleogels, the crystal rearrangement around the air bubbles did not contribute significantly to the rheology of the material, both due to the lesser extent of air incorporated and to the presence of a stronger fat crystal network, as highlighted by the higher elastic modulus compared to 15% w/w and 22% w/w samples. It is worth noticing that the variation of G' and G" was affected mostly by the different CB concentrations in the originating oleogels, as the amount of incorporated air was relatively similar between the oleofoam samples (see Appendix A, Figure A9). In fact, the air volume fraction was around 0.66 for samples containing 15% and 22% CB w/w, 0.64 for samples 30M and 30F and 0.60 for sample 30S. More details are provided in Table 3.5, which contains the flow point of oleofoams, their overrun, and the ratio between the G'_{LVER} of oleofoams and their respective oleogels.

A comparison of the values shown in Table 3.4 and Table 3.5 shows that whipping of CB/HOSO oleogels with 15% CB w/w increased both elastic and viscous moduli by a factor of 4 to 6 G'_{LVER} and generated an increase in volume of 200% compared with the oleogel precursors. Oleofoam samples with 22% CB w/w showed a smaller increase of G'_{LVER} (1.5 to 2 times), and an average volume increase of 200%. Finally, oleofoams with 30% CB w/w exhibited a modest decrease of G'_{LVER} after aeration (0.85 to 0.92 times), still

incorporating high amounts of air bubbles, with overrun values between 150% and 180%. As a reference, Binks & Marinopoulos (2017) reported that aeration of pure cocoa butter at 35°C – with a solid fat content between 15 and 30% – resulted in an oleofoam with 100% overrun (Binks & Marinopoulos, 2017).

Table 3.5. Linear Viscoelastic Regime (LVER) elastic modulus, viscous modulus, and flow points for oleofoams investigated in this paper.

Sample	Oleofoam G'_{LVER} (kPa)	Oleofoam τ_f (kPa)	Overrun (%)	Foam G'_{LVER}/Gel G'_{LVER}
15F	45.63 ± 0.64	4.77 ± 1.00	203 ± 9	6.06
15M	31.37 ± 0.32	4.57 ± 0.06	187 ± 10	4.07
15S	45.65 ± 0.60	6.91 ± 0.35	207 ± 19	4.98
22F	104.79 ± 2.84	21.93 ± 6.28	206 ± 24	1.50
22M	111.26 ± 2.40	11.07 ± 9.59	204 ± 33	1.56
22S	111.22 ± 1.47	19.53 ± 3.56	207 ± 16	1.97
30F	339.83 ± 3.71	40.67 ± 11.68	182 ± 22	0.85
30M	438.21 ± 7.52	56.38 ± 6.80	178 ± 25	0.88
30S	453.21 ± 5.75	60. 21 ± 13.03	150 ± 7	0.92

3.3.4 Oleofoam stability studies

Oleofoams are subject to the same destabilisation mechanisms found in aqueous foams, such as liquid drainage, bubble coalescence and coarsening. Specifically, oil drainage from the continuous phase causes film thinning between the bubbles, with increased probability of coalescence (Fameau & Saint-Jalmes, 2017b; Heymans et al., 2017). Nevertheless, the oleofoam samples studied in this work did not display measurable amounts of oil drainage (< 1 mL over 50 mL of sample) over 3 months (as shown in Figure A10 of Appendix A). This is in agreement with the behaviour of other stable oil foam systems reported in literature (Binks & Marinopoulos, 2017; Gunes et al., 2017; Mishima et al., 2016). A comparison between fresh and aged oleofoam samples was carried out using CryoSEM. This analysis showed that air bubbles retained a non-spherical shape during aging, as well as the presence of CNPs at the air/oil bubble boundary. The aged sample displayed fewer bubbles in the bulk, as shown in Figure A11 of Appendix A.

3.4 Conclusions

In the present work, the complex relationship between processing conditions and the physicochemical properties of oleogels and oleofoams was explored with a multiple characterization technique approach. Specifically, the effect of CB crystal size and shape distributions on the final oleofoam properties was determined. These results are relevant to Pickering-stabilized oleofoam; more specifically, for industries who seek to use oleofoams in their products and to implement them in their manufacturing processes. For them, being able to generate oleogels with tailored-made crystal properties is the key to produce highly aerated, stable oleofoams with desirable viscoelastic properties.

The oleofoams prepared in this work were found to be Pickering-stabilized by CB nanoplatelets in the β(V) polymorph, and were able to incorporate an air volume fraction of $\phi = 0.60$ to $\phi = 0.66$. CryoSEM enabled visualization of the CB crystals at the air/oil interface in the oleofoams. CB crystals appeared platelet-shaped with an estimated thickness of 50 nm and up to 500 nm in length, forming a layered shell of

oriented crystals around the air bubbles. This resulted in oleofoams having up to 1/3 of the calorific density compared to their oleogel precursors, which is beneficial for formulating products with lower calories. Moreover, the oleofoams were stable to oil drainage for up to 3 months at 20°C. The concentration of CB was the factor that affected more strongly the properties of both oleogels and oleofoams. In particular, by tuning the amount of CB in the oleogels, oleofoams with either higher or similar viscoelasticity to the oleogel could be produced. Oleogels containing spherical crystal aggregates of different size produced oleofoams with similar properties, as the aeration processes eliminated all differences in crystal size and shape distributions generated by applying different cooling rates during the oleogel formation. In this work the effect of shear and increased volume on the crystallization of CB/HOSO blends was also elucidated by comparing oleogel crystallization in quiescent capillaries and in a stirred lab-scale crystallization vessel. The use of online, *in situ* light turbidimetry enabled monitoring of the dynamic process of oleogels crystallization and to identify when the system reached equilibrium at the end of the cooling profile.

The CB-based oleofoams obtained in this work are relevant, novel materials that can promote the reformulation of healthier, more affordable and sustainable food products, such as fillings and chocolate spreads. Furthermore, they constitute also attractive scaffolds for cosmetic (*e.g.,* skincare) products, as well as carriers for active pharmaceutical ingredients.

Funding Sources

The authors would like to acknowledge the Engineering and Physical Sciences Research Council funded Centre for Doctoral Training in Soft Matter and Functional Interfaces, grant ref. no. EP/L015536/1 as well as Nestlé PTC Confectionery (York, UK) for the financial and writing support. Dr Simone also acknowledges Royal Society (grant ref. no. INF\R2\192018) for additional funding. Additional financial support was

provided by Diamond Light Source (Didcot, UK) through proposals SM24530-1, SM22659-1 and SM20481-1 at beamline I22.

Declaration of competing interests

The authors declare that they have no known competing financial interests or personal relationships that could have appeared to influence the work reported in this paper.

Acknowledgements

Dr Arwen Tyler, Prof Megan Povey and Prof Michael Rappolt are acknowledged for useful discussion on X-Ray data and cocoa butter polymorphism. Dr. Daniel Baker is acknowledged for his support on DSC measurements and data analysis. Dr. Teresa Roncal-Herrero and Mr. Stuart Micklethwaite are also acknowledged for their support in CryoSEM microscopy and data analysis. We also thank Prof. Nick Terrill and Dr Andy Smith from Diamond Light Source for their support and assistance in running synchrotron experiments.

Abbreviations

CB Cocoa Butter, HOSO High Oleic Sunflower Oil, PAT Processing Analytical Technologies

References

Acevedo, N. C., Block, J. M., & Marangoni, A. G. (2012). Critical laminar shear-temperature effects on the nano- and mesoscale structure of a model fat and its relationship to oil binding and rheological properties. *Faraday Discussions*, *158*, 171–194. https://doi.org/10.1039/c2fd20008b

Acevedo, N. C., & Marangoni, A. G. (2010). Characterization of the nanoscale in triacylglycerol crystal networks. *Crystal Growth and Design*, *10*(8), 3327–3333. https://doi.org/10.1021/cg100468e

Afshin, A., Forouzanfar, M. H., Reitsma, M. B., Sur, P., Estep, K., Lee, A., … Murray, C. J. L. (2017). Health Effects of Overweight and Obesity in 195 Countries over 25 Years. *The New England Journal of Medicine*, *377*(1), 13–27. https://doi.org/10.1056/NEJMoa1614362

Agrawal, S. G., & Paterson, A. H. J. (2015). Secondary Nucleation: Mechanisms and Models. *Chemical Engineering Communications*, *202*(5), 698–706. https://doi.org/10.1080/00986445.2014.969369

Bayés-García, L., Calvet, T., Cuevas-Diarte, M. À., Ueno, S., & Sato, K. (2011). Heterogeneous microstructures of spherulites of lipid mixtures characterized with synchrotron radiation microbeam X-ray diffraction. *CrystEngComm*, *13*(22), 6694–6705. https://doi.org/10.1039/c1ce05667k

Beg, M. S., Ahmad, S., Jan, K., & Bashir, K. (2017). Status, supply chain and processing of cocoa - A review. *Trends in Food Science and Technology*, *66*, 108–116. https://doi.org/10.1016/j.tifs.2017.06.007

Binks, B. P., Garvey, E. J., & Vieira, J. (2016). Whipped oil stabilised by surfactant crystals. *Chem. Sci.*, *7*(4), 2621–2632. https://doi.org/10.1039/C6SC00046K

Binks, B. P., & Marinopoulos, I. (2017). Ultra-stable self-foaming oils. *Food Research International*, *95*, 28–37. https://doi.org/10.1016/j.foodres.2017.02.020

Blom, W. A. M., Koppenol, W. P., Schuring, E. A. H., Abrahamse, S. L., Arnaudov, L. N., Mela, D. J., & Stoyanov, S. D. (2016). Sustained satiety induced by food foams is independent of energy content, in healthy adults. *Appetite*, *97*, 64–71. https://doi.org/10.1016/j.appet.2015.11.023

Brun, M., Delample, M., Harte, E., Lecomte, S., & Leal-Calderon, F. (2015). Stabilization of air bubbles in oil by surfactant crystals: A route to produce air-in-oil foams and air-in-oil-in-water emulsions. *Food Research International*, *67*, 366–375. https://doi.org/10.1016/j.foodres.2014.11.044

Campbell, G. M., & Mougeot, E. (1999). Creation and characterisation of aerated food products. *Trends in Food Science and Technology*, *10*(9), 283–296. https://doi.org/10.1016/S0924-2244(00)00008-X

Demirkesen, I., & Mert, B. (2019). Recent developments of oleogel utilizations in bakery products. *Critical Reviews in Food Science and Nutrition*, *0*(0), 1–20. https://doi.org/10.1080/10408398.2019.1649243

Doan, C. D., Patel, A. R., Tavernier, I., De Clercq, N., Van Raemdonck, K., Van de Walle, D., … Dewettinck, K. (2016). The feasibility of wax-based oleogel as a potential co-structurant with palm oil in low-saturated fat confectionery fillings. *European Journal of Lipid Science and Technology*, *118*(12), 1903–1914. https://doi.org/10.1002/ejlt.201500172

EFSA. (2010). Scientific Opinion on Dietary Reference Values for fats, including saturated fatty acids, polyunsaturated fatty acids, monounsaturated fatty acids, trans fatty acids, and cholesterol. *EFSA Journal*, *8*(3), 1–107. https://doi.org/10.2903/j.efsa.2010.1461

Fameau, A. L., Lam, S., Arnould, A., Gaillard, C., Velev, O. D., & Saint-Jalmes, A. (2015). Smart Nonaqueous Foams from Lipid-Based Oleogel. *Langmuir*, *31*(50), 13501–13510. https://doi.org/10.1021/acs.langmuir.5b03660

Fameau, A. L., & Saint-Jalmes, A. (2017a). Non-aqueous foams: Current understanding on the formation and stability mechanisms. *Advances in Colloid and Interface Science*, *247*, 454–464. https://doi.org/10.1016/j.cis.2017.02.007

Fameau, A. L., & Saint-Jalmes, A. (2017b). Non-aqueous foams: Current understanding on the formation and stability mechanisms. *Advances in Colloid and Interface Science*. https://doi.org/10.1016/j.cis.2017.02.007

FAO. (2008). *Food and Agriculture Organization of the United Nations, Fats and fatty acids in human nutrition - Report of an expert consultation*". *Fats and fatty acids in human nutrition* (Vol. 91).

https://doi.org/I1953E/1/11.10

Fernández-Moya, V., Martínez-Force, E., & Garcés, R. (2000). Identification of triacylglycerol species from high-saturated sunflower (Helianthus annuus) mutants. *Journal of Agricultural and Food Chemistry*, *48*(3), 764–769. https://doi.org/10.1021/jf9903861

Filik, J., Ashton, A. W., Chang, P. C. Y., Chater, P. A., Day, S. J., Drakopoulos, M., … Wilhelm, H. (2017). Processing two-dimensional X-ray diffraction and small-angle scattering data in DAWN 2. *Journal of Applied Crystallography*, *50*(3), 959–966. https://doi.org/10.1107/S1600576717004708

Ghotra, B. S., Dyal, S. D., & Narine, S. S. (2002). Lipid Shortenings: a Review. *Food Research International*, *35*, 1015–1048.

Gunes, D. Z., Murith, M., Godefroid, J., Pelloux, C., Deyber, H., Schafer, O., & Breton, O. (2017). Oleofoams: Properties of Crystal-Coated Bubbles from Whipped Oleogels-Evidence for Pickering Stabilization. *Langmuir*, *33*(6), 1563–1575. https://doi.org/10.1021/acs.langmuir.6b04141

H. Chisholm, Z.D. Gunes, C. Gehin-Delval, A. Nouzille, E. Garvey, M.J. Destribats, S.N. Chandrasekaran, J. Vieira, J. German and B.P. Binks. (2016). Aerated Confectionery Material *WO 2016/150977 Al*.

Haedelt, J., Beckett, S. T., Niranjan, K., & Pyle, D. L. (2005). Food Engineering and Physical Properties Vacuum-induced Bubble Formation in Liquid-tempered Chocolate. *Journal of Food Science*, *70*(2), 159–164.

Heymans, R., Tavernier, I., Danthine, S., Rimaux, T., Van Meeren, P., & Dewettinck, K. (2018). Food-grade monoglyceride oil foams: The effect of tempering on foamability, foam stability and rheological properties. *Food and Function*, *9*(6), 3143–3154. https://doi.org/10.1039/c8fo00536b

Heymans, R., Tavernier, I., Dewettinck, K., & Van der Meeren, P. (2017). Crystal stabilization of edible oil foams. *Trends in Food Science and Technology*, *69*, 13–24. https://doi.org/10.1016/j.tifs.2017.08.015

Himawan, C., Starov, V. M., & Stapley, A. G. F. (2006). Thermodynamic and kinetic aspects of fat crystallization. *Advances in Colloid and Interface Science*, *122*, 3–33. https://doi.org/10.1016/j.cis.2006.06.016

Jahurul, M. H. A., Zaidul, I. S. M., Norulaini, N. A. N., Sahena, F., Jinap, S., Azmir, J., … Mohd Omar, A. K. (2013). Cocoa butter fats and possibilities of substitution in food products concerning cocoa varieties, alternative sources, extraction methods, composition, and characteristics. *Journal of Food Engineering*, *117*(4), 467–476. https://doi.org/10.1016/j.jfoodeng.2012.09.024

Lipp, M., Simoneau, C., Ulberth, F., Anklam, E., Crews, C., Brereton, P., … Wiedmaier, C. (2001). Composition of genuine cocoa butter and cocoa butter equivalents. *Journal of Food Composition and Analysis*, *14*(4), 399–408. https://doi.org/10.1006/jfca.2000.0984

Liu, Y., & Binks, B. P. (2021). Foams of vegetable oils containing long-chain triglycerides. *Journal of Colloid and Interface Science*, *583*, 522–534. https://doi.org/10.1016/j.jcis.2020.09.043

Loisel, C., Keller, G., Lecq, G., Bourgaux, C., & Ollivon, M. (1998). Phase transitions and polymorphism of cocoa butter. *JAOCS, Journal of the American Oil Chemists' Society*, *75*(4), 425–439. https://doi.org/10.1007/s11746-998-0245-y

McClements, D. J. (2020). Future foods: A manifesto for research priorities in structural design of foods. *Food and Function*, *11*(3), 1933–1945. https://doi.org/10.1039/c9fo02076d

Mishima, S., Suzuki, A., Sato, K., & Ueno, S. (2016). Formation and Microstructures of Whipped Oils Composed of Vegetable Oils and High-Melting Fat Crystals. *JAOCS, Journal of the American Oil Chemists' Society*, *93*(11), 1453–1466. https://doi.org/10.1007/s11746-016-2888-4

Ng, M., Fleming, T., Robinson, M., Thomson, B., Graetz, N., Margono, C., … Gakidou, E. (2014). Global, regional, and national prevalence of overweight and obesity in children and adults during 1980-2013:

A systematic analysis for the Global Burden of Disease Study 2013. *The Lancet*, *384*(9945), 766–781. https://doi.org/10.1016/S0140-6736(14)60460-8

Palzer, S. (2017). Technological solutions for reducing impact and content of health sensitive nutrients in food. *Trends in Food Science and Technology*, *62*, 170–176. https://doi.org/10.1016/j.tifs.2016.11.022

Patel, A. R., & Dewettinck, K. (2016). Edible oil structuring: An overview and recent updates. *Food and Function*, *7*(1), 20–29. https://doi.org/10.1039/c5fo01006c

Patel, A. R., Rajarethinem, P. S., Gręd owska, A., Turhan, O., Lesaffer, A., De Vos, W. H., … Dewettinck, K. (2014). Edible applications of shellac oleogels: Spreads, chocolate paste and cakes. *Food and Function*, *5*(4), 645–652. https://doi.org/10.1039/c4fo00034j

Pehlivanoğlu, H., Demirci, M., Toker, O. S., Konar, N., Karasu, S., & Sagdic, O. (2018). Oleogels, a promising structured oil for decreasing saturated fatty acid concentrations: Production and food-based applications. *Critical Reviews in Food Science and Nutrition*, *58*(8), 1330–1341. https://doi.org/10.1080/10408398.2016.1256866

Pérez-Martínez, D., Alvarez-Salas, C., Morales-Rueda, J. A., Toro-Vazquez, J. F., Charó-Alonso, M., & Dibildox-Alvarado, E. (2005). The effect of supercooling on crystallization of cocoa butter-vegetable oil blends. *JAOCS, Journal of the American Oil Chemists' Society*. https://doi.org/10.1007/s11746-005-1096-z

Pérez-Martínez, J. D., Reyes-Hernández, J., Dibildox-Alvarado, E., & Toro-Vazquez, J. F. (2012). Physical properties of cocoa butter/vegetable oil blends crystallized in a scraped surface heat exchanger. *JAOCS, Journal of the American Oil Chemists' Society*, *89*(2), 199–209. https://doi.org/10.1007/s11746-011-1904-y

Perez-Martınez, D., Alvarez-Salas, C., Charo-Alonso, M., Dibildox-Alvarado, & Toro-Vazquez, J. . (2007). The cooling rate effect on the microstructure and rheological properties of blends of cocoa butter with vegetable oils. *Food Research International*, *40*, 47–62. https://doi.org/10.1016/j.foodres.2006.07.016

Raß, M., Schein, C., & Matthäus, B. (2008). Virgin sunflower oil. *European Journal of Lipid Science and Technology*, *110*(7), 618–624. https://doi.org/10.1002/ejlt.200800049

Rios, R. V., Pessanha, M. D. F., Almeida, P. F. de, Viana, C. L., & Lannes, S. C. da S. (2014). Application of fats in some food products. *Food Science and Technology (Campinas)*, *34*(1), 3–15. https://doi.org/10.1590/s0101-20612014000100001

Ruiz-Núñez, B., Dijck-Brouwer, D. A. J., & Muskiet, F. A. J. (2016). The relation of saturated fatty acids with low-grade inflammation and cardiovascular disease. *Journal of Nutritional Biochemistry*, *36*, 1–20. https://doi.org/10.1016/j.jnutbio.2015.12.007

Sato, K., Bayés-García, L., Calvet, T., Cuevas-Diarte, M. À., & Ueno, S. (2013). External factors affecting polymorphic crystallization of lipids. *European Journal of Lipid Science and Technology*, *115*(11), 1224–1238. https://doi.org/10.1002/ejlt.201300049

Si, H., Cheong, L. Z., Huang, J., Wang, X., & Zhang, H. (2016). Physical Properties of Soybean Oleogels and Oil Migration Evaluation in Model Praline System. *JAOCS, Journal of the American Oil Chemists' Society*, *93*(8), 1075–1084. https://doi.org/10.1007/s11746-016-2846-1

Simone, E., McVeigh, J., Reis, N. M., & Nagy, Z. K. (2018). A high-throughput multi-microfluidic crystal generator (MMicroCryGen) platform for facile screening of polymorphism and crystal morphology for pharmaceutical compounds. *Lab on a Chip*, *18*(15), 2235–2245. https://doi.org/10.1039/c8lc00301g

Sonwai, S., & Mackley, M. R. (2006). The effect of shear on the crystallization of cocoa butter. *JAOCS, Journal of the American Oil Chemists' Society*, *83*(7), 583–596. https://doi.org/10.1007/s11746-006-1243-6

Toro-vazquez, J. F., Charó-alonso, M. A., Morales-rueda, J. A., & Pérez-martínez, J. D. (2012). Molecular Interactions of Triacylglycerides in Blends of Cocoa Butter with. In N. R. W. Nissim Garti (Ed.), *Cocoa butter and related compounds* (First Edit, pp. 393–416). AOCS Press.

Tran, T., Ghosh, S., & Rousseau, D. (2014). Spheroidal fat crystal microstructures formed with confined gap shearing. *Crystal Growth and Design*, *14*(12), 6383–6390. https://doi.org/10.1021/cg501221d

Tran, T., & Rousseau, D. (2016). Influence of shear on fat crystallization. *Food Research International*, *81*, 157–162. https://doi.org/10.1016/j.foodres.2015.12.022

Truong, T., Prakash, S., & Bhandari, B. (2019). Effects of crystallisation of native phytosterols and monoacylglycerols on foaming properties of whipped oleogels. *Food Chemistry*, *285*(January), 86–93. https://doi.org/10.1016/j.foodchem.2019.01.134

Wright, A. J., Narine, S. S., & Marangoni, A. G. (2000). Comparison of experimental techniques used in lipid crystallization studies. *JAOCS, Journal of the American Oil Chemists' Society*, *77*(12), 1239–1242. https://doi.org/10.1007/s11746-000-0194-2

Z.D. Gunes, O. Schafer, H. Chisholm, H. Deyber, C. P. and B. P. B. (2016). Lipid Based Foam *WO 2016/150978 Al*.

Chapter 4: Real-time monitoring of fat crystallization using pulsed acoustic spectroscopy

Abstract

Being able to monitor and control lipid crystallization is important for many industrial fields, including pharmaceuticals, cosmetic and food industries. Due to the multicomponent nature of natural fats and oils, lipid crystallization processes are complex and require an in-depth understanding and control, to ensure high quality end products with tailored functionality. Studying nucleation and crystal growth in lipid systems is usually carried out with offline techniques such as nuclear magnetic resonance, microscopy, rheology and calorimetry; however, fast, inline measurements of the crystal properties, for example the solid fat content (SFC%), are highly desirable, especially in large-scale, sheared crystallizers. Ultrasound measurements have been proposed as an effective non-invasive, non-destructive technique to monitor phase transitions in lipid-based emulsions and fat/oil blends. However, sound is highly attenuated by solid fat, and high-power instruments might chemically change the material analysed. For these reasons, the implementation of acoustic techniques for the monitoring of lipid crystallization, especially at large scales, is extremely challenging. In this work, the use of a novel immersion ultrasonic probe was applied to monitor the crystallization of a model fat system. Light turbidimetry was used as validation technique. The acoustic measurements were coupled with ex-situ pulsed NMR, and supervised machine learning (ML), to develop a predictive model for calculating SFC% from the velocity of sound, sample composition and temperature.

4.1 Introduction

The crystallization of lipids is a fundamental unit operation for several manufacturing industries, including pharmaceuticals (Jose & Netto, 2019), cosmetic (Duprat-De-Paule et al., 2018; Patel et al., 2021) and food products (Rios et al., 2014). Recently, the use of crystalline fat to produce structured oils (oleogels) has gained significant attention from academia and industry alike, due to the potential to produce solid-like materials with low amounts of saturated fat and specific macroscopic properties (Patel & Dewettinck, 2016).

Furthermore, oleogels may be used as precursors for the production of oil-continuous foams (Binks & Vishal, 2021) and emulsified oil foams (Brun et al., 2015; Goibier et al., 2019) that can find application in the cosmetic, food and pharmaceutical industry as nutrients or drug delivery vehicle or as structuring material for food products. In all of the above examples, the properties of the fat crystals, such as crystal size, shape and polymorphism, affect significantly the stability and functionality (*e.g.*, drug delivery, oil binding capacity, air incorporation) of the end material (Co & Marangoni, 2012; Heymans et al., 2017). The total amount of crystals, *i.e.* the solid fat content (SFC%), is a general parameter strongly related to some macroscopic properties of fat-based materials, such as the melting point, hardness and texture (Himawan et al., 2006). Furthermore, tracking SFC% during crystallization processes is important to determine when equilibrium conditions are reached; hence, maximizing the yield of crystallization.

The SFC% is routinely measured by means of nuclear magnetic resonance (NMR) (Cerdeira et al., 2004), differential scanning calorimetry (DSC) (Foubert et al., 2008) or small-angle X-Ray scattering (SAXS) (Parada et al., 2019); however, these techniques are all off-line, they require the collection of a sample (not always a trivial operation, especially if the melting point is close to ambient temperature) and some degree of sample preparation, which can significantly affect the measurement. In the context of industrial large-scale crystallization, the issues related to offline analysis and sampling are tackled by applying process analytical technology (PAT) tools, which enable real-time monitoring of the product properties, enhanced process understanding, and the application of the so called “Quality by Design” (QbD) strategy (Rathore et al., 2010). Common PAT tools used to monitor crystallization include usually *in situ* probes that exploit the scattering or absorption of electromagnetic radiation (visible light, ultra-violet (UV) or infra-red) by the sample to monitor phase transitions, polymorphic transformations or crystal morphology (Hansen et al., 2017; Simone et al., 2019; Simone et al., 2015) . In the case of lipid crystallization, however, inline characterization of the process is challenging. Fat crystals forms a viscous three-dimensional network of aggregates with a fractal pattern (Tang & Marangoni, 2008), whose measurement is non-trivial. Moreover, (partially) crystalline fat is often opaque to electromagnetic radiation, limiting the analysis to the surface of the sample.

The use of low-power ultrasound for studying the crystallization of lipids has been proposed as an non-invasive, non-destructive method since the 1990s (Fairley & McClements, 1992;McClements & Fairley, 1991; McClements & Povey, 1987). Low-power ultrasounds, *i.e.,* sound waves exceeding 20 kHz frequencies, can penetrate opaque media, without causing physical and chemical changes in the sample. The technique involves the propagation of a short (few microseconds) ultrasonic pulse from a transducer into the sample; such pulse is received by either another transducer on the other side of the measuring apparatus (pitch-and-catch mode) or it is reflected back and received by the same emitting transducer (pulse-echo mode). The velocity of sound (c_{sample}) is then calculated from the travelled pathlength as a function of time and temperature. The acoustic attenuation (α), *i.e.,* the ratio of the amplitude of the sent and received pulse, may also be calculated. As both the velocity of sound and acoustic attenuation depend on the physicochemical properties of the sample, such as density and compressibility, and the presence of heterogeneities, acoustic measurements can be used to monitor phase transitions such as crystallization (McClements & Povey, 1992). Several authors demonstrated the use of custom-made acoustic cells to study fat crystallization using acoustic signal, with particular emphasis on determining the SFC(%) (Birkhofer et al., 2008; Martini et al., 2005b, Martini et al., 2005a; Singh et al., 2002, Singh et al., 2004). Moreover, most of the previous fat crystallization studies were carried out in quiescent conditions, and/or with small sample volumes, thus excluding the effect of shear and secondary nucleation on crystallization (Agrawal & Paterson, 2015).

Despite its several advantages and ease of implementation, there are only sporadic examples in the literature on the use of acoustic probes as a PAT tool for studying lipid crystallization. The immersion probe described in Titiz-Sargut & Ulrich (2003), which featured two 2 MHz transducers in pitch-and-catch mode, was applied to the determination of the metastable zone width (MSZW) of coconut oil, and validated by optical back-reflectance measurements (ORM). The authors focused their study on the effect of different levels of shear, cooling rates and the presence of additives on the MSZW, however no quantitative measurement of the sample was performed. Due to the complexity involved in the crystallization of lipids, such as the occurrence of melt-mediated polymorphic transformations and the development of crystalline networks whose size

range from nanometres to several hundreds of microns, the determination of the solid fat content directly from acoustic parameters might be challenging. One of the growing trends in the use of PAT tools is the implementation of machine learning (ML) algorithms to facilitate analysis of real-time data provided by sensors, and to enable prediction of material properties of interest based on training the algorithm with known outcomes (supervised machine learning) (Wasalathanthri et al., 2020). This strategy may be applied to identify crystal aggregation from microscopic images (Ochsenbein et al., 2015) or to dissolve undesired crystallized impurities in the crystallization of active pharmaceutical ingredients (APIs), using convolutional neural network (CNN) feedback control (Salami et al., 2021).

In this work, a novel acoustic probe recently described in the literature (Morris et al., 2021) was applied as a PAT sensor to monitor the crystallization of a cocoa butter / sunflower oil oleogel system, in a 1L scale vessel and under shear. The ultrasonic data was validated with light turbidimetry, and offline pulsed NMR (*pNMR*) measurements to determine the SFC% of crystallized samples at equilibrium conditions and specific temperatures. The data obtained from the ultrasonic probe was used in combination with the *pNMR* results and supervised machine learning, to develop a predictive model for determining SFC% in-situ.

4.2 Materials and Methods

4.2.1 Cocoa butter–based oleogels

Refined, bleached and deodorized cocoa butter (CB) and high-oleic sunflower oil (HOSO) were kindly provided by Nestlé PTC (York, UK) and used without any further purification. CB was melted at 65°C for 1 hour, and then mixed with HOSO at 9, 11, 13 and 15% concentration by weight.

4.2.2 Fat crystallization rig

The CB-HOSO mixture (900 g) was transferred to the crystallization vessel (capacity *ca.*1 L, diameter 15 cm) (Radley, UK) connected to a Huber Ministat 230 thermostat (Huber, Germany), filled with silicon oil as a heating/cooling medium. The sample was stirred continuously at 200 rpm with a DLH overhead stirrer (VELP Scientifica, Italy), equipped with an anchor-shaped mixer (8 cm diameter). A Pt-100 temperature probe

(Omega Engineering, UK), placed in the vessel, was used to monitor the sample temperature during the experiment. The crystallization process was followed using a Control 4000 turbidity meter (Optek, Germany) fitted with an ASD12-N absorption probe, which measured the light transmittance and absorbance. Finally, the velocity of sound and the acoustic attenuation of the crystallizing mixture were measured using a custom acoustic probe, recently described in literature (Morris et al., 2021). Briefly, the probe comprised a 2.25 MHz broadband transducer coupled with a Rexolite buffer rod (Sonatest model RDT5025, Sonatest, UK), which was connected to a UT320 pulser/receiver (UTEX scientific instruments inc., Canada) and a HDO3034 digital oscilloscope (Teledyne LeCroy, USA). A schematic of the equipment is shown in Figure 4.1.

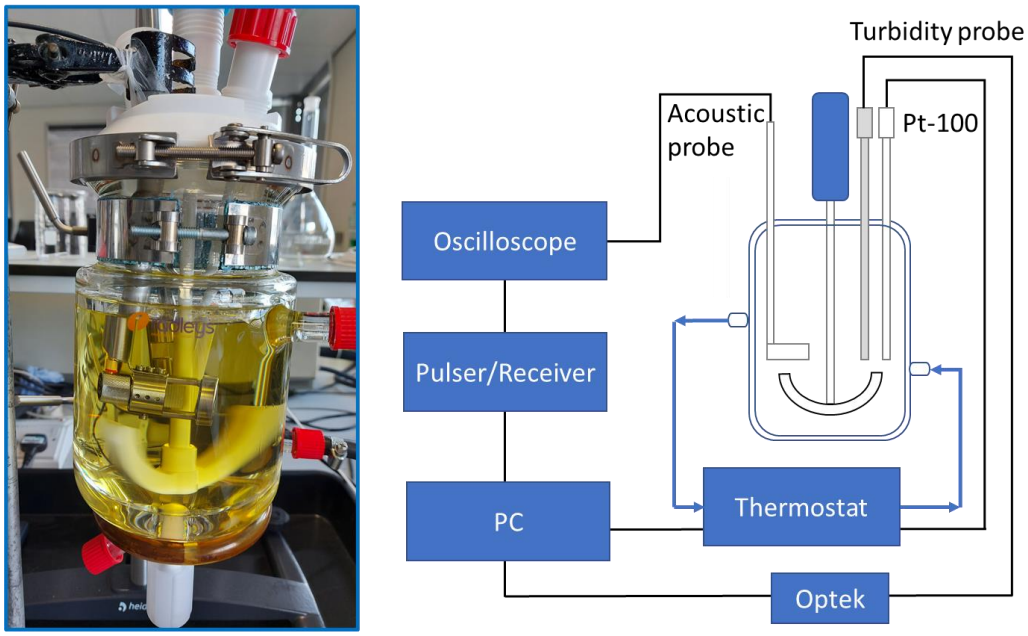

Figure 4.1. Crystallization vessel fitted with a Pt-100 thermocouple, the turbidity probe and the custom ultrasound probe (left), schematic depiction of the rig used in this paper (right).

The thermal profile of the experiment was set to the following: equilibration of the fat blend mixture at 45°C for 10 minutes, cooling to 0°C at a nominal rate of –0.5 °C/min and holding at 0°C for 3 hours. The sample was then heated back to 45°C at 1°C/min. The process temperature and the acoustic waveforms were collected using an in-house script with MATLAB2021a (MathWorks, USA) every 10 seconds. Each experiment was repeated three times.

4.2.3 Determination of the acoustic parameters

Velocity of Sound

Figure 4.2 contains a diagram describing the design of the acoustic probe, and an example of waveform acquired from the oscilloscope with MATLAB.

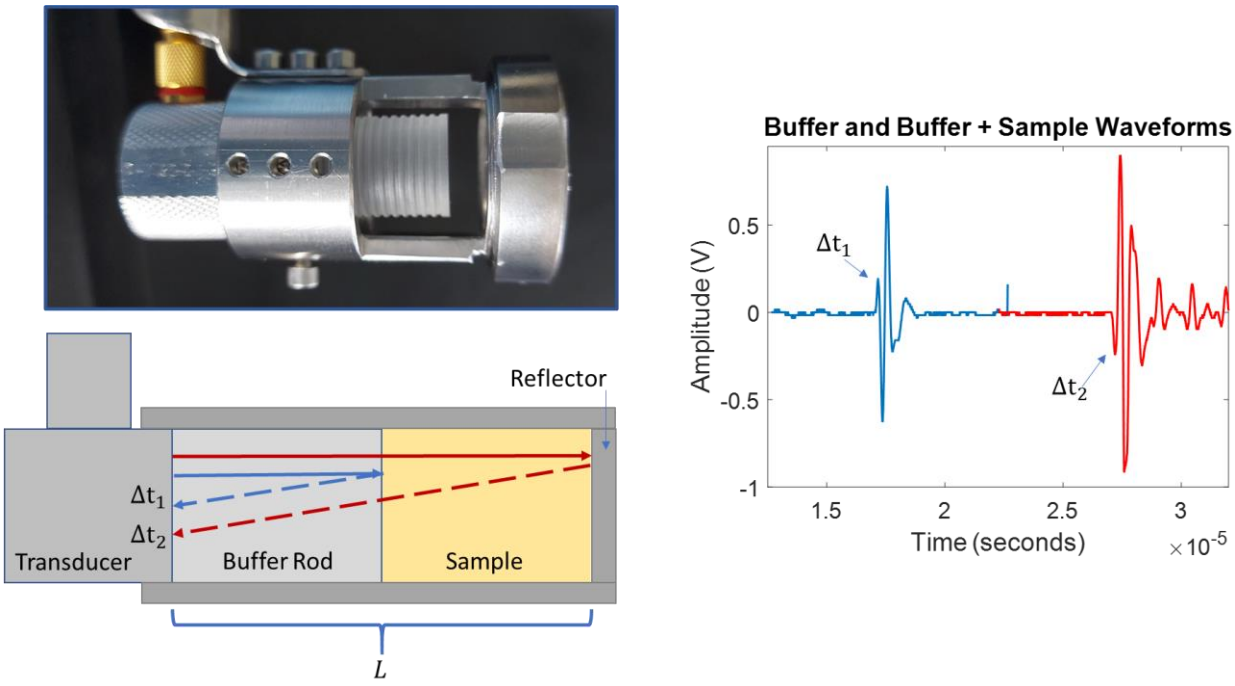

Figure 4.2. Schematic drawing of the custom acoustic probe (left) and the measured waveforms obtained by the reflection of the buffer rod (blue), and buffer rod and sample (red) (right).

The ultrasonic pulse generated from the transducer travels through the buffer rod, and it is partially reflected at the buffer rod/sample interface, due to the acoustic impedance mismatch (*i.e.*, the difference in density and compressibility of the two materials). The pulse is then received back by the transducer after a time Δt_1, shown in Figure 4.2 as the blue trace. Part of the initial pulse, however, is transmitted through the sample, and it is reflected by the stainless-steel reflector to the transducer after a time Δt_2 (Figure 4.2, red trace). In order to calculate the velocity of sound in the sample, the time of flight in the sample is required. To calculate it, the initial value of Δt_1 and Δt_2 were first determined with MATLAB2021a from the original waveform, using the leading-edge method (*i.e.*, detecting the arrival time of the pulse envelope when it crosses a set voltage threshold). Afterwards, the shifts of the pulses' position ($\Delta\Delta t_1$ and $\Delta\Delta t_2$) during the experiment were

calculated with the cross-correlation function (*xcorr*) implemented in MATLAB. Briefly, the cross-correlation compares the analysed pulse with a reference signal, allowing an easy calculation of the delay between the two. This method proved to be more robust to analyse the set of waveforms compared to applying the leading-edge technique on all collected waveforms. This is because the pulse envelop was subject to distortion due to signal attenuation through the experiment. The variation in the sample time of flight ($\Delta\Delta t_3$) was then calculated with Equation 4.1:

$$\Delta\Delta t_3 = \Delta\Delta t_2 - \Delta\Delta t_1 \quad \text{(Eq. 4.1)}$$

In order to obtain an accurate value of the velocity of sound, however, it was necessary to determine the pathlength dependence on the temperature with a calibration experiment. The velocity of sound in distilled water (c_{water}) with respect to temperature (T) may be calculated using a fifth-order polynomial, as first described by Chávez et al. (1985) (Eq. 4.2):

$$c_{water} = 3.16 \cdot 10^{-9}T^5 - 1.48 \cdot 10^{-6}T^4 + 3.35 \cdot 10^{-4}T^3 - 5.81 \cdot 10^{-2}T^2 + 5.04 \cdot T + 1.40 \cdot 10^3 \quad \text{(Eq. 4.2)}$$

The shift in the time of flight in distilled water ($\Delta\Delta t_{3,water}$) was then measured between 50°C and 5°C, using a –0.01 °C/min cooling rate to allow the probe to reach thermal equilibrium with the surrounding medium. The corresponding experimental pathlength ($L_{calibrated}$) was calculated with Equation 4.3

$$L_{calibrated} = \Delta\Delta t_{3,water} \times c_{water} \quad \text{(Eq. 4.3)}$$

The dependence of the pathlength on the temperature was then obtained by fitting a fifth-order polynomial to $L_{calibrated}$ against the temperature (Figure 4.3).

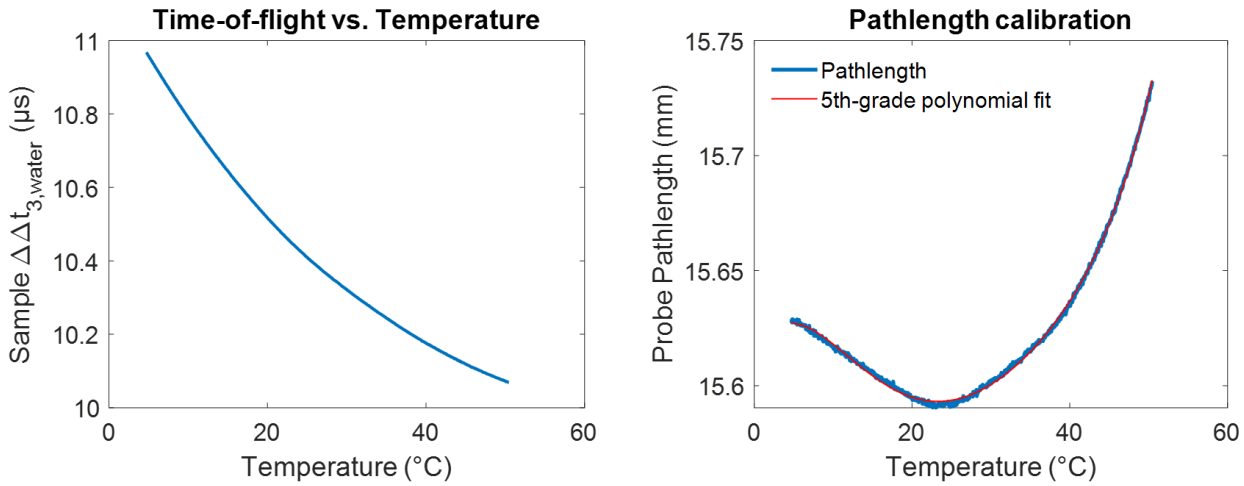

Figure 4.3. Measured time-of-flight in distilled water between 60°C and 5°C (left), calculated sample pathlength and 5th-order polynomial fitting (right).

The coefficients estimated for the pathlength calculation were then used to calculate accurately the velocity of sound during the crystallization experiments with Equation 4.4

$$c_{sample} = \frac{L_{calibrated}}{\Delta\Delta t_3} \quad \text{(Eq. 4.4)}$$

Acoustic Attenuation

The acoustic attenuation, which represents the amount of acoustic power absorbed by the sample, is affected by several factors, including the presence of phase transitions and scattering phenomena generated by the presence of dispersed objects in the sample (McClements & Povey, 1992). In this work, the acoustic attenuation was used to monitor crystal growth during the crystallization experiment. The acoustic attenuation was calculated according to Equation 4.5

$$\alpha = -20 \log \frac{A}{A_0} \quad \text{(Eq. 4.5)}$$

where A and A_0 are the peak-to-peak amplitudes of the sample signal during the experiment, and at the start of the experiment, respectively.

Solid Fat Content

The solid fat content (SFC%), defined as the mass fraction of solid to liquid material in a fat blend, was calculated by applying a prediction model, developed with the Regression Learner app in MATLAB2021a,

(MathWorks, USA). Regression Learner is a supervised machine learning utility, where a regression algorithm is applied to an observation matrix and compared with a response matrix. The observation matrix comprised the temperature (T), velocity of sound in the sample (c_{sample}) and the amount of added cocoa butter (CB%) for each crystallization experiment; the response matrix contained the SFC% values, measured with pNMR, between 5 and 10°C for the respective samples. The velocity of sound and temperature of pure sunflower oil were added to the observation matrix as well, with a corresponding solid fat content of 0. Three models available in the MATLAB app were tested for training, and their predictive ability compared: "Linear", "Fine Tree" and "Gaussian Process Regression – Rational Quadratic". The Linear model uses a linear regression to fit the data from the observation matrix. The "Fine Tree" model, instead, is a type of nonlinear model based on regression trees, which applies a recursive partition of the observation matrix to improve the prediction of the response value. Lastly, the Gaussian Process Regression model, which is also nonlinear, works by predicting the probability distribution of responses for each parameter in the observation matrix. Cross-validation was performed both using the in-built function in Regression Learner, as well as by removing from the observation matrix the entries related to one set of CB% experiments, and validating the obtained model with the rest of the data. The predicted SFC% was then compared for the different crystallization experiments.

4.2.4 Pulsed Nuclear Magnetic Resonance (pNMR)

The solid fat content (SFC%) of the CB-HOSO mixtures was determined with pNMR using a Bruker Minispec NMR (Bruker, Switzerland). The samples were collected at the end of the crystallization experiment, transferred to a 10mm inner diameter NMR tube and stored in a fridge at 4°C. The SFC% was measured between 5 and 45°C, in steps of 5°C each. During the experiment, the NMR tube was left to equilibrate for 90 minutes for each temperature step. The measurements were carried out in triplicates.

4.3 Results and Discussion

4.3.1 Fat crystallization monitored by PAT tools

The crystallization of a 9% CB w/w in HOSO sample, monitored with turbidity and the acoustic probe, is shown in Figure 4.4.

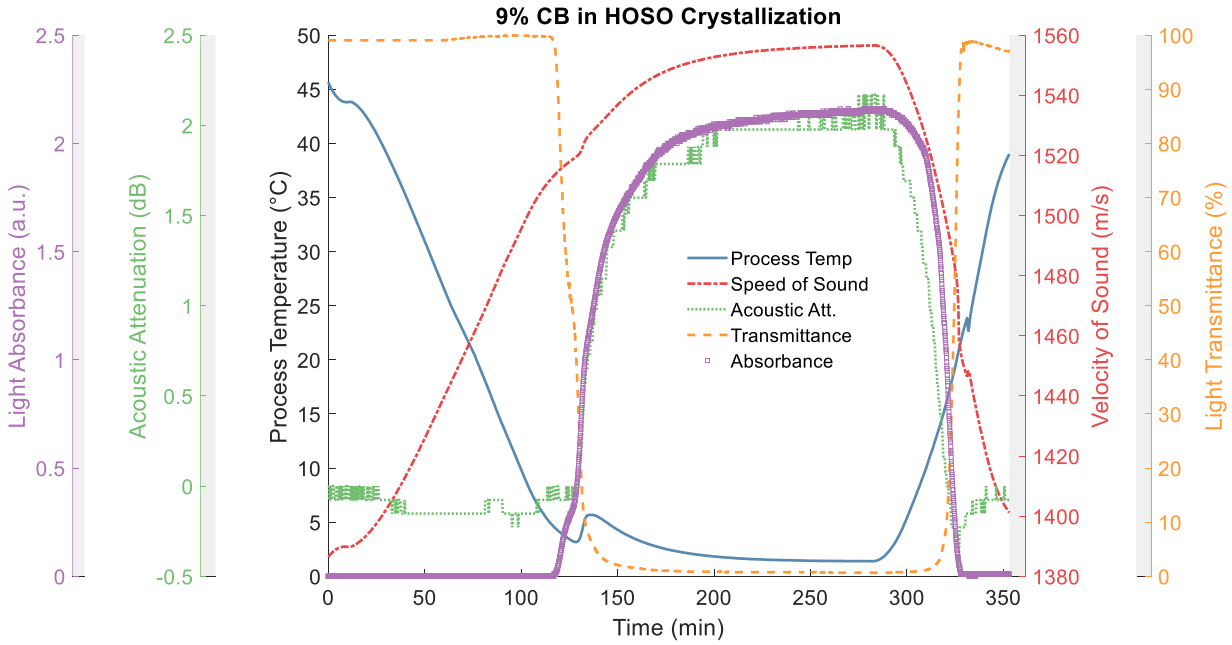

Figure 4.4. Process Analytical Technologies (PAT) tools plot of the crystallization of a 9% w/w CB in HOSO blend. Process temperature (-), velocity of sound (-·-), acoustic attenuation (···), light transmittance (--) and light absorbance (o).

The crystallization of CB/HOSO sample can be divided into four steps. Between 0 and 115 minutes, the temperature of the sample followed the cooling profile, from 45°C to 5°C, accompanied by an increase in the velocity of sound, from 1390 to 1510 m/s, due to the negative velocity coefficient with respect to temperature (McClements & Povey, 1992). After 115 minutes, the onset of nucleation was detected by a sharp decrease in the light transmittance, due to the sample becoming turbid. At the same time, only a slight increase in the acoustic attenuation was detected (115 – 129 minutes). The attenuation of the ultrasonic pulse due to scattering is frequency dependent and it is higher when the pulse wavelength is comparable in size with the crystal nuclei, resulting in significant scattering of sound (Morris et al., 2021). In the early stages of crystal nucleation higher frequencies (20-50 MHz) are possibly more sensitive to the appearance of nuclei

than lower ones (1-10 MHz). The pulse wavelength (λ), which can be calculated from the velocity of sound and frequency (f) (Eq. 4.6)

$$\lambda = \frac{c}{f} \qquad \text{Eq. 4.6}$$

was 750 µm for a 2 MHz pulse. Hence, it was likely that in the region between 115 and 129 min the crystals were smaller than the pulse wavelength, but comparable in size with the turbidity probe wavelength (700 nm) at the onset of nucleation. As previously observed for CB/HOSO mixtures, cocoa butter nucleates as spherical aggregates of crystalline nanoplatelets (CNPs), which grow to form a three-dimensional network of fat crystal aggregates. Within the crystallization conditions tested in this work, the CB aggregates were found to be in the β(V) form (Metilli et al., 2021). Once the fat crystal network developed, increasing in size, the acoustic attenuation and light absorbance both increased significantly at 130 min. The crystal growth caused simultaneously a steep increase in the velocity of sound, as ultrasounds travel faster in the solid compared to the liquid, and release of the latent heat of solidification in the sample, as shown by the increase in the process temperature from 130 to 137 minutes. After 150 minutes, the sample cooled further to *ca.* 3 °C, and the observed sample properties (acoustic and light attenuation, velocity of sound) were linearly dependent with respect to the temperature. Finally, after 275 minutes the sample was heated back to 45°C; after 310 minutes. During heating a significant increase in light transmittance was detected, as the fat crystals melted and the sample returned to its liquid state. At the same time, the acoustic attenuation and light absorbance returned to their values prior to crystallization. Therefore, the acoustic probe developed in this work was able to monitor fat crystallization accurately through the measurement of the velocity of sound and acoustic attenuation, and was corroborated by light turbidimetry, both at the cloud point (nucleation) and the clear point (melting).

Experiments carried out with higher % of CB showed similar trends for the acoustic and light signals. The velocity of sound, measured between 5 and 10°C during the heating step, is shown in Figure 4.5 for different % of added CB.

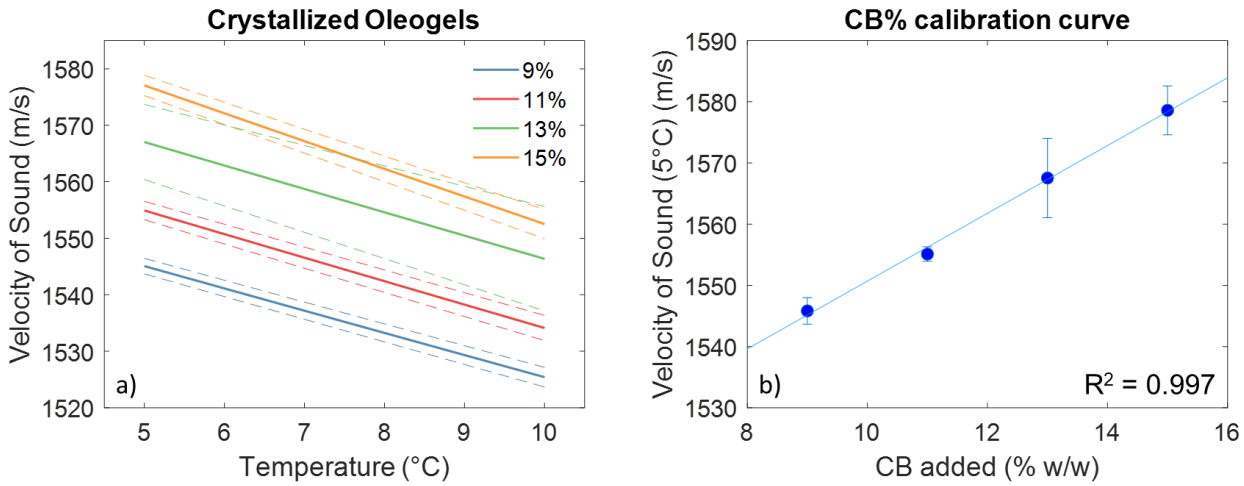

Figure 4.5. Velocity of sound of crystallized CB/HOSO oleogels between 5 and 10°C (a) and corresponding velocity of sound at 5°C, plotted against the amount of added % w/w of cocoa butter (b).

As expected, the velocity of sound was linearly dependent on the amount of added cocoa butter, increasing by approximately 10 m/s every 2% of added CB. The acoustic attenuation increased with the amount of solids in the oleogel as well, as shown in Table 4.1.

Table 4.1. Velocity of sound and acoustic attenuation for oleogel samples at the end of the crystallization (5°C).

CB % (w/w)	Velocity of Sound (5°C) (m/s)	Acoustic Attenuation (5°C) (dB)
9	1545.8 ± 2.2	2.25 ± 1.13
11	1555.1 ± 1.2	2.42 ± 0.09
13	1567.5 ± 6.5	2.61 ± 0.06
15	1578.6 ± 4.0	3.31 ± 0.42

The velocity of sound at 5°C for each sample was taken as a reference and plotted against the % of CB within the sample, providing a straightforward equation to predict the amount of cocoa butter in the sample from the velocity of sound (Eq. 4.7):

$$CB(\%) = 0.18 \times (Velocity\ of\ Sound) - 269.2 \qquad \text{Eq. 4.7}$$

However, the actual amount of solid fat (SFC%) developed during crystallization is affected by several factors, including the degree of undercooling, the level of shearing and the polymorph nucleated (Sonwai & Mackley, 2006)(Sato et al., 2013). Therefore, *pNMR* was used to determine the SFC% for the CB/HOSO blends at the end of the crystallization profile, and to study how SFC% changes with temperature. The velocity of sound at 5°C was then plotted as a function of SFC%, rather than the amount of added CB. The result are shown in Figure 4.6.

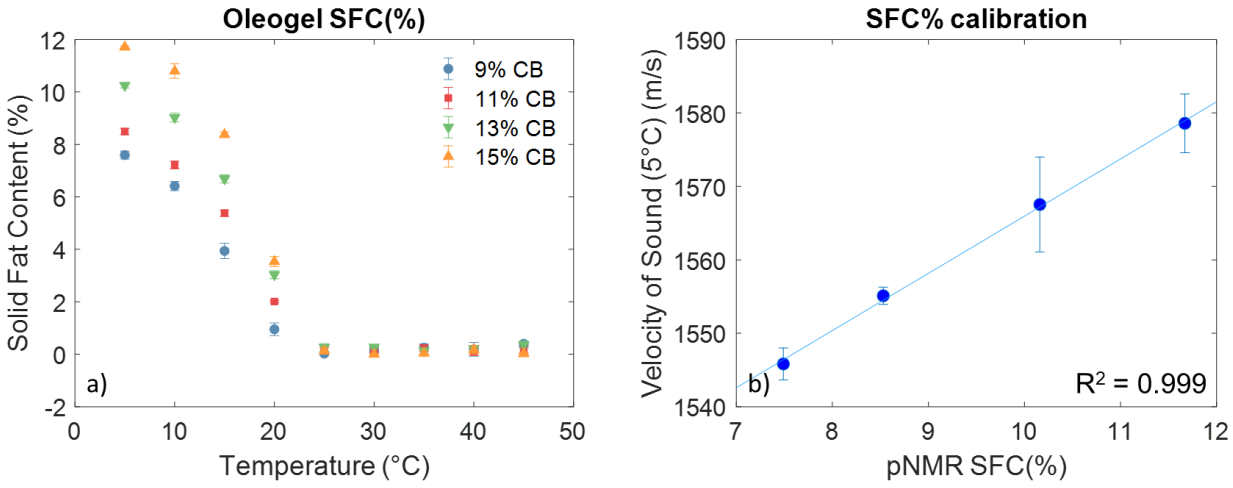

Figure 4.6. SFC% calculated with pNMR with respect to temperature for the different CB/HOSO blends (left) and corresponding velocity of sound values for the SFC% at 5°C for the different CB/HOSO blends (left).

By inspecting the SFC% values at 5°C, it can be noted that all samples displayed a lower SFC% compared to the total amount of added cocoa butter. This is because the main triacylglycerides species that are solid at ambient temperature, POP, SOS and POS, constitute about 80% w/w of cocoa butter, while the remaining 20% comprises mono- and di-glycerides, phospholipids, sterols and free fatty acids that are liquid at ambient conditions (Dimick, 1991). Nevertheless, the relationship between the velocity of sound and the SFC% at 5°C was linear (Figure 4.6b); the SFC% could be calculated from Eq. 4.8:

$$SFC(\%) = 0.13 \times (Velocity\ of\ Sound) - 190.7 \qquad \text{Eq. 4.8}$$

4.3.2 Solid fat content predicted by Regression Learner model

The validation data from the three predictive models tested for determining SFC% is shown in Figure 4.7.

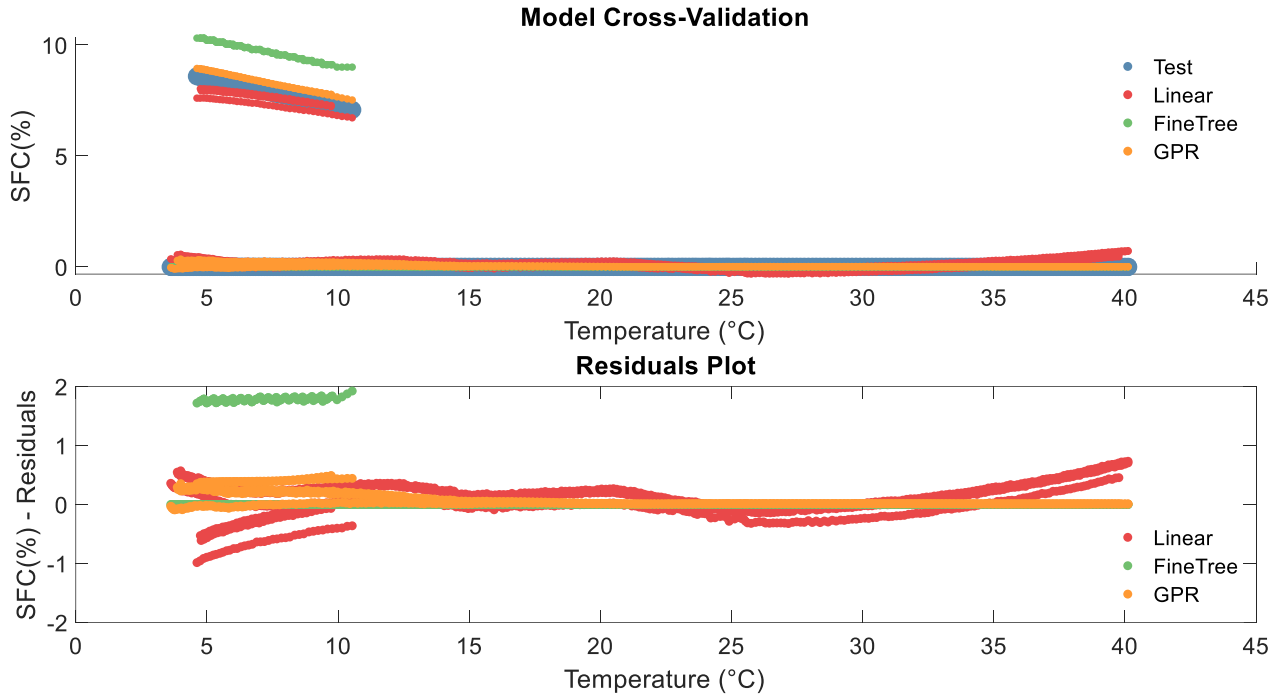

Figure 4.7. Cross-validation of the predictive models on the 11% CB in HOSO dataset, as a function of temperature (a). Residuals plot of the three predictive models (b).

The blue circles in Figure 4.7a represent the SFC% of a 11% CB/HOSO sample as a function of temperature, as obtained from the acoustic probe during crystallization and *pNMR* measurements on the crystallized oleogel. The red, green and orange dots represent the predicted value of SFC%, as a function of temperature, velocity of sound and initial % of CB, using the three different prediction models: Linear, Fine Tree and Rational Quadratic – Gaussian Process Regression (GPR), respectively. The root mean square error (RMSE) of the three models was lower for the Fine Tree (0.00013) and the GPR (0.00018) compared to the Linear model (0.0034). While the Linear model prediction of the SFC% between 5 and 10°C was more accurate than the Fine Tree model, could not model the SFC% prior to the crystallization (10 – 40°C) as accurately as the others. Therefore, the GPR model was selected as the most accurate of the three. Figure 4.8 shows the SFC% evolution during the experiment of Figure 4.4, as predicted by the GPR model.

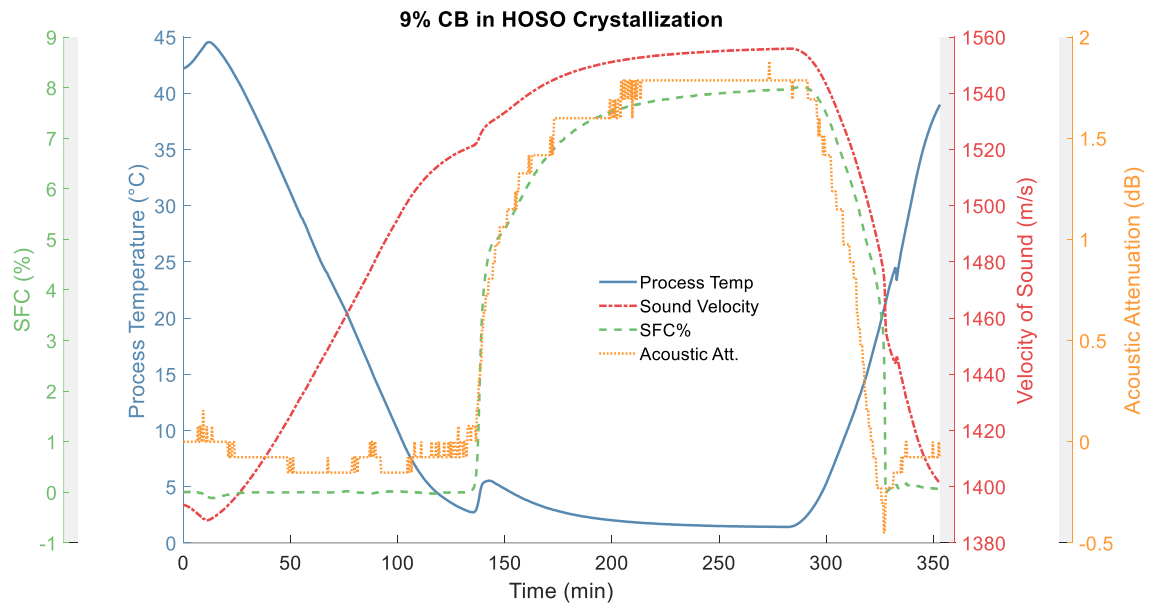

Figure 4.8. Process Analytical Technologies (PAT) tools plot of the crystallization of a 9% w/w CB in HOSO blend. Process temperature (-), velocity of sound (--), acoustic attenuation (···), and predicted SFC% with the GPR model (--).

The evolution of the solid fat in the oleogel matched the increase in the acoustic attenuation at 130 min, reaching 5% over few minutes and then levelling to 8% at the end of the holding step. During the heating phase, the SFC% started decreasing, falling sharply to 0% when the temperature was raised above 20°C and remaining constant afterwards until the end of the experiment. Hence, the GPR model was able to describe the evolution of the SFC% during the crystallization experiment accurately. The predicted SFC% for the samples at different CB % was plotted as a function of temperature in Figure 4.9.

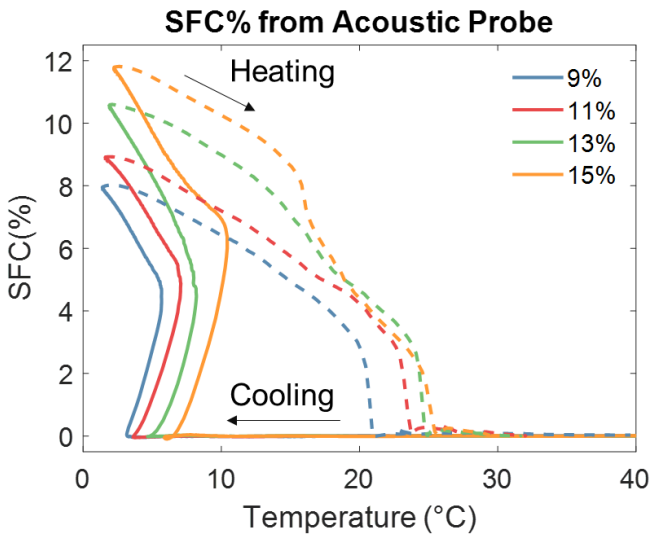

Figure 4.9. Evolution of predicted SFC% during cooling (-) and heating (--) for oleogels containing different CB %.

By inspecting the cooling profile, it can be noted that crystal growth, signalled by the increase in SFC%, occurred at higher crystallization temperatures for oleogels containing higher % of CB, as also reported previously in Metilli et al. (2021) for this type of system. In agreement with the *pNMR* results, the oleogels reached 7.6%, 8.5%, 10.3% and 11.4% SFC for 9, 11, 13 and 15% CB in HOSO samples, at 5°C after the end of the holding time. By inspecting the heating profile, the SFC% decreased linearly with the temperature; although a direct comparison with the melting profile obtained from the *pNMR* experiments in Figure 4.6 is not feasible, both techniques showed that the samples returned to the liquid state at 25°C.

4.4 Conclusions

In this work, the crystallization of cocoa butter–based oleogels was characterized using light turbidimetry and pulsed acoustic spectroscopy as PAT tools, within a small-scale reactor under shear. The development of the solid fat in the oleogel was monitored through measurement of the velocity of sound and acoustic attenuation, and was corroborated by turbidity measurements. The onset of crystal nucleation was detected by the turbidity probe, whereas the acoustic probe was more effective in monitoring the crystal growth process. Using a higher frequency transducer could increase the sensitivity of the ultrasonic probe to crystal nucleation, however might result in excessive signal attenuation at equilibrium conditions, at which SFC% needs to be calculated. Results showed that the velocity of sound in the oleogel was proportional to the

amount of added CB in the mixture. In order to calculate the solid fat content (SFC%) of oleogel at different CB concentrations, a novel approach that exploited supervised machine learning was adopted. The data, including the temperature, velocity of sound, amount of added CB and SFC% measured by *pNMR* in the solid oleogels was used to train a Gaussian Process Regression model, which was in turn applied for the prediction of the SFC% during the crystallization experiments. The predicted SFC% increased at the same time of the acoustic attenuation during crystal growth, and decreased to 0% during melting, in agreement with the melting profile measured by *pNMR* for the same oleogel samples. Therefore, pulsed acoustic spectroscopy may be applied as a PAT tool to the large-scale manufacturing of oleogels for accurate monitoring of the crystallization process and determination of the SFC% in an inline fashion.

Declaration of Competing Interests

The authors declare that they have no known competing financial interests or personal relationships that could have appeared to influence the work reported in this paper.

Acknowledgements

The authors would like to acknowledge the Engineering and Physical Sciences Research Council funded Centre for Doctoral Training in Soft Matter and Functional Interfaces, grant ref. no. EP/L015536/1 as well as Nestlé PTC Confectionery (York, UK) for the pulsed NMR analysis, and the financial and writing support. E.S. also acknowledges Royal Society (Grant ref. no. INF\R2\192018) for additional funding.

References

Agrawal, S. G., & Paterson, A. H. J. (2015). Secondary Nucleation: Mechanisms and Models. *Chemical Engineering Communications*, *202*(5), 698–706. https://doi.org/10.1080/00986445.2014.969369

Binks, B. P., & Vishal, B. (2021). Particle-stabilized oil foams. *Advances in Colloid and Interface Science*, *291*, 102404. https://doi.org/10.1016/j.cis.2021.102404

Birkhofer, B. H., Jeelani, S. A. K., Windhab, E. J., Ouriev, B., Lisner, K. J., Braun, P., & Zeng, Y. (2008). Monitoring of fat crystallization process using UVP-PD technique. *Flow Measurement and Instrumentation*, *19*(3–4), 163–169. https://doi.org/10.1016/j.flowmeasinst.2007.08.008

Brun, M., Delample, M., Harte, E., Lecomte, S., & Leal-Calderon, F. (2015). Stabilization of air bubbles in oil by surfactant crystals: A route to produce air-in-oil foams and air-in-oil-in-water emulsions. *Food Research International*, *67*, 366–375. https://doi.org/10.1016/j.foodres.2014.11.044

Cerdeira, M., Candal, R.J., Herrera, M. L. (2004). Analytical Techniques for Nucleation Studies in Lipids : Advantages and Disadvantages. *Journal of Food Science*, *69*(9), R185–R191.

Chávez, M., Sosa, V., & Tsumura, R. (1985). Speed of sound in saturated pure water. *Journal of the Acoustical Society of America*, *77*(2), 420–423. https://doi.org/10.1121/1.391861

Co, E. D., & Marangoni, A. G. (2012). Organogels: An alternative edible oil-structuring method. *JAOCS, Journal of the American Oil Chemists' Society*, *89*(5), 749–780. https://doi.org/10.1007/s11746-012-2049-3

Dimick, P. S. (1991). Principles of cocoa butter crystallization. *Manufacturing Confectioner*, *71*(5), 115–125. Retrieved from http://apps.webofknowledge.com.ezproxy.lib.ryerson.ca/full_record.do?product=UA&search_mode=AdvancedSearch&qid=11&SID=2DYqpx1Zm6a3srAjVAI&page=1&doc=8

Duprat-De-Paule, S., Guilbot, J., Roso, A., Cambos, S., & Pierre, A. (2018). Augmented bio-based lipids for cosmetics. *OCL - Oilseeds and Fats, Crops and Lipids*, *25*(5). https://doi.org/10.1051/ocl/2018036

Fairley, P., & McClements, D. J. (1992). Frequency scanning ultrasonic pulse echo reflectometer. *Ultrasonics*, *30*(6), 403–405.

Foubert, I., Fredrick, E., Vereecken, J., Sichien, M., & Dewettinck, K. (2008). Stop-and-return DSC method to study fat crystallization. *Thermochimica Acta*, *471*(1–2), 7–13. https://doi.org/10.1016/j.tca.2008.02.005

Goibier, L., Pillement, C., Monteil, J., Faure, C., & Leal-Calderon, F. (2019). Emulsification of non-aqueous

foams stabilized by fat crystals: Towards novel air-in-oil-in-water food colloids. *Food Chemistry*, *293*. https://doi.org/10.1016/j.foodchem.2019.04.080

Hansen, T. B., Simone, E., Nagy, Z., & Qu, H. (2017). Process Analytical Tools to Control Polymorphism and Particle Size in Batch Crystallization Processes. *Organic Process Research and Development*, *21*(6), 855–865. https://doi.org/10.1021/acs.oprd.7b00087

Heymans, R., Tavernier, I., Dewettinck, K., & Van der Meeren, P. (2017). Crystal stabilization of edible oil foams. *Trends in Food Science and Technology*, *69*, 13–24. https://doi.org/10.1016/j.tifs.2017.08.015

Himawan, C., Starov, V. M., & Stapley, A. G. F. (2006). Thermodynamic and kinetic aspects of fat crystallization. *Advances in Colloid and Interface Science*, *122*, 3–33. https://doi.org/10.1016/j.cis.2006.06.016

Jose, J., & Netto, G. (2019). Role of solid lipid nanoparticles as photoprotective agents in cosmetics. *Journal of Cosmetic Dermatology*, *18*(1), 315–321. https://doi.org/10.1111/jocd.12504

Ladd Parada, M., Povey, M. J., Vieira, J., Rappolt, M., & Ries, M. E. (2019). Early stages of fat crystallisation evaluated by low-field NMR and small-angle X-ray scattering. *Magnetic Resonance in Chemistry*, *57*(9), 686–694. https://doi.org/10.1002/mrc.4860

Martini, S., Bertoli, C., Herrera, M. L., Neeson, I., & Marangoni, A. (2005a). Attenuation of ultrasonic waves: Influence of microstructure and solid fat content. *JAOCS, Journal of the American Oil Chemists' Society*, *82*(5), 319–328. https://doi.org/10.1007/s11746-005-1073-6

Martini, S., Bertoli, C., Herrera, M. L., Neeson, I., & Marangoni, A. (2005b). *In situ* monitoring of solid fat content by means of pulsed nuclear magnetic resonance spectrometry and ultrasonics. *JAOCS, Journal of the American Oil Chemists' Society*, *82*(5), 305–312. https://doi.org/10.1007/s11746-005-1071-8

McClements, D. J., & Fairley, P. (1991). Ultrasonic pulse echo reflectometer. *Ultrasonics*, *29*(1), 58–62. https://doi.org/10.1016/0041-624X(91)90174-7

McCLEMENTS, D. J., & POVEY, M. J. W. (1987). Solid fat content determination using ultrasonic velocity

measurements. *International Journal of Food Science & Technology*, *22*(5), 491–499. https://doi.org/10.1111/j.1365-2621.1987.tb00514.x

McClements, D. Julian, & Povey, M. J. W. (1992). Ultrasonic analysis of edible fats and oils. *Ultrasonics*, *30*(6), 383–388. https://doi.org/10.1016/0041-624X(92)90094-3

Metilli, L., Lazidis, A., Francis, M., Marty-terrade, S., Ray, J., & Simone, E. (2021). The Effect of Crystallization Conditions on the Structural Properties of Oleofoams Made of Cocoa Butter Crystals and High Oleic Sunflower Oil. *Crystal Growth and Design*. https://doi.org/10.1021/acs.cgd.0c01361

Morris, L., Simone, E., Glover, Z. J., Powell, H., Marty-Terrade, S., Francis, M., & Povey, M. J. (2021). Dynamic monitoring of glycine crystallisation with low power ultrasound reflection spectroscopy. *Chemical Engineering Research and Design*, *170*, 213–223. https://doi.org/10.1016/j.cherd.2021.04.003

Ochsenbein, D. R., Vetter, T., Schorsch, S., Morari, M., & Mazzotti, M. (2015). Agglomeration of needle-like crystals in suspension: I. Measurements. *Crystal Growth and Design*, *15*(4), 1923–1933. https://doi.org/10.1021/acs.cgd.5b00094

Patel, A. R., & Dewettinck, K. (2016). Edible oil structuring: An overview and recent updates. *Food and Function*, *7*(1), 20–29. https://doi.org/10.1039/c5fo01006c

Patel, D., Patel, B., & Thakkar, H. (2021). Lipid Based Nanocarriers: Promising Drug Delivery System for Topical Application. *European Journal of Lipid Science and Technology*, *123*(5), 1–12. https://doi.org/10.1002/ejlt.202000264

Rathore, A. S., Bhambure, R., & Ghare, V. (2010). Process analytical technology (PAT) for biopharmaceutical products. *Analytical and Bioanalytical Chemistry*, *398*(1), 137–154. https://doi.org/10.1007/s00216-010-3781-x

Rios, R. V., Pessanha, M. D. F., Almeida, P. F. de, Viana, C. L., & Lannes, S. C. da S. (2014). Application of fats in some food products. *Food Science and Technology (Campinas)*, *34*(1), 3–15. https://doi.org/10.1590/s0101-20612014000100001

Salami, H., McDonald, M. A., Bommarius, A. S., Rousseau, R. W., & Grover, M. A. (2021). *In situ* Imaging Combined with Deep Learning for Crystallization Process Monitoring: Application to Cephalexin Production. *Organic Process Research and Development*, *25*(7), 1670–1679. https://doi.org/10.1021/acs.oprd.1c00136

Sato, K., Bayés-García, L., Calvet, T., Cuevas-Diarte, M. À., & Ueno, S. (2013). External factors affecting polymorphic crystallization of lipids. *European Journal of Lipid Science and Technology*, *115*(11), 1224–1238. https://doi.org/10.1002/ejlt.201300049

Simone, E., Tyler, A. I. I., Kuah, D., Bao, X., Ries, M. E., & Baker, D. (2019). Optimal design of crystallization processes for the recovery of a slow-nucleating sugar with a complex chemical equilibrium in aqueous solution: The case of lactose. *Organic Process Research and Development*, *23*(2), 220–233. https://doi.org/10.1021/acs.oprd.8b00323

Simone, E., Zhang, W., & Nagy, Z. K. (2015). Application of process analytical technology-based feedback control strategies to improve purity and size distribution in biopharmaceutical crystallization. *Crystal Growth and Design*, *15*(6), 2908–2919. https://doi.org/10.1021/acs.cgd.5b00337

Singh, A. P., McClements, D. J., & Marangoni, A. G. (2002). Comparison of ultrasonic and pulsed NMR techniques for determination of solid fat content. *JAOCS, Journal of the American Oil Chemists' Society*, *79*(5), 431–437. https://doi.org/10.1007/s11746-002-0501-y

Singh, A. P., McClements, D. J., & Marangoni, A. G. (2004). Solid fat content determination by ultrasonic velocimetry. *Food Research International*, *37*(6), 545–555. https://doi.org/10.1016/j.foodres.2003.12.010

Sonwai, S., & Mackley, M. R. (2006). The effect of shear on the crystallization of cocoa butter. *JAOCS, Journal of the American Oil Chemists' Society*, *83*(7), 583–596. https://doi.org/10.1007/s11746-006-1243-6

Tang, D., & Marangoni, A. G. (2008). Fractal dimensions of simulated and real fat crystal networks in 3D space. *JAOCS, Journal of the American Oil Chemists' Society*, *85*(6), 495–499. https://doi.org/10.1007/s11746-

008-1237-7

Titiz-Sargut, S., & Ulrich, J. (2003). Application of a protected ultrasound sensor for the determination of the width of the metastable zone. *Chemical Engineering and Processing: Process Intensification*, *42*(11), 841–846. https://doi.org/10.1016/S0255-2701(02)00215-5

Wasalathanthri, D. P., Rehmann, M. S., Song, Y., Gu, Y., Mi, L., Shao, C., … Li, Z. J. (2020). Technology outlook for real-time quality attribute and process parameter monitoring in biopharmaceutical development—A review. *Biotechnology and Bioengineering*, *117*(10), 3182–3198. https://doi.org/10.1002/bit.27461

Chapter 5: Investigating the microstructure of soft, microporous matter with synchrotron X-ray Tomography

Abstract

Soft porous matter is commonly encountered in artificial tissue applications, pharmaceuticals delivery systems and in cosmetic and food products. These materials are typically opaque and tend to deform under very small levels of shear; this makes the characterization of their microstructure very challenging, particularly in the native state. Air-in-oil systems (oleofoams) are an emerging type of soft material with promising applications in cosmetics and foods, which contain air bubbles stabilized by Pickering fat crystals dispersed in a liquid oil phase. Synchrotron radiation X-ray computed tomography (SR - XCT) is a non-invasive, non-destructive technique increasingly used to investigate multiphasic, porous materials, owing to its high flux which enables sub-micron resolution and significant statistics at rapid acquisition speed. While the penetration of high energy X-rays can provide high resolution images and allows the reconstruction of the 3D structure of samples, the experimental setup and measuring parameters need to be carefully designed to avoid sample deformation or beam damage.

In this work, a robust methodology for investigating the 3D microstructure of soft, porous matter was developed. Sample preparation and experimental setup were chosen to allow synchrotron tomographic analysis of soft oleofoams with a low melting point (<30°C). In particular, the use of cryogenic conditions (plunge-freeze in liquid nitrogen) provided stability against melting during the acquisition. Additionally, an image processing workflow was designed for analysing the 3D microstructure of the samples using ImageJ. Hence, the size and shape distribution of the air phase, as well as the thickness of the continuous gel phase could be determined for samples with significantly different microstructures (fresh vs. heated). Furthermore, the use of time-resolved X-ray radiography (XRR) enabled the investigation of dynamic changes in the microstructure of the samples during thermal destabilization, visualizing bubble coalescence and growth in optically opaque foam samples with a sub-second timescale.

5.1 Introduction

Soft porous matter features in numerous contexts of scientific and commercial interests, ranging from hydrogel-based scaffold for tissue regeneration (Sato et al., 2018; Kinoshita et al., 2020), porous nanocellulose for delivery of pharmaceuticals (Sehaqui et al., 2010; Iftimi et al., 2019) gas marbles (Timounay et al., 2017) to aqueous and non-aqueous foams used in food and personal care products (Fameau & Fujii, 2020; Hill & Eastoe, 2017; Luengo et al., 2021). These systems are comprised of a dispersed gaseous phase, a liquid or semi-solid continuous phase and, in the case of foams, suspended stabilizing molecules, particles or crystals that can also adsorb at the air phase boundary (Murray et al., 2011; Murray, 2020). The 3D microstructure dictates the macroscopic properties of these materials, which in turn affects their functionality, their stability against liquid drainage and liquid coalescence and, in the case of food, texture and mouthfeel (Ciurzyńska & Lenart, 2016; Ellis et al., 2017; Herremans et al., 2013) Furthermore, the relationship between raw ingredients, processing conditions and resulting microstructure in porous matter is complex and still not fully understood. Nevertheless, it is vital to develop techniques and methodologies which clarify such a relationship for the design of novel products with tuned properties (Lazidis et al., 2017).

Investigating the microstructure of soft porous matter is a challenging task, as these materials are usually optically opaque, prone to deformation and often subject to melting at room temperatures (Ubbink et al., 2008; Murray et al., 2011). Standard optical microscopy is a readily available and commonplace technique for characterization of materials; however, sample preparation is intrusive, as it requires the sample to be placed between two glass covers, which can affect significantly the native structure of the specimen (Metilli et al., 2020) and consequently, the measured bubble size and shape distribution. Furthermore, most microscopy techniques provide only 2D, surface information on the sample microstructure, limiting the accuracy of the measurement. Even confocal microscopy, which can probe the sample along the z-axis, suffers from a limited field of view and accessible depth range, which hinders the collection of statistically significant 3D data of macroscopic samples.

X-ray computed tomography (XCT) has been increasingly used to analyse the microstructure of soft and porous materials, owing to its non-invasive and non-destructive approach (Barigou & Douaire, 2013). Soft biological matter is usually weakly absorbing with respect to X-rays, and hence a contrast agent may be added during sample preparation to stain the continuous phase. Contrast agents such as sodium iodide (NaI) increase the absorption of X-rays, which improves the contrast of different phases during acquisition. However, the addition of the contrast agent might cause either excessive absorption of X-rays by the sample, or alter its properties prior to imaging. The image contrast can also be enhanced using phase-contrast imaging (PCI), which measures the X-ray refractivity in the sample, rather than the attenuation (Wang et al., 2018). Benchtop XCT instruments are becoming increasing accessible; however, they require lengthy acquisition times, which make this technique unsuitable for temperature sensitive (*e.g.*, low melting point) or delicate samples, as prolonged beam exposure can cause heating, X-ray radiation damage and deformation in the microstructure due to sample movement (Wang et al., 2018). Synchrotron radiation XCT (SR-XCT), on the other hand, provides high flux X-ray sources with short exposure times and high signal-to-noise ratio, reducing significantly the length of the experiment, as well as sub-micron voxel resolution. Customizable sample environments, such as temperature and humidity control, and application of shear on the sample allow dynamic microstructural investigation of specimens when subject to external stimuli (Rau et al., 2017).

Bread dough can be considered a model soft porous material of great industrial relevance, in which the microstructure is intimately linked to its rheology and ultimately taste perception (Jekle & Becker, 2011). Wheat flour dough displays relatively high viscosity, no creaming of air bubbles and good tolerance to X-ray exposure, without requiring carefully designed imaging protocols. Early work reported by Babin and colleagues demonstrated the efficacy of synchrotron XCT in characterizing the microstructure of bread dough during its processing steps (*i.e.* proofing and baking) with a spatial resolution of 15 µm (Babin et al., 2006). Owing to the ability to track individual bubbles in the sample, the authors were able to model the growth of gas cells developing in the dough, as well as their coalescence during proofing. The spatial resolution of the instruments was a critical parameter in the detection of smaller air bubbles, as reported by more recent

publications by Trinh et al. (2013) and Koksel et al. (2016). Here the smaller voxel size (*ca.* 10 and 8.75 µm, respectively) of the instrument resulted in a ten-fold increase in the bubble density detected in dough samples compared with previous works; this enabled a more accurate description of the gas phase evolution during dough mixing (Trinh et al., 2013) and of the time-dependent bubble disproportionation in non-yeasted samples (Koksel et al., 2016). Sample density calculated from gravimetric methods is routinely used to validate XCT results in these works (Campbell et al., 2001).

In the case of soft porous materials with higher susceptibility to shear and melting, additional steps are required during sample preparation and characterization. Ice cream is a complex multiphasic porous material made of a dispersed gas phase, ice crystals, and a continuous aqueous phase. The complex interplay between its ingredients and phases – which is still not fully understood – is crucial in ensuring high quality products and for the design of novel ice cream formulations (Bahram-Parvar, 2015). Over the last decade, XCT has been increasingly used to characterize ice cream. Pinzer et al. (2012) used a benchtop XCT scanner to investigate the microstructure of ice cream and its evolution upon thermal cycling. The instrument had a nominal 6 µm voxel resolution, and sodium iodide was added to the ice cream recipe to enhance contrast between the air and the ice crystals. To successfully segment the three main phases from the tomography images, the authors developed an edge-preserving smoothing filter, based on the anisotropic diffusion algorithm. The segmentation was then validated using the calculated ice fraction of the sample from differential scanning calorimetry measurements.

A similar method was applied more recently on frozen sorbets by Masselot et al. (2021), using a 3D-printed cold stage to keep a low sample temperature during the measurements. The voxel resolution of the scanner used was 9 microns. This study focused mostly on measuring the size distribution of the air bubbles and the ice crystals; CryoSEM was used to validate the XCT measurements and the two techniques showed values of the same order of magnitude and similar range. In both this work and that of Pinzer et al. (2012), however, the scanning time for one sample was between 10 and 15 minutes, which might not be suitable for other types of soft porous materials that are particularly susceptible to X-ray damage. Furthermore, the authors

acknowledged that, due to low spatial resolution, air bubbles smaller than 20 – 15 microns were not measured.

These limitations were overcome by the use of a synchrotron source, as presented by Guo and co-workers in a series of recent publications (Guo et al., 2017; Guo et al., 2018; Mo et al., 2018). Here the authors focused on the characterization of ice cream microstructure using SR-XCT, with a nominal voxel resolution of 0.8 µm and fast acquisition times (in the order of minutes). The sample was initially maintained at low temperatures (- 15°C). To improve further the segmentation of the different phases in ice cream – air, ice crystals and unfrozen matrix – a novel computational approach was developed to reduce noise and improve intensity homogeneity in the different phases. The effects of thermal cycling on individual air cells and ice crystals and on the unfrozen matrix were investigated using a bespoke temperature-controlled stage and short acquisition times for tomography scans (~ 2.5 minutes each). Nevertheless, there are still destabilization mechanisms in soft matter that occur on shorter time scales than minutes (*i.e.,* seconds or milliseconds), such as droplet or bubble coalescence, Ostwald ripening or disproportionation, or liquid film rupturing, which require suitable time-resolved techniques to be captured and investigated.

Despite these recent advances in the use of SR-XCT in soft porous materials, at present many relevant materials are still missing a suitable three-dimensional, close-to-native state methodology for the characterization of their microstructure and its dynamics of destabilisation. Moreover, in light of the current trends of products reformulation with more sustainable and biocompatible ingredients, soft material characterization is of paramount importance (Cornwell, 2018; Manzocco et al., 2021; McClements, 2020). Personal care products such as shampoos, which are surfactant-stabilized aqueous foams, owe their consumer appeal to their foamability and foam stability (Luengo et al., 2021); yet a description of their aerated microstructure is currently lacking. Similarly, the fire suppression dynamics of firefighting foams are highly correlated with their bubble size distribution and coarsening, which would benefit from a suitable 3D characterization (Kennedy et al., 2015). Low-viscosity samples prone to movement may benefit from the use of ultra-fast tomography techniques, which enable total acquisition times close to the second (Dittmann et al., 2016).

Recently, air-in-oil systems have received significant attention due to their untapped potential in the field of low-fat food products, oil-based cosmetics and pharmaceutical delivery systems (Heymans et al., 2017; Fameau & Binks, 2021). Air-in-oil systems, also called oleofoams, consist of a continuous liquid oil phase in which gas bubbles are stabilized by fat crystals. These materials exhibit a melting range close to body temperature, they deform under small levels of shear and are subject to destabilization mechanisms such as oil drainage and bubble coalescence (Heymans et al., 2018; Saha et al., 2020; Truong et al., 2019). For these reasons the analysis of their microstructure is very challenging. While several studies have focused on the relationship between crystal properties and resulting microstructure, the characterization of these materials is usually carried out using optical or confocal microscopy. Up to the present, the native, three-dimensional arrangement of the air bubbles in oleofoams has not been investigated due to the lack of suitable techniques and methods to obtain meaningful parameters describing the microstructure.

In this paper, a novel methodology is proposed, which aims at investigating the microstructure of delicate soft porous matter in a non-invasive fashion (*i.e.,* without the use of contrast agents), with a straightforward cryogenic procedure to prevent deformation in the sample caused by melting, stage rotation or beam damage. The method was demonstrated using cocoa butter-based oleofoams recently characterized in a previous publication (Metilli et al., 2021). The effect of temperature on the microstructure of the specimens was studied using SR-XCT and X-ray Radiography (SR-XRR), to track fast dynamic changes in the sample during heating or cooling. The methodology presented in this work enables the extraction of several microstructure descriptors, including the air volume fraction and its distribution within the sample, the size and shape distribution of the gas phase and the thickness of the continuous phase. Furthermore, SR-XRR was also used to dynamically monitor changes in the air phase heating of samples. While this method was demonstrated with edible oleofoams, it is applicable to the analysis of similar types of sensitive, soft porous materials.

5.2 Materials and Methods

5.2.1 Sample preparation

The oleofoams investigated in this paper have been described and characterized in a previous publication (Metilli et al., 2021). Briefly, mixtures of cocoa butter (CB) and high oleic sunflower oil in different weight ratios were crystallized under shear in a lab-scale vessel to obtain an oleogel. For this work the samples were obtained using two crystallization conditions: (1) samples containing 15% w/w CB and crystallized at a -0.10 °C/min nominal cooling rate (sample named "15S") and (2) samples containing 30% w/w CB and crystallized at -0.75 °C/min (sample named "30F"). The oleogel was then aerated using a kitchen mixer in cycles of 5 minutes whipping and 10 minutes resting, for a total whipping time of 30 minutes. The whipping temperature was monitored during aeration and increased between 7 °C and 20 °C. In order to measure the air incorporation, during the rest step the sample was weighed in triplicates using a cup of fixed volume (30 mL). To ensure proper filling of the cup, the sample was added stepwise and set through percussion of the cup. The oleofoam overrun (related to air incorporation) was calculated using Equation 5.1:

$$Overrun\ (\%) = \frac{(w_{oleogel} - w_{oleofoam})}{w_{oleofoam}} \times 100 \qquad \text{Eq. 5.1}$$

where $w_{oleogel}$ and $w_{oleofoam}$ are the weight of the un-whipped oleogel and the weight of the oleofoam, respectively. To calculate the overrun from the tomography data, the following equation was used (Equation 5.2):

$$Overrun\ (\%) = \frac{\varphi_{air}}{1 - \varphi_{air}} \times 100 \qquad \text{Eq. 5.2}$$

where ϕ_{air} is the air volume fraction of the measured Volume of Interest (VOI) of each sample. The relationship between Equation 5.1 and Equation 5.2 is explained in the Supporting Information (Appendix B). In this work, both oleofoam samples 15S and 30F were analysed with X-ray Tomography after 5 minutes of aeration and at the end of the aeration step. The overrun measured with the cup method was compared with the overrun calculated from the X-ray Tomography data. To verify any statistically significant difference

between the two datasets, a t-test with a *p*-value of 0.05 was performed. The analysis was carried out on two repetitions.

5.2.2 Beamline setup

The experiments were carried out at beamline I13-2, Diamond Light Source (Didcot, UK), using a pink beam source with a mean energy of 27 keV ($\sigma_E = 5\ keV$).The 2D projections for tomography and radiography were acquired with a PCO edge 5.5 CMOS camera (2560 x 2160 pixels). The total optical magnification was set to 8x, with an effective pixel size of 0.8125 µm. A small amount (*ca.* 1 mm^3) of oleofoam sample was then gently mounted on the top of a cut toothpick, minimizing deformation prior to the analysis. The toothpick was then glued to a cryocap, and mounted on the tomography stage. A cryo-jet (Cryojet XL, Oxford Instruments, UK) was installed to allow cooling and heating of samples on the beamline. A schematic of the experimental setup is provided in Figure 5.1

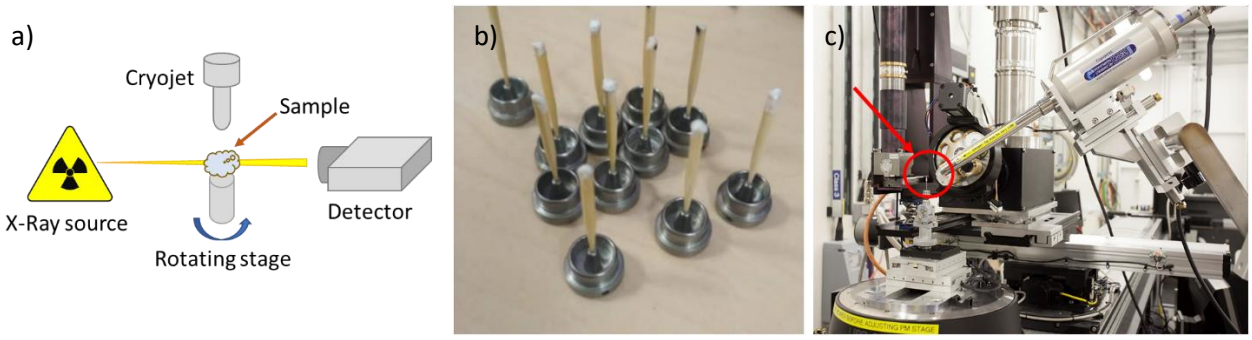

Figure 5.1. Schematic of the tomography setup (a), oleofoam samples on cut toothpicks (b) and sample mounted on the rotational stage with the Cryojet temperature control.

Two experimental protocols were tested: in the first, samples were mounted on the rotational stage and imaged directly at room temperature without temperature control, with an exposure time of 10 ms and for a total acquisition time of 20 seconds. The second protocol involved flash-freezing samples by immersion in liquid nitrogen (-196 °C) prior to imaging and controlling their temperature during scanning using a cryogenic nitrogen jet (Figure 5.1c). The Cryojet temperature was set to -40°C, which enabled sample handling without the need of using cryogenic gloves. The exposure time for each X-ray projection was set to 100 ms, for a total acquisition time of 5 minutes. For both experimental protocols, the number of projections was set to 1001,

from an optimization range between 2000 and 500, while the optimal propagation distance was empirically determined and found to be 80 mm.

5.2.3 Synchrotron X-ray Radiography of heated samples

Selected oleofoam samples were subjected to controlled heating using the Cryojet. The evolution of their microstructure was monitored using SR-XRR. The temperature profile was set as follows: equilibration at 293 K for 1 min, heating from 293 K to 300 K at 1 K/min, hold at 300 K for 5 minutes, and finally cooling from 300 K to 273 K at -6 K/min. The samples were imaged with X-ray Tomography before and after the thermal treatment. Around 1500 2D radiographies of the oleofoam samples were collected during the heating profile, with the aim of tracking dynamic changes in the microstructure due to temperature. The frames were collected every 0.677 seconds. The radiography images were normalized with respect to the camera *background* (dark field images) and the beam intensity distribution (flat field images), according to Equation 5.3:

$$I_{norm} = \frac{I_{raw} - I_{dark}}{I_{flat} - I_{dark}} \qquad \text{Eq. 5.3}$$

where I_{norm} is the normalized pixel intensity of the image, I_{raw} is the pixel intensity of the sample image (projection) and I_{dark} and I_{flat} are averaged pixel intensities of 20 dark field and 20 flat field images, respectively. Due to the superimposition of bubbles in the 2D projection, a stack of difference images was produced by subtracting the pixel values between the *i*-th and the *i+1*-th frame, in order to visualize changes in the microstructure. The outline of the bubbles in the difference images was detected using the Image Processing Toolbox in MATLAB (Mathworks, USA), and the equivalent diameter and circularity of 10 bubbles was measured and compared with the 3D data obtained from X-ray Tomography.

To quantify the extent of microstructural changes in the sample during thermal treatment, the difference image stack was further analysed with Principal Component Analysis (PCA) in MATLAB (Mathworks, USA), using the *pca* function. The choice of PCA was justified due its ability to reduce redundancy in large datasets,

and to detect changes in image sequences in an unsupervised fashion (Hussain et al., 2013; Celik, 2009), as bubble segmentation from the 2D difference images proved challenging to automate for analysis.

5.2.4 Reconstruction and Image post-processing

The 2D projections were reconstructed into a tomography volume using the Savu processing pipeline (Wadeson & Basham, 2016) using the gridrec algorithm in TomoPy (Gürsoy et al., 2014). The reconstruction pipeline included the following steps: image normalization using dark and flat field images, correction of the ring artefacts (Vo et al., 2018) and a Paganin filter, which is used to restore the phase information generated by the inline phase contrast (Paganin et al., 2002). Finally, the reconstructed volume was obtained using the *Gridrec* reconstruction algorithm in the TomoPy software package (Dowd et al., 1999).

Image post-processing was applied to the reconstructed tomography volumes to obtain quantitative parameters describing the air phase and the continuous phase of oleofoams. To facilitate the computation burden, each tomography volume was divided into a number of Volumes of Interest (VOI) of approximately 500x500x500 μm^3. A minimum of 5 randomly selected VOI were analysed and averaged for each sample. The stack of tomographic slices were processed using ImageJ 1.53 (National Institute of Health, USA) according to the following workflow: 3D median filtering, Otsu thresholding, 3D-Euclidean Distance Map Watershed (Legland et al., 2016).

The air cells were counted and measured using the BoneJ plugin for ImageJ (Doube et al., 2010) and excluding the objects on the edges of the VOI. For each air bubble, the volume (V) and surface area (A) were obtained. The volume V is defined as the number of voxels in the tomogram occupied by the bubble, whereas the surface area A represents the number of voxels on the surface of the bubble. The volume and surface areas were then used to compute the equivalent diameter (D_{eq}) and the sphericity (Φ) of each air cell, according to the following equations (Eq. 5.4 and Eq. 5.5)

$$D_{eq} = \sqrt[3]{\frac{6V}{\pi}} \qquad \text{Eq. 5.4}$$

$$\Phi = \frac{\pi^{\frac{1}{3}}(6V)^{\frac{2}{3}}}{A} \qquad \text{Eq. 5.5}$$

D_{eq} was used to calculate the volume-weighted diameter (D[4,3]) of the air cells for a specific sample, using Eq. 5.6

$$D[4,3] = \frac{\sum_{i=1}^{N} D_{eq} i^4}{\sum_{i=1}^{N} D_{eq} i^3} \qquad \text{Eq. 5.6}$$

Moreover, the BoneJ plugin measured the major, intermediate and minor axis (a ≥ b ≥ c, respectively) of each air bubble, which were used to calculate two aspect ratios: the Elongation Index (EI = b/a) and the Flat Index (FI = c/b). By plotting EI against FI, four shape classes were described: spheroids, oblate, prolate and blade (Blott & Pye, 2008; Zhao & Wang, 2016), and the number of air bubbles belonging to each shape class counted. Finally, BoneJ was also used to calculate the air volume fraction and overrun of each VOI, according to Eq. 2. The thickness of the oleogel phase (*i.e.* the continuous phase) was also calculated using the same plugin, following the method described by Hildebrand & Rüegsegger (1997). The algorithm works by inscribing spheres of maximal volume into the continuous phase structure and assigning each voxel the diameter of the largest sphere it belongs to (Pinzer et al., 2012). In this publication, the distribution of the assigned voxels for each sample is represented, alongside with the volume-weighted average thickness value.

5.3 Results and Discussion

5.3.1 Comparison of different imaging techniques

A comparison of different microscopy techniques for investigating the microstructure of oleofoams is presented in Figure 5.2, using a 30F oleofoam as a sample.

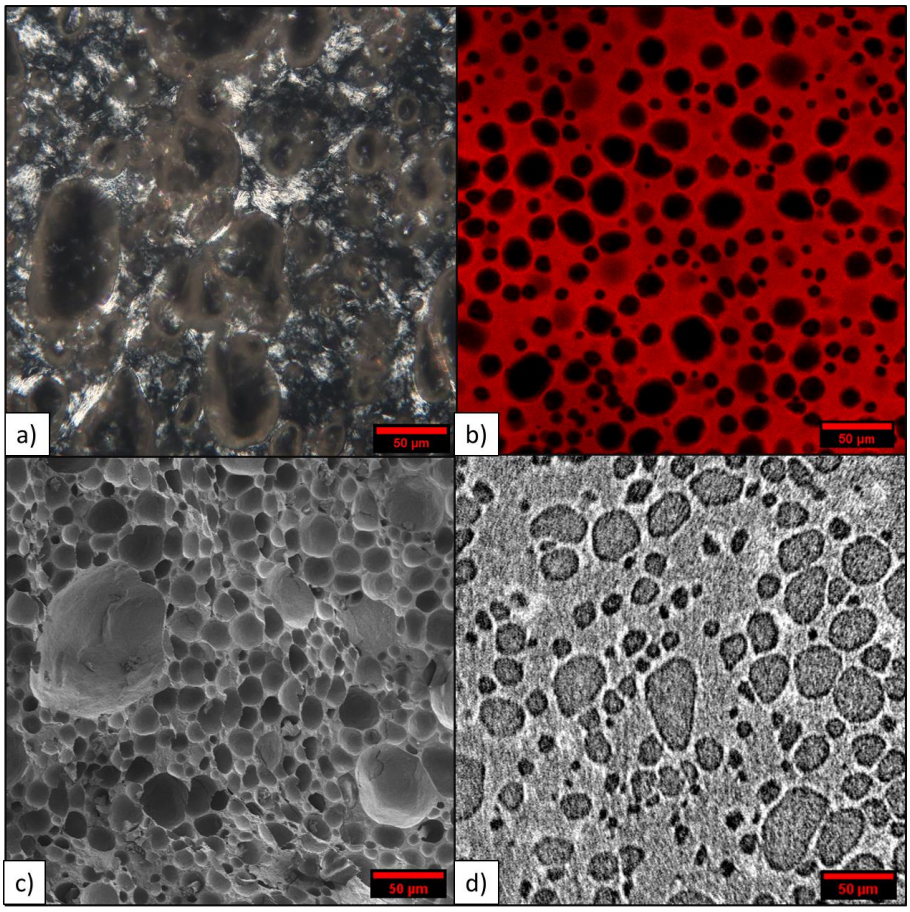

Figure 5.2. Comparison of microscopy techniques for the characterization of the microstructure of oleofoams. Polarized light microscopy (a) confocal microscopy (b), CryoSEM (c) and one 2D slice taken from XCT (d). Figure (a) and (c) are adapted from Metilli et al. (2021).

Polarized light microscopy (PLM) (Figure 5.2a) images enabled visualization the air bubbles and the birefringent fat crystals, which were found to stabilize the air-oil interface in oleofoams (Metilli et al., 2021). The fat crystals were clearly visible in the continuous phase and bridging neighbouring bubbles. Non-spherical air cells were detected, with diameters between 10 and 100 µm. However, estimating a size distribution of the air bubbles with this method was challenging, as air bubbles were subject to severe deformation and coalescence during sample preparation. Confocal microscopy images (Figure 5.2b) provided better-resolved air bubbles, which also appeared non-spherical. Information on the fat crystals was not available, as the fluorescent dye stained both the oil and the fat crystals. Despite the ability of CSLM to provide stacks of images in the z direction, lengthy acquisition times and a smaller field of view (FoV) compared with tomography constituted a hindrance for measuring the bubbles' size and morphology, as the microscopy images might not be representative of the whole 3D sample. Micrographs collected with CryoSEM (Figure

5.2c) show a freshly cut surface from the bulk of the oleofoam, which is not accessible with other microscopy techniques. The higher resolution of this technique and the cryogenic conditions made it possible to visualize the porous microstructure closer to its native state. Similarly to CSLM, the field of view of CryoSEM is limited compared with tomography techniques, and the sample preparation is also lengthier, not to mention the introduction of artefacts while imaging soft materials (Groves & Parker, 2013). Figure 5.2d shows a 2D tomography slice of an oleofoam sample, where the air bubbles appeared darker compared to the continuous oil phase. Clusters of brighter pixels were visible and, by comparison with Figure 5.2a, this suggested that XCT could locate the presence of fat crystals in oleofoams. However, further experiments with higher spatial resolution and improved contrast are required to confirm this hypothesis.

5.3.2 Comparison of different imaging protocols for SR-XCT

The first imaging protocol – room temperature, 10 ms exposure time, for a 20 seconds total acquisition time – resulted in an acceptable tomogram, with most of the air bubbles having a defined boundary (Figure B1, Appendix B). However, significant deformation on the edge of the sample occurred during stage rotation, as highlighted with red circles in Figure B1. In some instances, the deformation was excessive and prevented the reconstruction and the analysis of the 3D sample microstructure. Longer exposure times resulted in sample melting, again preventing reconstruction. Considering that CB oleofoams display a melting point between 25 and 27°C (Metilli et al., 2021), enhanced stabilization by cooling and controlling the sample temperature was sought to improve tomography acquisition procedure and the quality of the images.

Figure 5.3 shows a tomography slice of an oleofoam sample (15S) acquired using the second imaging protocol, *i.e.,* sample cooling with liquid nitrogen, temperature control with the Cryojet and 100 ms exposure time.

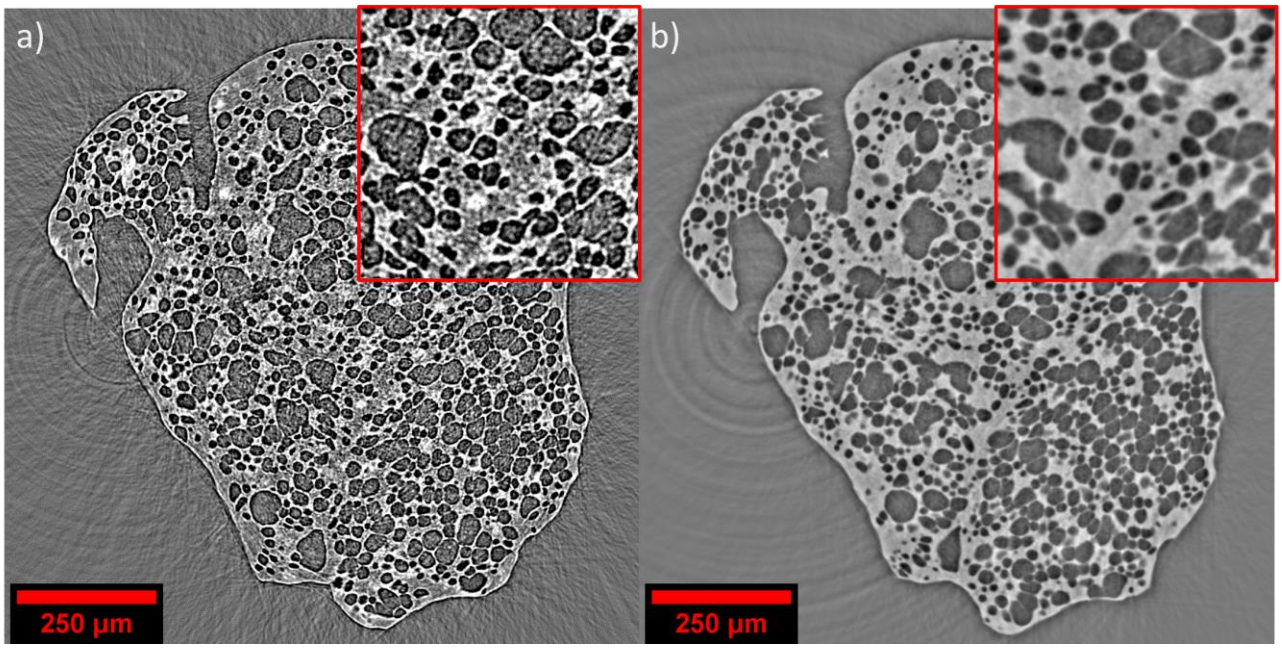

Figure 5.3 Tomography slice of a 15S oleofoam sample obtained with the second acquisition protocol (sample cooled with liquid nitrogen, maintained at -40°C and using 100 ms exposure time), reconstructed displaying the attenuation contrast (a). Same sample, displaying the phase-contrast mode (b). Zoomed areas showing crystal aggregates are displayed in the top right part of the image.

Because of the temperature control during the measurements and the cooling with liquid nitrogen applied to the samples prior the experiment, no deformation was detected in the reconstructed tomogram. To further improve the quality of the images, the phase-contrast mode, which is commonly used for weakly absorbing specimen in XCT, was applied during reconstruction (Nielsen et al., 2016; Guo et al., 2017; Wang et al., 2018). The Paganin-filtered image is shown in Figure 5.3b, displaying a more homogeneous pixel intensity across the image compared with the attenuation-contrast mode (Figure 5.3a). The phase imaging mode also resulted in a smoother contour for the brighter crystal aggregates visible in Figure 5.3a (insert, top right), leading to their pixel intensity being similar to the continuous phase and thus not distinguishable in the reconstructed image. Hence, the improved signal-to-noise ratio induced by the Paganin filter was beneficial for the characterization of the porous microstructure of the samples.

5.3.3 ImageJ Post-Processing

On closer inspection of Figure 5.4a, it can be seen that bright pixels were present inside air cells – especially larger ones – which was mostly caused by ring artefacts in the tomography reconstruction. Hence, a segmentation of the air phase based on the greyscale value alone was not feasible.

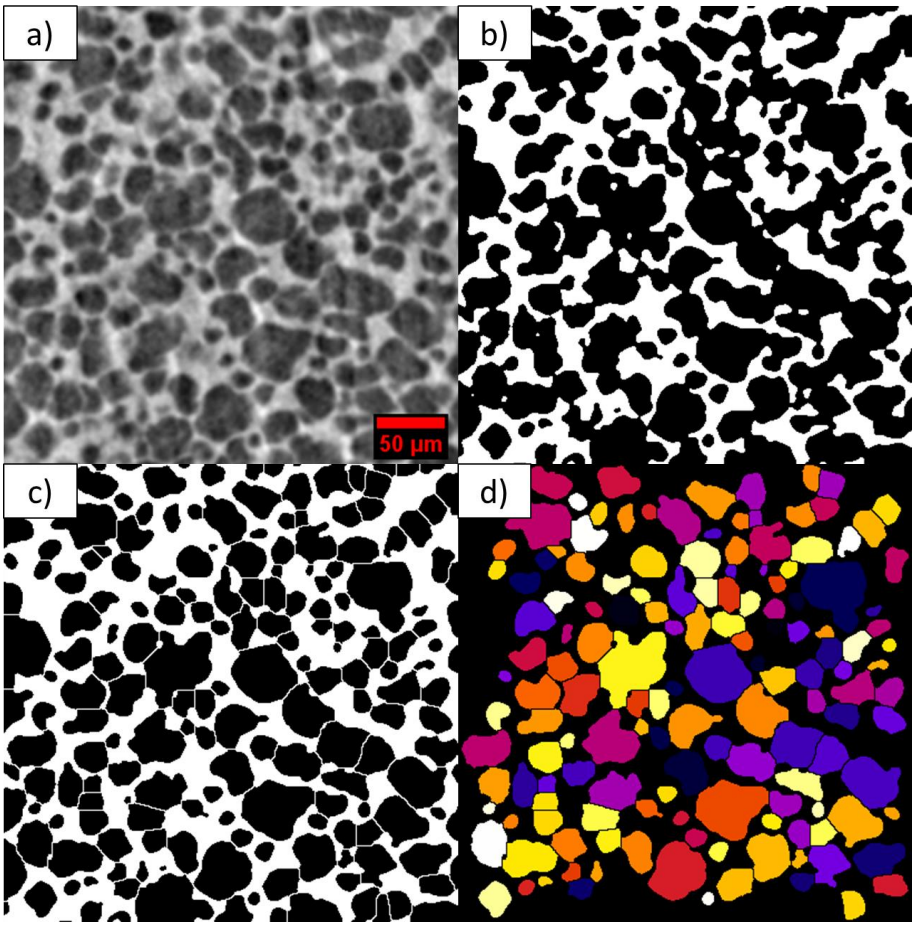

Figure 5.4. Image post-processing workflow developed in this methodology using ImageJ 1.53. Original reconstructed slice (a), binarized using Otsu threshold method (b), segmented with 3D Euclidean distance map watershed (c) and objects counted with the "Analyze Particles" function in BoneJ (d).

Therefore, an image post-processing workflow was then applied to enhance the quality of the images to separate the air bubbles from the continuous phase. Application of 3D median filter and thresholding resulted in a binarized image with several bubbles appearing connected (Figure 5.4b). The thresholding method chosen was based on the Otsu algorithm, which returns for each image a threshold value that maximizes inter-class variance; in other words, it divides the pixels into two classes, background and foreground (Russ, 2015). The validity of the method was assessed by visually comparing the thresholded images with the starting greyscale analogues. The watershed function based on the Euclidean Distance Map was then successfully applied to separate the connected air cells (Figure 5.4c). The counted objects in the slice are displayed in Figure 5.4d, which excluded air cells partially on the edge of the VOI, to avoid underestimation of the bubble size distribution. Recently, the use of machine learning-driven segmentation

for image analysis has become popular, and may be considered a promising alternative to more traditional workflows. However, it does require a set of synthetic images to train the algorithm, which implies prior knowledge of the sample microstructure (Ali et al., 2021).

5.3.4 Estimation of sample density

Tomography data were used to calculate the samples' bulk density and the values estimated were compared with the overrun values measured using the cup method described in the methodology section. Two oleofoam samples, 15S and 30F, were analysed after 5 minutes of aeration (Figure 5.5a and Figure 5.5c), and after 30 minutes of aeration (Figure 5.5b and Figure 5.5d). Table 5.1 contains the overrun of four individual VOI and its average, compared with the overrun measured experimentally.

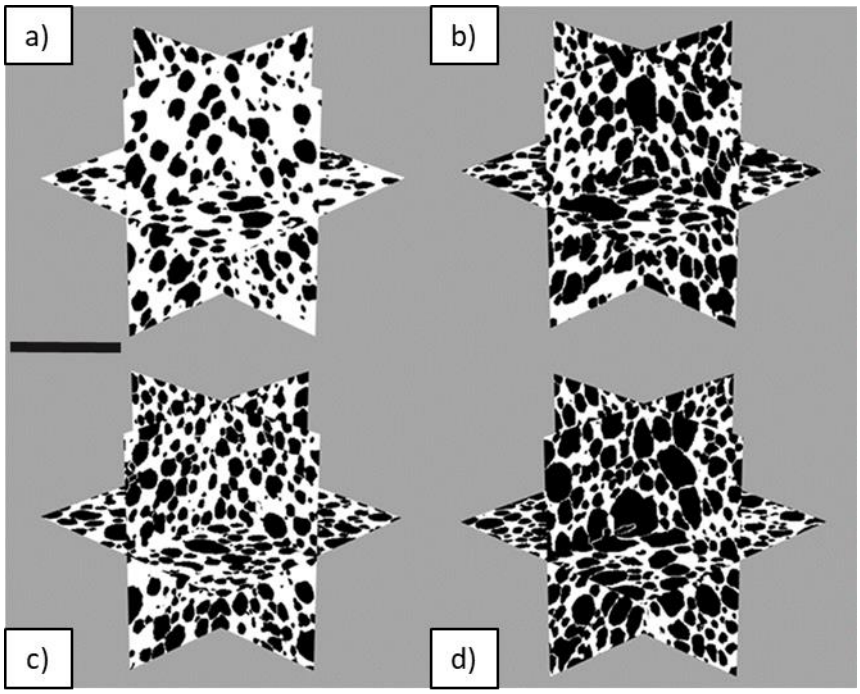

Figure 5.5. Orthogonal projections of selected VOI, obtained from ImageJ 3D viewer plugin, of samples 15S 5Min (a), 15S 30Min (b), 30F 5Min (c) and 30F 30Min (d). Scale bar represents 250 µm.

	15S 5 Minutes		15S 30 Minutes	
	Sample 1	Sample 2	Sample 1	Sample 2
VOI 1	76.3	87.1	131.3	137.1
VOI 2	78.8	139.0	119.9	146.3
		128		

VOI 3	71.0	95.5	109.2	185.7
VOI 4	70.9	115.9	138.0	216.8
OR % XCT	**73.7 ± 3.4[a]**	**118.7 ± 24.0[a]**	**125.9 ± 15.7[a]**	**171.2 ± 26.0[a]**
OR % Cup	76.3 ± 2.7[a]	75.0 ± 11.5[b]	183.7 ± 11.8[b]	196.7 ± 10.2[a]
	30F 5 Minutes		30F 30 Minutes	
	Sample 1	Sample 2	Sample 1	Sample 2
VOI 1	92.0	62.4	139.8	85.2
VOI 2	88.6	72.5	128.1	194.1
VOI 3	89.7	54.7	134.1	163.2
VOI 4	90.8	75.2	127.6	204.9
OR % XCT	**89.7 ± 1.9[a]**	**61.2 ± 11.3[a]**	**135.4 ± 6.6[a]**	**125.8 ± 31.9[a]**
OR % Cup	68.1 ± 19.4[b]	70.8 ± 6.4[a]	170.5 ± 17.3[b]	133.5 ± 16.2[a]

Table 5.1. Calculated overrun from SR-XCT data for individual VOI from selected oleofoam samples, their average and the respective overrun measured with the cup method. Values in the same column labelled with different letters have a statistically significant difference (p = 0.05).

The comparison of overrun estimation with the two different methods did not present a clear trend between the two techniques, for both 15S and 30F oleofoams, after 5 minutes of aeration. While for some samples the overrun measured with the cup method and SR-XCT were in agreement, in other repeats SR-XCT overestimated the overrun by 60% or 20% (see Table 5.1, 15S 5 minutes sample 2 and 30F 5 minutes sample 1). After 30 minutes of aeration, on the other hand, there was a consistent overestimation by the cup method of the overrun calculated by SR-XCT, for all samples. In particular, for sample 15S the overestimation was between 15% and 43%, whereas for sample 30F was between 6% and 26%. The differences in estimated density with the two techniques were most likely due to the difference in volume being analysed, 30 mL for the cup method and few cubic millimetres with SR-XCT. The overestimation by the cup method suggested the presence of larger voids in the sample, which might result from filling the cup during weighing, or being already present in the specimen, but remaining undetected by SR-XCT. Similarly, the presence of air bubbles

of comparable size with the VOI resulted in overrun values with large standard deviation in several samples (Figure B2 in Appendix B).

However, SR-XCT provides information on the distribution of the air bubbles and the homogeneity of overrun within samples that are not detectable with the cup measurement. From the observation of the different VOIs measured for each sample it is clear that sample 30F displayed, on average, more overrun homogeneity (smaller standard deviation) compared with sample 15S (larger standard deviation).

Density validation of XCT in bread dough research showed better agreement with gravimetric methods (Trinh et al., 2013; Koksel et al., 2016); however, it should be noted that the sampled XCT volume was in the magnitude of centimetres cube (as opposed to few millimetre cubes of this work) and that the method for measuring dough density involves fluid displacement (Campbell et al., 2001), which is may not be applicable to highly porous materials such as oleofoams. In other research fields, such as artificial bone scaffolds, cake filters and steel pipes corrosion, the density of porous matter measured by XCT is routinely validated by gas pycnometry or mercury injection porosimetry (Jones et al., 2007; Feng et al., 2020; Wang et al., 2021). However, these techniques are destructive and might not be suitable for soft materials that do not possess a continuous pore network. The authors reported that differences in estimated density between porosimetry and XCT are affected by the resolution of the tomographic scanner, and by the choice of thresholding method. The air bubbles in oleofoams, in particular, usually cover the range between 10 and 100 µm in diameter (Fameau & Saint-Jalmes, 2020; Heymans et al., 2017), hence are likely to be detected by the current SR-XCT setup.

The effect of thresholding on the resulting overrun for oleofoams samples was also explored. The Huang and Wang (Huang & Wang, 1995) and Renyi's Entropy (Sahoo et al., 1997) methods were tested on sample 15S after 30 minutes of aeration, and compared with the default Otsu method used in this work (Table 5.1). The image segmentation and calculated overrun were similar between the Huang and Wang, and Otsu methods (134.7 ± 7.2 % vs. 152.3 ± 6.7), whereas the Renyi's Entropy produced binary images with excessive void

compared with the greyscale 2D image, and very high overrun values (241.5 ± 33.2) (see Appendix B, Table B1 and Figure B3). Therefore, the Otsu method was found to be the most reliable of the ones tested.

While the increase in overrun between 5 and 30 minutes of aeration was observed by both SR-XCT and the gravimetric method (*i.e.,* the cup method), the latter technique provides a more reliable bulk density measurement due to the larger volume analysed. Nevertheless, SR-XCT provided essential information about the degree of aeration homogeneity in at the microscale, which directly affects the stability of the product during storage (Heymans et al., 2017; Fameau & Saint-Jalmes, 2020).

5.3.5 Effect of heating on oleofoam microstructure quantified by SR-XCT

After the image pre- and post-processing, SR-XCT data were used to estimate quantitative information about the air phase in oleofoams. Two samples with significantly different microstructure were analysed and compared. The first sample, 30F Fresh, was collected from the vessel after 30 minutes of aeration and imaged at -40°C with SR-XCT. The second sample, 30F Heated, was collected from the same batch of sample 30F Fresh, but was subjected to controlled heating, and then imaged with SR-XCT. The microstructure of the two samples is presented in Figure 5.6, as reconstructed tomographic slices.

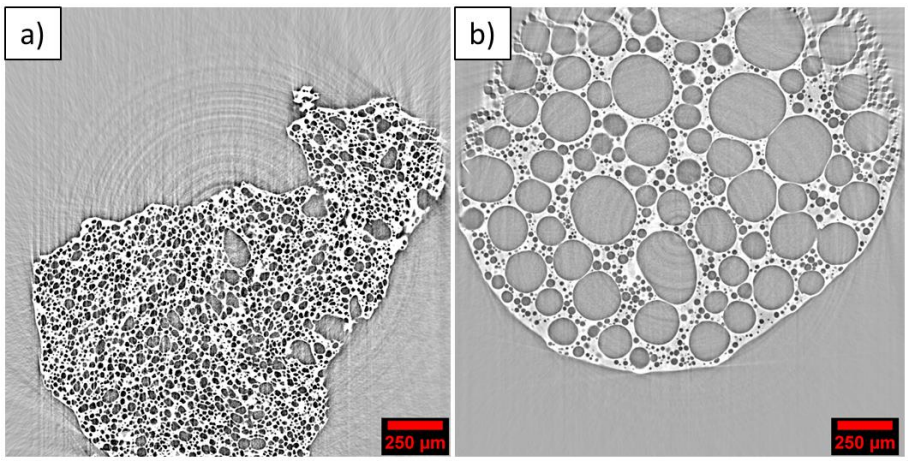

Figure 5.6. Tomographic slices of a fresh 30F oleofoam sample (a) and a 30F Heated sample (b), obtained after holding the sample at 300K (27°C) for 5 minutes.

The fresh sample (Figure 5.6a) contained mostly non-spherical small bubbles (average diameter < 50 µm), with few larger ones (diameter *ca.* 100 µm). The air phase was distributed homogeneously in the continuous oleogel phase, with domains containing both bubbles and a thin layer of oleogel in between. The heated

sample (Figure 5.6b), on the other hand, presented fewer larger and rounder air bubbles, with diameters exceeding 300 µm, along with a population of smaller bubbles (average diameter < 50 µm). The oleogel phase comprised either very thin layers separating large bubbles, or areas where bubbles were not present at all. The effect of heating on the microstructure of oleofoams was monitored with XRR, where 2D projections of the sample from the side were collected during the temperature ramp.

The evolution of the microstructure of sample 30F Fresh to 30F Heated is shown in Figure 5.7.

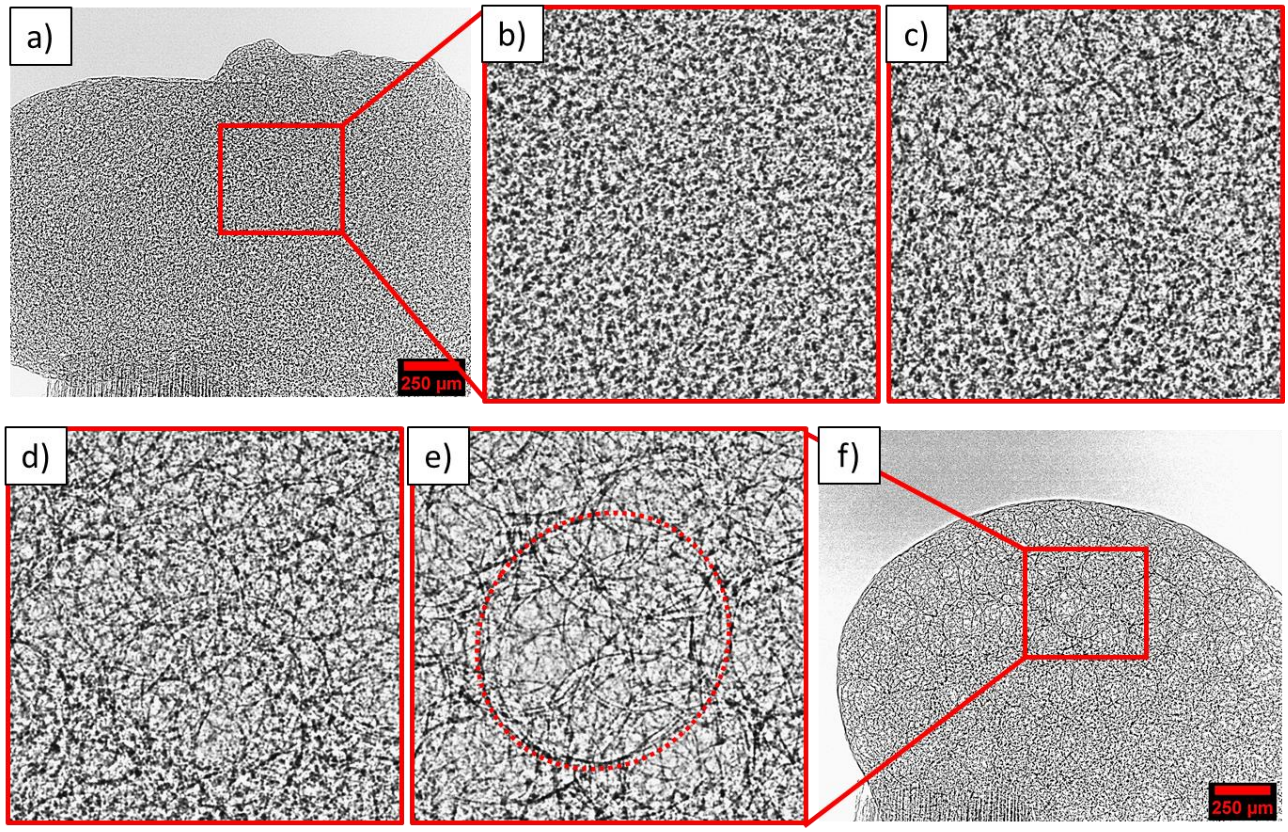

Figure 5.7. XRR images of the 30F fresh oleofoam before heating (a) and at the end of the temperature ramp (f). Magnifications (b) to (e) highlight the occurrence of a large air bubble during heating. Frame b) was taken after 7.21 minutes, c) after 8.29 minutes, d) after 8.45 minutes and e) after 12.37 minutes.

By inspecting Figure 5.7a, the porous microstructure of the sample was not straightforward to resolve, as multiple layers of air bubbles were overlaid in the 2D projections due to the large field of view. However, with increasing temperature (from Figure 5.7b to Figure 5.7e) larger bubbles, approximately 300 µm in diameter, appeared, as a result of the heating step. Moreover, by comparison of Figure 5.7a and Figure 5.7f, it can be noticed that the whole sample partially collapsed to a rounder structure, owing to the partial melting

of the fat network in the continuous phase, as well as the rearrangement of the air bubbles driven by the surface tension forces at the air-oil interface. In order to highlight the changes in the microstructure during heating, a stack of difference images was calculated from the stack of radiography frames by subtracting the pixel values of the *i*-th frame from the pixel values of the *i+1*-th frame. An example of processed image can be found in Figure B4 (Appendix B), as well as the time-lapse sequence of the difference images (Figure B5, Appendix B). From these images, it can be seen that the air bubbles were subject first to a rapid expansion (between one frame and the following, hence with a speed equal or faster to 0.667 seconds), followed by a slower expansion that lasted over several frames (hence seconds). In particular, the coalescence of two neighbouring air bubbles was captured during the experiment, showing that the newly-formed bubble relaxed "slowly" (*i.e.* over a few seconds in the following frames) to a slightly more spherical shape. Analysis of ten difference images containing the contours of different air bubbles revealed that, during heating, bubbles with an average equivalent diameter of 140.2 ± 35.2 μm and an average circularity of 0.94 ± 0.02 appeared in the oleofoam microstructure. The values are clearly an estimate, as some larger bubbles did not display a complete contour in the difference image to allow precise measurements of their size and shape, and smaller bubbles did not exhibit enough contrast to be detected. To further characterize the effects of heating on the sample, a principal component analysis (PCA) was performed on the stack of the difference images collected during the heating profile. the first principal component (PC) score was plotted against time and the temperature profile during heating (Figure B6, Appendix B).

The PC score, which describes the changes in the pixel distribution in the stack of difference images, remained constant during most of heating ramp. A large variation in the PC score was observed in correspondence with the sample reaching 300 K (27 °C), which corresponded to the melting temperature of sample 30F. This variation reflected the occurrence of large air bubbles while the crystals melted, as the air phase was subject to coalescence without the stabilization of the Pickering crystals. Upon the start of the cooling ramp, the PC score returned to the baseline value with a steeper rate than the heating ramp, as the destabilisation of the foam microstructure was reduced at lower temperatures.

The microstructure characterization of some representative oleofoam samples is presented in Figure 5.8 – 5.10, displaying the three-dimensional rendering of a representative VOI each, the size distribution and the sphericity distribution, respectively. Table 5.2 contains the relevant parameters describing the size and shape of the air bubbles and the oleogel phase for each of the samples depicted in Figure 5.8.

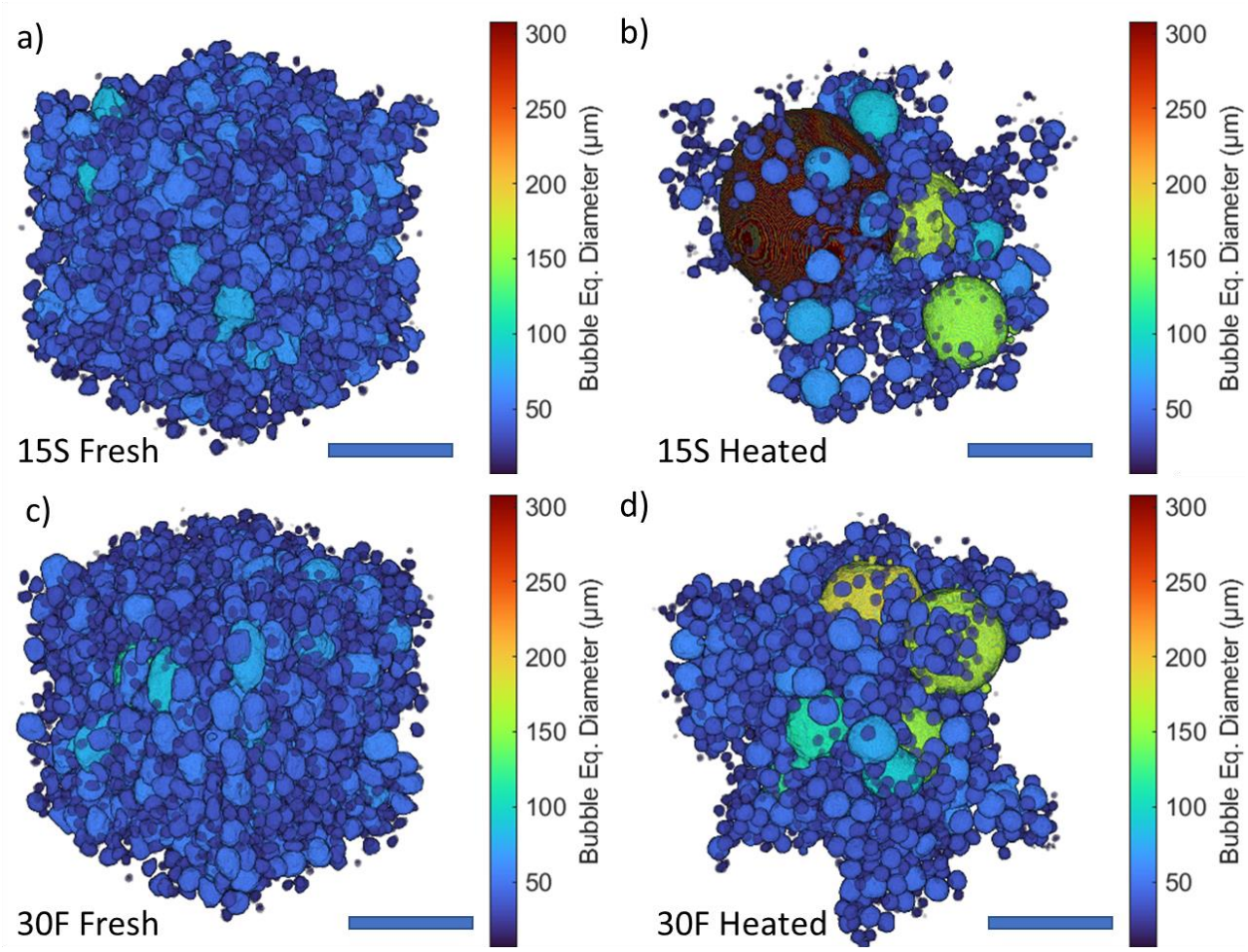

Figure 5.8. 3D MATLAB renderings of selected VOIs of samples 15S Fresh (a), 15S Heated (b), 30F Fresh (c) and 30F Heated (d). Scale bar is 250 µm. The air bubbles are colour-coded based on their equivalent diameter, from smallest (blue) to largest (red).

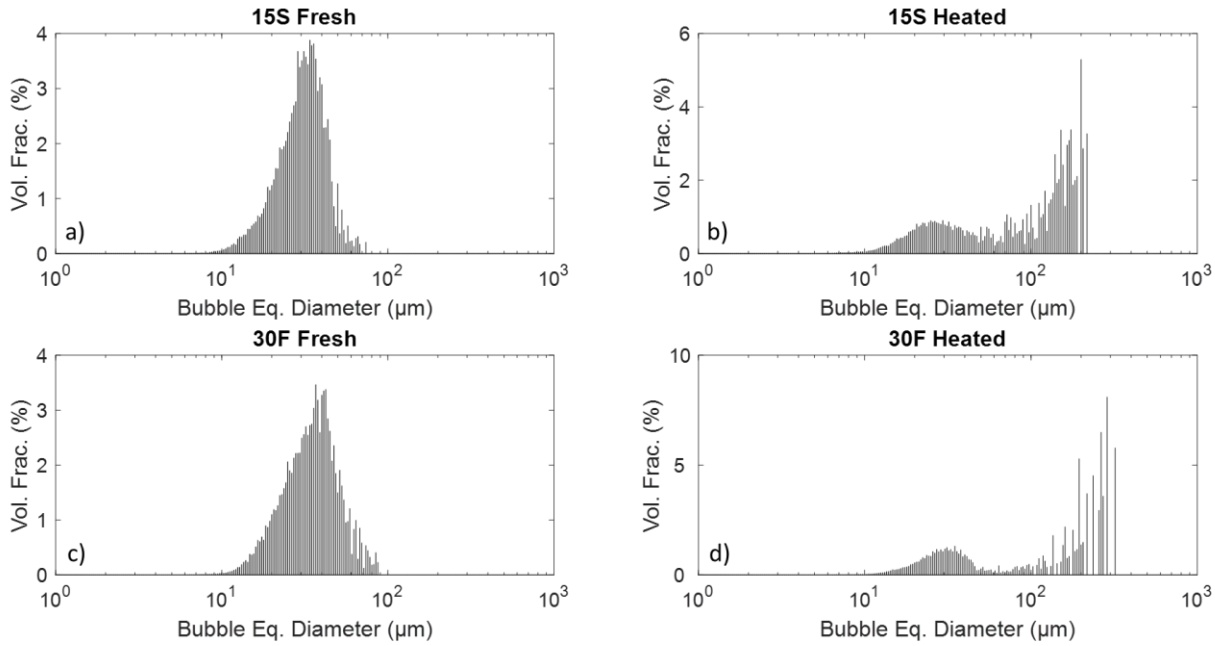

Figure 5.9. Air bubbles' size distribution for samples 15S Fresh (a), 15S Heated (b), 30F Fresh (c) and 30F Heated (d), calculated with MATLAB.

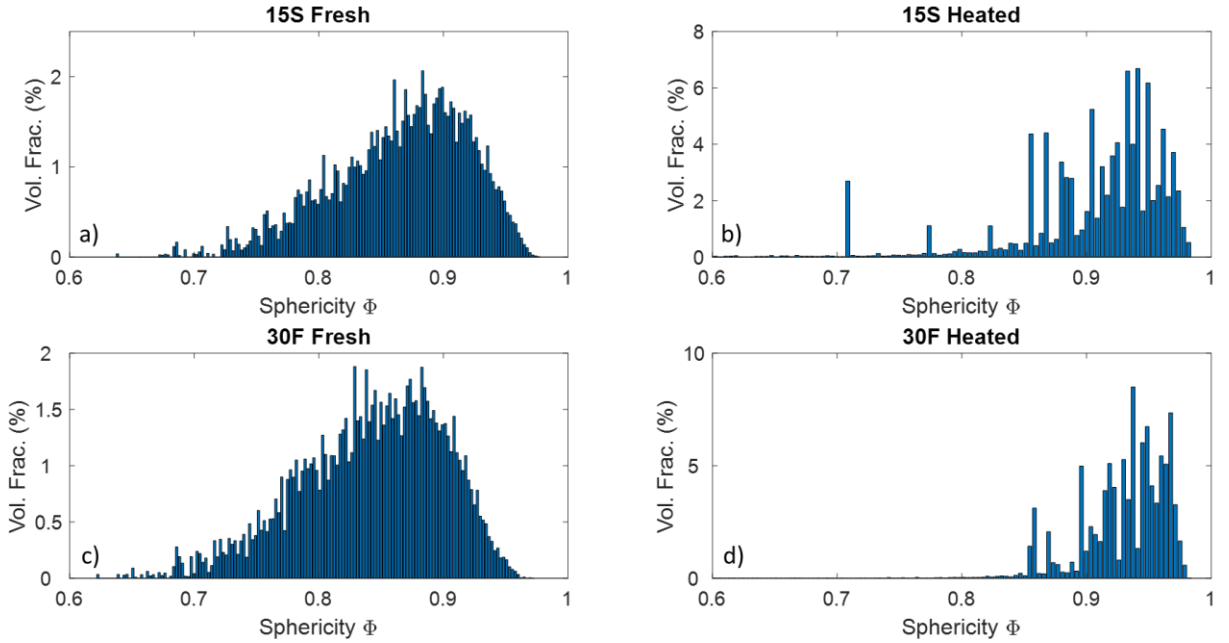

Figure 5.10. Air bubbles' sphericity distribution for samples 15S Fresh (a), 15S Heated (b), 30F Fresh (c) and 30F Heated (d), calculated with MATLAB.

Both fresh samples (15S and 30F) displayed a similar bell-shaped distribution, with an equivalent diameter of 32.10 ± 10.3 µm and 34.2 ± 14.1 µm, respectively (Figure 5.9a, c). This value was in agreement, for sample 30F, with the microstructure shown in Figure 5.6a. At the same time, the sphericity distribution of the two

fresh samples were similar, ranging from 0.70 to 0.95, with a mean value of 0.91 ± 0.06 (15S Fresh) and 0.89 ± 0.06 (30F Fresh) (Figure 5.10a, c). This large distribution reflected the non-spherical shape of the air bubbles, also visible in the volume rendering of Figure 5.8a and Figure 5.8c. For sample 30F Fresh, this was confirmed by the low volume fraction (44%) of spheroid-shaped bubbles; sample 15S Fresh, on the other hand, contained a higher amount of spheroid-shaped bubbles (75%) (See Appendix B, Figure B7) (Table 5.2).

Upon heating, both 15S and 30F samples displayed a significant change in their microstructure, exhibiting a bimodal size distribution with presence of two populations of bubbles: the first at *ca.* 27 µm for sample 15S and at *ca.* 32 µm for sample 30F, and the second with a maximum volume at *ca* 180 µm and *ca.* 287 µm, respectively (Figure 5.9b, d). In fact, the D[4,3] value for heated samples increased to 107.7 ± 67.1 µm (15S Heated) and 152.5 ± 106.3 µm (30F Heated), as the larger air bubbles contributed more significantly to the distribution. The average diameter for sample 30F was also close with the value obtained from the radiography images (140.2 ± 35.2 µm). The average sphericity increased for both samples, as well as the volume fraction of spheroidal bubbles; in particular, for sample 30F, the variation in the shape of the air bubbles was more significant (44% vs. 98%), in agreement with the observed relaxation of the air bubbles following the thermal treatment observed with XRR in Figure 5.7.

Furthermore, the normalized number density of bubbles decreased for both samples after heating: 47.1 ± 4.8 vs. 21.3 ± 3.0 for sample 15S and from 33.9 ± 1.9 to 13.6 ± 4.1 for sample 30F, explained by the occurrence of fewer, but larger bubbles due to coalescence after subjecting the sample to heating. This was visible also in Figure 5.6 by comparison of fresh and heated microstructure. The change in the microstructure was also reflected in the oleogel phase thickness, which increased from 11.5 ± 5.2 µm to 20.0 ± 9.9 µm (sample 15S) and from 8.8 ± 3.6 µm to 15.1 ± 5.8 µm (sample 30F). The change in the continuous gel phase was in agreement, for sample 30F, with the images in Figure 5.6a and Figure 5.6b.

Table 5.2. Summary of the parameters describing the microstructure of sample 30F Fresh and 30F Heated, including the volume-weighted mean equivalent diameter (D[4,3]), the sphericity, volume fraction of spheroidal bubbles, number of bubbles per VOI, and mean oleogel thickness.

	15S Fresh	15S Heated	30F Fresh	30F Heated
D[4,3] (µm)	32.0 ± 10.3	107.7 ± 67.1	34.2 ± 14.1	152.5 ± 106.3
Sphericity	0.91 ± 0.06	0.93 0.06	0.89 ± 0.06	0.94 ± 0.04
Vol. % of spheroidal bubbles (%)	75.7	89.5	44.0	98.6
Number of bubbles / 10^6 * μm^3	47.1 ± 4.8	21.3 ± 3.0	33.9 ± 1.9	13.6 ± 4.1
Mean Oleogel Thickness (µm)	11.1 ± 5.2	20.0 ± 9.9	8.8 ± 3.6	15.1 ± 5.8

5.4 Conclusions

This work demonstrated the use of SR-XCT as a non-invasive technique for fast and accurate quantitative investigation of the microstructure of thermally sensitive, soft porous matter specimens prone to deformation with a straightforward, adaptable sample preparation and beamline setup. Sample stabilization by means of plunge-freezing with liquid nitrogen prior to XCT analysis, followed by the use of a Cryojet temperature control, enabled the collection of high-quality tomography data, suitable for the extraction of quantitative information. Using propagation-based phase-contrast mode allows to achieve the image quality needed for segmentation without staining the samples with contrast agents. In particular, the phase-contrast mode was applied to improve the quality of the reconstructed images.

The overrun of the samples calculated with XCT was compared with gravimetric measurements, which highlighted the advantage of SR-XCT to study the aeration homogeneity of the specimen at the microscale. A custom image processing workflow was developed to extract relevant descriptors of the porous microstructure, such as bubble size distribution and morphology, together with the thickness of the continuous phase. Furthermore, the use of time-resolved X-ray radiography enabled to track changes in the microstructure of samples subject to external stimuli such as heating. While the method was demonstrated

using edible oil-based foams, it is applicable to all porous soft matter that presents similar challenges in its characterization.

Supporting Information

Supporting information contain additional figures, a time-lapse video of the radiography experiment, as well as the scripts used in ImageJ and MATLAB for the current work.

Declaration of Competing Interests

The authors declare that they have no known competing financial interests or personal relationships that could have appeared to influence the work reported in this paper.

Acknowledgements

The X-ray tomography and radiography data were collected during beamtime MT21081 and MG24233-1 at beamline I13-2, Diamond Light Source, Didcot (UK). The authors would like to acknowledge the Engineering and Physical Sciences Research Council funded Centre for Doctoral Training in Soft Matter and Functional Interfaces, grant ref. no. EP/L015536/1 as well as Nestlé PTC Confectionery (York, UK) for the financial and writing support.

References

Ali, S., Mayo, S., Gostar, A. K., Tennakoon, R., Bab-Hadiashar, A., Cann, T. M., … Favaro, J. (2021). Automatic segmentation for synchrotron-based imaging of porous bread dough using deep learning approach. *Journal of Synchrotron Radiation*, *28*, 566–575. https://doi.org/10.1107/S1600577521001314

Babin, P., Della Valle, G., Chiron, H., Cloetens, P., Hoszowska, J., Pernot, P., … Dendievel, R. (2006). Fast X-ray tomography analysis of bubble growth and foam setting during breadmaking. *Journal of Cereal Science*, *43*(3), 393–397. https://doi.org/10.1016/j.jcs.2005.12.002

Bahram-Parvar, M. (2015). A review of modern instrumental techniques for measurements of ice cream characteristics. *Food Chemistry*, *188*, 625–631. https://doi.org/10.1016/j.foodchem.2015.05.017

Barigou, M., & Douaire, M. (2013). *X-ray micro-computed tomography for resolving food microstructures*. *Food Microstructures: Microscopy, Measurement and Modelling*. Woodhead Publishing Limited. https://doi.org/10.1533/9780857098894.1.246

Blott, S. J., & Pye, K. (2008). Particle shape : a review and new methods of characterization and classification. *Sedimentology*, *55*, 31–63. https://doi.org/10.1111/j.1365-3091.2007.00892.x

Campbell, G. M., Herrero-Sanchez, R., Payo-Rodriguez, R., & Merchan, M. L. (2001). Measurement of dynamic dough density and effect of surfactants and flour type on aeration during mixing and gas retention during proofing. *Cereal Chemistry*, *78*(3), 272–277. https://doi.org/10.1094/CCHEM.2001.78.3.272

Ciurzyńska, A., & Lenart, A. (2016). Effect of the aerated structure on selected properties of freeze-dried hydrocolloid gels. *International Agrophysics*, *30*(1), 9–17. https://doi.org/10.1515/intag-2015-0067

Cornwell, P. A. (2018). A review of shampoo surfactant technology: consumer benefits, raw materials and recent developments. *International Journal of Cosmetic Science*, *40*(1), 16–30. https://doi.org/10.1111/ics.12439

Dittmann, J., Eggert, A., Lambertus, M., Dombrowski, J., Rack, A., & Zabler, S. (2016). Finding robust descriptive features for the characterization of the coarsening dynamics of three dimensional whey protein foams. *Journal of Colloid and Interface Science*, *467*, 148–157. https://doi.org/10.1016/j.jcis.2015.12.055

Doube, M., Klosowski, M. M., Arganda-Carreras, I., Cordelières, F. P., Dougherty, R. P., Jackson, J. S., … Shefelbine, S. J. (2010). BoneJ: Free and extensible bone image analysis in ImageJ. *Bone*, *47*(6), 1076–1079. https://doi.org/10.1016/j.bone.2010.08.023

Dowd, B. A., Campbell, G. H., Siddons, D. P., & Marr, R. B. (1999). Developments in synchrotron x-ray computed microtomography at the National Synchrotron Light Source. *Proc. SPIE. 3772, Developments*

in X-Ray Tomography II, (July 1999).

Ellis, A. L., Norton, A. B., Mills, T. B., & Norton, I. T. (2017). Stabilisation of foams by agar gel particles. *Food Hydrocolloids*, *73*, 222–228. https://doi.org/10.1016/j.foodhyd.2017.06.038

Fameau, A.-L., & Saint-Jalmes, A. (2020). Recent Advances in Understanding and Use of Oleofoams. *Frontiers in Sustainable Food Systems*, *4*(August), 1–6. https://doi.org/10.3389/fsufs.2020.00110

Fameau, A. L., & Binks, B. P. (2021). Aqueous and Oil Foams Stabilized by Surfactant Crystals: New Concepts and Perspectives. *Langmuir*, *37*(15), 4411–4418. https://doi.org/10.1021/acs.langmuir.1c00410

Fameau, A. L., & Fujii, S. (2020). Stimuli-responsive liquid foams: From design to applications. *Current Opinion in Colloid and Interface Science*, *50*, 101380. https://doi.org/10.1016/j.cocis.2020.08.005

Feng, Z., Dong, X., Fan, Y., Li, H., Dong, Y., Ma, X., & Chen, R. (2020). Use of X-ray microtomography to quantitatively characterize the pore structure of three-dimensional filter cakes. *Minerals Engineering*, *152*(May 2019), 106275. https://doi.org/10.1016/j.mineng.2020.106275

Groves, K., & Parker, M. L. (2013). *Appendix: Electron microscopy: principles and applications to food microstructures*. *Food Microstructures*. Woodhead Publishing Limited. https://doi.org/10.1533/9780857098894.2.386

Guo, E., Kazantsev, D., Mo, J., Bent, J., Van Dalen, G., Schuetz, P., … Lee, P. D. (2018). Revealing the microstructural stability of a three-phase soft solid (ice cream) by 4D synchrotron X-ray tomography. *Journal of Food Engineering*, *237*(May), 204–214. https://doi.org/10.1016/j.jfoodeng.2018.05.027

Guo, E., Zeng, G., Kazantsev, D., Rockett, P., Bent, J., Kirkland, M., … Lee, P. D. (2017). Synchrotron X-ray tomographic quantification of microstructural evolution in ice cream – a multi-phase soft solid. *RSC Adv.*, *7*(25), 15561–15573. https://doi.org/10.1039/C7RA00642J

Gürsoy, D., De Carlo, F., Xiao, X., & Jacobsen, C. (2014). TomoPy: A framework for the analysis of synchrotron tomographic data. *Journal of Synchrotron Radiation*, *21*(5), 1188–1193. https://doi.org/10.1107/S1600577514013939

Herremans, E., Bongaers, E., Estrade, P., Gondek, E., Hertog, M., Jakubczyk, E., … Nicolaï, B. (2013). Microstructure-texture relationships of aerated sugar gels: Novel measurement techniques for analysis and control. *Innovative Food Science and Emerging Technologies*, *18*, 202–211. https://doi.org/10.1016/j.ifset.2013.02.003

Heymans, R., Tavernier, I., Danthine, S., Rimaux, T., Van Meeren, P., & Dewettinck, K. (2018). Food-grade monoglyceride oil foams: The effect of tempering on foamability, foam stability and rheological properties. *Food and Function*, *9*(6), 3143–3154. https://doi.org/10.1039/c8fo00536b

Heymans, R., Tavernier, I., Dewettinck, K., & Van der Meeren, P. (2017). Crystal stabilization of edible oil foams. *Trends in Food Science and Technology*, *69*, 13–24. https://doi.org/10.1016/j.tifs.2017.08.015

Hildebrand, T., & Rüegsegger, P. (1997). A new method for the model-independent assessment of thickness in three-dimensional images. *Journal of Microscopy*, *185*(1), 67–75. https://doi.org/10.1046/j.1365-2818.1997.1340694.x

Hill, C., & Eastoe, J. (2017). Foams: From nature to industry. *Advances in Colloid and Interface Science*, *247*(May), 496–513. https://doi.org/10.1016/j.cis.2017.05.013

Huang, L. K., & Wang, M. J. J. (1995). Image thresholding by minimizing the measures of fuzziness. *Pattern Recognition*, *28*(1), 41–51. https://doi.org/10.1016/0031-3203(94)E0043-K

Hussain, M., Chen, D., Cheng, A., Wei, H., & Stanley, D. (2013). Change detection from remotely sensed images: From pixel-based to object-based approaches. *ISPRS Journal of Photogrammetry and Remote Sensing*, *80*, 91–106. https://doi.org/10.1016/j.isprsjprs.2013.03.006

Iftimi, L. D., Edinger, M., Bar-Shalom, D., Rantanen, J., & Genina, N. (2019). Edible solid foams as porous substrates for inkjet-printable pharmaceuticals. *European Journal of Pharmaceutics and Biopharmaceutics*, *136*(December 2018), 38–47. https://doi.org/10.1016/j.ejpb.2019.01.004

Jekle, M., & Becker, T. (2011). Dough microstructure: Novel analysis by quantification using confocal laser scanning microscopy. *Food Research International*, *44*(4), 984–991.

https://doi.org/10.1016/j.foodres.2011.02.036

Jones, J. R., Poologasundarampillai, G., Atwood, R. C., Bernard, D., & Lee, P. D. (2007). Non-destructive quantitative 3D analysis for the optimisation of tissue scaffolds. *Biomaterials*, *28*(7), 1404–1413. https://doi.org/10.1016/j.biomaterials.2006.11.014

Kennedy, M. J., Conroy, M. W., Dougherty, J. A., Otto, N., Williams, B. A., & Fleming, J. W. (2015). Bubble coarsening dynamics in fluorinated and non-fluorinated firefighting foams. *Colloids and Surfaces A: Physicochemical and Engineering Aspects*, *470*, 268–279. https://doi.org/10.1016/j.colsurfa.2015.01.062

Kinoshita, N., Sasaki, Y., Marukawa, E., Hirose, R., Sawada, S. ichi, Harada, H., & Akiyoshi, K. (2020). Crosslinked nanogel-based porous hydrogel as a functional scaffold for tongue muscle regeneration. *Journal of Biomaterials Science, Polymer Edition*, *31*(10), 1254–1271. https://doi.org/10.1080/09205063.2020.1744246

Koksel, F., Aritan, S., Strybulevych, A., Page, J. H., & Scanlon, M. G. (2016). The bubble size distribution and its evolution in non-yeasted wheat flour doughs investigated by synchrotron X-ray microtomography. *Food Research International*. https://doi.org/10.1016/j.foodres.2015.12.005

Lazidis, A., de Almeida Parizotto, L., Spyropoulos, F., & Norton, I. T. (2017). Microstructural design of aerated food systems by soft-solid materials. *Food Hydrocolloids*, *73*, 110–119. https://doi.org/10.1016/j.foodhyd.2017.06.032

Legland, D., Arganda-Carreras, I., & Andrey, P. (2016). MorphoLibJ: Integrated library and plugins for mathematical morphology with ImageJ. *Bioinformatics*, *32*(22), 3532–3534. https://doi.org/10.1093/bioinformatics/btw413

Luengo, G. S., Fameau, A. L., Léonforte, F., & Greaves, A. J. (2021). Surface science of cosmetic substrates, cleansing actives and formulations. *Advances in Colloid and Interface Science*, *290*. https://doi.org/10.1016/j.cis.2021.102383

Manzocco, L., Mikkonen, K. S., & García-González, C. A. (2021). Aerogels as porous structures for food applications: Smart ingredients and novel packaging materials. *Food Structure*, *28*(February). https://doi.org/10.1016/j.foostr.2021.100188

Masselot, V., Bosc, V., & Benkhelifa, H. (2021). Analyzing the microstructure of a fresh sorbet with X-ray micro-computed tomography: Sampling, acquisition, and image processing. *Journal of Food Engineering*, *292*(July 2020), 2–10. https://doi.org/10.1016/j.jfoodeng.2020.110347

McClements, D. J. (2020). Future foods: A manifesto for research priorities in structural design of foods. *Food and Function*, *11*(3), 1933–1945. https://doi.org/10.1039/c9fo02076d

Metilli, L., Francis, M., Povey, M., Lazidis, A., Marty-Terrade, S., Ray, J., & Simone, E. (2020). Latest advances in imaging techniques for characterizing soft, multiphasic food materials. *Advances in Colloid and Interface Science*, *279*, 102154. https://doi.org/10.1016/j.cis.2020.102154

Metilli, L., Lazidis, A., Francis, M., Marty-terrade, S., Ray, J., & Simone, E. (2021). The Effect of Crystallization Conditions on the Structural Properties of Oleofoams Made of Cocoa Butter Crystals and High Oleic Sunflower Oil. *Crystal Growth and Design*. https://doi.org/10.1021/acs.cgd.0c01361

Mo, J., Guo, E., Graham McCartney, D., Eastwood, D. S., Bent, J., Van Dalen, G., … Lee, P. D. (2018). Time-resolved tomographic quantification of the microstructural evolution of ice cream. *Materials*, *11*(10), 1–14. https://doi.org/10.3390/ma11102031

Murray, B. S. (2020). Recent Developments in Food Foams. *Current Opinion in Colloid & Interface Science*, *50*, 101394. https://doi.org/10.1016/j.cocis.2020.101394

Murray, B. S., Durga, K., Yusoff, A., & Stoyanov, S. D. (2011). Stabilization of foams and emulsions by mixtures of surface active food-grade particles and proteins. *Food Hydrocolloids*, *25*(4), 627–638. https://doi.org/10.1016/j.foodhyd.2010.07.025

Nielsen, M. S., Munk, M. B., Diaz, A., Pedersen, E. B. L., Holler, M., Bruns, S., … Feidenhans'l, R. (2016). Ptychographic X-ray computed tomography of extended colloidal networks in food emulsions. *Food*

Structure, *7*, 21–28. https://doi.org/10.1016/j.foostr.2016.01.001

Paganin, D., Mayo, S. C., Gureyev, T. E., Miller, P. R., & Wilkins, S. W. (2002). Simultaneous phase and amplitude extraction from a single defocused image of a homogeneous object. *Journal of Microscopy*, *206*(1), 33–40. https://doi.org/10.1046/j.1365-2818.2002.01010.x

Pinzer, B. R., Medebach, A., Limbach, H. J., Dubois, C., Stampanoni, M., & Schneebeli, M. (2012). 3D-characterization of three-phase systems using X-ray tomography: Tracking the microstructural evolution in ice cream. *Soft Matter*, *8*(17), 4584–4594. https://doi.org/10.1039/c2sm00034b

Rau, C., Bodey, A. J., Marathe, S., Cipiccia, S., Zdora, M.-C., Zanette, I., … Storm, M. (2017). Micro- and nano-tomography at the DIAMOND beamline I13L imaging and coherence. *Proceedings of SPIE*, *10391*(October 2017), 28. https://doi.org/10.1117/12.2274514

Russ, J. C. (2015). Image Analysis of Foods. *Journal of Food Science*, *80*(9), 1974–1987. https://doi.org/10.1111/1750-3841.12987

Saha, S., Saint-Michel, B., Leynes, V., Binks, B. P., & Garbin, V. (2020). Stability of bubbles in wax-based oleofoams: decoupling the effects of bulk oleogel rheology and interfacial rheology. *Rheologica Acta*, *59*(4), 255–266. https://doi.org/10.1007/s00397-020-01192-x

Sahoo, P., Wilkins, C., & Yeager, J. (1997). Threshold selection using Renyi's entropy. *Pattern Recognition*, *30*(1), 71–84. https://doi.org/10.1016/S0031-3203(96)00065-9

Sato, Y., Yamamoto, K., Horiguchi, S., Tahara, Y., Nakai, K., Kotani, S. ichiro, … Mazda, O. (2018). Nanogel tectonic porous 3D scaffold for direct reprogramming fibroblasts into osteoblasts and bone regeneration. *Scientific Reports*, *8*(1), 1–10. https://doi.org/10.1038/s41598-018-33892-z

Sehaqui, H., Salajková, M., Zhou, Q., & Berglund, L. A. (2010). Mechanical performance tailoring of tough ultra-high porosity foams prepared from cellulose i nanofiber suspensions. *Soft Matter*, *6*(8), 1824–1832. https://doi.org/10.1039/b927505c

Timounay, Y., Pitois, O., & Rouyer, F. (2017). Gas Marbles: Much Stronger than Liquid Marbles. *Physical*

Review Letters, *118*(22). https://doi.org/10.1103/PhysRevLett.118.228001

Trinh, L., Lowe, T., Campbell, G. M., Withers, P. J., & Martin, P. J. (2013). Bread dough aeration dynamics during pressure step-change mixing: Studies by X-ray tomography, dough density and population balance modelling. *Chemical Engineering Science*. https://doi.org/10.1016/j.ces.2013.06.053

Truong, T., Prakash, S., & Bhandari, B. (2019). Effects of crystallisation of native phytosterols and monoacylglycerols on foaming properties of whipped oleogels. *Food Chemistry*, *285*(January), 86–93. https://doi.org/10.1016/j.foodchem.2019.01.134

Turgay Celik. (2009). Unsupervised Change Detection in Satellite Images Using Principal Component Analysis and k-Means Clustering. *IEEE Geoscience and Remote Sensing Letters*, *6*(4), 772–776.

Ubbink, J., Burbidge, A., & Mezzenga, R. (2008). Food structure and functionality: a soft matter perspective. *Soft Matter*, *4*(6), 1569–1581. https://doi.org/10.1039/b800106e

Vo, T. N., Atwood, C. R., & Drakopoulos, M. (2018). Superior techniques for eliminating ring artifacts in X-ray micro-tomography. *Optics Express*, *26*(22), 28396–28412.

Wadeson, N., & Basham, M. (2016). Savu: A Python-based, MPI Framework for Simultaneous Processing of Multiple, N-dimensional, Large Tomography Datasets. *ArXiv*. Retrieved from http://arxiv.org/abs/1610.08015

Wang, C., Hua, Y., Nadimi, S., Taleb, W., Barker, R., Li, Y., … Neville, A. (2021). Determination of thickness and air-void distribution within the iron carbonate layers using X-ray computed tomography. *Corrosion Science*, *179*, 109153. https://doi.org/10.1016/j.corsci.2020.109153

Wang, Z., Herremans, E., Janssen, S., Cantre, D., Verboven, P., & Nicolaï, B. (2018). Visualizing 3D Food Microstructure Using Tomographic Methods: Advantages and Disadvantages. *Annual Review of Food Science and Technology*, *9*(1), 323–343. https://doi.org/10.1146/annurev-food-030117-012639

Zhao, B., & Wang, J. (2016). 3D quantitative shape analysis on form, roundness, and compactness with μCT. *Powder Technology*, *291*, 262–275. https://doi.org/10.1016/j.powtec.2015.12.029

Chapter 6: Investigating the effect of aeration, storage and heating on the microstructure of fat–based oleofoams with X-ray microcomputed tomography and radiography

Abstract

Non-aqueous foams (also called oleofoams) are an emerging type of soft matter material comprising a liquid oil phase and gas bubbles stabilized by surface-active crystals or molecules, with potential applications in several industrial fields. Oleofoams are optically opaque, deform easily under shear and display a melting range close to room or body temperature, thus making their microstructure challenging to be probed by commonly used imaging techniques. Nevertheless, understanding the relationship between the processing conditions, the microstructure and the resulting oleofoam properties (*i.e.*, rheology, stability) is pivotal to design materials with tailor-made features. Up to the present, however, there are no information on the three-dimensional microstructure of oleofoams, and how it is affected by aeration time, storage conditions and heating. In this work, synchrotron X-Ray microcomputed tomography (XCT) and X-Ray radiography (XRR) were applied to the study of model fat-based oleofoams in both static and dynamic conditions, using two reference samples with low and high fat content. Results showed that the aeration affected mostly the amount of air incorporated and the thickness of the continuous phase, while the bubble size distribution did not change significantly after the first five minutes of aeration. Samples with high solid fat content retained more air over 15 months of storage compared to lower solid fat samples; nevertheless, relaxation of the air bubbles shape and Ostwald ripening occurred in both samples after 3 and 15 months. Finally, heating caused a mechanical destabilization of the oleofoams, with partial melting of the fat crystals, air diffusion and evident bubble coalescence, which was observed with XRR. The destabilization could be slowed significantly upon lowering the temperature below the melting point of the fat crystals in the samples, demonstrating the thermal responsiveness of these novel materials.

6.1 Introduction

Non-aqueous foams, also called oil-based foams or oleofoams, are an emerging type of soft matter with remarkable potential for application in pharmaceuticals, cosmetic, care and food products. (Binks & Vishal, 2021; Fameau & Binks, 2021). Oleofoams comprise an oil continuous phase and a dispersed gas phase that is stabilized by adsorbed solid particles, or molecular surfactants. As aqueous foams, oleofoams are thermodynamically unstable and eventually phase-separate *via* the typical destabilization mechanisms of bubble disproportionation, coalescence, and drainage or creaming. In contrast to aqueous foams, however, their production is more challenging, mostly due to the limited availability of suitable stabilizers for air/oil interfaces. Early examples reported in the literature featured the use of either fluorocarbon-based molecules (Bergeron et al., 1997) or liquid crystalline monoglycerides (Shrestha et al., 2008) to produce oil-continuous foams stable from minutes to hours, depending on the concentration of the surfactant. In comparison, over the last five years several publications appeared, which describe the use of fat crystals to produce oleofoams with high air volume fraction and outstanding stability, up to several months.

The use of oleofoams in consumer products affects several industrial fields. In fact, these novel colloidal systems constitute promising materials for pharmaceuticals and cosmetic products as the oil continuous phase can dissolve and deliver lipophilic drugs, as well as increase the stability of water-sensitive molecules. Moreover, the presence of gas bubbles enhances both the permeation within the skin layer, and improves customer compliance compared to other solvents (Luengo, 2021; Parsa et al., 2019). Oleofoams can also be emulsified to produce air-in-oil-in-water systems (A/O/W), where both hydrophilic and lipophilic active pharmaceutical ingredients can be incorporated in the same material (Goibier et al., 2019). A further advantage in the use of oleofoams is the absence of added surfactants in the formulation to produce the foam, which are perceived negatively by consumers and associated with negative health effects (Asioli et al., 2017). The use of oleofoams in food is particularly compelling, as oleofoams can be used to reduce the calorific density of fat-based foods and provide novel, attractive mouthfeel to consumers due to their aerated nature (Heymans et al., 2017). The industrial interest in oleofoams resulted already in several patents for their use as fat-replacers in baked goods (Chisholm et al., 2016; Gunes et al., 2016) and to enhance drug

delivery in water-free formulations (Tamarkin et al., 2019) . Finally, understanding the foaming of crude oil and its stability is a relevant topic in the petroleum industry. On one hand, oil foams can be exploited to enhance oil recovery operations (Karthick et al., 2019), on the other, undesired oil foaming lowers the efficiency of crude oil fractionation (Chen et al., 2018). Despite their wide potential, research on the properties of oleofoams is still scarce compared to their aqueous counterparts.

Oleofoams are typically fabricated from a dispersion of fat crystals or appropriate surfactants in a liquid oil phase, also termed oleogel. Various molecular species have been used as a source of solid fat, including tri- (Binks & Marinopoulos, 2017; Liu & Binks, 2021b; Metilli et al., 2021; Mishima et al., 2016), di- (Du et al., 2021) and monoglycerides (Binks et al., 2016; Gunes et al., 2017; Heymans et al., 2018; Truong et al., 2019) and fatty alcohols (Callau et al., 2020;Fameau et al., 2015). More recently, the use of sucrose esters in their molecular state for producing and stabilizing oleofoams has been reported (Liu & Binks, 2021a). Following the production of the oleogel, aeration is carried out most efficiently by mechanical whipping. Air bubbles are then incorporated and can be stabilized by the fat crystals through a Pickering mechanism. The remaining crystals form an extended, three-dimensional network around the air bubbles, which provides additional bulk stabilization against bubble coalescence and oil drainage (Heymans et al., 2017). Most of the research on oleofoams has focused on the relationship between the properties of crystals within the oleogel (size, shape, polymorph) and the resulting foamability and foam stability in the whipped state (Metilli et al., 2021). There seem to be an optimal range of solid content in the oleogel that can deliver an oleofoam, as crystals need to place themselves both at the interface and in the bulk in order to provide sufficient stabilization. However, a too high solid content can result in an excessively viscous oleogel that cannot be aerated. Fat crystals with platelet or needle morphology can be used to produce oleofoams, which can be obtained either through a tempering process (Heymans et al., 2018; Mishima et al., 2016), or by breakage of larger crystal aggregates into smaller crystals during whipping (Metilli et al., 2021). There is no clear consensus on the effect of the polymorphism (α, β’ or β) on the foaming properties of oleofoams at present (Binks & Vishal, 2021).

In the manufacture of soft porous materials, there is a complex relationship between formulation, processing conditions (*e.g.,* crystallization and aeration in the case of oleofoams), material microstructure in terms of

pore size and shape distribution, and macroscopic properties of the final product, such as heat and mass transfer, rheology and stability. Understanding how these factors affect each other is fundamental in fine-tuning the properties of the desired aerated material, in improving design of the unit operations required to manufacture oleofoams, in better estimating the shelf-life of consumer products, and finally in controlling the responsiveness of oleofoams to stimuli, such as changes in temperature (Fameau & Fujii, 2020). Despite the relevance of these novel materials, research is still needed to gain a full understanding of how the structure of oleofoams affects their functionality (Fameau & Binks, 2021; Kinoshita et al., 2020; Manzocco et al., 2021). The reason for this gap in knowledge is that the 3D characterization of oleofoams in their native state is extremely challenging. In fact, these materials are optically opaque, they deform under small level of shear, and display a range of melting points close to room or body temperature.

The microstructure of oleofoams is normally investigated by polarized light microscopy (PLM) in combination with confocal scanning laser microscopy (CSLM) or cryogenic scanning electron microscopy (CryoSEM). All these techniques involve some degree of sample preparation and provide 2D information, which leads to artefacts in the observed microstructure, and a limited understanding of such a complex three-dimensional structure. In the work of Du et al. (2021), the authors attempted to follow the bubble size distribution during aeration of a diglyceride-stabilized oleofoam using optical microscopy; however, the poor stability of the bubbles during the analysis affected significantly the results.

The effect of ageing on oleofoams is usually assessed by measuring the amount of oil drainage, or by using a texture analyser (Heymans et al., 2018). Similarly, the effect of heating is monitored through the amount of drained oil (Binks et al., 2016; Binks & Marinopoulos, 2017; Fameau et al., 2015; Liu & Binks, 2021b), or by observing individual bubbles with hot-stage microscopy (HSM). Saha et al. (2020) reported that the air bubbles retained their non-spherical shape for longer times during heating if bulk stabilizing crystals were present around the bubble, as opposed to Pickering stabilization only (Saha et al., 2020). Hence, the shape of air bubbles can provide information about the surface tension and the stabilization of the air/oil interface. Both the three-dimensional distribution of the crystal network in the bulk, and the shape of gas bubble are relevant parameters to study for the understanding of the physical behaviour of foams under static and

dynamic conditions. In fact, during ageing or heating, crystals and air bubbles are subjected to several physical phenomena, such as disproportionation, which can alter the microstructure of the material significantly (Fameau & Saint-Jalmes, 2017; Himawan et al., 2006). However, commonplace microscopic techniques cannot provide accurate characterization of both crystals and air bubbles in the complex, three-dimensional microstructure of oleofoams.

In this work, synchrotron-radiation X-Ray microcomputed tomography (XCT) and X-Ray radiography (XRR) were applied to study the microstructure of oleofoams in their native state, obtaining unprecedented results on the three-dimensional characterization of these materials. In particular, the effect of aeration time, storage time and the dynamics of thermal destabilization on a model cocoa butter-based oleofoam were evaluated. Cocoa butter can be used as a source of crystalline fat for oleogelation of vegetable oils, which is a precursor to produce oleofoams, as recently demonstrated by Metilli et al. (2021). As the foam properties (foamability, rheology and stability) were mainly affected by the amount of solid fat in the oleogel precursor (Metilli et al., 2021), in this study samples with either relatively low (15% w/w) or high (30% w/w) cocoa butter content were investigated and compared. To the best of knowledge of the authors, this publication is the first providing information on the three-dimensional, native microstructure of oil-based foams in both static and dynamic conditions.

6.2 Materials and Methods

6.2.1 Sample preparation

Mixtures of cocoa butter (CB) and high oleic sunflower oil (HOSO) were prepared by melting CB at 65°C and adding it to HOSO at the same temperature in concentration of either 15% or 30% w/w. The mixtures were then cooled to obtain a dispersion of fat crystals in oil (oleogel) and then aerated to produce an oleofoam. The crystallization was carried out in a 2L jacketed metal vessel, which was connected to a Huber Ministat 250 thermostat (Huber, Germany) for temperature control. The sample temperature was monitored with a Pt-100 temperature probe immersed in the vessel. The sample was maintained under shear (200 rpm) using a DLH overhead stirrer (VELP Scientifica, Italy) equipped with an anchor-shape mixer (8 cm diameter). The

samples, termed “15S” for the 15% w/w CB in HOSO and “30F” for the 30% w/w CB in HOSO mixture, were cooled from 65°C to 0°C at a nominal cooling rate of – 0.10 °C/min and – 0.75 °C/min, respectively. The samples were subsequently aerated using a planetary mixer (model 5KPM50, Kitchenaid, USA) with a constant shear rate (250 rpm). The oleogels were whipped for a total time of 30 minutes, collecting samples every 5 minutes to study the effect of aeration time (Metilli et al., 2021). At each step, the overrun (*i.e.,* the increase in the sample volume) was calculated with the technique most commonly known as cup method, where the sample is weighed in a cup of known volume. The overrun is then determined through Equation 6.1

$$OR_{CUP}\ (\%) = \frac{(w_{oleogel} - w_{oleofoam})}{w_{oleofoam}} \times 100 \qquad \text{Eq. 6.1}$$

where $w_{oleogel}$ and $w_{oleofoam}$ are the weight of the un-whipped oleogel and the weight of the oleofoam, respectively. The samples were imaged with XCT shortly after being whipped, or after 3 and 15 months of storage at 20°C.

6.2.2 Beamline setup

The samples were analysed at the I13-2 beamline at Diamond Light Source synchrotron (Didcot, UK), using a pink beam source with a mean energy of 27 keV ($\sigma_E = 5\ keV$).The 2D projections for tomography and radiography were acquired with a PCO edge 5.5 CMOS camera (2560 x 2160 pixels). The camera objective used was 4X, with a total optical magnification of 8X and an effective pixel size of 0.8125 µm. A small amount of sample (approximately 1 mm^3) was placed on top of a toothpick glued to the base of a cryocap. The samples were immersed in liquid nitrogen (-196°C) and installed on the tomography rotating stage. The sample temperature was controlled with a Cryojet device (Cryojet XL, Oxford Instruments, UK) and set to -40°C during the tomography acquisitions. The exposure time for each X-ray projection was set to 100 ms for 1001 projections, for a total acquisition time of 5 minutes (Metilli et al., 2021). Each acquisition was carried out in triplicate on every sample.

6.2.3 Time–resolved XRR

Samples were subjected to heating and the changes in their microstructure was studied using both X-Ray tomography and radiography. The thermal treatment involved heating the sample from 20°C to the melting temperature (T_m) of the sample (25°C for 15S and 27°C for 30F), and holding at T_m for 2 minutes. Afterwards the sample was cooled to 0 °C at -6 °C/min and maintained at such temperature for 5 minutes. Radiography images were collected every 0.5 seconds during heating and cooling, and their intensity was normalized according to Equation 6.2:

$$I_{norm} = \frac{I_{raw} - I_{dark}}{I_{flat} - I_{dark}} \qquad \text{Eq. 6.2}$$

where I_{norm} is the normalized pixel intensity of the analysed image, I_{raw} is the pixel intensity of the sample image (projection) and I_{dark} and I_{flat} are averaged pixel intensities of 20 dark field (instrument background) and 20 flat field (beam intensity distribution) images, respectively. The normalized radiography images were converted to a difference image stack, where each image is obtained from the absolute difference of pixel intensity between the i-*th* and the i+1-*th* frame. The difference image stack was then analysed with a Principal Component Analysis (PCA), using the *pca* function in MATLAB R2021a (Mathworks, USA). The score of the first principal component was plotted versus the sample temperature to detect the onset of microstructural destabilization observed by XRR. Radiography data were compared with differential scanning calorimetry (DSC) measurements obtained with a TA 8000 calorimeter (TA Instruments, USA). This onset temperatures obtained were compared with the TA Universal Analysis software (TA Instruments, USA). The 15S and 30F samples were heated up from 10°C to 65°C at a rate of 5°C/min. The onset of the main melting endotherm peak was compared with the onset temperature of destabilization from XRR.

6.2.4 Image Post-Processing

The tomographic dataset were processed using the *savu* framework developed at Diamond Light Source (Wadeson & Basham, 2016). The projections were corrected for dark image and flat-fields (see above) and a ring-removal algorithm was applied (Vo et al., 2018). A Paganin filter was applied to enhance the contrast in the low-density samples. The tomography reconstruction was perfomed using the *Gridrec* reconstruction

algorithm (Dowd et al., 1999) from the TomoPy software package (Gürsoy et al., 2014) – a python-based, open-source framework. The 3D volumes were then processed using ImageJ (National Institute of Health, USA). At least five Volume of Interest (VOI) of 500x500x500 μm^3 were selected in each sample. The VOIs were then filtered using a 3D median filter, converted to binary images with Otsu thresholding, and segmented using a 3D Euclidean distance map. An example of a reconstructed three-dimensional VOI is shown in Figure 6.1. Bubbles were counted using the BoneJ plugin (Doube et al., 2010) and their volume (V) and surface area (A) was measured. The air volume fraction was also measured (ϕ_{air}), and used to calculate the sample overrun (OR_{XCT}). Finally, BoneJ was used to calculate the oleogel thickness, which is expressed as the volume of the sphere of maximum diameter that can be fitted in the oleogel phase (Doube et al., 2010). The descriptors of the sample microstructure used in this work are summarized in Table 6.1.

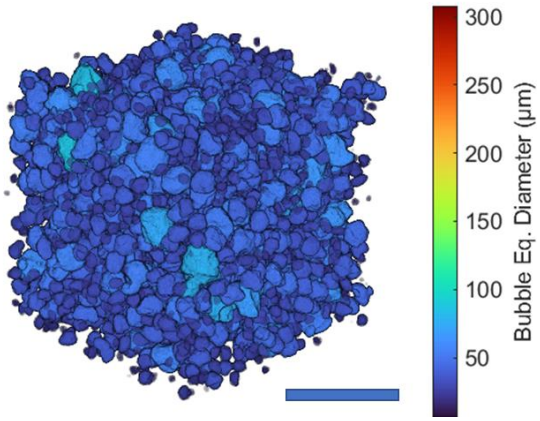

Figure 6.1. Example of a Volume of Interest (VOI) obtained from the reconstruction of tomographic projections, rendered using MATLAB. Scale bar in blue represents 250 µm.

Table 6.1. Descriptors for the sample microstructure obtained from each VOI.

Bubble Equivalent Diameter	D_{eq}	$D_{eq} = \sqrt[3]{\frac{6V}{\pi}}$
Bubble Sphericity	Φ	$\Phi = \frac{\pi^{\frac{1}{3}}(6V)^{\frac{2}{3}}}{A}$

Volume-weighted mean bubble diameter	D[4,3]	$D[4,3] = \frac{\sum_{i=1}^{N} D_{eq} i^4}{\sum_{i=1}^{N} D_{eq} i^3}$
Overrun calculated from XCT	OR_{XCT}	$OR_{XCT}(\%) = \frac{\varphi_{air}}{1 - \varphi_{air}} \times 100$
Oleogel thickness	$D_{oleogel}$	Calculated with BoneJ using Hildebrand & Rüegsegger (1997) method

A bubble cut-off diameter was set to 2.5 µm, to avoid noise caused by the voxel resolution limit (0.8125 µm). The number of bubbles counted for each sample was between 20,000 and 60,000, depending on its conditions (fresh, stored, or heated).

6.3 Results and Discussion

6.3.1 Effect of Aeration on oleofoam microstructure

The effect of aeration time on the microstructure of samples 15S and 30F is shown in Figure 6.2.

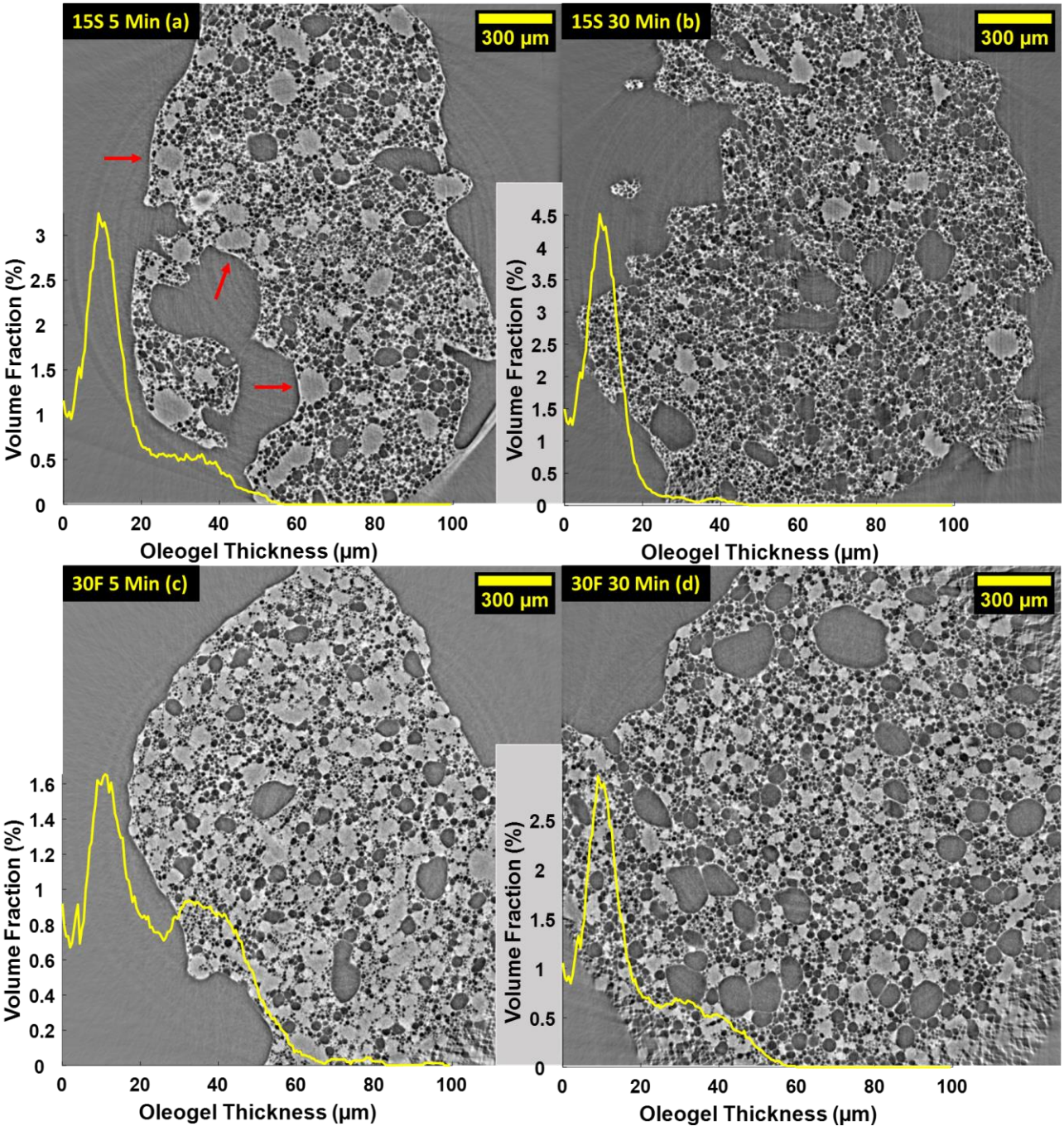

Figure 6.2. Tomographic slice of a 15S sample after 5 and 30 minutes of aeration (a, b) compared with a 30F sample after 5 and 30 minutes of aeration (c, d). The distribution of the oleogel thickness (yellow) is overlaid on the respective samples' images. Large oleogel fragments are highlighted with a red arrow. Artefacts in the corners are due to the limited information in these regions and these regions are ignored for the analysis.

Slices of the reconstructed volumes, represented in a 2D plane, showed a clear distinction between the gas phase (dark grey pixels) and the continuous oleogel phase (light grey pixels) for all samples. The thickness of the oleogel phase, calculated from the tomography data, is shown as a volume distribution for the samples. As the continuous phase is an oleogel, it comprises both the fat crystal network and the entrapped oil. The oleogel thickness, which cannot measured accurately with bidimensional microscopy techniques, is fundamental in the study of foams microstructure, and its relation to their rheology and stability. It contributes, together with the air phase, to the viscoelastic profile of the oleofoams (Heymans et al., 2017); furthermore, the continuous lipid phase has a significant role in stabilizing the air bubbles against coalescence, as demonstrated by several authors (Gunes et al., 2017; Heymans et al., 2018; Saha et al., 2020). The evolution of the continuous phase thickness during storage is also of great importance, as lipid crystals dispersed in the oleogels are subjected to Ostwald ripening and sintering (formation of crystal bridges) (Heymans et al., 2018; Himawan et al., 2006). Finally, the fat crystal network present in the oleogel phase also affects the oil binding capacity of oleofoams (Ramel et al., 2016), which prevents liquid drainage from the structure.

The samples analysed in this work exhibited a distribution of the oleogel thickness with two main peaks: a smaller one at *ca.* 10 ± 9 μm, which represents the size of the channels of oleogel surrounding the air bubbles, and a larger, broader peak centred at approximately 35 ± 25 μm, resulting from the presence of large domains of unwhipped oleogel in the samples (highlighted in Figure 6.2a by red arrows). By comparing samples 15S and 30F after 5 and 30 minutes of aeration (Figure 6.2a and c compared to Figure 6.2b and d), the peak centred at 35 μm decreased in intensity more significantly for sample 15S than sample 30F. This observation is in agreement with Metilli et al. (2021), where 30 % w/w oleofoams displayed a coarse microstructure even after vigorous whipping, with domains of oleogel still detectable both in optical microscopy images and with the naked eye.

The dispersed gas phase is displayed in Figure 6.3 as two representative VOIs, and described in terms of bubble size and shape distribution in Figure 6.4.

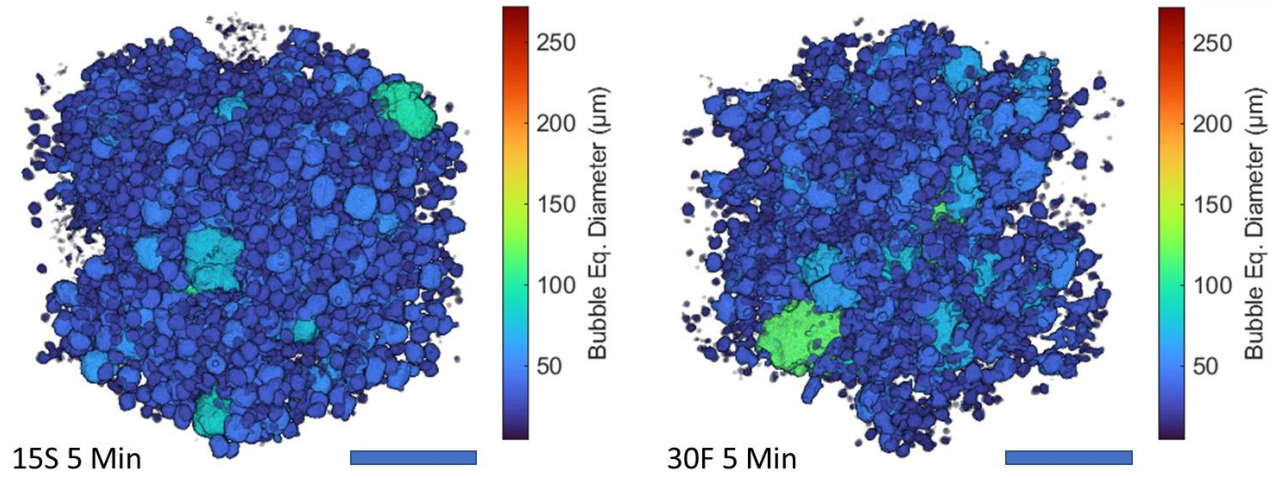

Figure 6.3. 3D renderings of representative Volumes of Interest (VOI) of sample 15S (left) and sample 30F (right) after 5 minutes of aeration. Scale bar is 250 µm. Smaller bubbles are coloured in deep blue, and larger bubbles in red.

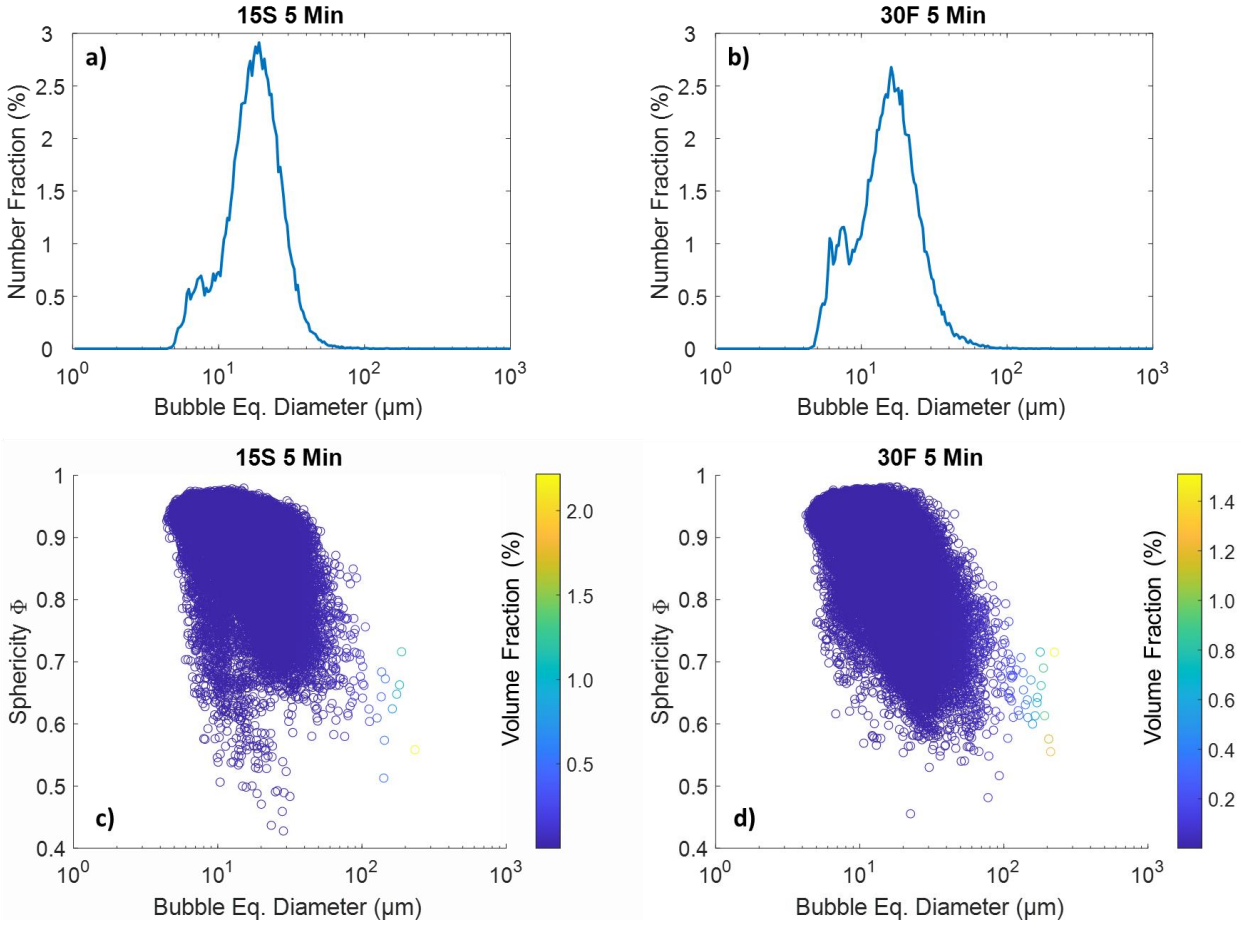

Figure 6.4. Bubble equivalent diameter distribution for samples 15S 5 Min (a) and 30F 5 Min (b). Corresponding scatter plot with bubble size and sphericity (c,d). The colorbar shows the volume fraction occupied by each bubble.

The size distribution of the gas bubbles was bimodal for both samples, with a main peak centred at 20 ± 9 and 19 ± 11 µm for samples 15S and 30F, respectively. A smaller shoulder in the distribution, centred at *ca.* 7 µm was detected as well. By inspecting the scatter plots in Figure 6.4c and Figure 6.4d, it can be seen that the bubble sphericity ranged between 0.60 and 0.90, with an average value of 0.88 ± 0.11 for both samples. The non-spherical nature of the bubbles can also be seen from the volume renderings in Figure 6.3. In particular, from the scatter plot of Figure 6.4 it can be noted that large air bubbles (diameter ≥ 100 µm) displayed low sphericity (Φ = 0.65). This observation could be explained by considering the Laplace pressure inside a bubble, which decreases with increasing bubble diameter: hence, larger bubbles tend to be more deformable than smaller ones (Heymans et al., 2017). Large, non-spherical bubbles are visible in the samples, as shown in Figure 6.2.

These results are in line, although with higher accuracy, with previous observations from Binks and Marinopoulos (2017), who reported an average bubble size between 20 and 30 µm for whipped pure cocoa butter, observed by optical microscopy. Similarly, air bubbles in oleofoams display a non-spherical shape, due to the presence of a jammed layer of adsorbed crystals at the air/oil interface (Binks et al., 2016; Callau et al., 2020; Heymans et al., 2018; Liu & Binks, 2021b). Accurate measurements of the bubble sphericity are, however, only possible with three-dimensional, tomographic methods. As air bubbles in foams tend to minimize their surface tension by assuming a spherical shape (Subramaniam et al., 2005), the sphericity parameter obtained in this work could be used to describe qualitatively the extent of Pickering stabilisation of the air/oil interface.

The average bubble size of the cocoa butter-based oleofoams does not seem to be affected by the amount of fat crystals (i.e., solid fat content, SFC%), which was also reported by Gunes et al.(2017) and by Brun et al. (2015). This behaviour could stem from the mechanical breakage of cocoa butter crystal aggregates being broken to cocoa butter nanoplatelets (CNPs) of similar size during aeration. Therefore, the stabilizing crystals would have similar properties for samples with different SFC% values, leading to the same bubble size distribution. Nevertheless, the total amount of crystals is not affected by aeration, hence samples with higher CB % w/w, such as sample 30F, will contain larger amounts of CNPs in the bulk, which may have an effect on

the rate of air incorporation, and on the stability of the oleofoam. Similarly, an effect of the SFC% on the sphericity distribution of the air bubbles was not observed.

The evolution of the gas bubbles' size during aeration is shown in more detail in Figure 6.5.

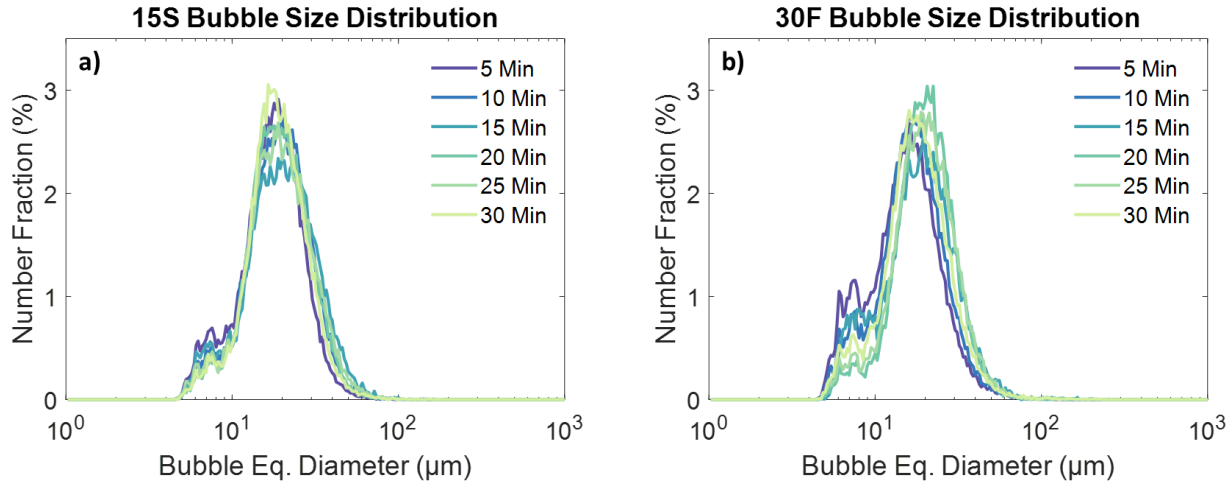

Figure 6.5. Evolution of the bubbles' equivalent diameter number distribution during aeration for sample 15S (left) and sample 30F (right).

For both samples (15S and 30F), the size distribution was not affected significantly by the aeration time; only a slight decrease in intensity of the peak at 7 µm was observed for sample 30F. No significant variations were observed in the sphericity distribution with increasing aeration time either (Figure C1, Appendix C). This result implies that a characteristic bubble size (and shape) distribution is reached during the first 5 minutes of aeration, after which the main changes occurring in the oleofoam microstructure concerned the oleogel phase and the amount of incorporated air.

The overrun calculated from XCT and by the cup method, and the evolution of the oleogel thickness for samples 15S and 30F are shown in Figure 6.6a and Figure 6.6b, respectively.

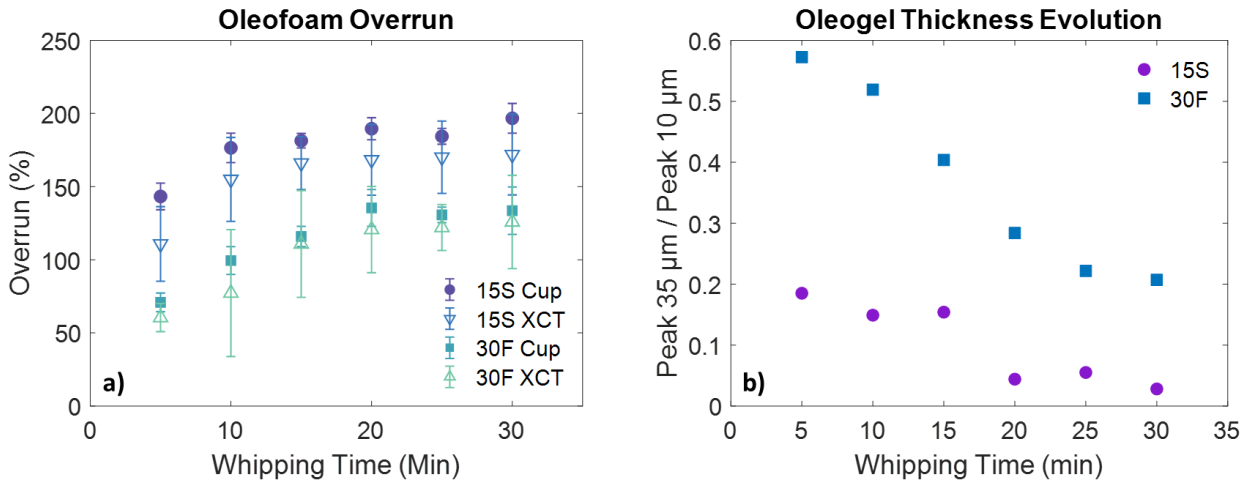

Figure 6.6. Evolution of the oleofoam overrun during whipping for samples 15S and 30F, as calculated from the cup method and XCT (a). Intensity ratio of the oleogel thickness peaks (35 µm vs. 10 µm) during whipping (b).

Sample 15S displayed high overrun values (both via XCT and cup method) already after 5 minutes of aeration, followed by a modest increase until reaching almost 200% overrun. Sample 30F, on the other hand, exhibited a lower initial overrun (70%), which increased more slowly than sample 15S until reaching a final value of 130%. The overrun values obtained from XCT were systematically lower than the overrun calculated by the cup method, and displayed larger standard deviation values. It is hypothesized that the presence in the samples of air cavities larger than or of comparable size to the volume analysed with XCT (about 1 mm^3) led to the underestimation of the overrun because these cannot be included in the XCT analysis. Additionally, the occurrence of air bubbles with comparable size to the VOI might have caused the large standard deviation in the XCT overrun (Metilli et al., 2021)). Figure 6.6b displays the variation of oleogel thickness, as the ratio between the intensity of the peak at 35 µm (i.e., the unwhipped oleogel domains) and the peak at 10 µm (i.e., oleogel surrounding the air bubbles). Hence, the plot describes the depletion of the unwhipped oleogel domains during whipping. Waterfall plots showing the whole oleogel thickness evolution are also available in the Supporting Information (Figure C2, Appendix C). As already demonstrated in Figure 6.2, the amount of unwhipped oleogel was lower for sample 15S after 5 minutes, decreasing abruptly after 20 minutes of aeration. For sample 30F, on the other hand, the depletion of the oleogel phase followed a step-wise trend, but starting from a higher amount of unwhipped oleogel which persisted in the sample even after 30 minutes of aeration.

The results presented so far provide a hypothesis regarding the mechanism underlying the aeration of oleofoams using a planetary mixer. Whipping breaks down fat crystals agglomerates to particles with similar properties (*i.e.*, size, shape, polymorphism), which act as Pickering stabilizers at the air/oil interface. Therefore, while maintaining a constant shear rate in the planetary mixer, the bubble size (and shape) distribution does not change significantly with the SFC%, or the prolonged aeration time, as reported by Denkov et al. (2020). Instead, the effect of sample viscosity, which depends on the solid fat content, is visible in the different air incorporation profiles: higher viscosity samples (30F) are characterized by a slower air incorporation and eventually a low final overrun. Whereas low-viscosity samples (15S) present higher overruns, which are reached in the first stages of aeration. Air incorporation is followed by depletion of the oleogel domains, which are used as a source of fat crystals for stabilizing newly-entrained air bubbles. This observation agrees with the findings of Mishima et al. (2016), in which work IR-probe microscopy demonstrated that the amount of crystalline material in the bulk decreased with increasing aeration times. In particular, for sample 15S, most of the air phase (170% overrun) was incorporated within the first 15 minutes of aeration, during which the oleogel thickness decreased accordingly. For sample 30F, instead, air incorporation proceeded slowly with a step-wise profile, followed by decrease in the oleogel thickness until the end of aeration.

Therefore, 15S samples required less time to reach equilibrium in terms of overrun and microstructural homogeneity, whereas 30F samples required at least 30 minutes to reach a constant overrun. Nevertheless, these samples also contained unwhipped material that might affect their functionality and quality.

6.3.2 Effect of Storage

The effect of storage conditions on the microstructure of 15S and 30F oleofoams is shown in Figure 6.7.

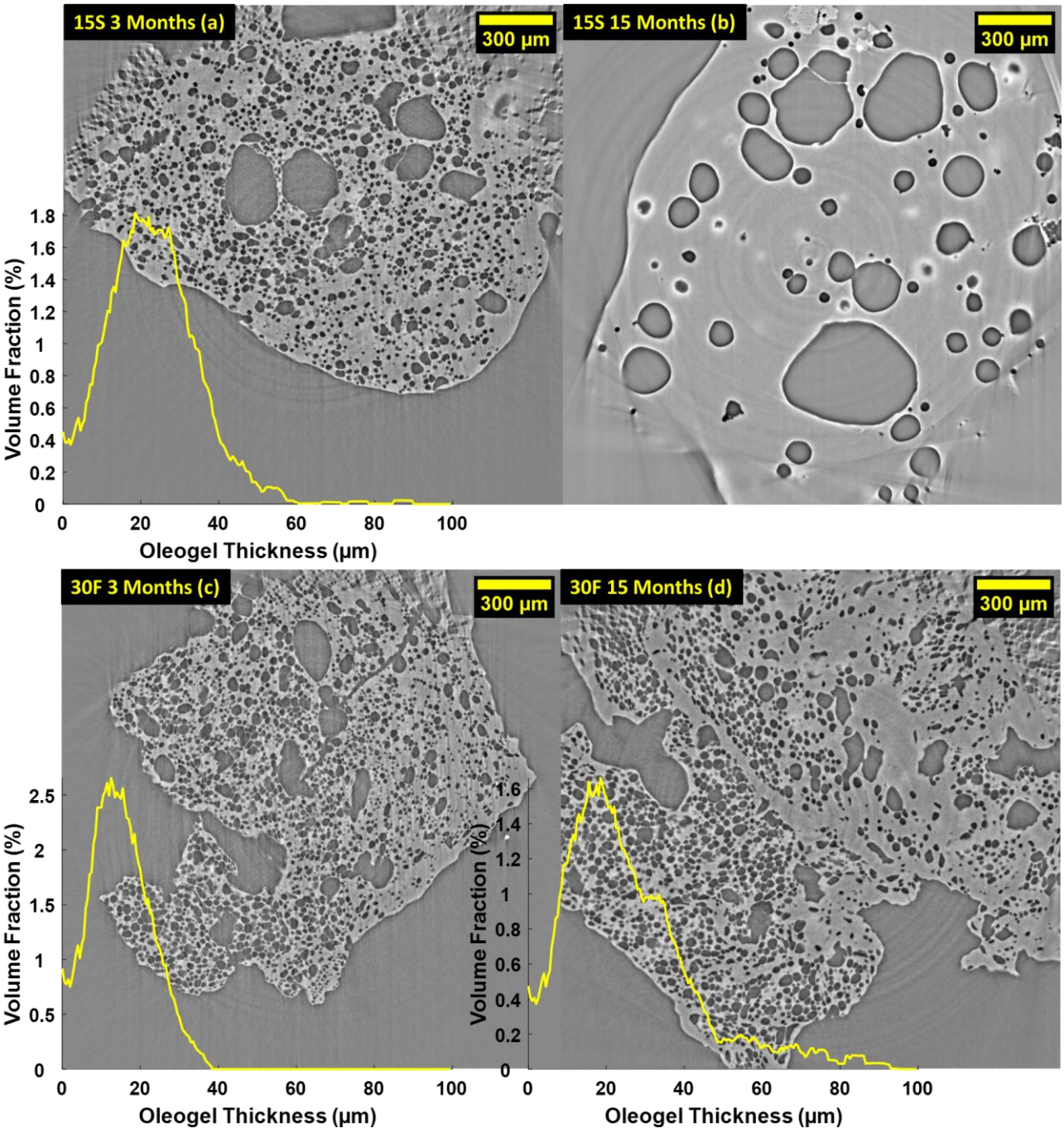

Figure 6.7. Comparison of the oleofoam microstructure during storage conditions for sample 15S, 3 months (a), 15S 15 months (b), 30F 3 months (c) and 30F 15 months (d). The oleogel thickness distribution is overlaid on the respective tomography slices.

After three months of storage at 20°C (Figure 6.7a and c) both 15S and 30F oleofoams contained a lower amount of air bubbles and displayed a larger oleogel thickness, compared to their respective fresh samples

in Figure 6.2. After 15 months of storage, however, sample 15S contained only few, large bubbles (diameter 100 – 300 μm) (Figure 6.7b), whereas sample 30F (Figure 6.7d) retained a similar microstructure to after 3 months of storage. For this specific sample, however, the mean oleogel thickness increased further. From a macroscopic perspective, the aged oleofoam samples did not display significant oil drainage, however their volume decreased, as shown in Figure C3 (Appendix C). The samples exhibited large voids along the graduated cylinder, with visible fractures throughout the foam. Hence, it was not possible to determine accurately the decrease in overrun using volumetric measurements. Table 6.2 contains the parameters describing the microstructure of the aged foams.

Table 6.2 Parameters describing the microstructure of fresh and aged oleofoams (15S and 30F) in comparison with their fresh analogues.

Sample	OR_{XCT}	$D_{oleogel}$	Bubbles / μm^3 ($\times 10^{-6}$)	Mean D_{eq}	Mean Φ
15S 30 Min (Fresh)	171.2 ± 26.0	11 ± 6	51.10 ± 5.97	20 ± 9	0.86 ± 0.11
15S 3 Months	50.0 ± 7.5	25 ± 10	20.16 ± 2.20	21 ± 10	0.93 ± 0.08
15S 15 Months	13.6 ± 9.4	n/a	1.28 ± 0.65	27 ± 19	0.86 ± 0.15
30F 30 Min (Fresh)	125.8 ± 31.2	20 ± 13	46.45 ± 5.52	19 ± 11	0.88 ± 0.11
30F 3 months	71.5 ± 12.5	18 ± 8	30.90 ± 1.87	18 ± 8	0.92 ± 0.09
30F 15 months	69.7 ± 35.7	26 ± 12	22.85 ± 7.47	24 ± 10	0.92 ± 0.07

In agreement with what is observed in Figure 6.7, the increase in the mean oleogel thickness was larger for sample 15S than sample 30F, after 3 months; for sample 15S 15 months it was not possible to determine the oleogel thickness from image analysis, however it was comparable in length with the edge of the sampling VOI (500 μm). After 15 months of storage, sample 30F displayed further increase in the thickness of the oleogel phase. At the same time, the decrease in overrun calculated from XCT was more significant for sample 15S (from 170 to 50%) compared to sample 30F (from 125 to 75%). After 15 months, sample 15S barely contained any air (10% overrun), whereas sample 30F maintained a similar overrun value to after 3 months,

however with larger standard deviation. With the same trend, the normalized number of bubbles for each VOI decreased by 60% for sample 15S and by 34% for sample 30F after three months. Therefore, higher SFC% was beneficial to oleofoam stability during storage conditions.

3D renderings of the dispersed gas phase for the aged samples are shown in Figure 6.8; the bubble size and shape distributions are displayed in Figure 6.9, in comparison with the fresh samples.

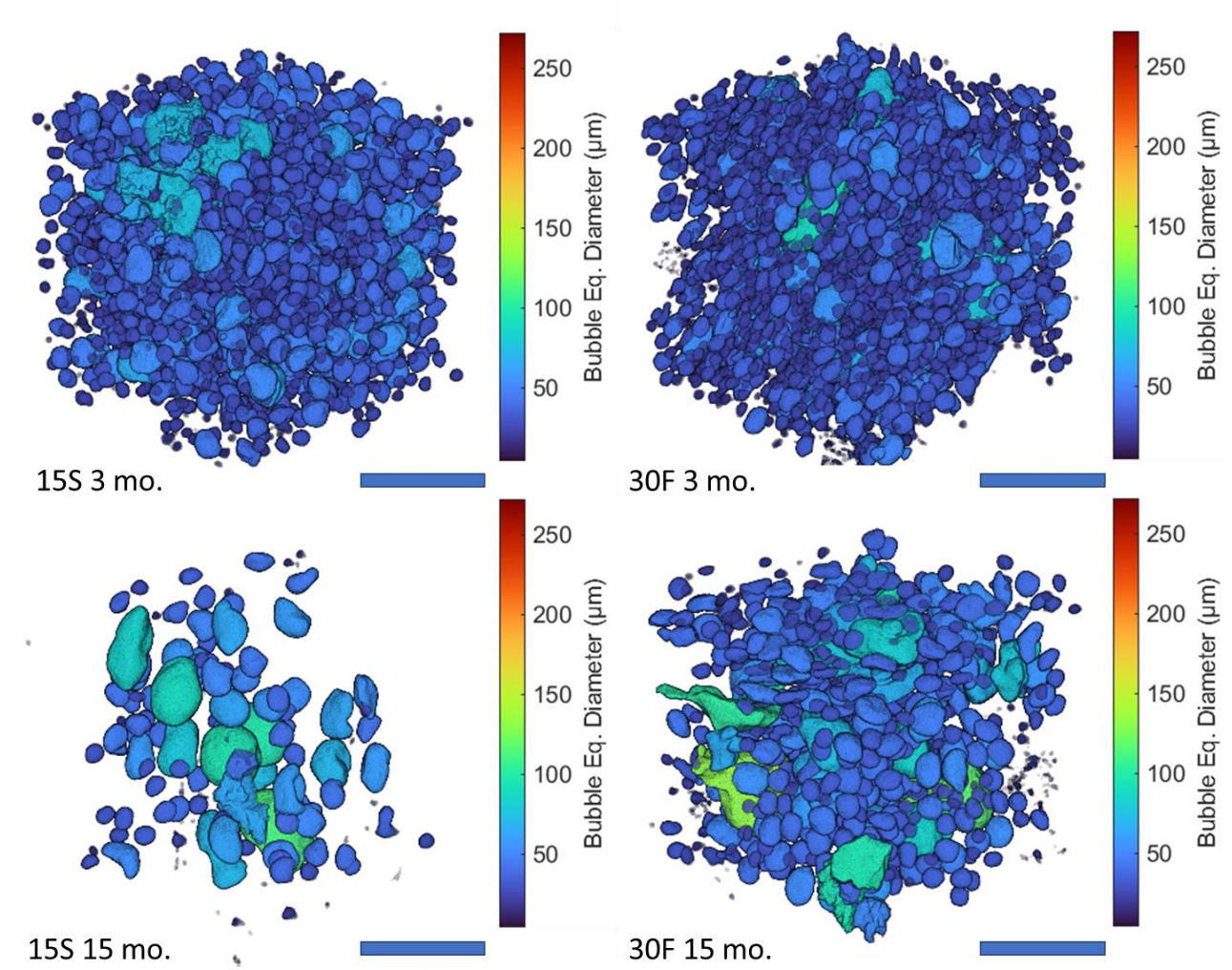

Figure 6.8. 3D renderings of representative VOI for each of the aged oleofoam samples. Scale bar is 250 µm. Smaller bubbles are displayed in blue, larger bubbles in red.

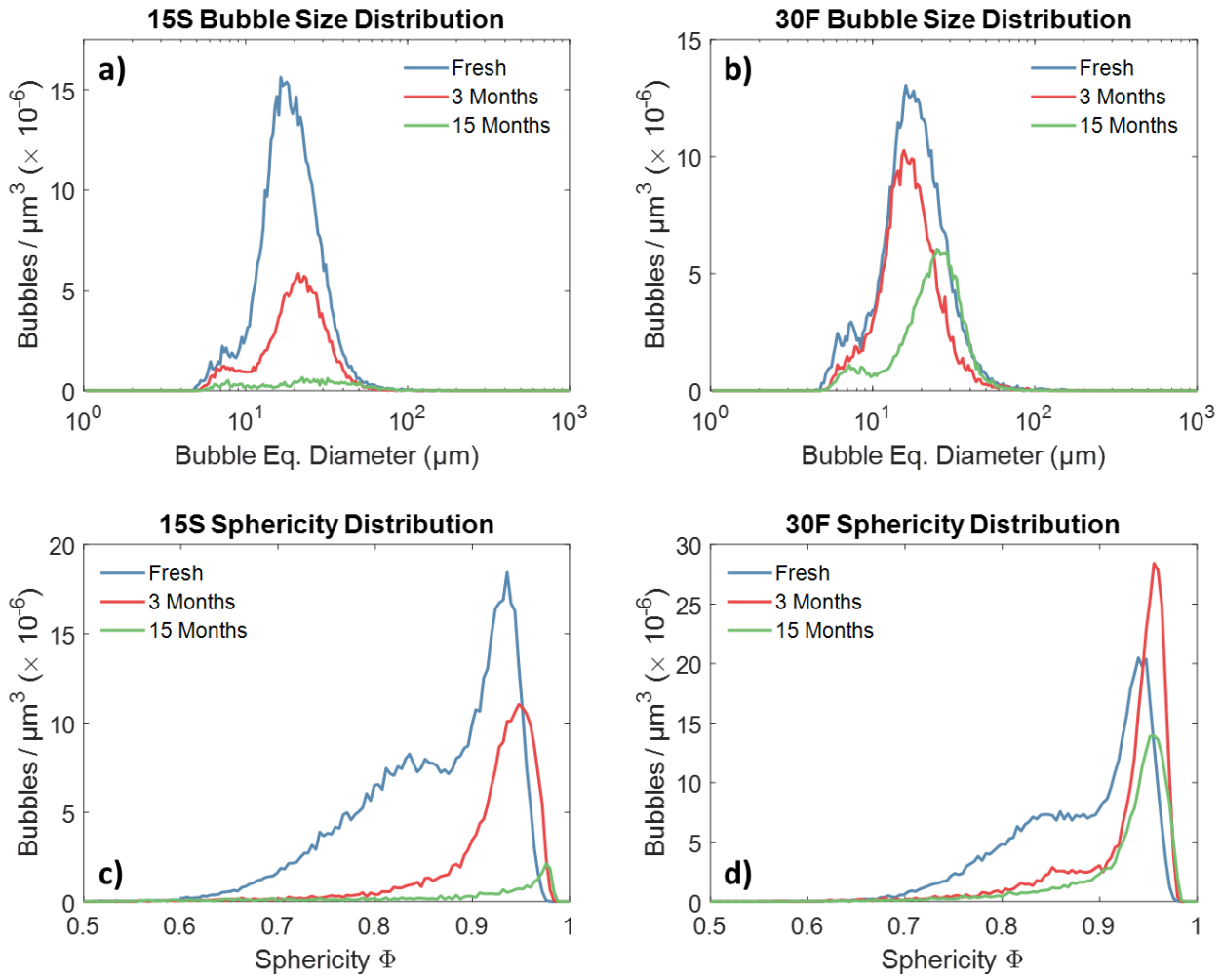

Figure 6.9. Volume-normalized bubble size distribution for 15S (a) and 30F (b) fresh samples and after 3 and 15 months of storage at 20°C. Bubble sphericity distribution of the samples is shown for sample 15S (c) and 30F (d).

As mentioned earlier, sample 30F retained a larger amount of air bubbles during storage, as it is visible from the plots in Figure 6.9. The mean bubble size did not change significantly for samples after 3 months, however their average sphericity increased to 0.93 ± 0.08 and 0.92 ± 0.09 for samples 15S and 30F, respectively. After 15 months of storage, the amount of air bubbles in sample 15S decreased by an order of magnitude compared to 3 months and increased in size (mean diameter 27 ± 19 µm); the number of bubbles decreased, although less dramatically, for sample 30F, which also displayed an increase in the bubble size, from 19 to 24 ± 10 µm. These variations in the air phase properties are also visible by comparing the volume renderings of Figure 6.3 with Figure 6.8.

From these results, it is evident that oleofoam systems are subjected to post-processing physical phenomena that affect significantly the microstructure, and therefore the overall properties of the material during storage. It is hypothesized that there are several concurring processes that involve both the air bubbles and the fat crystals. The decrease in overrun implies that air bubbles escaped the oleofoam, potentially by diffusion to the sample surface, or towards large, macroscopic air bubbles which eventually result in fractures in the material, as shown in Figure C3 of the Appendix C. The former pathway is more probable, as the average bubble size increased only slightly after three months. This could be ascribed to the effect of Pickering stabilisation, which resist the disproportionation of air bubbles; the persistence of the peak at *ca.* 7 µm in the bubble size distribution during storage supports this remarkable stability against phase separation in oleofoams.

At the same time, the fat crystals were subject to Ostwald ripening, with small CNPs dissolving in favour of large crystalline aggregates. This was observed with polarized microscopy of both aged samples, which displayed larger quantities of birefringent fat crystals in the bulk after 3 months and 15 months (Figure C4, Appendix C). In fact, the oleogel thickness was seen to increase during storage time; a contribution to such increase is also due to the decrease in overrun, as fewer air bubbles were present in the continuous phase. The observed increase in the average sphericity of the air bubbles could result from both the dissolution of the smaller CNPs attached at the air/oil interface, which caused the air bubble boundary to relax, as well as the decrease in the number of neighbouring bubbles in the microstructure. Analysis of the viscoelastic profile of the aged samples showed that storage resulted also in a slight increase in the loss modulus (G”), as shown in Figure C5 (Appendix C). After 15 months of storage, only samples with higher amounts of stabilizing crystals (i.e., higher SFC%) can retain an aerated structure. Therefore, the amount of fat crystals plays a significant role in the stability of the oleofoams. At this stage of ageing, however, the effect of disproportion was indeed obvious, with a visible increase in the average bubble size.

6.3.3 Effect of Heating

Figure 6.10 shows the microstructure of fresh samples (15S and 30F) after being heated to 25 and 27°C, respectively.

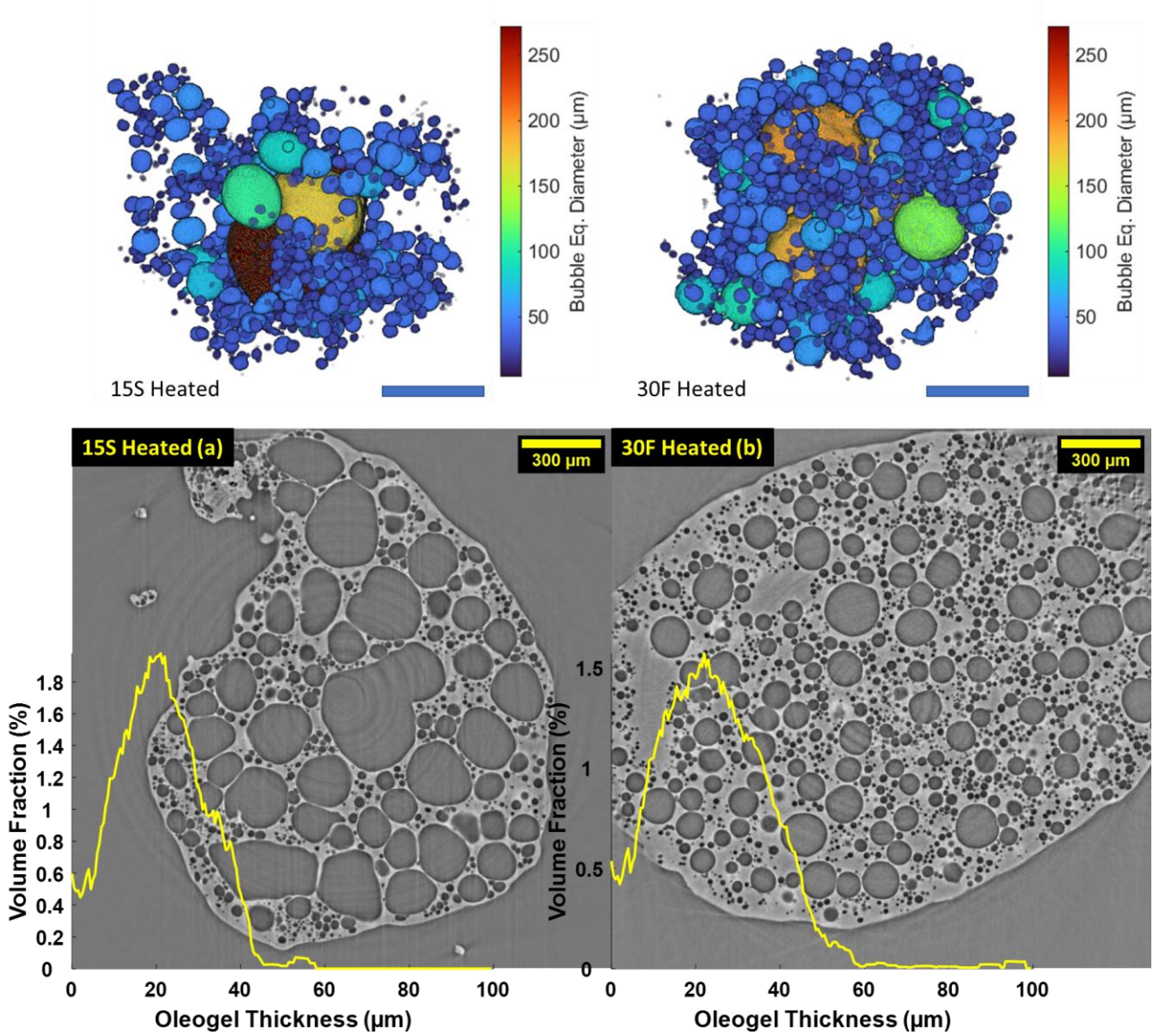

Figure 6.10. 3D renderings (top row) and tomography slices (bottom row) of samples 15S and 30F after being heated. The oleogel thickness distribution is overlaid on the tomography images. Scale bar for the 3D renderings is 250 µm.

Heating the oleofoams to their respective peak melting temperatures caused melting of the fat crystals surrounding the air bubbles, as well as the ones in the bulk, resulting in the coalescence of the air bubbles, and the relaxation of surface of the air bubbles to a more spherical shape. The oleogel thickness of both samples increased compared to the respective fresh samples; however, in contrast with aged samples, such increase was due to the dissolution of the air bubbles, rather than the growth of the crystals in the continuous phase. By comparing Figure 6.10a and Figure 6.10b, sample 15S displayed larger coalesced bubbles,

potentially due to the lower amount of fat crystals in the bulk that prevented aggregations of neighbouring bubbles. Table 6.3 summarizes the changes in the microstructure of heated samples.

Table 6.3. Parameters describing the microstructure of the heated samples (15S and 30F) compared to their fresh analogues.

Sample	$D_{oleogel}$	Bubbles / μm^3 ($\times 10^{-6}$)	Mean D_{eq}	D[4,3]	Mean Φ
15S Fresh	11 ± 6	51.1 ± 5.97	20 ± 9	45 ± 37	0.86 ± 0.11
15S Heated	20 ± 26	20.49 ± 5.41	18 ± 12	105 ± 74	0.93 ± 0.06
30F Fresh	20 ± 13	46.45 ± 5.52	19 ± 11	78 ± 69	0.88 ± 0.11
30F Heated	23 ± 33	23.58 ± 15.15	19 ± 13	164 ± 136	0.95 ± 0.05

During the thermal treatment, the samples became less viscous, flowing partially out of the field of view of the X-ray beam. Hence, a direct comparison of the fresh and heated samples could not be made. In fact, the calculated overrun for the heated samples resulted higher (> 200 %) compared to the fresh samples. As no air was further incorporated during heating, this observation could be explained only with partial loss of the continuous phase. Nevertheless, a qualitative description of the effect of heating on the oleofoam microstructure was carried out. The normalized amount of air bubbles decreased more significantly for sample 15S Heated, with a similar trend observed during ageing. The sphericity of the air bubbles increased for both samples, as visible in Figure 6.10. The effect of heating on the air phase is shown in more detail in Figure 6.11.

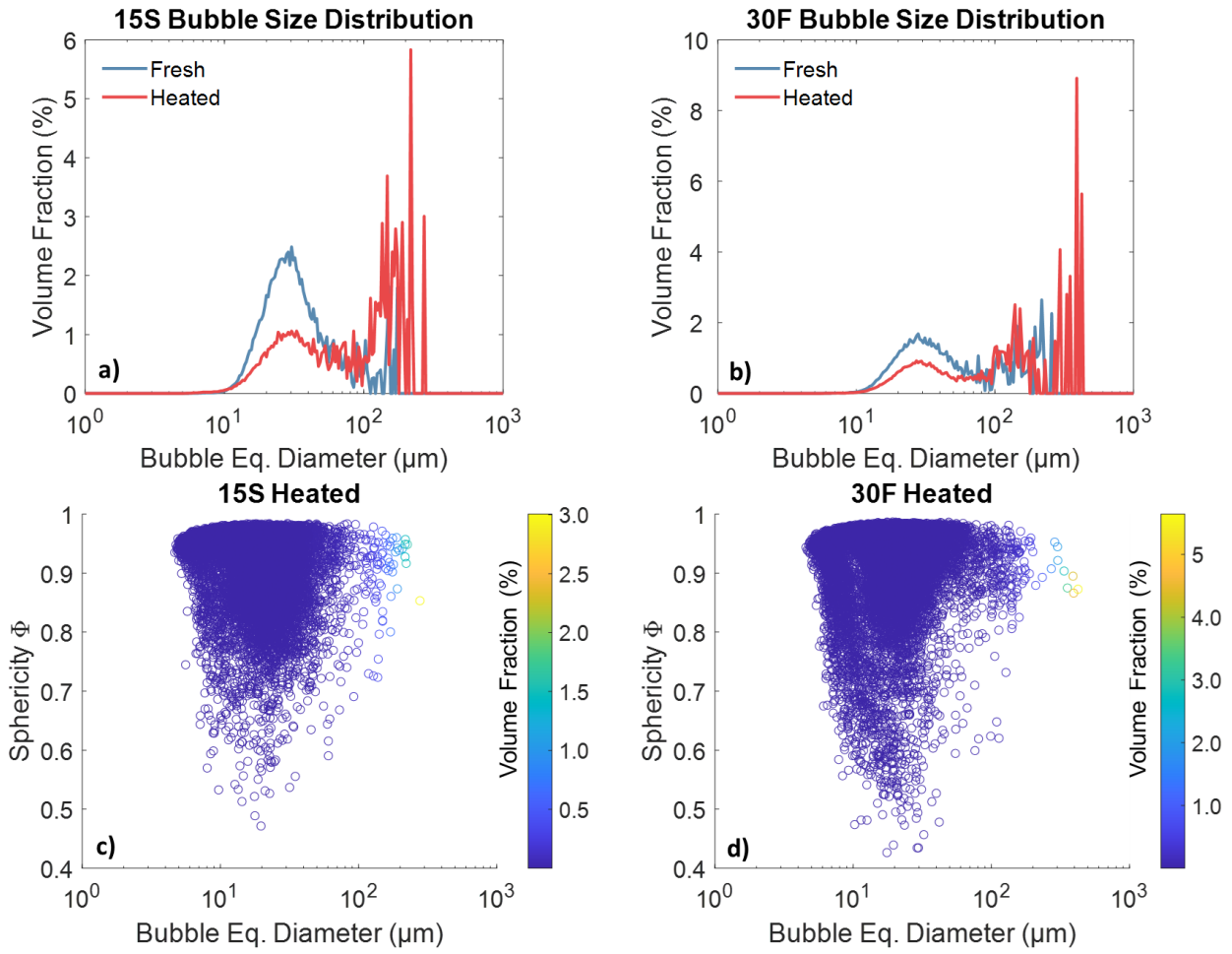

Figure 6.11. Volume-weighed size distribution of sample 15S Heated (a) and 30F Heated (b) compared with their respective fresh samples. Scatter plot showing the size and sphericity distribution of the air phase for sample 15S Heated (c) and 30F Heated (d).

Analysis of the volume-weighed size distribution resulted more revealing in describing the changes in the microstructure for the heated samples. In particular, the main distribution peak, centred at 30 µm, decreased in favour of several peaks between 100 and 500 µm, which represented the coalesced air bubbles. In fact, the volume-weighed mean diameter D[4,3], increased by 130% for sample 15S, and by 109% for sample 30F. The effect of heating was also visible in the scatter plots (Figure 6.10c and d), with a shift in the bubble population towards higher sphericity values, compared to the fresh samples from the fresh samples from Figure 6.4. In particular, coalesced bubbles with diameter exceeding 100 µm and high sphericity are visible in the top-right area of the plot. The melting of the stabilizing CNPs, both at the interface and in the continuous phase, caused the oleofoam to behave more like a liquid foam.

In order to study the destabilization mechanism that caused the changes in the microstructure of the heated samples, the sequence of XRR frames was analysed. Figure 6.12 contains selected difference image frames of a 30F sample during heating.

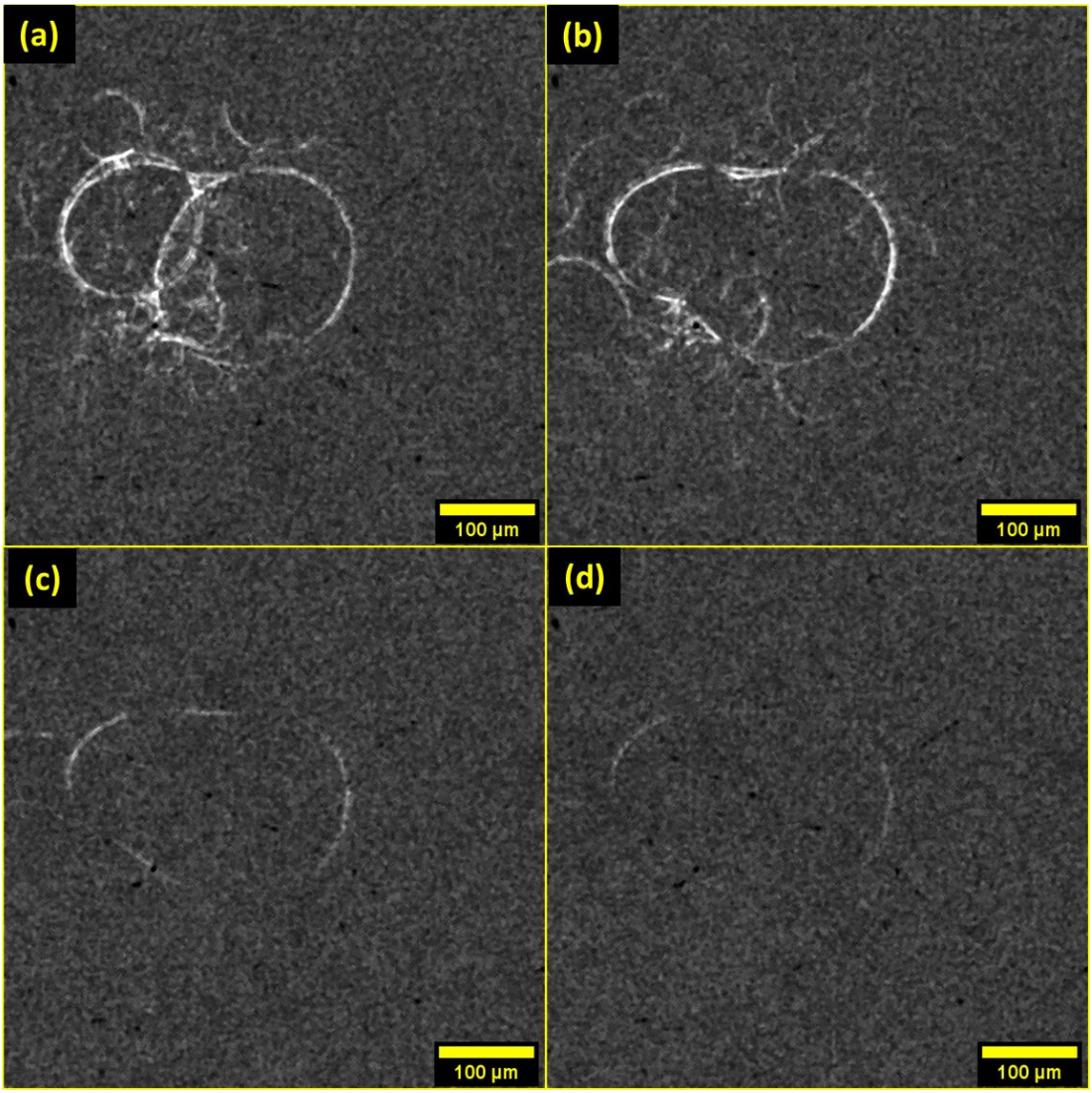

Figure 6.12 . Sequence of difference images, obtained from XRR, showing the coalescence of two neighbouring bubbles from a 30F fresh sample during thermal treatment.

During heating, the main events captured involved either sample movement, as the partially melted oleogel phase became less viscous, or bubble coalescence, which occurred by sequential merging of neighbouring bubbles. More specifically, bubbles were seen to aggregate (Figure 6.12a), with consequent film rupturing and merging (Figure 6.12b), followed by bubble shape relaxation (Figure 6.12c and d). This phenomenon was

observed also for droplets in water-in-oil emulsions (Ghosh & Rousseau, 2011). From this analysis, it can also be appreciated that bubble aggregation was irreversible, and that film rupturing and merging occurred on a shorter timescale (*ca.* 0.5 seconds) compared to the relaxation of the newly-coalescence air bubble. It is highly likely that coalescence was accompanied by Ostwald ripening of the air bubbles, considering that during heating the CNPs that act as Pickering stabilizers melt, leaving no physical barrier to prevent gas diffusion between bubbles. However, the shrinkage of air bubbles could not be observed unambiguously from the XRR difference images. This could be ascribed to the high level of noise in the difference image stack, and that bubble shrinkage affects mainly small bubbles rather than large, more visible ones.

The occurrence of coalescence events in the difference image stack can be monitored to determine the corresponding temperature at which the oleofoam begins to destabilize. To do so, the sequence of XRR images were analysed using Principal Component Analysis. The principal score 1, which accounts for most of the variance in the image sequence dataset, was plotted against the temperature to establish precisely the onset of microstructural destabilisation in the oleofoam samples. The results are shown in Figure 6.13 for a 15S sample.

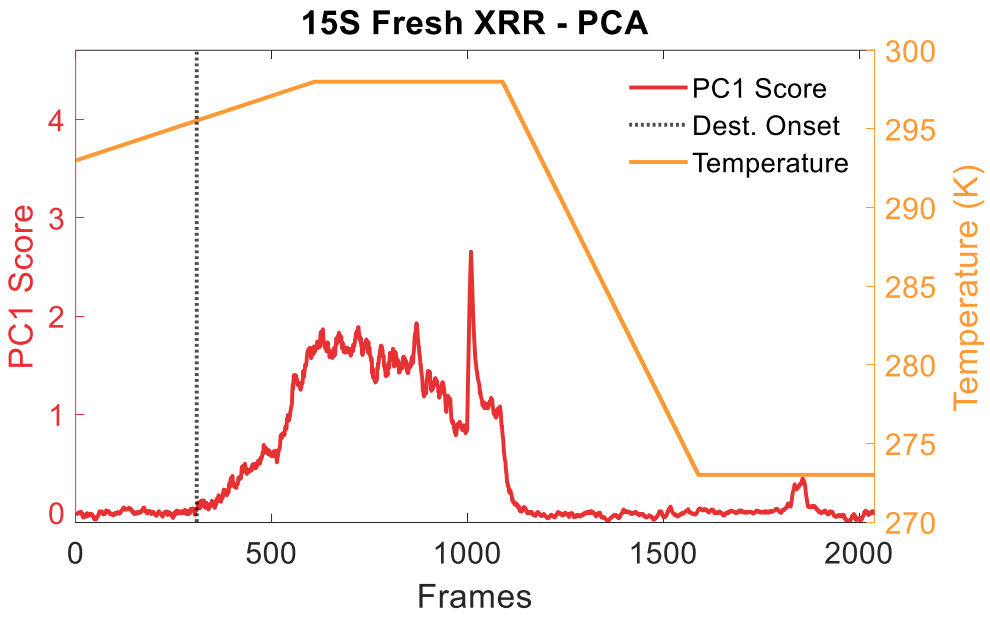

Figure 6.13. PCA Score plot of the difference image stack collected during heating of sample 15S (red), together with the temperature profile during the thermal treatment (orange) The onset of destabilisation (T_{onset}) is shown with the black dotted line.

Changes in the pixel intensity caused by either sample movement or bubble coalescence are shown as an abrupt increases of the PC1 Score value (red trace). In particular, a significant deviation of the PC1 score from the baseline during heating was as attributed to the onset of mechanical destabilization of the oleofoam sample. The corresponding temperature onset (XRR T_{onset}) is shown in Figure 6.13 as a dotted black line. An overview of Figure 6.13 demonstrated that the oleofoam microstructure is subject to changes after the melting onset (DSC T_{onset}), and that the destabilisation is promptly halted as soon as the temperature is lowered below the DSC $T_{melting}$. Table 6.4 displays the melting parameters, calculated from DSC, and the XRR T_{onset} for samples 15S and 30F.

Table 6.4. Oleogel thickness, number of bubbles and onset temperatures of melting for fresh oleofoam samples.

Sample	DSC T_{onset} (°C)	DSC $T_{melting}$ (°C)	XRR T_{onset} (°C)	ΔT_{onset}
15S Fresh	21.28 ± 0.27	24.98 ± 0.67	23.53 ± 0.50	2.25
30F Fresh	21.87 ± 0.82	27.30 ± 0.08	25.21 ± 0.58	3.34

Comparison of the onset temperatures calculated from DSC and XRR suggests that structural destabilisation in oleofoams occurred at higher temperatures compared to the onset of crystal melting. In particular, the difference in onset temperature (ΔT_{onset}) demonstrated that sample 30F exhibited a larger thermal delay in its mechanical destabilisation than sample 15S, confirming the higher stability endowed by the higher concentration of fat crystals. Furthermore, the air phase could also act as a thermal insulator, slowing the heat transfer towards the centre of the sample and causing a delay in the melting of the crystals.

6.4 Conclusions

In this paper, the three-dimensional native microstructure of fat stabilized oleofoams was investigated for the first time, both in static and dynamic experiments, using X-Ray Tomography and Radiography. These techniques enabled the measurement of the thickness of the continuous phase, and the bubble size and

shape distribution of two cocoa butter–based oleofoams, with either low or high fat crystal content, in relation to the effects of aeration, storage, and heating. Air incorporation in oleofoams resulted in a gradual increase in overrun, concomitant with a decrease in the oleogel thickness. In particular, low-cocoa butter samples displayed a higher overrun (170%) and a smaller oleogel thickness (10 μm), reaching an overrun equilibrium value after 15 minutes of whipping. Samples with higher cocoa butter content, on the other hand, incorporated less air (125% overrun) and featured a coarse final microstructure, retaining fragments of unwhipped oleogel with an average diameter of 35 μm after 30 minutes of whipping. The air bubble size distribution, centred at 20 μm, was not affected by the amount of solid fat or the whipping time, suggesting that the shear induced during aeration produced stabilizing crystals with similar properties (size, shape and polymorphism) regardless of the sample and the duration of whipping. Both samples contained a small number of large, deformed bubbles, potentially resulting from coalescence during air entrainment.

Oleofoam samples in storage were subjected to significant post-processing phenomena, as the continuous gel phase increased its thickness after 3 months and the overrun decreased significantly for both samples. The mean sphericity of the air bubbles increased, as a consequence of dissolution of smaller cocoa butter CNPs on the bubble surface in favour of larger crystal aggregates in the bulk phase, driven by Ostwald ripening of the crystals. Higher concentration of fat crystals in the sample (higher SFC) contributed to slow disproportionation of the air bubbles, with sample 30F retaining a similar size distribution profile after 3 months. After prolonged storage conditions, however, only samples with 30% cocoa butter retained an aerated structure. Ostwald ripening of the gas bubbles was also observed for these samples, with a modest increase in their mean equivalent diameter (from 19 to 24 μm). Therefore, higher amounts of stabilizing crystals were beneficial to retaining the overrun and counteracting phase separation.

Finally, heating the oleofoam samples to their melting point resulted in an increase in bubble sphericity, bubble coalescence, increase in the oleogel thickness, and reduction of the total number of air bubbles. Similarly to the results from storage conditions, sample 15S was more prone to coalescence than sample 30F, potentially due to the lower amount of stabilizing crystals. By comparing the volume-weighted average (D[4,3]), the effect of heating caused a percentage increase by 130 and 109% for samples 15S and 30F,

respectively. The increase in the bubble size followed by melting of the crystals both at the interface and in the bulk supports the hypothesis that bulk contribution to stability in oleofoams is fundamental to prevent gas diffusion. Most importantly, the dynamic changes in the oleofoam microstructure were captured for the first time with XRR, showing clear evidence of bubble coalescence during heating. Finally, XRR data combined with statistical analysis provided a mechanical destabilization parameter, XRR T_{onset}, which gives a more accurate temperature for the mechanical collapse of the oleofoams as compared with traditional DSC data.

This body of work, unprecedented due to the non-invasive, three-dimensional approach to the study of oleofoams, contains significant information on the physical behaviour of these emerging materials, in relation to relevant processes such as their aeration, storage conditions that will contribute to their understanding and use in material formulation.

Declaration of Competing Interests

The authors declare that they have no known competing financial interests or personal relationships that could have appeared to influence the work reported in this paper.

Acknowledgements

We acknowledge Diamond Light Source for time on I13-2 under proposal MG24233-1 and MG25431-3. The authors would like to acknowledge the Engineering and Physical Sciences Research Council funded Centre for Doctoral Training in Soft Matter and Functional Interfaces, grant ref. no. EP/L015536/1 as well as Nestlé PTC Confectionery (York, UK) for the financial and writing support. E.S. also acknowledges Royal Society (Grant ref. no. INF\R2\192018) for additional funding.

References

Asioli, D., Aschemann-Witzel, J., Caputo, V., Vecchio, R., Annunziata, A., Næs, T., & Varela, P. (2017). Making sense of the “clean label” trends: A review of consumer food choice behavior and discussion of industry implications. *Food Research International*, *99*(April), 58–71.

https://doi.org/10.1016/j.foodres.2017.07.022

Bergeron, V., Hanssen, J. E., & Shoghl, F. N. (1997). Thin-film forces in hydrocarbon foam films and their application to gas- blocking foams in enhanced oil recovery. *Colloids and Surfaces A: Physicochemical and Engineering Aspects*, *123–124*, 609–622. https://doi.org/10.1016/S0927-7757(96)03808-3

Binks, B. P., Garvey, E. J., & Vieira, J. (2016). Whipped oil stabilised by surfactant crystals. *Chem. Sci.*, *7*(4), 2621–2632. https://doi.org/10.1039/C6SC00046K

Binks, B. P., & Marinopoulos, I. (2017). Ultra-stable self-foaming oils. *Food Research International*, *95*, 28–37. https://doi.org/10.1016/j.foodres.2017.02.020

Binks, B. P., & Vishal, B. (2021). Particle-stabilized oil foams. *Advances in Colloid and Interface Science*, *291*, 102404. https://doi.org/10.1016/j.cis.2021.102404

Brun, M., Delample, M., Harte, E., Lecomte, S., & Leal-Calderon, F. (2015). Stabilization of air bubbles in oil by surfactant crystals: A route to produce air-in-oil foams and air-in-oil-in-water emulsions. *Food Research International*, *67*, 366–375. https://doi.org/10.1016/j.foodres.2014.11.044

Callau, M., Sow-Kébé, K., Jenkins, N., & Fameau, A. L. (2020). Effect of the ratio between fatty alcohol and fatty acid on foaming properties of whipped oleogels. *Food Chemistry*, *333*(June), 127403. https://doi.org/10.1016/j.foodchem.2020.127403

Chen, J., He, L., Luo, X., & Zhang, C. (2018). Foaming of crude oil: Effect of acidic components and saturation gas. *Colloids and Surfaces A: Physicochemical and Engineering Aspects*, *553*(March), 432–438. https://doi.org/10.1016/j.colsurfa.2018.05.097

Denkov, N., Tcholakova, S., & Politova-Brinkova, N. (2020). Physicochemical control of foam properties. *Current Opinion in Colloid and Interface Science*, *50*, 101376. https://doi.org/10.1016/j.cocis.2020.08.001

Doube, M., Klosowski, M. M., Arganda-Carreras, I., Cordelières, F. P., Dougherty, R. P., Jackson, J. S., … Shefelbine, S. J. (2010). BoneJ: Free and extensible bone image analysis in ImageJ. *Bone*, *47*(6), 1076–

1079. https://doi.org/10.1016/j.bone.2010.08.023

Dowd, B. A., Campbell, G. H., Siddons, D. P., & Marr, R. B. (1999). Developments in synchrotron x-ray computed microtomography at the National Synchrotron Light Source. *Proc. SPIE. 3772, Developments in X-Ray Tomography II*, (July 1999).

Du, L., Jiang, Q., Li, S., Zhou, Q., Tan, Y., & Meng, Z. (2021). Microstructure evolution and partial coalescence in the whipping process of oleofoams stabilized by monoglycerides. *Food Hydrocolloids*, *112*(May 2020), 106245. https://doi.org/10.1016/j.foodhyd.2020.106245

Fameau, A. L., & Binks, B. P. (2021). Aqueous and Oil Foams Stabilized by Surfactant Crystals: New Concepts and Perspectives. *Langmuir*, *37*(15), 4411–4418. https://doi.org/10.1021/acs.langmuir.1c00410

Fameau, A. L., & Fujii, S. (2020). Stimuli-responsive liquid foams: From design to applications. *Current Opinion in Colloid and Interface Science*, *50*, 101380. https://doi.org/10.1016/j.cocis.2020.08.005

Fameau, A. L., Lam, S., Arnould, A., Gaillard, C., Velev, O. D., & Saint-Jalmes, A. (2015). Smart Nonaqueous Foams from Lipid-Based Oleogel. *Langmuir*, *31*(50), 13501–13510. https://doi.org/10.1021/acs.langmuir.5b03660

Fameau, A. L., & Saint-Jalmes, A. (2017). Non-aqueous foams: Current understanding on the formation and stability mechanisms. *Advances in Colloid and Interface Science*, *247*, 454–464. https://doi.org/10.1016/j.cis.2017.02.007

Ghosh, S., & Rousseau, D. (2011). Fat crystals and water-in-oil emulsion stability. *Current Opinion in Colloid and Interface Science*, *16*(5), 421–431. https://doi.org/10.1016/j.cocis.2011.06.006

Goibier, L., Pillement, C., Monteil, J., Faure, C., & Leal-Calderon, F. (2019). Emulsification of non-aqueous foams stabilized by fat crystals: Towards novel air-in-oil-in-water food colloids. *Food Chemistry*, *293*. https://doi.org/10.1016/j.foodchem.2019.04.080

Gunes, D. Z., Murith, M., Godefroid, J., Pelloux, C., Deyber, H., Schafer, O., & Breton, O. (2017). Oleofoams: Properties of Crystal-Coated Bubbles from Whipped Oleogels-Evidence for Pickering Stabilization.

Langmuir, *33*(6), 1563–1575. https://doi.org/10.1021/acs.langmuir.6b04141

Gürsoy, D., De Carlo, F., Xiao, X., & Jacobsen, C. (2014). TomoPy: A framework for the analysis of synchrotron tomographic data. *Journal of Synchrotron Radiation*, *21*(5), 1188–1193. https://doi.org/10.1107/S1600577514013939

H. Chisholm, Z.D. Gunes, C. Gehin-Delval, A. Nouzille, E. Garvey, M.J. Destribats, S.N. Chandrasekaran, J. Vieira, J. German and B.P. Binks (2016). Aerated confectionery material. *WO 2016/150977 Al*.

Heymans, R., Tavernier, I., Danthine, S., Rimaux, T., Van Meeren, P., & Dewettinck, K. (2018). Food-grade monoglyceride oil foams: The effect of tempering on foamability, foam stability and rheological properties. *Food and Function*, *9*(6), 3143–3154. https://doi.org/10.1039/c8fo00536b

Heymans, R., Tavernier, I., Dewettinck, K., & Van der Meeren, P. (2017). Crystal stabilization of edible oil foams. *Trends in Food Science and Technology*, *69*, 13–24. https://doi.org/10.1016/j.tifs.2017.08.015

Hildebrand, T., & Rüegsegger, P. (1997). A new method for the model-independent assessment of thickness in three-dimensional images. *Journal of Microscopy*, *185*(1), 67–75. https://doi.org/10.1046/j.1365-2818.1997.1340694.x

Himawan, C., Starov, V. M., & Stapley, A. G. F. (2006). Thermodynamic and kinetic aspects of fat crystallization. *Advances in Colloid and Interface Science*, *122*, 3–33. https://doi.org/10.1016/j.cis.2006.06.016

Karthick, A., Roy, B., & Chattopadhyay, P. (2019). A review on the application of chemical surfactant and surfactant foam for remediation of petroleum oil contaminated soil. *Journal of Environmental Management*, *243*(January), 187–205. https://doi.org/10.1016/j.jenvman.2019.04.092

Kinoshita, N., Sasaki, Y., Marukawa, E., Hirose, R., Sawada, S. ichi, Harada, H., & Akiyoshi, K. (2020). Crosslinked nanogel-based porous hydrogel as a functional scaffold for tongue muscle regeneration. *Journal of Biomaterials Science, Polymer Edition*, *31*(10), 1254–1271. https://doi.org/10.1080/09205063.2020.1744246

Liu, Y., & Binks, B. P. (2021a). A novel strategy to fabricate stable oil foams with sucrose ester surfactant. *Journal of Colloid and Interface Science*, *594*, 204–216. https://doi.org/10.1016/j.jcis.2021.03.021

Liu, Y., & Binks, B. P. (2021b). Foams of vegetable oils containing long-chain triglycerides. *Journal of Colloid and Interface Science*, *583*, 522–534. https://doi.org/10.1016/j.jcis.2020.09.043

Luengo, G. S., Fameau, A. L., Léonforte, F., & Greaves, A. J. (2021). Surface science of cosmetic substrates, cleansing actives and formulations. *Advances in Colloid and Interface Science*, *290*. https://doi.org/10.1016/j.cis.2021.102383

Manzocco, L., Mikkonen, K. S., & García-González, C. A. (2021). Aerogels as porous structures for food applications: Smart ingredients and novel packaging materials. *Food Structure*, *28*(February). https://doi.org/10.1016/j.foostr.2021.100188

Metilli, L., Lazidis, A., Francis, M., Marty-terrade, S., Ray, J., & Simone, E. (2021). The Effect of Crystallization Conditions on the Structural Properties of Oleofoams Made of Cocoa Butter Crystals and High Oleic Sunflower Oil. *Crystal Growth and Design*. https://doi.org/10.1021/acs.cgd.0c01361

Metilli, L., Storm, M., Bodey, A. J., Wanelik, K., Tyler, A. I. I., Lazidis, A., … Simone, E. (2021). Investigating the microstructure of soft, microporous matter with synchrotron X-ray tomography. *Materials Characterization*, *180*(October), 111408. https://doi.org/10.1016/j.matchar.2021.111408

Mishima, S., Suzuki, A., Sato, K., & Ueno, S. (2016). Formation and Microstructures of Whipped Oils Composed of Vegetable Oils and High-Melting Fat Crystals. *JAOCS, Journal of the American Oil Chemists' Society*, *93*(11), 1453–1466. https://doi.org/10.1007/s11746-016-2888-4

Parsa, M., Trybala, A., Malik, D. J., & Starov, V. (2019). Foam in pharmaceutical and medical applications. *Current Opinion in Colloid and Interface Science*, *44*, 153–167. https://doi.org/10.1016/j.cocis.2019.10.007

Ramel, P. R., Co, E. D., Acevedo, N. C., & Marangoni, A. G. (2016). Structure and functionality of nanostructured triacylglycerol crystal networks. *Progress in Lipid Research*, *64*, 231–242.

https://doi.org/10.1016/j.plipres.2016.09.004

Saha, S., Saint-Michel, B., Leynes, V., Binks, B. P., & Garbin, V. (2020). Stability of bubbles in wax-based oleofoams: decoupling the effects of bulk oleogel rheology and interfacial rheology. *Rheologica Acta*, *59*(4), 255–266. https://doi.org/10.1007/s00397-020-01192-x

Shrestha, L. K., Shrestha, R. G., Sharma, S. C., & Aramaki, K. (2008). Stabilization of nonaqueous foam with lamellar liquid crystal particles in diglycerol monolaurate/olive oil system. *Journal of Colloid and Interface Science*, *328*(1), 172–179. https://doi.org/10.1016/j.jcis.2008.08.051

Subramaniam, A. B., Abkarian, M., Mahadevan, L., & Stone, H. A. (2005). Colloid science: Non-spherical bubbles. *Nature*, *438*(7070), 930. https://doi.org/10.1038/438930a

Tamarkin, D, Shifrin, H, Keynan, R, Ziv, E, Berman, Tal, Schuz, D, Gazal, E. (2019). Oil Foamable Carriers and Formulation. *US 2019 / 0091149 A1*, *1*, 1–10.

Truong, T., Prakash, S., & Bhandari, B. (2019). Effects of crystallisation of native phytosterols and monoacylglycerols on foaming properties of whipped oleogels. *Food Chemistry*, *285*(January), 86–93. https://doi.org/10.1016/j.foodchem.2019.01.134

Vo, T. N., Atwood, C. R., & Drakopoulos, M. (2018). Superior techniques for eliminating ring artifacts in X-ray micro-tomography. *Optics Express*, *26*(22), 28396–28412.

Wadeson, N., & Basham, M. (2016). Savu: A Python-based, MPI Framework for Simultaneous Processing of Multiple, N-dimensional, Large Tomography Datasets. *ArXiv*. Retrieved from http://arxiv.org/abs/1610.08015

Z.D. Gunes, O. Schafer, H. Chisholm, H. Deyber, C. P. and B. P. B. (2016). Lipid based foam. *WO 2016/150978 Al*.

Chapter 7: Conclusions and Future Developments

Investigating the process-structure-function relationship of a novel material such as oleofoams is a complex and challenging task due to complexity and delicacy of these types of materials.

In this doctoral project, the research questions were motivated by the paucity of information on air-in-oil systems, despite their significant potential for application in the field of low-calories food products, active ingredient delivery for cosmetic and pharmaceuticals and, in general, thermo-responsive soft matter. The research questions were set to explore the process-structure-function relationship of a model oleofoam system, which plays a fundamental role in tailoring the properties of the material, as well as in optimizing the processing conditions for its manufacturing.

In this section a summary of the findings from the experimental work is presented, to address the research questions outlined in Chapter 1 of the Thesis.

What are the crystal properties that more significantly affect the functionality of cocoa butter–based oleofoams in terms of foamability and foam stability against phase separation, melting point, viscoelastic profile, morphology and stability of air bubbles?

Cocoa butter (CB) and sunflower oil (HOSO) oleogels were prepared according to different crystallization conditions, and subsequently aerated to investigate the effect of processing conditions on the properties of the related oleofoams. CB crystallized as spherical aggregates of crystalline nanoplatelets (CNPs), which size and concentration increased with slower cooling rates and higher % of added CB. The CNPs were found to crystallize in the β(V) polymorph under all conditions; X-Ray scattering experiments carried in quiescent conditions suggested that CB might have first nucleated as α or β’ crystals, but then quickly transformed to the more stable form through a melt-mediated polymorphic transition. The aeration broke down the spherical aggregates to crystal nanoplatelets of similar size which stabilized the entrained air

bubbles with a Pickering mechanism. The excess CB crystals formed a three-dimensional network in the bulk that provided further stabilisation to the oleofoam. Hence, the amount of added CB was the parameter that affected more strongly the foamability of oleofoams, in particular samples with high CB % could reach a lower overrun and contained visible domains of unwhipped oleogel. The aeration led to an increase both in the elastic (G') and viscous (G") from the unwhipped oleogel at 15% CB concentration, which was ascribed to the re-organization of the fat crystals structure around the air bubbles. This effect was less significant for samples with 22% CB, and was negligible for samples with 30% CB, potentially due to the existence of a sufficiently strong fat network which viscoelastic properties were not affected as much by aeration. Nevertheless, all samples had their density reduced by a factor between 3 and 1.6 compared to their respective oleogels, and were stable against oil drainage for at least three months in storage.

The results of this work provided useful characterization of the processes relevant to the production of oleofoams, *i.e.*, shear crystallization and aeration, and demonstrated that the amount of fat crystals was the main parameter affecting the foamability and quality of the oleofoam samples.

Can ultrasound spectroscopy, which is a non-invasive, non-destructive technique, be implemented in a small-scale reactor as a PAT tool to follow fat crystallization, and to extract quantitative information about the amount of crystals in the oleogel?

A novel acoustic immersion probe, based on pulsed acoustic spectroscopy technique, was developed and applied to the study of fat crystallization in a small-scale vessel under shear. In particular, the probe was used as a process analytical technology (PAT) tool, in combination with light turbidimetry, to monitor nucleation and crystal growth, and to calculate the solid fat content (SFC%) of the oleogel during the crystallization process. Cocoa butter and sunflower oil oleogels with increasing CB % were crystallized under shear. A significant decrease in light transmittance signalled the onset of nucleation; the light

absorbance and acoustic attenuation increased during the growth of the fat crystalline network, exhibiting a similar trend over time. The velocity of sound, which was linearly dependent on the temperature of the sample in the liquid phase, displayed a sharp increase as the sample transformed from liquid to solid. The velocity of sound in the oleogel sample, at the end of the crystallization process (5°C), was dependent on the amount of added CB, increasing by *ca.* 10 m/s every 2% of added CB. The SFC% was determined ex-situ using pulsed nuclear magnetic resonance (*p*NMR), which showed that, at the same temperature (5°C), the SFC% was slightly lower than the total amount of CB %, due to the presence in cocoa butter of non-TAG molecules that potentially do not crystallize under these conditions. By combining the velocity of sound, sample temperature and SFC% calculated from *p*NMR, it was possible to train a predictive model using the Regression Learner app in MATLAB2021a to predict the SFC% evolution during the crystallization experiment. The model, based on the Gaussian Process Regression, showed a sharp increase in the SFC% during crystal growth, with the same trend of the light absorbance and acoustic attenuation. Moreover, the SFC% decreased during the heating of the samples, following the same melting profile obtained during the *p*NMR experiment.

This work demonstrated the capability of pulsed acoustic spectroscopy to monitor fat crystallization in oleogels, and to determine quantitatively, and accurately, the amount of crystals during the crystallization process in a rapid, online fashion. Moreover, as acoustic techniques are scarcely used in PAT frameworks, these results are encouraging in promoting their implementation for other melt crystallization operations. As mentioned in the previous research question, the total amount of fat crystals was the main parameter affecting the oleofoam properties, hence this technique will prove useful in the design a large-scale manufacturing process unit.

What is a suitable technique for investigating the internal microstructure of oleofoams, which are soft, low-melting and opaque materials? What parameters may be obtained and used to describe the microstructure of oleofoams?

A novel methodology was applied with synchrotron radiation X-Ray tomography and radiography to the study of soft microporous samples, to provide high quality, three-dimensional tomography images, both in static conditions and under external stimuli. The methodology was demonstrated with two reference oleofoam samples, one with low (15% w/w) and one with high (30% w/w) CB content. The samples were placed on top of a toothpick, in front of the X-Ray beam. Sample pre-stabilization by immersion in liquid nitrogen, temperature control and optimization of the beamline setup enabled the reconstruction of tomography images of the samples without any distortion. The application of a Paganin filter, which displays the X-Ray refractivity of the sample, rather than the attenuation, resulted in further improvement of the signal-to-noise ratio. The image post-processing step, which was developed in ImageJ, was able to segment the air phase from the continuous phase, and enabled calculation of the bubble size and shape distribution, air volume fraction, and continuous phase thickness. Comparison of the overrun (calculated from the air volume fraction) obtained from the cup method (i.e., weighing the sample in a cup of fixed volume), and from tomography measurements of the same samples, showed that some degree of discrepancy between the two techniques, ascribed to the different sampling volumes. While the cup method was more representative, due to the larger volume (30 mL compared to 1 mL), the overrun calculated from tomography enabled the determination of the aeration heterogeneity in the sample. Finally, samples with significantly different microstructure (fresh and heated) were analysed and compared, showing that the bubbles volume-weighted equivalent diameter (D[4,3]) increased from 30 µm to 100 – 150 µm. The bubble sphericity, and the volume fraction of spherical bubbles, increased as well. These changes were attributed to the presence of large, coalesced bubbles with rounder shape, resulting from the partial melting of the stabilizing fat crystals at the interface. Moreover, the average oleogel thickness increased, due to part of the bubbles dissolving and leaving the sample.

Therefore, it was demonstrated that, with the aid of temperature control and optimization of the beamline setup, the internal microstructure of soft, microporous matter was accessible, providing high-

quality reconstructed images of the samples. Furthermore, the post-processing workflow enabled the extraction of meaningful parameters to describe the microstructure, for both the dispersed and continuous phase. While the method was demonstrated with oleofoams, it may be applied in the future to soft materials that share similar challenges in its characterization in the native state.

How does the three-dimensional microstructure of oleofoams evolve during manufacturing, storage and upon application of external stimuli?

The methodology developed in the previous section was applied to an extensive study of the microstructure of cocoa butter–based oleofoams, in relation to the aeration time, storage conditions, and the effect of heating. As the amount of cocoa butter (SFC%) was the main parameter affecting the oleofoam properties, two reference samples were chosen for analysis: one with low and one with high cocoa butter content. With regards to the aeration, it was shown that, already after 5 minutes, both samples displayed a similar bubble size distribution, log-normal in shape and centred at 20 μm. The bubble sphericity distribution was broad, ranging from 0.6 to 0.95, with an average value of 0.86 and 0.88 for samples 15S and 30F. The overrun, on the other hand, reached an equilibrium value of 170%, as calculated from tomography, already after 15 minutes of aeration for sample 15S; sample 30F, on the other hand, reached a final overrun of 130% after 30 minutes. The oleogel thickness decreased following the same trend of the overrun evolution, as large domains of unwhipped oleogel were dissolved to incorporate more air; therefore, sample 30F displayed a larger oleogel thickness, at the end of the aeration, compared to sample 15S. Hence, the SFC% played an important part in the rate of air incorporation and thickness of the continuous phase. As the CNPs spherical aggregates were broken down by aeration to individual CNPs of similar size, the bubble size distribution was not affected by SFC%.

With regards to the storage effect, sample 30F showed better stability to overrun loss, and bubble size disproportionation, compared to sample 15S. After 3 months, in fact, sample 15S exhibited a decrease of

overrun from 170% to 50%, and a decrease in the number of bubbles by more than 50%. At the same time, the oleogel thickness increased from an average 10 µm to 25 µm. Sample 30F, on the other hand, exhibited lesser decrease in overrun (from 130% to 70%), and a similar bubble size distribution to the fresh analogue. For both 15S and 30F samples, however, the bubble sphericity increased from an average of 0.86 and 0.88 to 0.93 and 0.92, respectively. This observation could be ascribed to the Ostwald ripening of the CNPs, where small platelets on the surface of the bubbles dissolved in favour of larger crystals, both at the interface and in the bulk. This hypothesis was confirmed by polarized light images of the same samples, which showed an increase in the thickness of birefringent crystals between bubbles during storage. The small changes in the bubble size distribution were attributed to the remarkable stability of oleofoams imparted by Pickering stabilisation of the fat crystals. After 15 months of storage, however, sample 15S lost its aerated microstructure, whereas sample 30F exhibited some degree of Ostwald ripening in the dispersed phase.

Heating the samples to their respective melting point resulted in an increase in the D[4,3], a decrease in the number of bubbles and an increase in the oleogel thickness. The use of X-Ray radiography enabled visualization of coalescence between bubbles, elucidating which destabilisation mechanism was predominant in the microstructure during heating. While gas transfer could not be observed directly, it is likely that it occurred during heating as well, considering that the stabilising fat crystals melted, offering no physical barrier between the bubbles to prevent disproportionation. Interestingly, the onset of destabilisation, as observed from X-Ray radiography, was delayed by 2.25 and 3.35 °C compared to melting onset calculated from differential scanning calorimetry (DSC), which was ascribed to the thermal insulation provided by air bubbles during heating of the samples.

Synchrotron radiation X-Ray tomography and radiography provided unprecedented results on the microstructure of oleofoams, which are challenging to image due to their soft nature. In particular, the information obtained within this work was instructive about the mechanism of aeration during whipping

of the oleofoams, which might be used to design improved aeration processes for the production of aerated oils. Furthermore, the complex interplay between ageing of the fat crystals and air bubbles was unveiled, highlighting the role of SFC% into the stability of the samples. Finally, as oleofoams constitute an attractive, thermo-responsive materials, information about the dynamics of destabilisation will be useful for the design of release profiles of flavours, bioactive ingredients or pharmaceuticals.

In summary, this doctoral project provided the results of an extensive study on the process-structure-function relationship of oleofoams. In particular, the main parameter affecting the properties of oleofoams - the SFC% - was identified, and a method to monitor its evolution during crystallization proposed and validated successfully, using a fast, reliable and non-invasive technique, aided by novel machine learning methods. This result is encouraging not only for the crystallization of oleofoam precursors, but for other processing operations that still rely on ex-situ methods. Similarly, a novel methodology for imaging soft microporous matter was developed within this doctoral project, which holds potential for being applied to soft materials which need to be further characterized.

Future Developments

- The current doctoral project focused on specific processing conditions and explored the effect of a limited set of variables, which were in this case the concentration of added fat and the cooling rate, and studied such effects on the properties of the related oleofoams. As the research on crystal-stabilized oleofoams is still in its infancy, an extended study on the stabilisation of the air/oil interface with different crystal properties (e.g. polymorphism, morphology) would be relevant to obtain oleofoams with different properties. These would include different bubble size distributions, different types of stabilizing fat networks in the bulk, with consequent novel rheological behaviour. This diversity could be achieved also by exploring other aeration

parameters, such as the geometry of the stirrer, and aeration speed. Moreover, the presence of an air/oil interface may be exploited to affect crystallization of fat crystals, as recently demonstrated by Mishra et al. (2020).

- Having developed the method for imaging soft, microporous matter, it would be relevant to attempt tomography experiments at higher resolution, such as the nanoscale, to visualize individual crystals adsorbed at the bubble interface, and to couple such experiments with external stimuli. In this way, precise arrangement of the fat crystals at the air/oil interface could be studied, which is currently lacking due to the complexity of the microstructure in oleofoams. At present, only the orientation of the stabilising crystals was investigated, using synchrotron radiation micro beam X-ray diffraction (SR-μ-XRD) (Mishima et al., 2016). This type of analysis may be applied to other soft multiphasic materials stabilized by particles, such as emulsions or aqueous foams, for which information about the adsorption of particles at the interfaces, in three-dimensions and in the native state, is also lacking.
- The use of pulse ultrasonic spectroscopy to characterize the properties of oleofoams has been attempted during this doctoral project, but it was not possible to obtain a robust correlation between acoustic data and, for example, sample density. Variations in density may be correlated to the increase in overrun during aeration, which is the main parameter used to describe the foamability of an oleogel. So far, foam density (and overrun) can be measured through gravimetric methods, or with tomography techniques. However, both methods require sample collection or off-line analysis. Hence, developing a hardware solution able to estimate the density of oleofoams in a non-invasive, non-destructive fashion could be a useful addition to the set of PAT tools available during manufacturing.

References

Mishima, S., Suzuki, A., Sato, K., & Ueno, S. (2016). Formation and Microstructures of Whipped Oils Composed of Vegetable Oils and High-Melting Fat Crystals. *JAOCS, Journal of the American Oil Chemists' Society*, *93*(11), 1453–1466. https://doi.org/10.1007/s11746-016-2888-4

Mishra, K., Bergfreund, J., Bertsch, P., Fischer, P., & Windhab, E. J. (2020). Crystallization-Induced Network Formation of Tri- And Monopalmitin at the Middle-Chain Triglyceride Oil/Air Interface. *Langmuir*, *36*(26), 7566–7572. https://doi.org/10.1021/acs.langmuir.0c01195

Appendix A: supporting information for Chapter 3

The solvent-subtracted diffraction patterns of crystallizing CB/HOSO mixtures were obtained by the following steps. In order to account for the relative amount of the liquid and solid phase, the baseline of the molten phase was corrected prior to being subtracted from the signal of the crystallized samples.

For the SR-XRD experiments, the integral of the diffraction patterns between q = 0.05 $Å^{-1}$ and q = 0.09 $Å^{-1}$ and q = 1.0 $Å^{-1}$ and q = 1.3 $Å^{-1}$ were calculated for SAXS and WAXS, respectively.

The integrals of the crystallized samples $Int_{mixture}$ (*i.e.* at 10 and 7°C) were then divided by the integral of the molten phase Int_{melt} (25°C or 20°C) to obtain a correction factor k (Equation A1):

$$\frac{Int_{mixture}}{Int_{melt}} = k \qquad \text{Eq. A1}$$

The intensity of the melt of each experiment was multiplied by the corresponding k factor (Equation A2), after which the subtraction of the background was carried out (Equation A3):

$$I_{melt} \times k = I'_{melt} \qquad \text{Eq. A2}$$

$$I_{subtracted} = I_{mixture} - I'_{melt} \qquad \text{Eq. A3}$$

The X-Ray diffraction patterns were also plotted according to the Lorentzian representation (q plotted against Iq^2) in order to investigate further the presence of additional peaks. For the benchtop X-Ray experiments, the integrals between q = 0.5 $Å^{-1}$ and q = 0.9 $Å^{-1}$ (SAXS) and q = 11.0 $Å^{-1}$ and q = 13.0 $Å^{-1}$ (WAXS) were instead evaluated, due to the different resolution of the instrument.

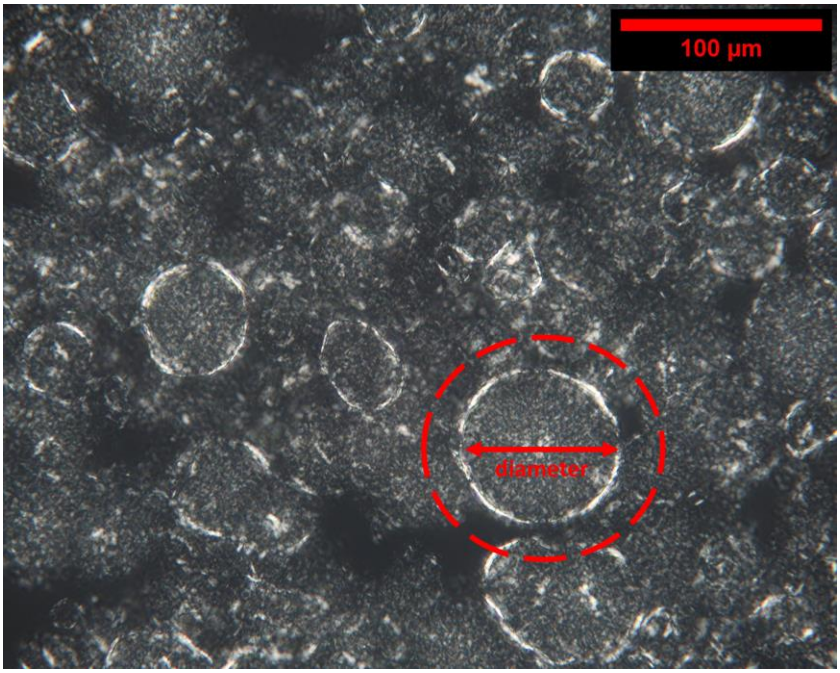

Figure A1 Polarized light image of a 22M oleogel, highlighting a single CB spherical aggregate and its diameter.

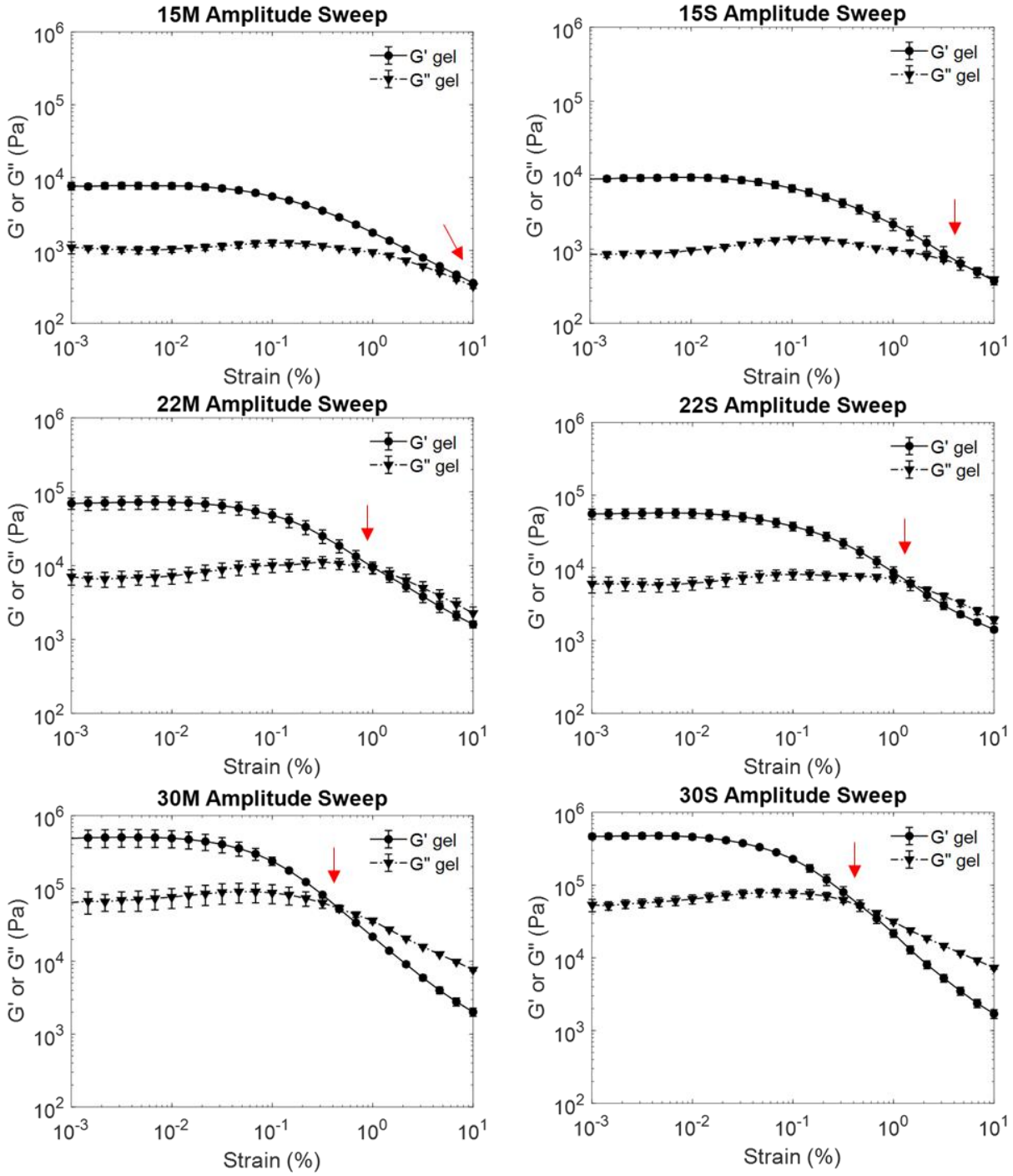

Figure A2. Oscillatory rheology of medium and slow-cooled oleogels crystallized in the lab-scale vessel. Elastic modulus (G') and viscous modulus (G") are plotted as a function of strain (%). The flow point (τf) is highlighted with a red arrow.

Table A1. Onset temperature and peak melting temperature of oleofoam samples after 30 minutes of aeration measured using differential scanning calorimetry.

Sample (oleofoam)	T_{onset} oleofoam (°C)	T_m oleofoam (°C)
15F	21.68 ± 0.04	25.01 ± 0.18
15M	21.40 ± 0.43	24.87 ± 0.25
15S	21.28 ± 0.27	24.98 ± 0.67
22F	21.15 ± 0.69	26.30 ± 0.33
22M	20.34 ± 0.08	25.80 ± 0.08
22S	22.43 ± 0.52	26.28 ± 0.21
30F	21.87 ± 0.82	27.30 ± 0.08
30M	22.01 ± 0.02	27.35 ± 0.20
30S	21.38 ± 0.17	27.39 ± 0.13

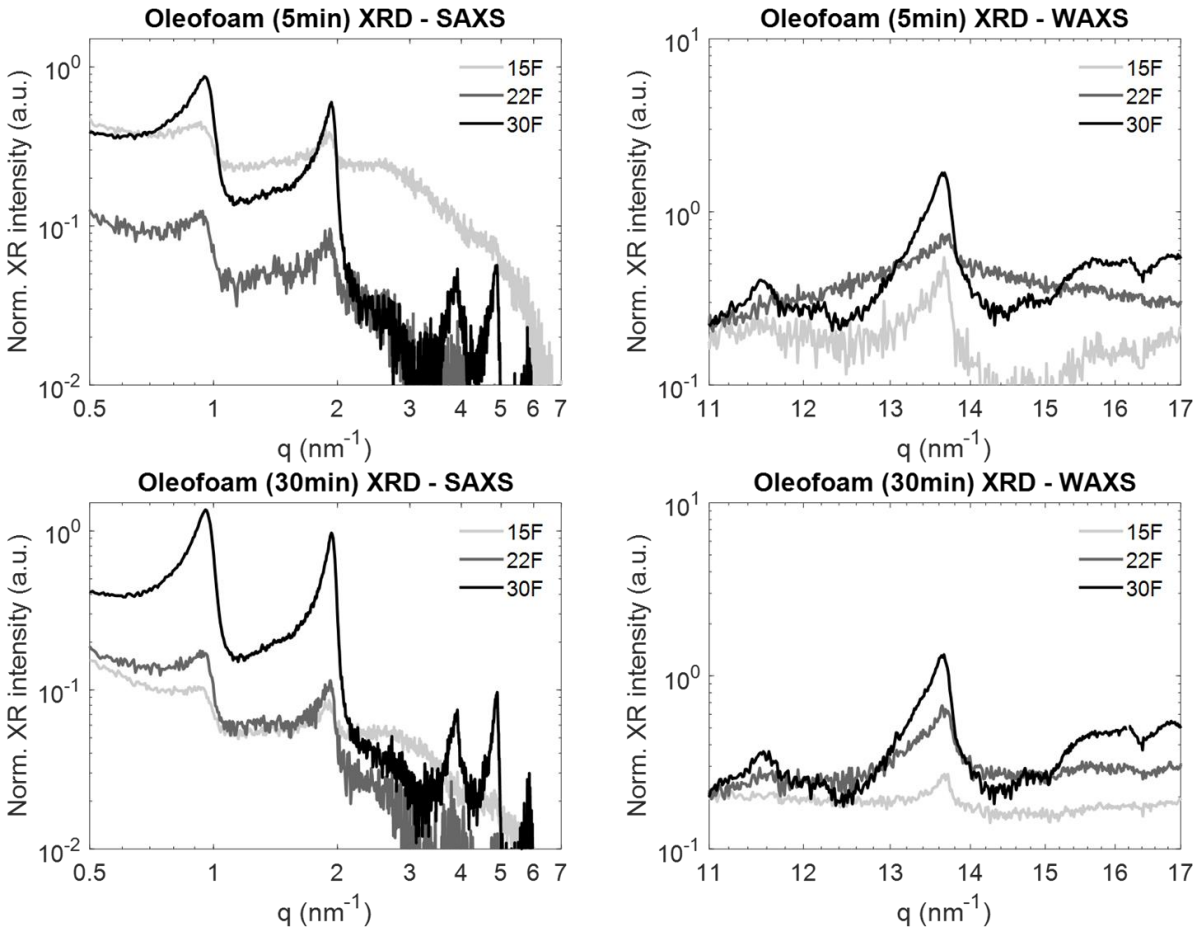

Figure A3. XRD patterns of oleofoams after 5 minutes of aeration (top row) and after 30 minutes of aeration (bottom row).

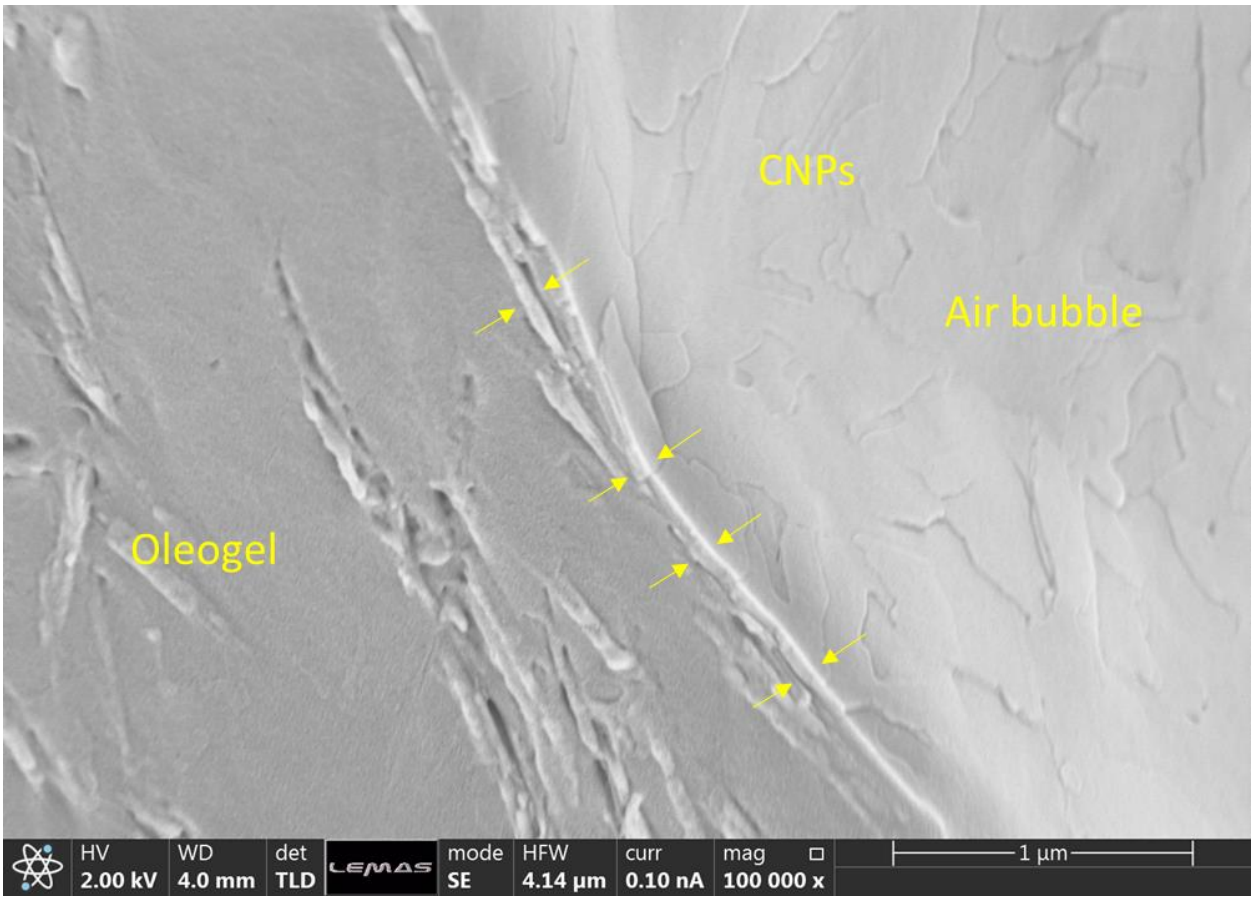

Figure A4. CryoSEM images of an oleofoam sample (15S). CNPs can be seen on the air/oil interface exposing their side (shown by arrows), as well as in the oleogel phase.

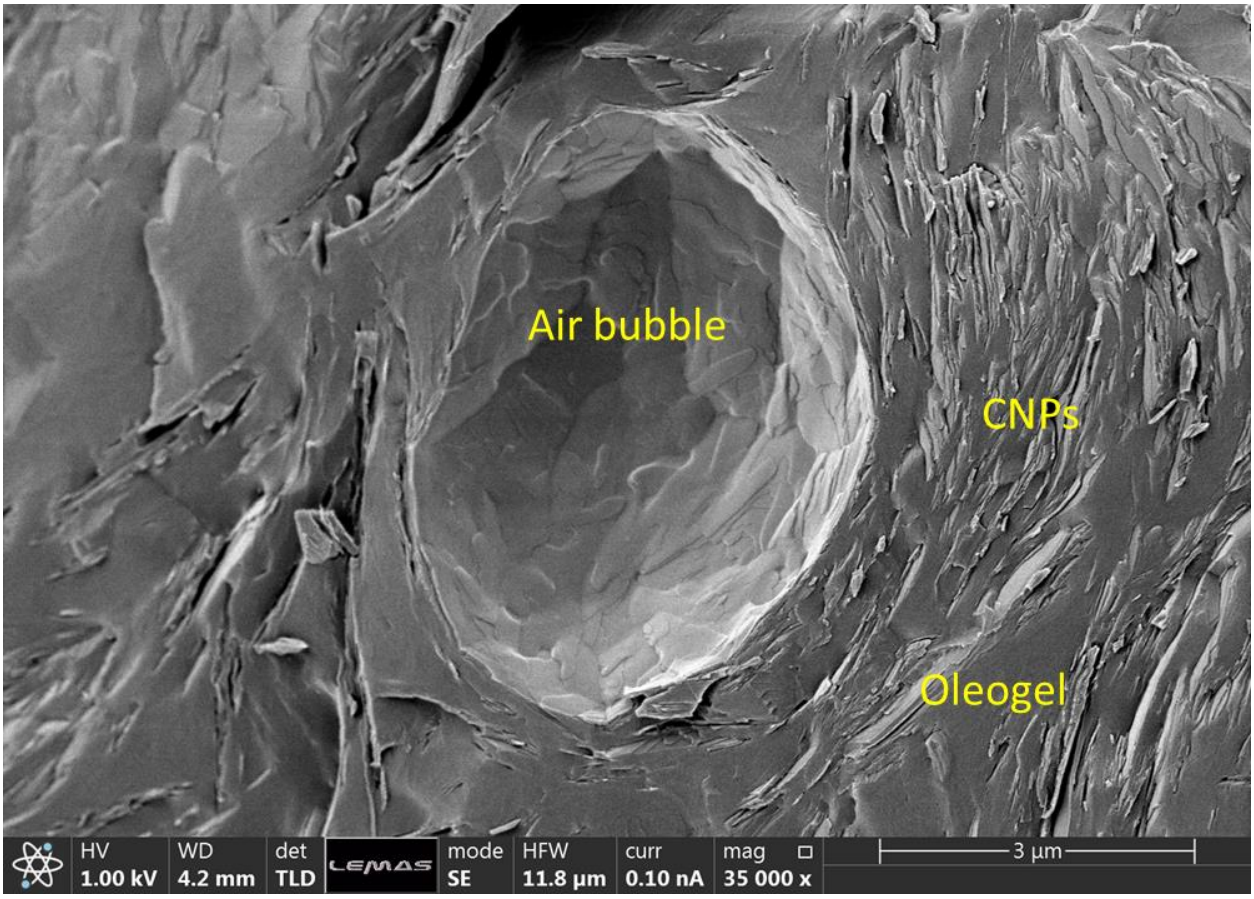

Figure A5. CryoSEM images of an oleofoam sample (30F). Stacked layers of CNPs appear in the continuous oleogel phase, and inside the air bubble in the centre where CNPs expose their large facet to the air/oil boundary

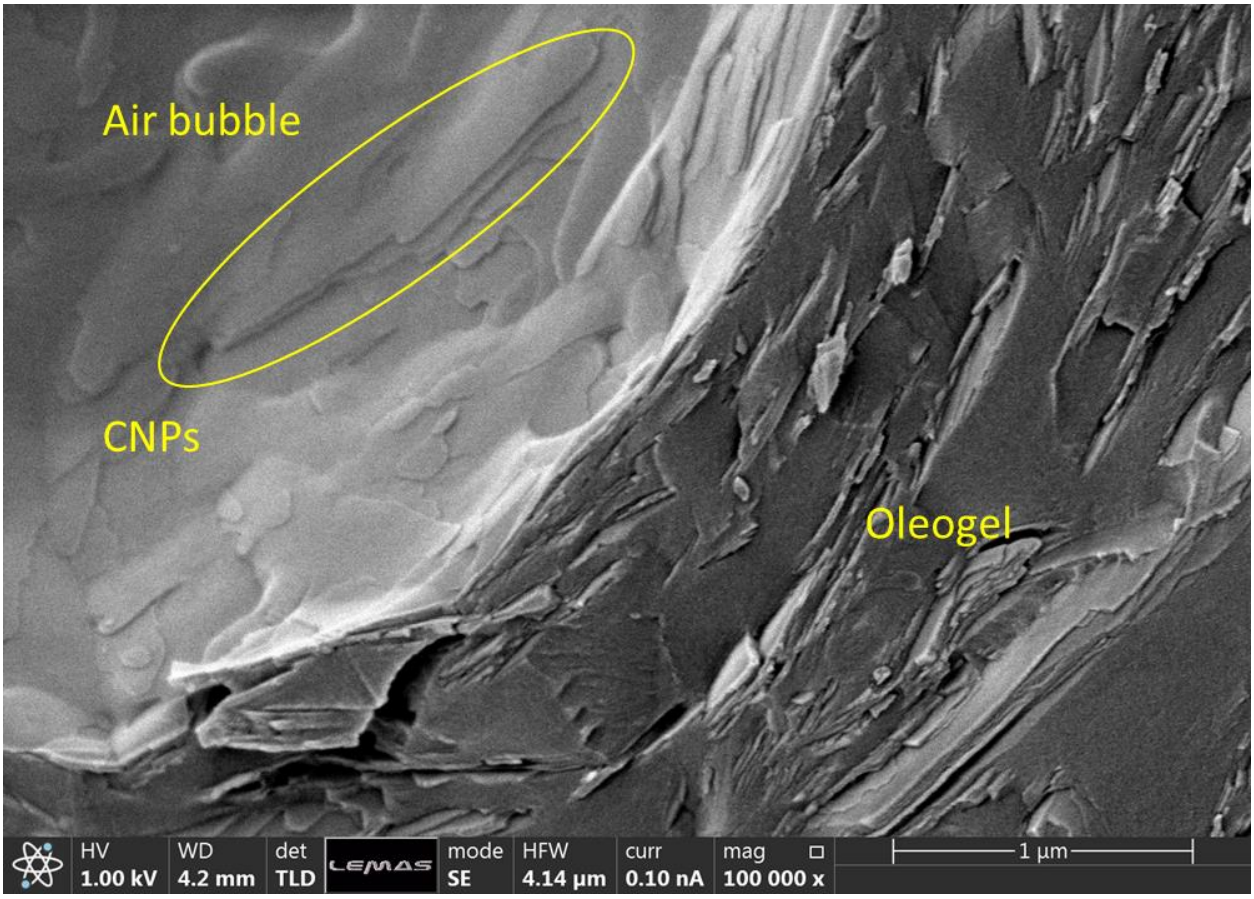

Figure A6. CryoSEM images of an oleofoam sample (30F), with higher magnification compared to Figure A5. A CNP is highlighted within the yellow circle

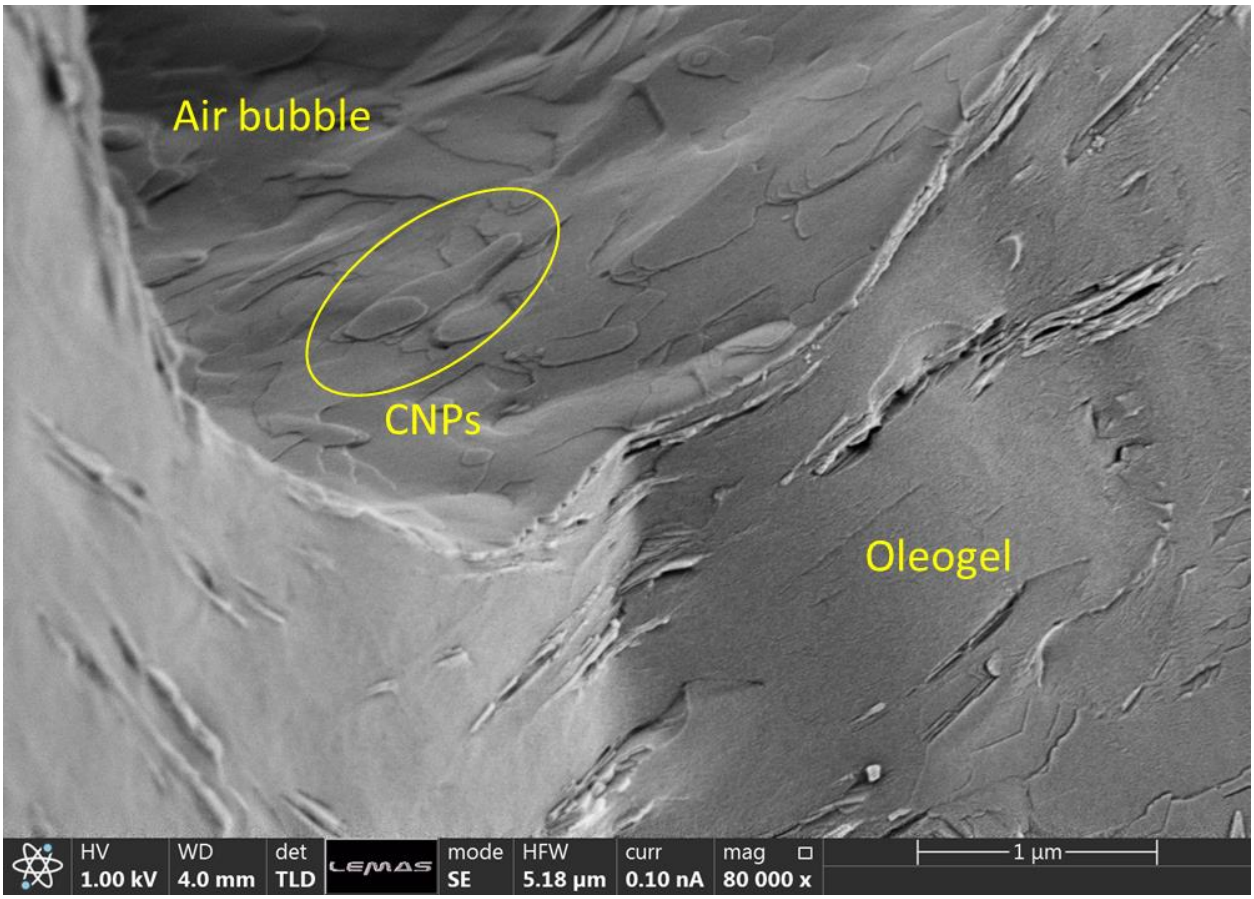

Figure A7. CryoSEM images of an oleofoam sample (30F), focused on the inside of an air bubble. CNPs are visible on the air/oil interface.

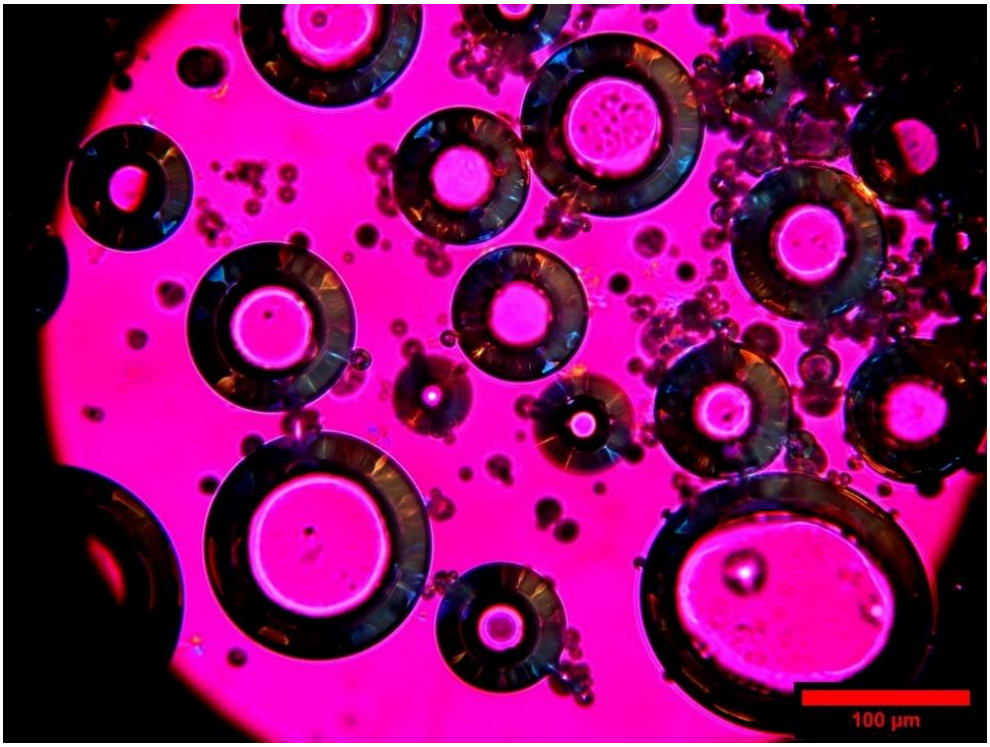

Figure A8. PLM image of a diluted 22F oleofoam with HOSO. Large air bubbles (diameter ~ 100 µm) and small bubbles (< 10 µm) are visible. The image contrast was enhanced using a full-wave plate

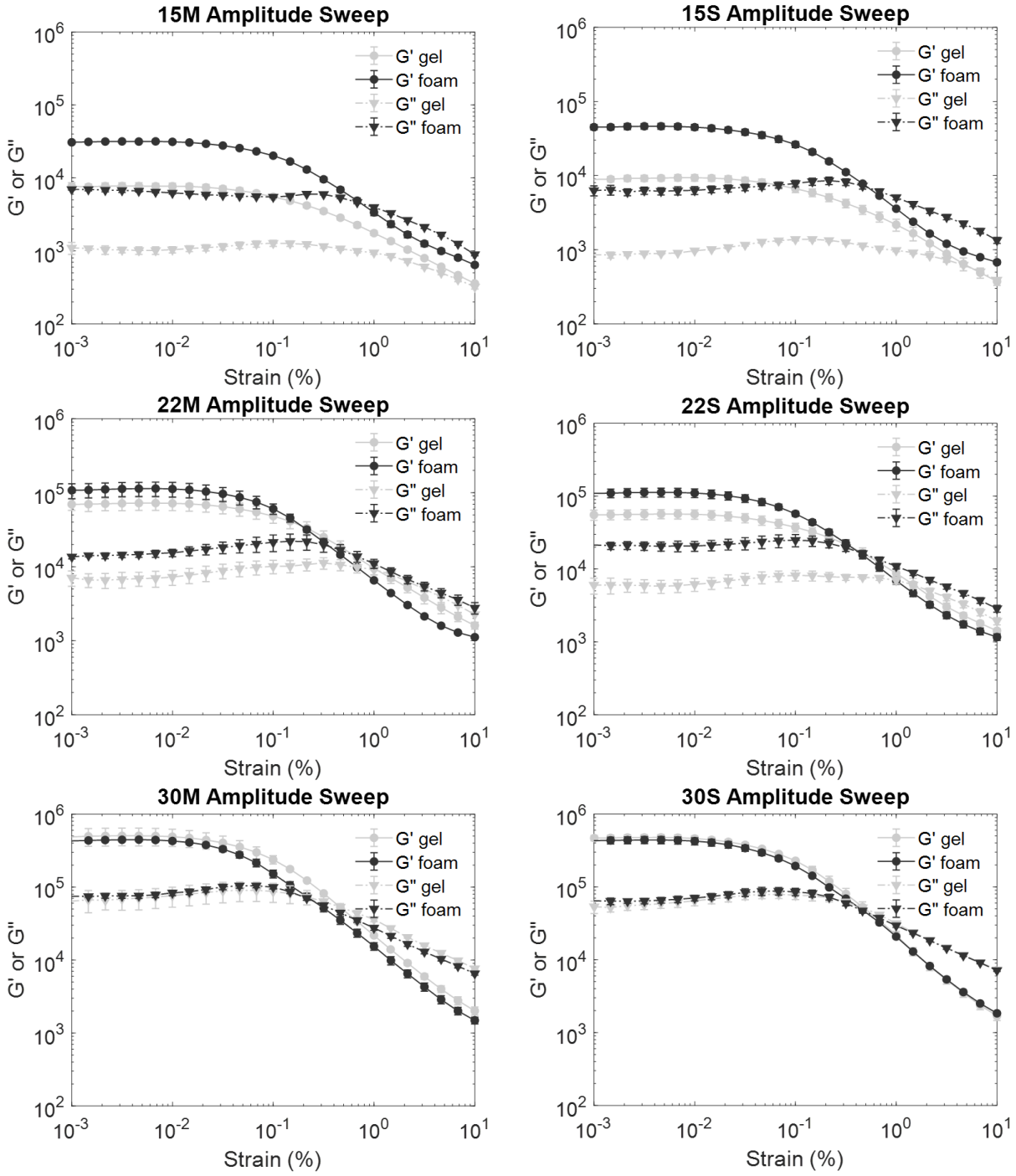

Figure A9. Oscillatory rheology of medium and slow-cooled oleofoams (grey) compared with their oleogel analogues (black). Elastic modulus (G') and viscous modulus (G") are plotted as a function of strain (%).

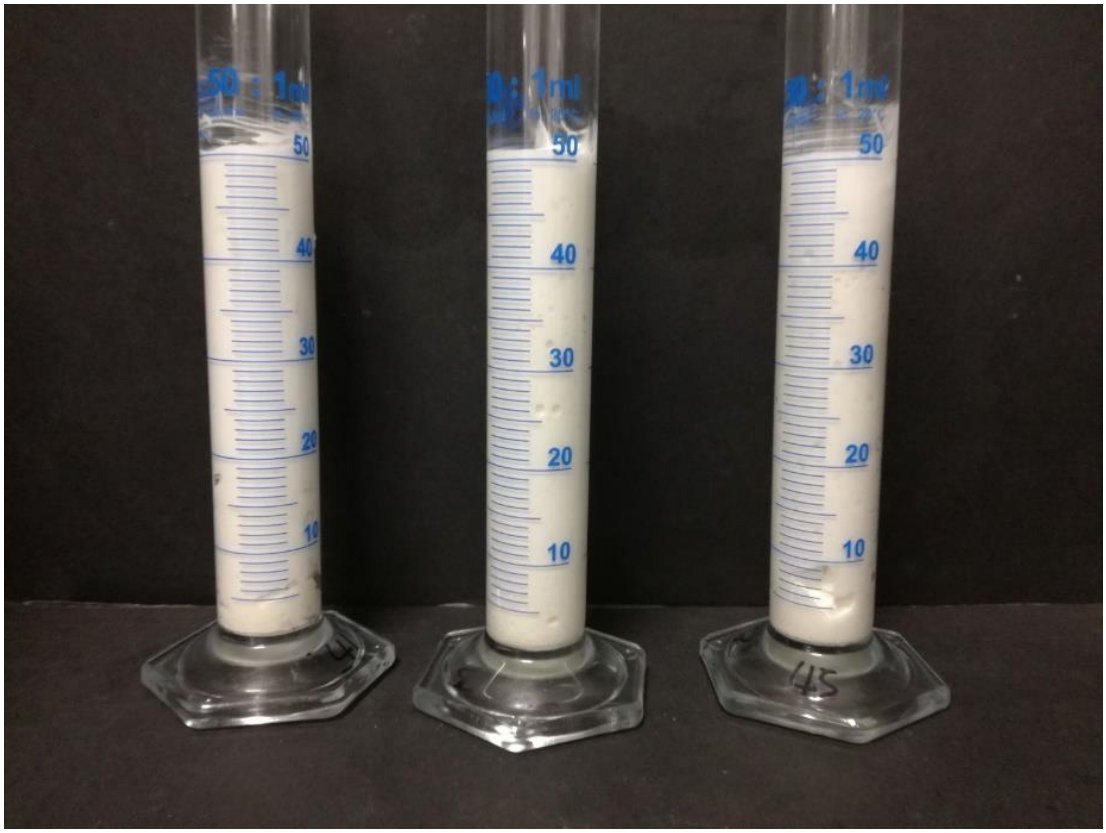

Figure A10. Oleofoams 15F, 15M and 15S after 3 months of storage at 20°C.

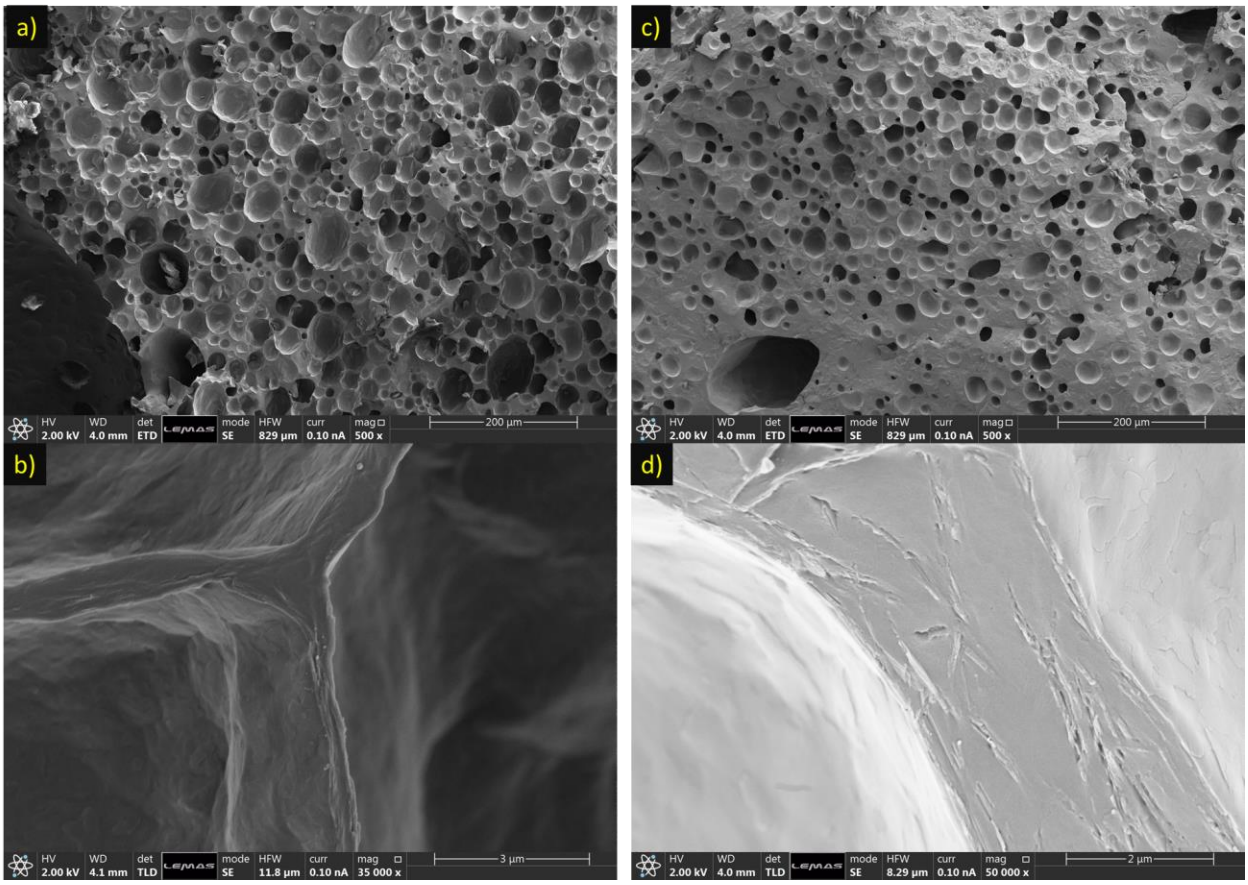

Figure A11. CryoSEM images of a fresh 15S foam (left, a and b) and a sample aged 3 months old at 20°C (right, c and d). Aged samples contain fewer air bubbles in the bulk (c) however still show CNPs at the air/oil interface (d).

Appendix B: supporting information for Chapter 5

The overrun for each volume of interest (VOI) was calculated from XCT data (OR_{XCT}) starting from the definition of overrun as calculated from the cup method (OR_{CUP}) (Eq. B1)

$$OR_{CUP}(\%) = 100 \times \frac{w_{oleogel} - w_{oleofoam}}{w_{oleofoam}} \quad \text{Eq. B1}$$

Where $w_{oleogel}$ and $w_{oleofoam}$ are the weight of a cup of fixed volume (30 mL) of the oleogel and the oleofoam, respectively. The weight can be expressed as the product of the volume (V) and the density (ρ), resulting in Equation B2:

$$OR_{CUP}(\%) = 100 \times \frac{\rho_{gel}V_{gel} - \rho_{foam}V_{foam}}{\rho_{foam}V_{foam}} \quad \text{Eq. B2}$$

One assumption is that the oleofoam can be considered as comprising two phases, the oleogel and the air phase (Equation B3)

$$OR_{CUP}(\%) = 100 \times \frac{\rho_{gel}V_{gel} - (\rho_{air}\phi_{air}V_{foam} + \rho_{gel}(1-\phi_{air})V_{foam})}{(\rho_{air}\phi_{air}V_{foam} + \rho_{gel}(1-\phi_{air})V_{foam})} \quad \text{Eq. B3}$$

OR_{XCT} is calculated from VOI having the same volume, hence $V_{gel} = V_{foam}$. The density of air at 20°C is 1.20 kg m^{-3}, whereas fats and oils display density values two orders of magnitude higher (*ca.* 973 kg m^{-3}). Therefore, the term $\rho_{air}\phi_{air}V_{foam} \ll \rho_{gel}(1-\phi_{air})V_{foam}$ and it can be cancelled out from the equation. Hence, Equation B3 simplifies to Equation B4

$$OR_{XCT}(\%) = 100 \times \frac{\phi_{air}}{(1-\phi_{air})} \quad \text{Eq. B4}$$

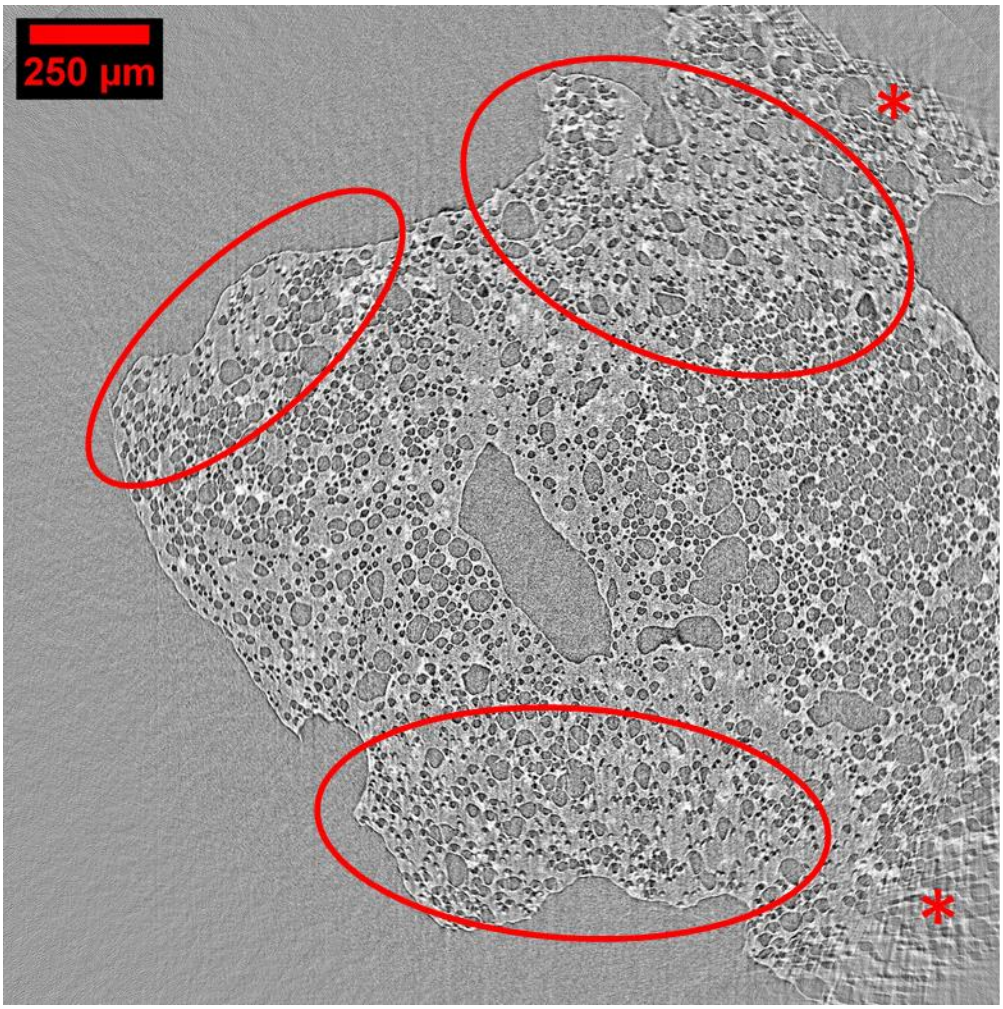

Figure B1. Tomography slice of a 15S fresh sample, using 10 milliseconds exposure time per projection. Slight deformation of the sample in the reconstruction is highlighted with red circles. Artefacts caused by the limited field of view, instead, are marked with an asterisk.

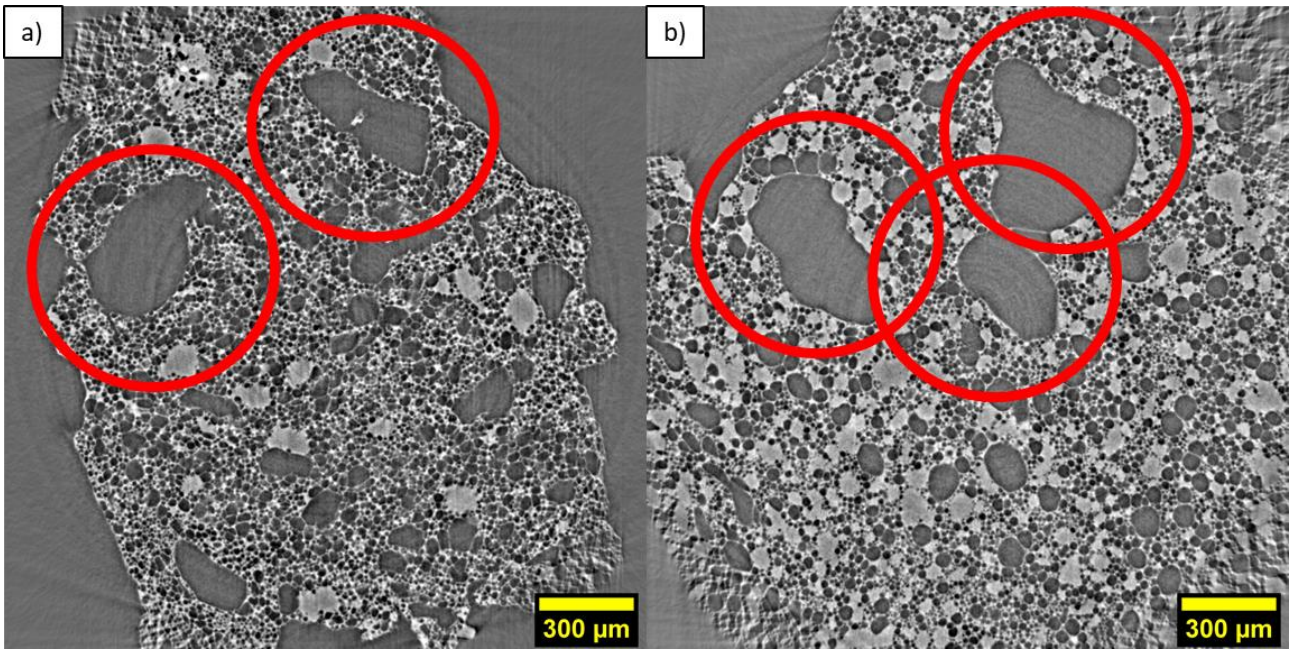

Figure B2. Tomography slices of sample 2 15S 30 Min (a) and sample 2 30F 30 Min (b) highlighting the presence of large air bubbles, with comparable size with the sampling VOI.

Table B1. Overrun values calculated from sample 15S 30 Minutes, using different thresholding methods in the post-processing workflow.

Method	Otsu	Huang and Wang	Renyi's Entropy
VOI1	153.1	146.4	213.1
VOI2	145.2	124.5	237.9
VOI3	150.3	133.3	244.0
VOI4	159.5	133.4	264.8
VOI5	145.3	133.2	198.8

VOI6	160.5	137.7	290.7
Mean (%)	**152.3 ± 6.7**	**134.7 ± 7.2**	**241.5 ± 33.5**

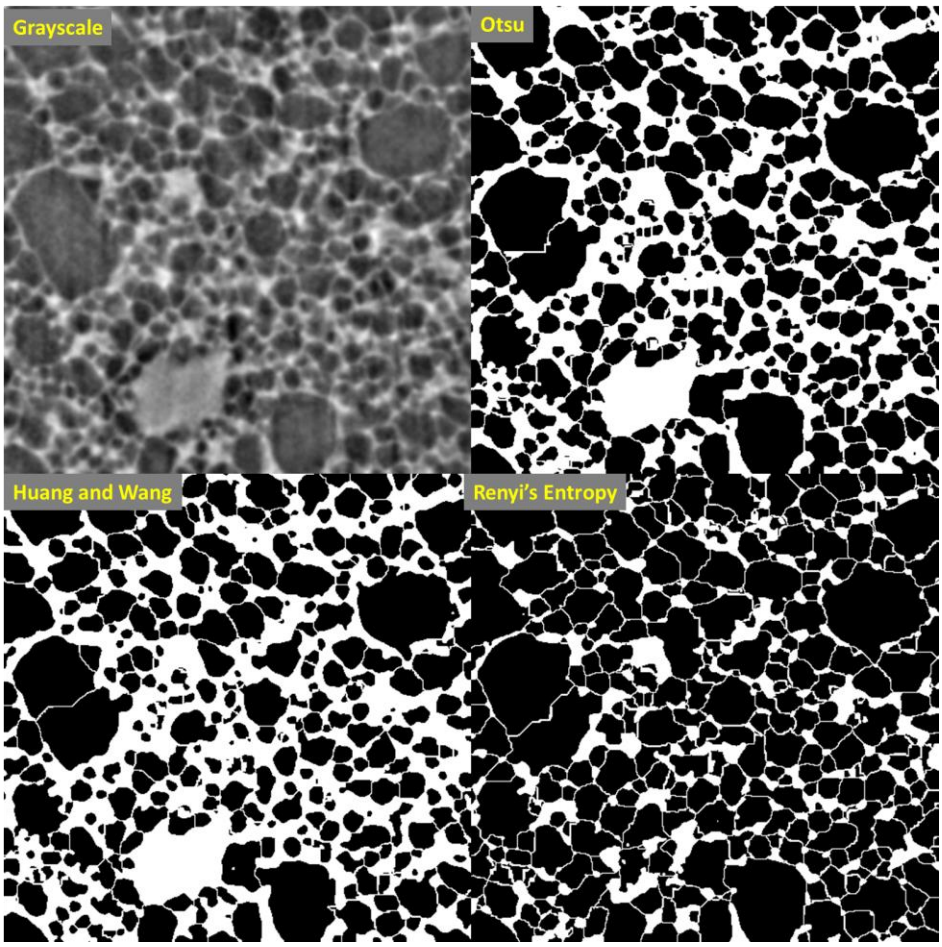

Figure B3. Comparison of different thresholding methods on the calculated sample overrun. Top left, grayscale image of one VOI of sample 15S, 30 minutes; top right, Otsu method; bottom left, Huang and Wang method; bottom right, Renyi's Entropy method.

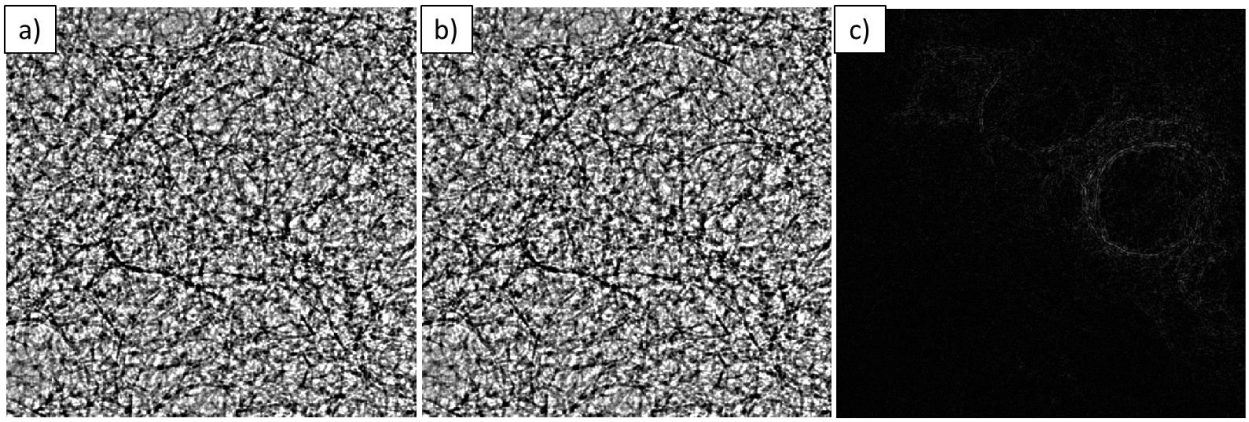

Figure B4. XRR i-th frame (a), i+1th frame (b) and the resulting difference image (c), showing the outline of a large bubble formed between the two frames. The frames were taken while heating sample 30F Fresh, from 293K (20°C) to 300K (27°C) at 1 K/min rate.

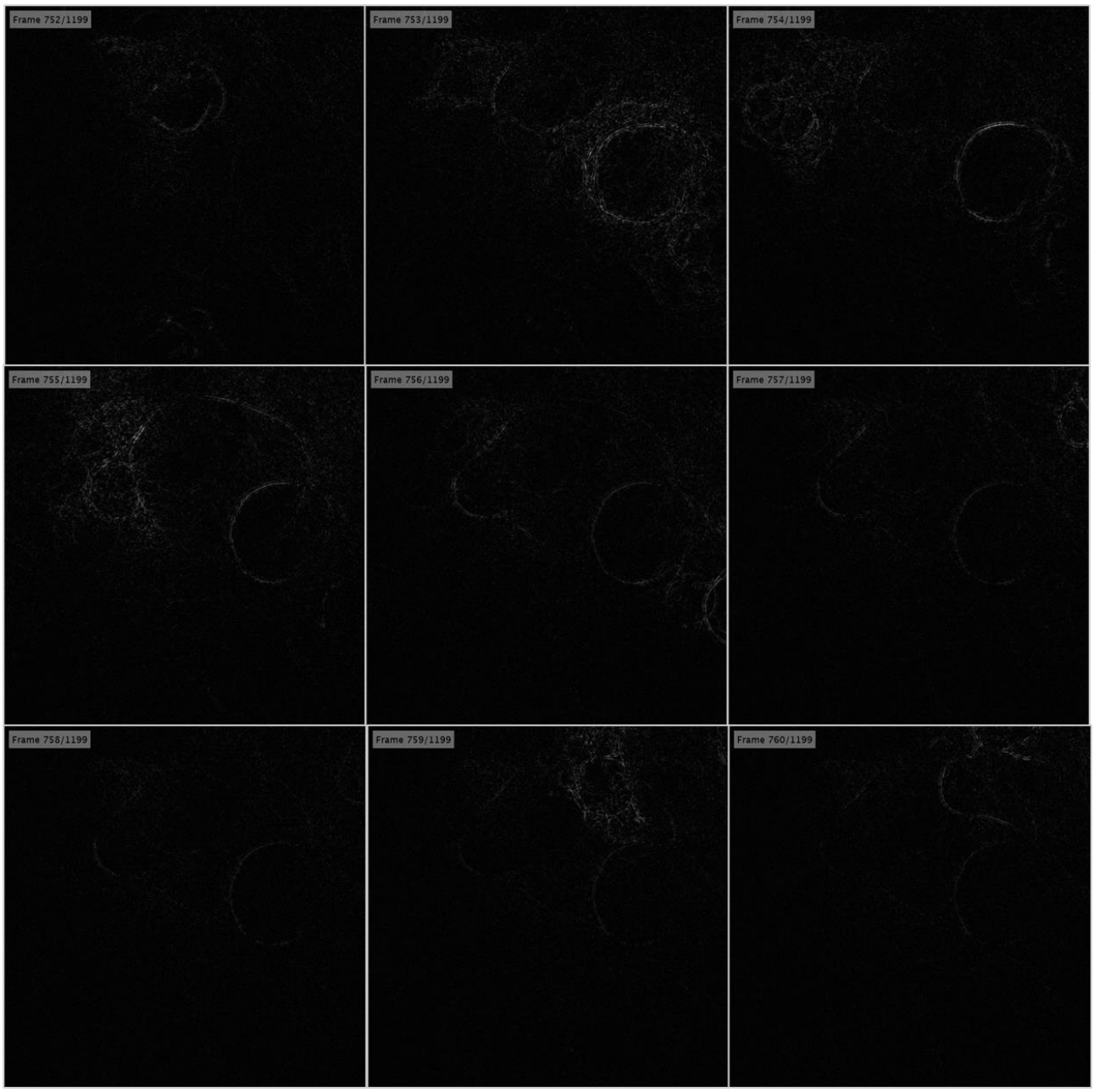

Figure B5. Frames of the difference image stack for sample 30F Fresh during heating. Each frame is separated by 0.667 seconds

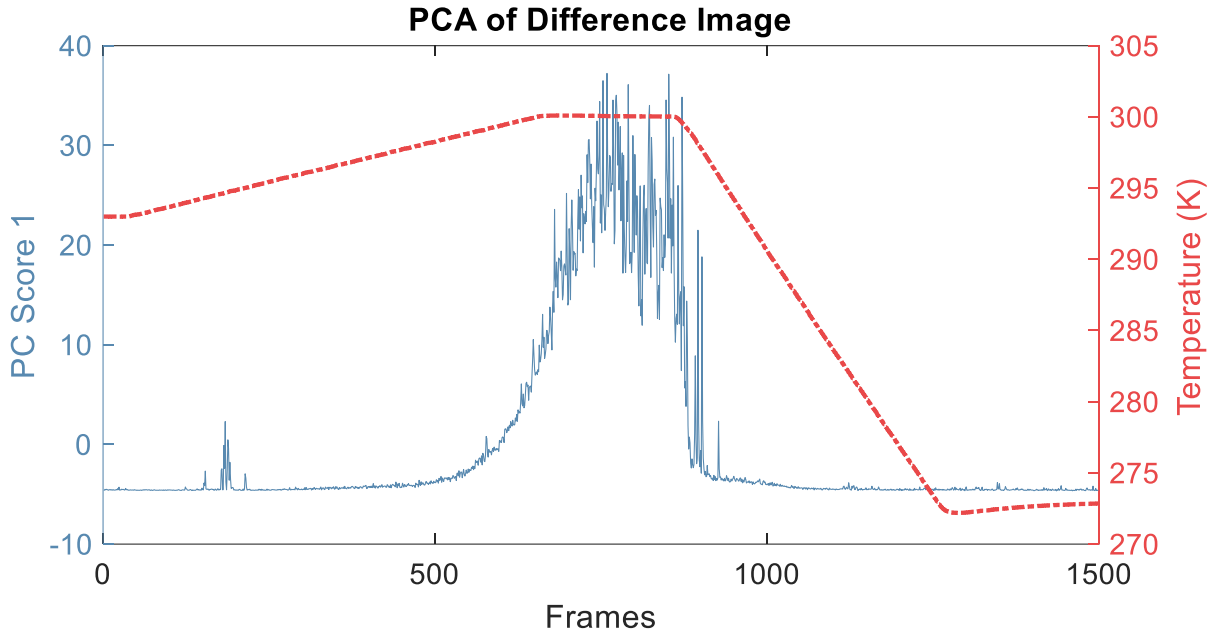

Figure B6. First principal component (PC) score of the PCA analysis of the difference image stack (solid line), and temperature profile (–·) plotted against frame number for the XRR heating experiment of the 30F Fresh sample.

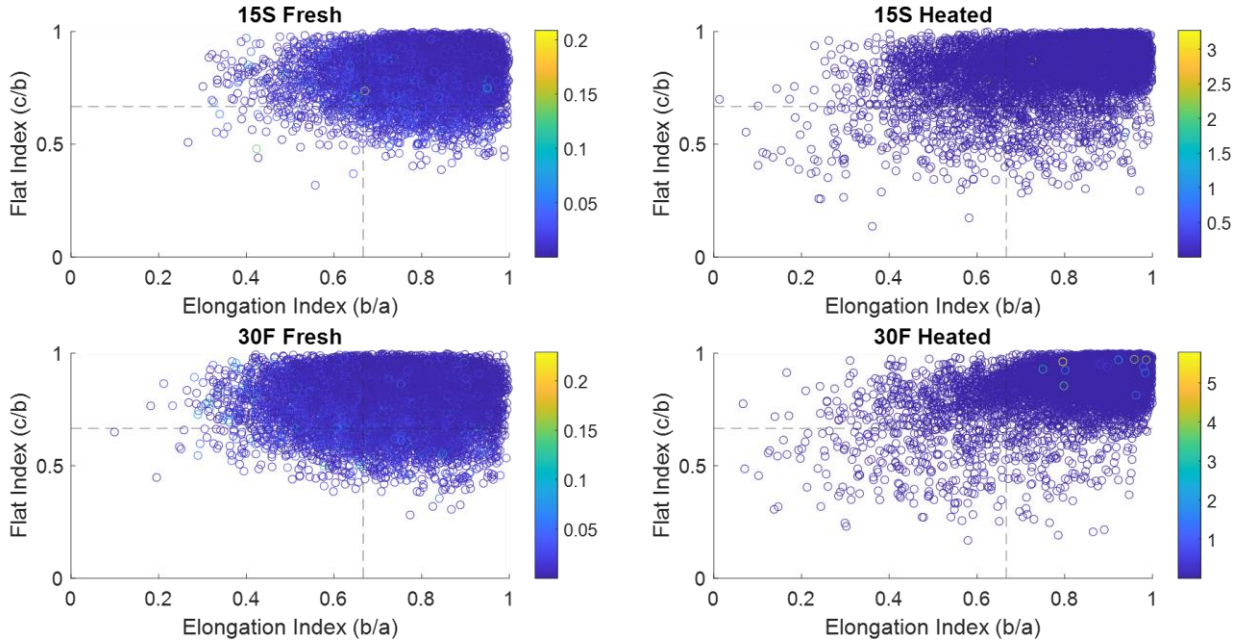

Figure B7. Air bubbles' shape distribution for samples 15S Fresh (a), 15S Heated (b), 30F Fresh (c) and 30F Heated (d). Objects with c/b and b/a ratios larger than 2/3 are classified as spheroidal.

Appendix C: supporting information for Chapter 6

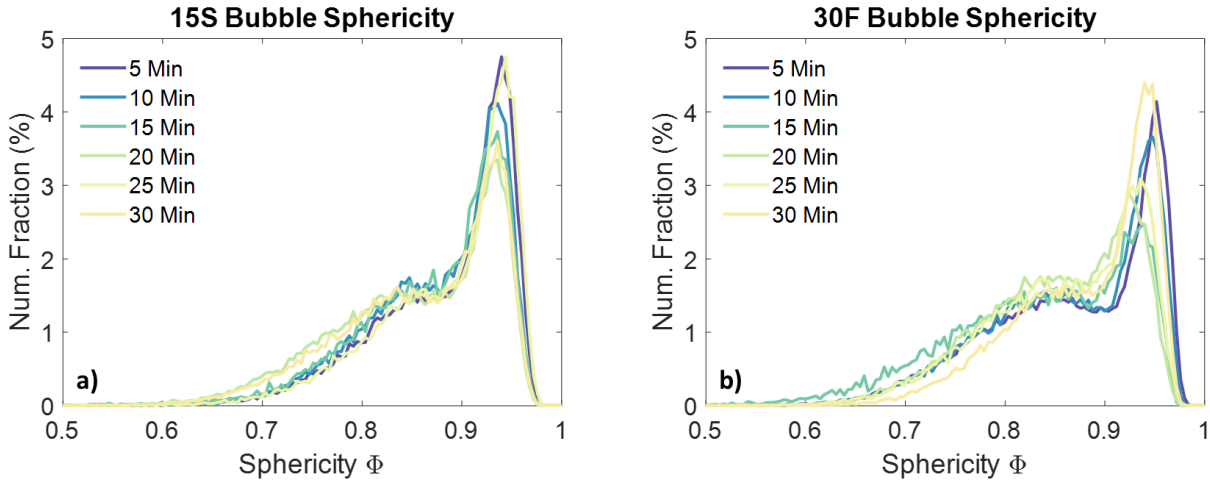

Figure C1. Evolution of the bubble sphericity during aeration for sample 15S (a) and 30F (b).

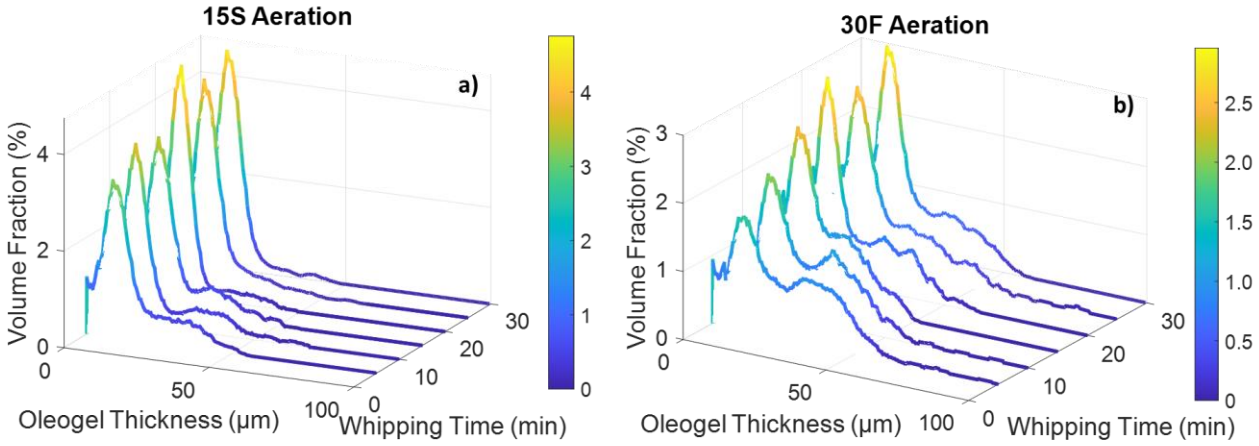

Figure C2. Waterfall plots displaying the evolution during aeration of the oleogel phase distribution for sample 15S (a) and sample 30F (b).

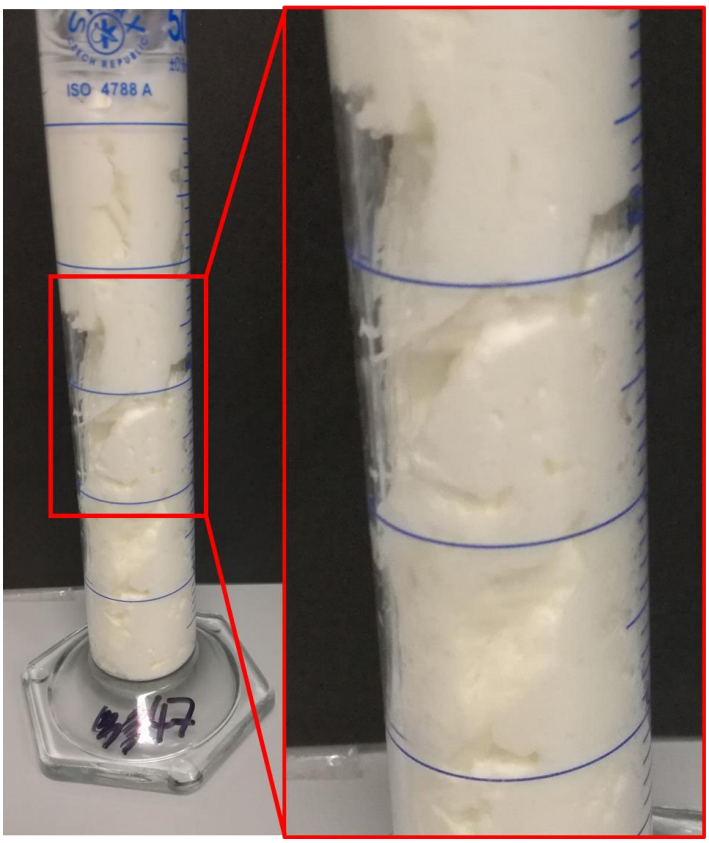

Figure C3. Sample 15S after three months of storage at 20°C. The magnification shows the internal fracture in the sample, with consequent loss of the air phase.

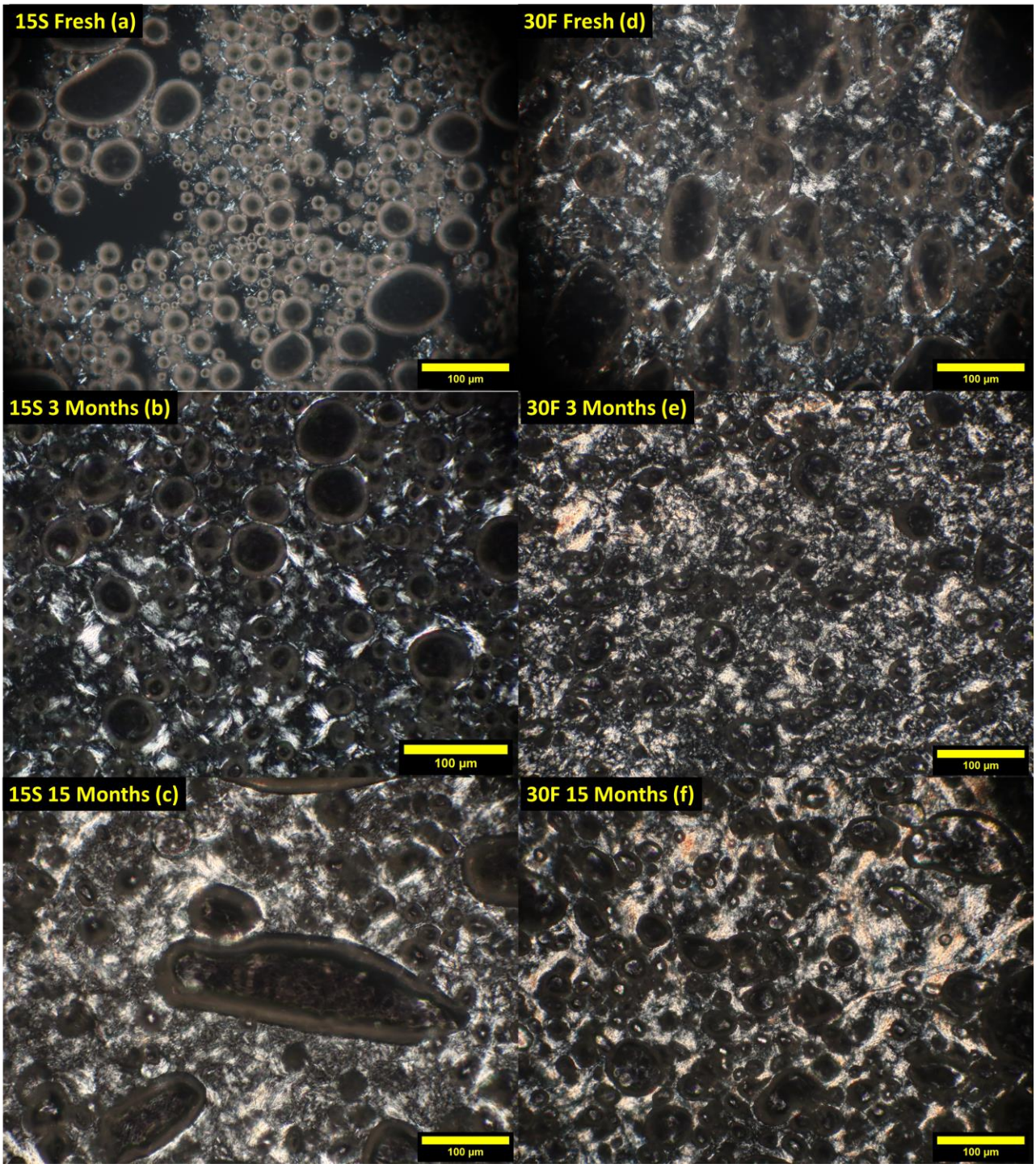

Figure C4. Polarized light images of oleofoam samples at different storage times: 15S fresh (a), after 3 months (b) and after 15 months (c); sample 30F fresh (d), after 3 months (e) and after 15 months (f).

Aged oleofoam samples were investigated with oscillatory rheology with an amplitude sweep experiment. The measurements were carried out on a MCR 302 stress-controlled rheometer (Anton Paar, Austria) using a 25 mm parallel plate, and a sample gap of 1.0 mm. The amplitude sweeps were applied between 0.001% and 10% strain, with a fixed frequency of 1 Hz. The temperature was set to 20°C and maintained using a Peltier hood connected to a F25-HE water circulator (Julabo, Germany). The samples were investigated after 15 months of storage at 20°C, in triplicate. Data analysis was carried out in the Rheocompass version 1.21 software (Anton Paar, Austria), and compared with the results from fresh oleofoam samples.

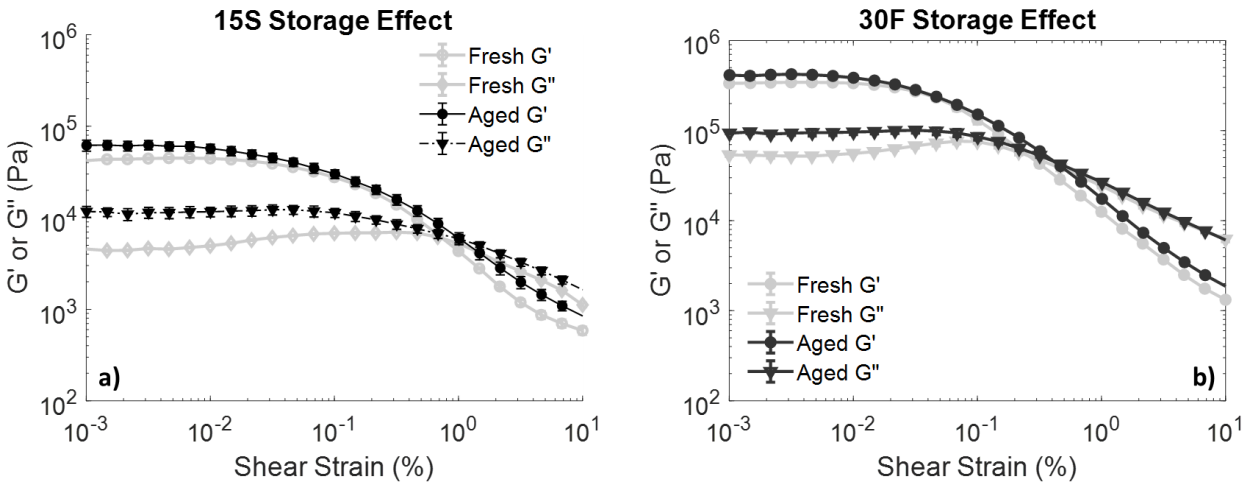

Figure C5. Elastic modulus (G') and viscous modulus (G") of 15S samples fresh and aged 15 months (left), 30F samples fresh and aged 15 months (right).